INFORMATION TO USERS

This manuscript has been reproduced from the microfilm master. UMI films the text directly from the original or copy submitted. Thus, some thesis and dissertation copies are in typewriter face, while others may be from any type of computer printer.

The quality of this reproduction is dependent upon the quality of the copy submitted. Broken or indistinct print, colored or poor quality illustrations and photographs, print bleedthrough, substandard margins, and improper alignment can adversely affect reproduction.

In the unlikely event that the author did not send UMI a complete manuscript and there are missing pages, these will be noted. Also, if unauthorized copyright material had to be removed, a note will indicate the deletion.

Oversize materials (e.g., maps, drawings, charts) are reproduced by sectioning the original, beginning at the upper left-hand corner and continuing from left to right in equal sections with small overlaps. Each original is also photographed in one exposure and is included in reduced form at the back of the book.

Photographs included in the original manuscript have been reproduced xerographically in this copy. Higher quality 6" x 9" black and white photographic prints are available for any photographs or illustrations appearing in this copy for an additional charge. Contact UMI directly to order.

UMI

A Bell & Howell Information Company
300 North Zeeb Road, Ann Arbor MI 48106-1346 USA
313/761-4700 800/521-0600

ASSESSING CLIMATE CHANGE IMPACTS ON RUNOFF FROM KARSTIC WATERSHEDS: NASA/GISS LAND-SURFACE MODEL IMPROVEMENT

by

REGINALD ALEXANDER BLAKE

A dissertation submitted to the Graduate Faculty in Engineering in partial fulfillment of the requirements for the degree of Doctor of Philosophy, The City University of New York.

1998

This manuscript has been read and accepted for the Graduate Faculty in Engineering in satisfaction of the dissertation requirement for the degree of Doctor of Philosophy.

Sept., 15, 1998
Date

Professor Reza Khanbilvardi
Chair of Examining Committee

Sept., 15, 1998
Date

Dean Mumtaz Kassir
Executive Officer

Dr. Lin Ferrand

Dr. Richard Birchwood

Dr. Stanley Gedzelman

Dr. Cynthia Rosenzweig

Dr. David Rind

Supervisory Committee

THE CITY UNIVERSITY OF NEW YORK

Abstract

ASSESSING CLIMATE CHANGE IMPACTS ON RUNOFF FROM KARSTIC WATERSHEDS: NASA/GISS LAND-SURFACE MODEL IMPROVEMENT

by

Reginald Alexander Blake

Adviser: Professor Reza Khanbilvardi

The off-line version of the Goddard Institute for Space Studies (GISS) land-surface hydrological model over-predicted runoff from the karstic Rio Cobre watershed in Jamaica. To assess possible climate change impacts on runoff from the watershed, the model's simulation of observed runoff was improved by adding to it a karst component that has pipe flow features. The improved model was tested on two other karstic watersheds (Yangtze- China and Rio Grande - USA) and the results were encouraging. The impacts that possible climate change may have on the three karstic watersheds were then

assessed. The assessment indicates that in a doubled carbon dioxide climate, the Rio Cobre and the Rio Grande may experience decreases in runoff, especially in low flow periods. The Yangtze, on the other hand, may not experience decreases in total runoff, but its peak flow which now occurs in July may be attenuated and shifted to September.

The results of the study also show that climate feedbacks convolute climate change assessments and that different results can be obtained from the same climate change scenario depending on the choice of the modeling methodology - that is, on whether the models are coupled or uncoupled.

Acknowledgements

My first thanks must be to my Lord and Savior Jesus Christ without whose guidance and grace my life and my achievements would be naught. To my well-beloved mother who, though she was poor, always made sure that as a boy I attended school. Mom I love you, and I thank you. Each of my siblings has played a productive role in my academic development - to them I say thanks. The prayers and encouragement of my pastor Bishop E. E. Williams and my church family at The Pentecostal Church of God have sustained me throughout my academic pursiuts.

Dr. Winfield B. Sylvester has been my mentor. "Doc", you taught me how to learn and how to use knowledge as a tool to aid nation building. The intrinsic continuity between us will never be broken. To my advisor, Professor Reza Khanbilvardi, and to my entire thesis committee, I thank you for your support and your nurturing. To Neal, Ainsley, Trevor, Duhane, Carlos, Noel, Bernard and to my other numerous friends from The City College of New York, I appreciate your friendship and encouragement. Professor Willard J. Pierson's interest in my academic development is appreciated. I say thanks to Deans Watkins and Lowen and to Dr. Akins for the financial support I received through

FORCE and CASI.

Finally, I am indeed very grateful to my wife Sonia, without whose patience, assistance and love this work may never have become a reality. She has been a beacon of inspiration throughout the entire project, unselfishly forfeiting many weeknights and weekends of family time to assist me. To her I say thanks for understanding and for motivating me to persevere.

Table of Contents

LIST OF TABLES

LIST OF FIGURES

1. Introduction

A greenhouse is a glass building used primarily to provide heat for growing plants, especially during the cold winter months. The glass of the greenhouse permits sunlight to enter the building, but it inhibits heat from escaping, thus warming the greenhouse. Similarly, the earth's atmosphere behaves like the glass of a greenhouse. It allows the sun's short-wave radiation to pass through with relatively no obstruction, but water vapor and some constituent trace gases - carbon dioxide (CO_2), methane (CH_4), nitrous oxide (N_2O) and chlorofluorocarbons (CFCs) - trap long-wave, infrared, terrestrial radiation emitted by the earth and re-emit it back toward the surface. This leads to a warming of both the lower atmosphere and the earth's surface.

Atmospheric concentration of greenhouse gases has been rapidly increasing since the beginning of the Industrial Revolution (IPCC, 1990). Anthropogenic activities - the burning of fossil fuels and deforestation - have increased the atmospheric concentration of CO_2 by about 25% in about a century (Rosenzweig and Hillel, 1993). As more and more heat-trapping, greenhouse gases load the atmosphere, the likelihood of substantial global climatic warming increases. Any change in global temperatures may perturb the entire climate system. The probable climate perturbation is usually expressed as

changes in the mean values of specific climate parameters, such as temperature or precipitation. With the mean global temperature expected to increase between 1.5 - 3.5°C by the middle of the next century (IPCC, 1990), researchers anticipate changes in global and regional rainfall patterns, increase in the frequency and intensity of hurricanes, alterations in the timing and magnitude of runoff, greater fluctuations in soil moisture storage, changes in lake levels, sea level rise and adverse impacts on water quality, among a host of other climatic, hydrological, medical and socio-economic changes.

Doubled CO_2 scenarios of runoff for the grid-box that contains Jamaica highlight some of these anticipated changes. Climate change scenarios from four general circulation models (GCMs) - Goddard Institute for Space Studies [GISS], Geophysical Fluid Dynamics Laboratory [GFDL], Canadian Climate Center Model [CCCM] and United Kingdom Hadley Center [UKHC] - point to varying degrees of changes in this crucial hydrologic variable. The GISS model expects about a 30% decrease, the GFDL model predicts a 45% decrease, the CCCM's runoff decreases only by about 5%, and the UKHC has the gridbox's runoff decrease by about 40%. Although the magnitudes of changes in runoff differ from model to model, perhaps due to differences in predicted rainfall and evapotranspiration, the signs are all the same. All four models point

to less streamflow in the near future.

The likely climate change impact on streamflow is a paramount concern, especially to water resource managers in under-developed and developing countries. These managers are grappling with managing currently available water as they consider implementing prudent mitigation strategies. Since water-resource management is already an acute problem for many countries, it is imperative that insight be gained from climate change research to ascertain how climate change may exacerbate the problem. In order to assess global climate change impacts on water resources, plausible scenarios of the future climate must first be obtained. One method of obtaining these climate scenarios is by using GCMs. The assessment of possible climate change impacts on water resources within a karstic watershed on the island of Jamaica via GCM scenarios is the theme of this research.

1.1 Statement of Problem and Hypothesis

The challenge of the research reported in this manuscript is to assess probable climate change impacts on the water resources of the karstic Rio Cobre watershed via the GCM of the Goddard Institute for Space Studies (GISS). The difficulty arises because the GISS GCM, like all other GCMs, does not include

some of the physical, hydrological processes necessary to capture and model this complex karst terrain. The land-surface model component of the GISS GCM in its present state is unable to realistically simulate runoff from a karst watershed. The model grossly over-predicts the runoff.

The hypothesis, therefore, is that the addition of a karst hydrological component to the model will substantially reduce over-predicted runoff and produce better simulations of streamflow for karst areas. This, in turn, would make climate change impact assessments more plausible.

1.2 Objectives

Before probable climate change impacts can be assessed for karstic areas of the world, the land-surface model of the GISS GCM must be enhanced. This is the chief goal of this research. After this karst component has been added to the model, climate change impact assessments can then be done not only for the Rio Cobre watershed, but also for other karst regions in the world.

The objectives of this research are, therefore, three-fold. They are the following:

1) Improve the off-line GISS land-surface model by developing and adding a karst component to it.

2) Develop a global karst map.

3) Use the improved off-line land-surface model to assess possible climate change impacts on the following karstic watersheds:

(a) Rio Cobre (Jamaica)

(b) Yangtze river (China)

(c) Rio Grande river (U.S.A.)

Part 1. Background

2. Climate and Climate Modeling

Unlike weather, which refers to the state (temperature, precipitation, cloud cover, etc.) of the lower troposphere at a given place for a **brief** period of time, climate encompasses "a more enduring regime of the atmosphere; it is an abstract concept. It represents a composite of the day-to-day weather conditions, and of the atmospheric elements, within a specified area over a **long** period of time" (Trewartha and Horn, 1980). Climate is not simply "average weather", for it includes the diurnal and the seasonal extremes in the atmospheric variables of a region. This is what Monin (1986) meant when he

described climate as " a set of weather conditions typical of a region, together with the frequency of these conditions and their seasonal variations."

Leith (1975) defines climate in terms of "... averages over an imagined ensemble of internal states which are in equilibrium with the slowly changing external influences." The internal states he is referring to include, for example, ground temperature, soil moisture, surface wind vector and cloud cover. Examples of external influences are: sea-surface temperature, greenhouse gas concentration and solar energy output.

2.1 General Circulation Models

General circulation models are highly complex, time-dependent, three-dimensional computer models that simulate the many inter-related physical and dynamic processes that are a part of the earth's intricate climate system. They are based on the known laws of physics (energy, mass and momentum conservation), and represent the interactions that exist between the atmosphere, the oceans, the land and the cryosphere. These interactions form feedback mechanisms which generally react on different time-scales. Ocean circulations, for example, typically have time-scales of the order of decades to millennia due to their vast energy storing capacity. The atmosphere, on the other hand,

responds to perturbations on the order of days to weeks and sometimes on even shorter timescales. A brief review of climate feedbacks is given in the next section, and a fundamental overview of feedback mechanisms in the climate system is provided by Peixoto and Oort (1995).

GCMs simulate, among many other things: (1) the large-scale atmospheric circulation that is due to the spatial inhomogeneity of solar heating of the earth's surface; (2) the temperature differences, mainly between the poles and the equator, but also from land-sea contrasts, that induce atmospheric density perturbations (baroclinic instability); (3) ocean circulation; (4) atmospheric-ocean interactions; (5) the planetary boundary layer and its associated turbulent behavior; (6) clouds; and (7) land-surface hydrology. Energy, mass and momentum are perpetually being transformed and exchanged between the components of the climate system. GCMs, therefore, provide numerical solutions for the prognostic simultaneous equations for conservation of energy, mass and momentum and the equation of state on a grid as shown in Figure 1, (Hansen et al., 1983). Figure 2 depicts the diversity of processes that comprise the global climatic system.

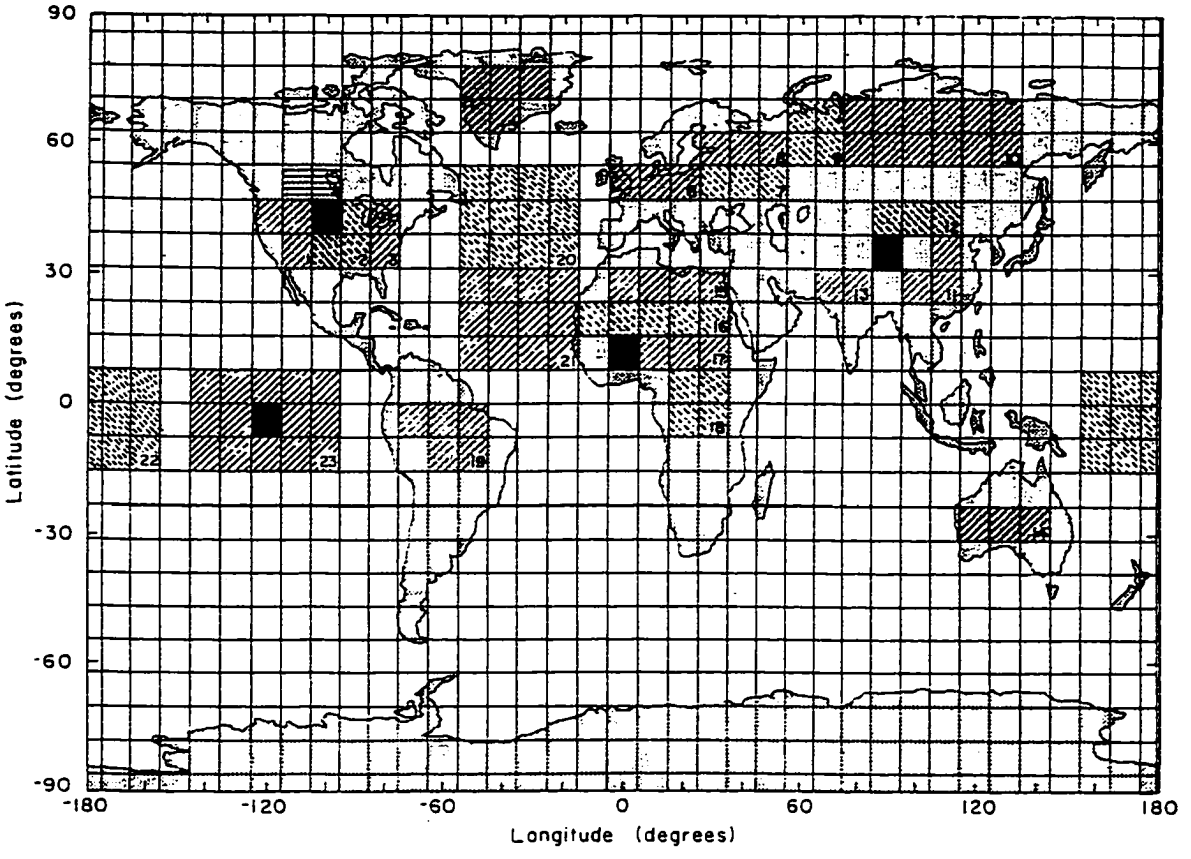

Fundamental equations.

Conservation of momentum: (Newton's second law of motion)	$\frac{d\mathbf{V}}{dt} = -2\Omega \times \mathbf{V} - \rho^{-1}\nabla p + \mathbf{g} + \mathbf{F}$	(T1)
Conservation of mass: (continuity equation)	$\frac{d\rho}{dt} = -\rho\nabla \cdot \mathbf{V} + C - D$	(T2)
Conservation of energy: (first law of thermodynamics)	$\frac{dI}{dt} = -p\frac{d\rho^{-1}}{dt} + Q$	(T3)
Ideal gas law: (approximate equation of state)	$p = \rho RT$	(T4)

Notation

$\mathbf{V}$	velocity relative to rotating earth
t	time
$\frac{d}{dt}$	total time derivative $\left[= \frac{\partial}{\partial t} + \mathbf{V}\cdot\nabla\right]$
Ω	planet's angular rotation vector
ρ	atmospheric density
$\mathbf{g}$	apparent gravity [=true gravity $- \Omega \times (\Omega \times \mathbf{r})$]
$\mathbf{r}$	position relative to planet's center
$\mathbf{F}$	force per unit mass
C	rate of creation of (gaseous) atmosphere
D	rate of destruction of atmosphere
I	internal energy per unit mass [$=c_v T$]
Q	heating rate per unit mass
R	gas content
c_v	specific heat at constant volume.

FIG. 1 GCM gridboxes and fundamental equations

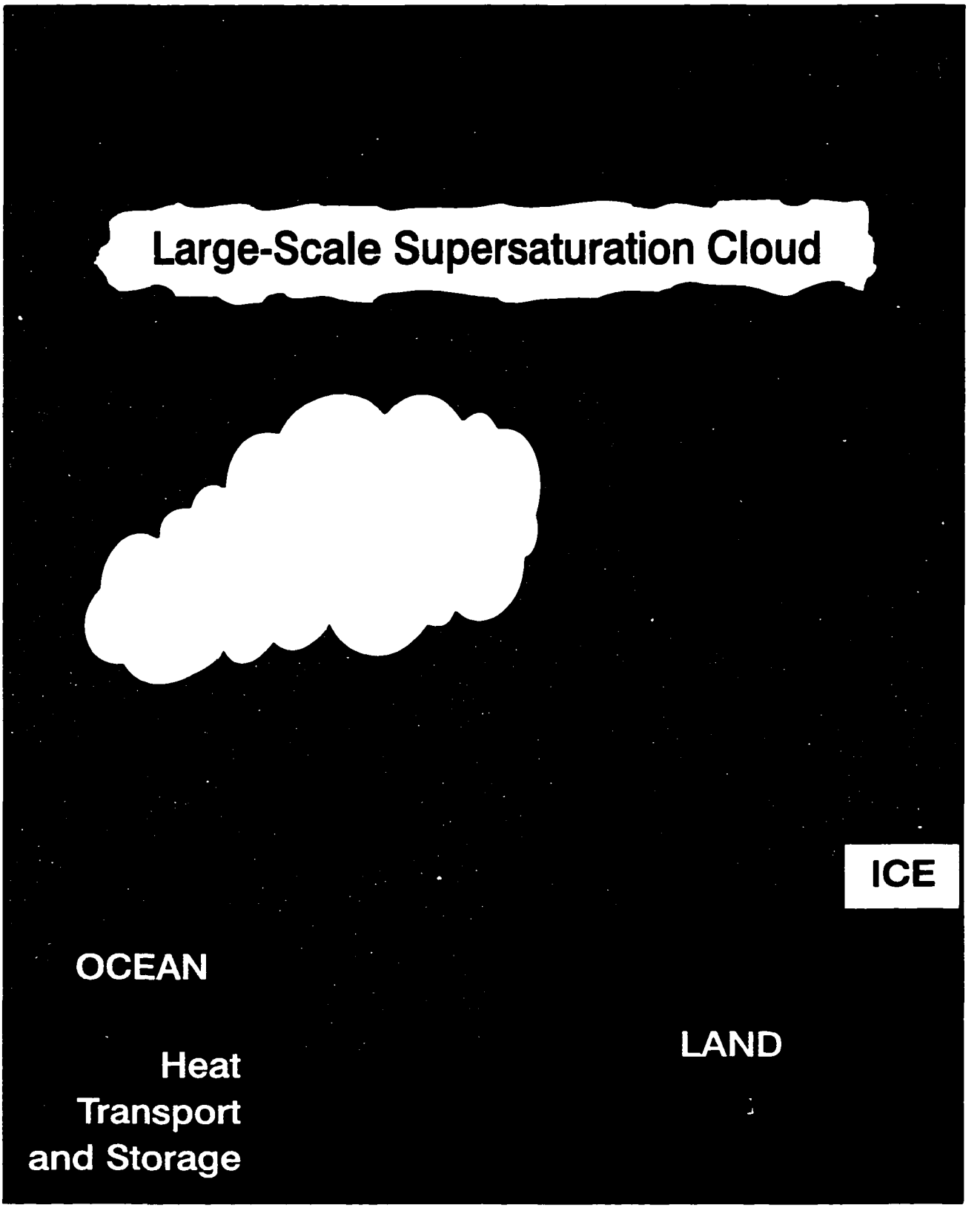

FIG. 2 Climate Processes

2.2 Climate Feedbacks

Studies that purport to assess climate change impacts ought to make deductions from their results in light of the feedback mechanisms that are inherent to the climate system. The climate system's complexity is such that caution must be exercised in the interpretation of results. In this study, for example, the results (some of which may seem anti-intuitive and inconsistent) should be interpreted in view of the complex nature of karst and the intricate feedbacks of the climate system. Climate feedbacks arise, for example, when the global climate is forced by greenhouse warming. The forcing induced by greenhouse gases such as CO_2 on atmospheric temperature affects the climate system to increase the surface temperature. As the surface temperature increases, it triggers a series of 'feedbacks' in the climate system that accentuate (positive feedback) or diminish (negative feedback) the effect of the greenhouse forcing. Climate feedbacks are highly non-linear, and some feedbacks even affect other feedbacks (interfeedback). Some of the feedbacks inherent to the climate system are: water vapor, cloud, surface albedo, soil moisture and vegetation.

Owing to its prominent role in climate change, the water vapor feedback is studied in great detail. Its positive feedback on the climate system has been long agreed upon. The water vapor feedback is as follows: Increased

concentrations of greenhouse gases result in increased infrared emissions to the Earth's surface and thus increasing the surface temperature. An increased surface temperature leads to greater ET and, therefore, increased absolute humidity. Tropospheric temperature increases as latent heat is released when the evaporated and transpired water vapor condenses. As the troposphere warms, its water vapor - holding capacity (humidity) increases according to the Clausius- Clapeyron equation. Since water vapor is an effective greenhouse gas, it traps infrared radiation, and along with the warmer troposphere as a whole, increases infrared emissions back to the surface, heating it up further. This heat input contributes to evaporation and thus completes the feedback loop for water vapor. The earth's blackbody cooling and the inverted lapse rate which results from an increasingly warm troposphere prevents uncontrolled warming of the earth's surface.

Unlike the water vapor feedback, great uncertainty abounds with regards to the cloud feedback. Clouds seem to induce both a positive and a negative feedback. The feedback may be positive as clouds trap infrared radiation and contribute to surface warming. Negative forcing may occur as the clouds reflect incoming solar radiation back to space, thereby reducing the flux of energy reaching the surface relative to clear-sky areas. Whether clouds reflect more

shortwave radiation than they trap infrared radiation thus having a net negative forcing is debatable. Interestingly enough, despite expected increases in humidity in a warmer climate, Cess et al., (1990) reported that most GCMs predicts decreasing global mean cloud cover. Increased drying in the upper troposphere by cumulus subsidence and midlatitude moisture flux divergence may be the reason for the decreased cloud cover, according to Del Genio (1993). Consequently, the overall predicted drop in cloudiness has a net positive (warming) feedback on the climate, according to most GCMs. Therefore, the cloud cover feedback of greenhouse warming appears to be positive according to various GCM simulations. The problem with clouds seem to be its inadequate parameterization and the simplistic treatment of cloud physics within GCMs.

Soil-moisture feedback is a primary process at the surface-atmosphere interface. Other important processes at the inerface are surface albedo and vegetation feedbacks. Soil-moisture feedback ought to be considered on a regional scale. Its feedback loop maybe the following: Warmer surface temperatures (especially if coupled with decreased precipitation) leads to a drier soil surface. A drier soil surface reduces ET and depletes soil moisture. This in turn results in less cloud cover, decreased evaporative cooling associated with the latent heat removal from the surface and increased sensible heating. Less

cloud cover formation enhances surface warming as the atmosphere becomes less reflective to solar radiation. The reduced evaporative cooling and the enhanced transparency of the atmosphere to shortwave radiation strenghten the soil-moisture feedback on surface warming. This is a positive feedback.

The surface albedo feedback refers mainly to ice-mass modifications in a warmer climate. A warmer climate would lead to melting ice and snow, and since ice and snow are more reflective than water or land, a warmer climate may reduce the planetary surface albedo (ratio of reflected to incoming shortwave radiation). The increased absorption of incoming solar radiation warms the surface further, giving rise to the ice-albedo feedback. This feedback would be more pronounced at higher latitudes.

Vegetation feedbacks on climate may be triggered by changes in vegetative areas and types of vegetative cover. These changes could affect ET, soil moisture, surface albedo, the surface-atmosphere temperature and the surface-atmosphere CO_2 exchange. The interdependency of these variables creates major uncertainties in the biosphere-climate system. Consequently, prediction of the sign of vegetation feedbacks on greenhouse warming may be infeasible.

Feedbacks, however difficult it may be to determine some of their signs,

play very crucial roles in the evolution of the future climate. From a hydrologic perspective, the consequences of greenhouse warming go beyond mere surface warming. The analyses of possible climate change impacts on the water balance variables for the three aforementioned karst river basins may show that seasonal modifications in precipitation and runoff, the severity of droughts and the amplification of the magnitude of floods are of special significance for future water supply.

3. Candidate Models for Climate Change Impacts on Water Resources

The literature is replete with models that are used to gain insight about the possible impacts climate change may have on water resources. In spite of this, the modeling community has yet to reach a concensus as to an accepted method or approach to properly assess climate change impacts on water resources, especially regional water resources. One approach is to use either hypothetical scenarios or GCM climate change outputs as inputs to the regional hydrological model. Some of the most prominent modeling approaches have been done by the following: Nemec and Shaake (1982), Gleick (1987), Lettenmaier and Gan (1990), Mimikou and Kouvopoulos (1991), McCabe and Wolock (1992), Nash and Gleick (1993), Kaczmark (1993), Reibsame et al., (1994), Skiles and

Hanson (1994) and Yates and Strzepek (1994). Some of the models that can be used for climate change impact assessment on river basin runoff will now be highlighted.

3.1 The Sacramento Watershed Model

The Sacramento watershed model (Burnash et al., 1973) simulates the hydrologic processes of a river basin, accounting for the movement of water from it initially enters the basin as precipitation until it leaves as runoff or evapotranspiration. It is a deterministic or conceptual hydrological, water balance model that expresses hydrological processes as mathematical equations and then solves them analytically. This model is generally accepted to be one of the most tested and reliable watershed models. It was constructed to adhere to Barnes' theory on recession analyses (Barnes, 1973), Darcy's law of flow through porous media and Hanks et al., (1969) work on moisture phases of water and their vertical movement.

The model's streamflow is a residual which results from the processing of precipitation through an algorithm which divides the soil mantle into an upper zone and a deeper lower zone. Runoff is then computed into the following five basic forms : 1) direct runoff from permanent and temporary impervious areas,

2) surface runoff due to precipitation occuring at a rate faster than infiltration, 3) interflow resulting from the lateral drainage of a temporary free water storage, 4) supplemental base flow, and 5) primary base flow. Schematics of the model and the results of its application to the Rio Cobre are shown in the analyses section (section 5.2).

3.2 GCM Land-Surface Schemes

The layer of the atmosphere closest to the ground, the atmospheric boundary layer, is characterized by significant vertical fluxes of momentum, heat and moisture. These often turbulent divergent fields result from the interactions and the coupling of the land-atmosphere system. The turbulent nature of the boundary layer fluxes facilitates the efficient exchange of momentum, heat and moisture between the ground and the 'free' atmosphere above. It ought, therefore, be obvious that GCMs would be highly deficient if they neglected the land-surfaces processes to which the lower and middle atmosphere are coupled. Carson (1986) defined land-surface processes as:

> " ...those phenomena which control the fluxes of heat, moisture and momentum between the surface and the atmosphere over the continents. These processes influence both the circulation of the atmosphere, often

remotely, and the climate of the surface."

Indeed, from the very inception of numerical weather prediction, the ingenious L. F. Richardson understood that the land-atmosphere coupling must be a necessary component to any numerical weather forecasting model. For example, he proposed that transpiration ought to be parameterized as a function of the conductance of stomatal openings and the saturated vapor density, (Richardson, 1922).

Today, every GCM has a land-surface scheme designed to simulate the momentum, energy and mass transfer between the land-biosphere and atmospheric systems. The current major challenge for modelers is to develop more realistic land-surface parameterizations. A review of some of the more prominent, GCM linked land-surface schemes (interactive Biosphere schemes) in use today follows.

3.2.1 Comparison of Current Land-surface Schemes

Land-surface schemes (models) are many and varied. Research groups involved in mesoscale modeling or GCM applications usually develop their own land-surface model for the sake of compatibility. Eight of the best known land-surface schemes are: the Goddard Institute for Space Studies model (GISS)

(Abramopoulos et al., 1988), the Biosphere-Atmosphere Transfer Scheme (BATS) (Dickinson et al., 1986, 1992), the Simple Biosphere scheme (SiB) (Sellers et al., 1986), Simple SiB (SSiB) (Xue et al., 1991), the Bare Essentials of Surface Transfer (BEST) (Pitman, 1988, Pitman et al., 1991), Interaction Soil-Biosphere-Atmosphere (ISBA) (Noilhan and Planton, 1989), the U.K. Meteorological Office (UKMO) model (Warrilow et al., 1986) and the Canadian Land Surface Scheme (CLASS) (Verseghy, 1991). Each of the eight schemes is just about a decade old, and all eight schemes have the following six, highly significant characteristics:

(1) They are one-dimensional. Although they are ultimately used in three-dimensional models, they only simulate physical processes in the vertical (z) direction. Horizontal interactions of land-surface processes are ignored (except for pseudo-horizontal underground runoff in the GISS model). Land-surface processes of one grid square are independent of those in the neighboring grid squares. Transfers between grid squares are not yet included in the models.

(2) Only soil, vegetation and snow are treated explicitly as land-surface components. Land ice and lakes are not included. This is still the state of affairs although Pitman (1991) showed that lakes significantly contribute to total land evaporation.(3) Carbon fluxes (uptake and release), nutrient fluxes and plant

growth are not included. (4) Vegetation and soil data sets are static. They do not reflect recent rapid changes in land surface cover and morphology. (5) Soil is treated as a layer system with a minimum of two layers. Deardorff (1977, 1978), Hunt (1985) and Wilson et al., (1987a) all show that at least two soil layers are necessary. Models need a top thin layer that responds rapidly to the diurnal cycle, and they need a deeper layer that reflects seasonal changes. (6) Each model has a vegetation canopy layer. However, Sellers et al., (1986), Sellers and Dorman (1987), Sellers et al., (1989) argue that multiple canopies are necessary to realistically model vegetative radiation and momentum transfers. They emphasize, though, that more canopies mean more parameters and more calibrations.

3.3 Data and Physical Processes of Land-Surface Schemes

Parameterization of land-surface models require vegetation and soil characteristics, ground and canopy temperatures, soil and canopy water, evapotranspiration and runoff rates. Each of these requirements will now be briefly examined.

3.3.1 Vegetation and Soil Data for Land-Surface Schemes

Globally digitized vegetation type and soil properties data sets are indispensable for usage and testing of each of the eight land-surface models. Models, however, differ in their assignments of the number of vegetation and soil types per grid square and of the dominant vegetation and soil type for a grid square. They also differ in their parameterization of "vegetation variables" like surface albedo, surface roughness and minimal stomatal resistance. Skelly et al., (1991) pointed out that research ought to be conducted to determine the sensitivity of each model to the above assignments and parameterizations. He further suggested that the models may be sensitive to the different aggregation procedures used to transform vegetation and soil data from their original (1° x 1°) resolution to the required resolution of the host GCM or mesoscale model.

Matthews (1983, 1984, 1985) global vegetation data set (Figure 3) has been widely used. Models like BATS, SiB, SSiB, and GISS use it completely, or they use it partially to augment their own vegetation data sets. BATS, for example, has combined Matthews' vegetation data set with that of Wilson and Henderson-Sellers (1985) while SiB has combined Matthews and Kuchler (1983). The GISS model uses Matthews' vegetation data set exclusively. BEST

FIG. 3 Major vegetation types

and UKMO use only the vegetation data set of Wilson and Henderson-Sellers. Except for BATS, BEST and UKMO which all use the soil data set of Wilson and Henderson-Sellers (1985), all the schemes use slightly different soil data. However, all soil data sets being used are some variant of the FAO/UNESCO (1974) data set.

The use of improved vegetation and soil data sets may bring increased consistency to land-surface modeling. State-of-the-art observation techniques and data digitization on a global scale is underway. They will go a long way in maintaining an up-to-date vegetation and soil data archive accessible to users of each of the eight models.

3.3.2 Physical Processes of Land-Surface Schemes

3.3.2.1 Ground and Canopy Temperatures

Two methods are used by the land-surface schemes to simulate soil heat flux. One method is to explicitly model the soil temperature profile and soil heat conduction with a multi-layer soil model of specified depth and with appropriate vertical resolution and boundary conditions. The heat conduction equation is then solved for temperature by using a finite difference scheme. The land-surface models of UKMO, GISS and CLASS use this method albeit they each use

different numbers of soil layers. The second method - the "force-restore" method, a term introduced by Deardorff (1978) - is currently being used by ISBA and SiB (SiB had first used the other method - Sellers et al., (1989)). The force-restore method is formulated from an analytical solution of the soil heat conduction equation for one-dimensional heat transfer in a semi-infinite, homogeneous soil whose surface is heated in a simple periodic manner. After Dickinson (1988) modified the force-restore method to account for snow and soil heterogeneity, it was used in an updated version of BATS. Cogley et al., (1990) included ideas from the force-restore method into the finite-difference method used by BEST. In BEST, they now solve for the multi-layer soil temperatures by taking into account the contribution to the thermal coefficients from snow, soil minerals, soil water and air.

In SiB, a single temperature and a single heat capacity is assigned to the whole canopy. A single canopy temperature is also prescribed in BATS and BEST, but they set the heat capacity to zero. In the UKMO land-surface model, thermal effects of the canopy are completely neglected while CLASS has not yet fully incorporated vegetation in its model. Since stomatal resistance depends on vapor pressure deficits which in turn depend on leaf temperature, assigning prescribed temperatures to the canopy probably misrepresents stomatal

resistance and thus transpiration. In the GISS land-surface model, canopy temperature is not assigned but elaborately calculated for both wet and dry canopies.

3.3.2.2 Soil and Canopy Water

The prognostic variables used to describe soil moisture movement vary from model to model. In BATS, soil moisture content is expressed in terms of water equivalent depth (m). In the GISS land-surface model, the mass of liquid water per unit lateral area in the soil layer - a product of water density and depth, ($kg\ m^{-2}$) - is determined. In ISBA, the actual volumetric soil moisture is described, ($m^3\ m^{-3}$). In SiB and BEST, the dimensionless ratio of actual volumetric soil moisture in a layer to its value at saturation is used to express soil moisture wetness. Soil moisture concentration is the variable used by both UKMO and CLASS. It is a product of water density and actual volumetric soil moisture, ($kg\ m^{-3}$). Essentially these different variables are all related.

For soil water flux, all eight schemes employ Darcy's law which is a relationship between a potential gradient, hydraulic conductivity and water flux. Therefore, all of them simulate the same processes when calculating the movement of soil water. Throughfall, canopy drip, snow melt, evaporation,

surface runoff, capillary and gravitational drainage and transpiration are included in soil water calculations. The GISS land-surface model additionally includes the surface slope and the interstream distance in underground runoff and soil moisture content calculations. Only BEST and CLASS explicitly include a frozen soil water budget.

A power law relationship between the fractional area of leaves covered by water and the ratio of water stored on leaf surfaces to its maximum value (Deardorff,1978) is used by BATS, BEST, GISS and ISBA to calculate the wet fraction of a canopy. Variants of this equation have been used by SiB, Sellers et al., (1986) and UKMO. In SiB, for example, the fractional area of leaves covered by water isgiven by this power law relationship only when the saturation vapor pressure (e_*) at the canopy temperature (T_c) is greater than the vapor pressure (e_a) in canopy air space. Otherwise, it is set equal to unity. However, the models differ in their specification of the maximum water the canopy can hold. In general, it is assigned a value of the order of 10^{-3} or 10^{-4}.

3.3.2.3 Evapotranspiration

Total evapotranspiration from the land-surface is comprised of soil evaporation, canopy evaporation and transpiration. Each component of total

evapotranspiration can be parameterized as a product of potential evaporation and an efficiency factor (β). For soil evaporation, β is controlled by the soil wetness and the soil properties (Eagleson, 1970, 1978, 1986; Clapp and Hornberger, 1978; Abramopoulos et al., 1988). For canopy evaporation, β depends on the amount of water on the canopy and on the plant morphology - vegetation cover and leaf area index (Rutter, 1975; Gash, 1979; Sellers et al., 1986). For canopy transpiration, β is determined by plant physiology, plant morphology and environmental conditions (Jarvis, 1976; Jarvis and McNaughton, 1986; Sellers et al., 1986).

Moisture flux from the ground to the air above is limited by diffusion. BATS, for example, specifies evaporation from the ground (E_s) as the minimum of potential evaporation (E_p) and the maximum moisture flux through a saturated soil surface (E_{max}). The potential evaporation is considered to be proportional to surface air density (ρ_a), an aerodynamic drag coefficient (C_D), wind speed (V_a) and the difference between saturated (q_g) and actual (q_a) mixing ratios. The maximum moisture flux through a saturated soil surface depends on the average soil diffusivity (D), the soil wetness of the active soil layer (s_o), and the depths of surface (Z_1) and active (Z_o) soil layers.

In BEST and GISS a similar approach is used. However, the exfiltration rate

(E_{max}) in BEST is obtained from Eagleson (1970) combined with measured soil properties of Clapp and Hornberger (1978) while E_{max} for GISS is given by Gardner and Hillel (1962).

In SiB a completely different approach is used. There the evaporation from the ground is determined explicitly as a function of the relative humidity of the air at the soil surface (f_h), the vapor pressure (e_t) at ground temperature (T_g), e_* , ρ_a, specific heat capacity of the soil at constant pressure (c_p), ground surface resistance (r_{surf}), aerodynamic resistance (r_a), a psychrometric constant (Υ), the latent heat of vaporization (λ) and the soil moisture in the top soil layer (W_1).

In the UKMO land-surface model, evaporation from the ground is crudely modeled as a simple product of β and the evaporation from the canopy.

Morton (1984) coined the term "wet-canopy" evaporation to distinguish canopy evaporation from canopy transpiration. Canopy evaporation or interception loss is rainfall that is held on canopy surfaces as liquid water and which then evaporates without reaching the soil below (Rutter, 1975; Gash, 1979). In all eight land-surface models, canopy evaporation is parameterized as a product of a wetting function and the potential evapotranspiration.

Canopy transpiration, dry-canopy evaporation, is a physiological process

involving water transfer from the soil through the roots, stems, branches and leaves (Sellers, 1992). Transpiration is limited by the supply of water to the roots and the atmospheric demand for water. The canopy cannot transpire when dew is forming onto its surface or when the soil moisture is below the wilting point. Each model uses some form of the Penman-Monteith equation for transpiration. However, they have different parameterizations for stomatal resistance, dry fraction of transpiring canopy and root-limiting factor. The root-limiting factors used are all some simplified variations of Cowan's (1965) formulation.

3.3.2.4 Runoff

Runoff is a crucial component of the hydrological cycle. Depending on the discipline (hydrology, climatology or oceanography), runoff may have slightly different definitions. However, in general, runoff can be understood as being the residual from precipitation after evaporation and soil moisture storage requirements have been met. Hydrologists are concerned with runoff at the catchment scale as a direct response to precipitation. Climatologists study it as part of the overall water-balance on a spatial scale greater than the catchment, e. g., at the continental scale (Eagleson, 1986; Shuttleworth, 1988b; Dickinson,

1992). Oceanographers are concerned with runoff for its net fresh water input (which alters oceanic salinity) and its points of discharge to the oceans. With the development of a more holistic approach to runoff (macrohydrology and global-scale hydrology), there has been a confluence of these different spatial scale studies of runoff (Eagleson, 1986; Shuttleworth, 1988b).

In the eight land-surface schemes, runoff is treated as a diagnostic variable. It is generally regarded as the excess of water in the soil reservoir. Total runoff, therefore, is the sum of surface runoff and subsoil drainage.

In BATS, surface runoff is calculated as a function of the wetness of active and surface soil layers, saturated soil water density, precipitation rate, canopy cover fraction, snowmelt rate, canopy drip rate and surface evaporation. In SiB, runoff is parameterized as excess precipitation rate minus infiltration rate plus gravitational outflow from the lowest soil moisture store. Runoff in BEST and ISBA is the same as it is in SiB except for the addition of overflow from each soil layer in BEST and the removal of drainage to the water table in ISBA. In the GISS land-surface model, Hortonian surface runoff (R) occurs whenever the precipitation rate is greater than the rate of maximum infiltration (N),

$$R = \max(0, P - N) \qquad (1)$$

Within f_p ,where the probability density function distributes the convective precipitation, the mean value of R is

$$\langle R \rangle = \int (P - N)\, p(P)\, dP \qquad (2)$$

Since the mean runoff for the gridbox, $\mathbb{R}$, is related to mean runoff in f_p as

$$\mathbb{R} = f_p \langle R \rangle \qquad (3)$$

the mean runoff for the gridbox is given by

$$\mathbb{R} = \mathcal{P} \exp(- f_p N / \mathcal{P}) \qquad (4)$$

The runoff is, therefore, assumed to be the probabilistic distribution of the positive difference (P - N). Similar to runoff in the GISS land-surface model, runoff in the UKMO model is assumed to be exponentially distributed at the sub-grid scale level (Warrilow et al., 1986; Gregory and Smith, 1990).

From these candidate models, the Sacramento Watershed model and the GISS land-surface model were chosen for this study. The Scaramento Watershed

model was chosen because the Jamaican water authorities are using it for the island's hydrological forcasting, and the GISS land-surface model was selected for its robust physical realism and its compatibility to the GISS GCM.

4. Karst

4.1 Introduction to Karst

The Slav word *Krš* which means crag or stone (*Krš* is also the name of the limestone country in western Slovenia), the Indo-European word *kar* which means rock and the Italian word *carso* which means stony and barren have all been Germanized into the word *karst*. Karst is the result of a geomorphological process driven by the dissolution of limestone and other soluble rocks. Water is the main agent for the dissolution process.

Karst terrain has distinctive characteristics and landforms above and below ground and hydrologic pathways that arise primarily from the high solubility of carbonate rocks by natural waters. These pathways may be described as a pronounced, well developed secondary porosity. In karst regions the landforms are characterized by: (1) closed depressions and sinkholes of a variety of sizes; (2) disrupted or sinking/losing streams and sometimes non-existent surface drainage; and (3) a complex, underground, conduit, cave

drainage system. The great variety of karst landforms include rough and jumbled land with deep depressions, isolated towers, pointed hills, gentle, soil-covered plains, gorges, meander caves, natural bridges, dry valleys, dolines, cockpits, uvalas and poljes in varying degrees of development. Underground, dissolution and mass transport by mechanical erosion produce huge voids, so that caves are more frequent, more elaborate and larger in karst than in any other terrain.

4.2 Global Karst Areas

If karst areas are defined as landforms produced by the solution process (regardless of scale, surface/underground features, or rock type) as the East Europeans and the Russians define it, then approximately 50,000,000 km^2 or 20% of the earth's land surface is karstic (Gvozdetskiy, 1965). If karst areas are defined only as landforms produced by the solution of carbonate rocks, then according to Ford and Williams (1989), a conservative estimate of global karst areas is approximately 12% of the earth's ice-free, land surface. Carbonates are much more abundant in the Northern Hemisphere than in the Southern Hemisphere. Much of the world's population live on carbonate rocks. Ford and Williams (1989) estimate that about 25% of the world's population is dependent on water that has been a part of the karst system.

One-third of the former Yugoslavia is karstic. Carbonate and other water-soluble rocks are widely distributed all over Italy. Most of France is karstic. In fact, the most important karst area in Europe (Vercors) is located in France. Three of the ten longest karst caverns, the three deepest karst caverns, and two of the largest underground rooms in the world are in France. One-sixth of Austria is karstic. More than 3,000 km^2 of the former Czechoslovkia is comprised of carbonate rocks. Karst is widely spread throughout Russia. Over 15% of Great Britain is karstic. About 15% of the continental United States, exclusive of Alaska, has limestone, gypsum and other karst rocks. More than 2 million km^2 of China's surface area is covered by limestone. Figure 4 (Ford and Williams, 1989) is the only global karst map, a very approximate one in fact, that has been published (personal communication with Ford). Ford has given this author permission and encouragement to reproduce Figure 4.

Figure 5 shows Ford and Williams data superimposed on the GISS GCM's 4 x 5 grid, and Figure 5a is its digitized version showing global percentages of karst. It is quite evident that much of the earth's surface is composed by rocks that are soluble in natural waters.

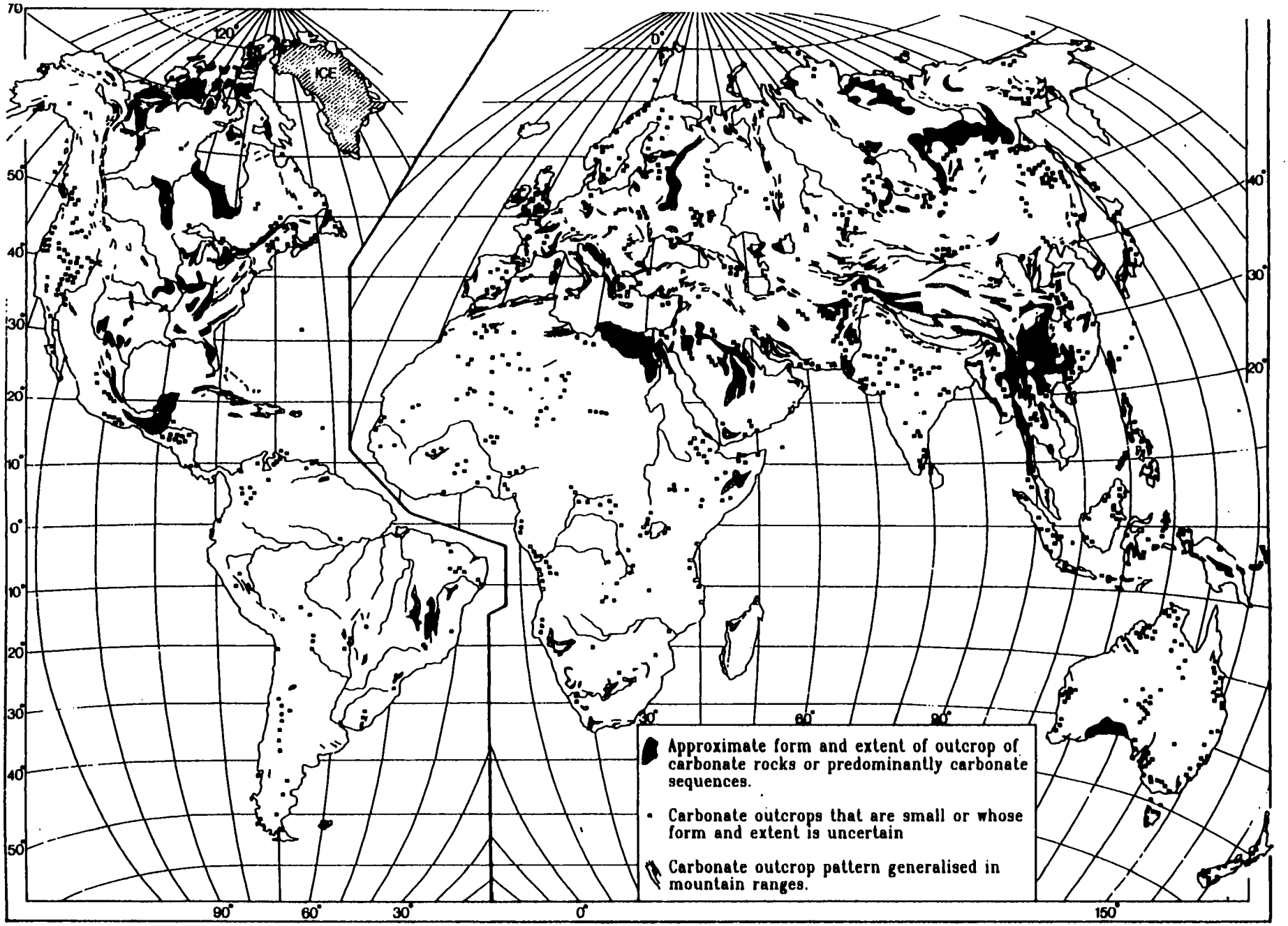

FIG. 4 Major outcrops of karst rocks

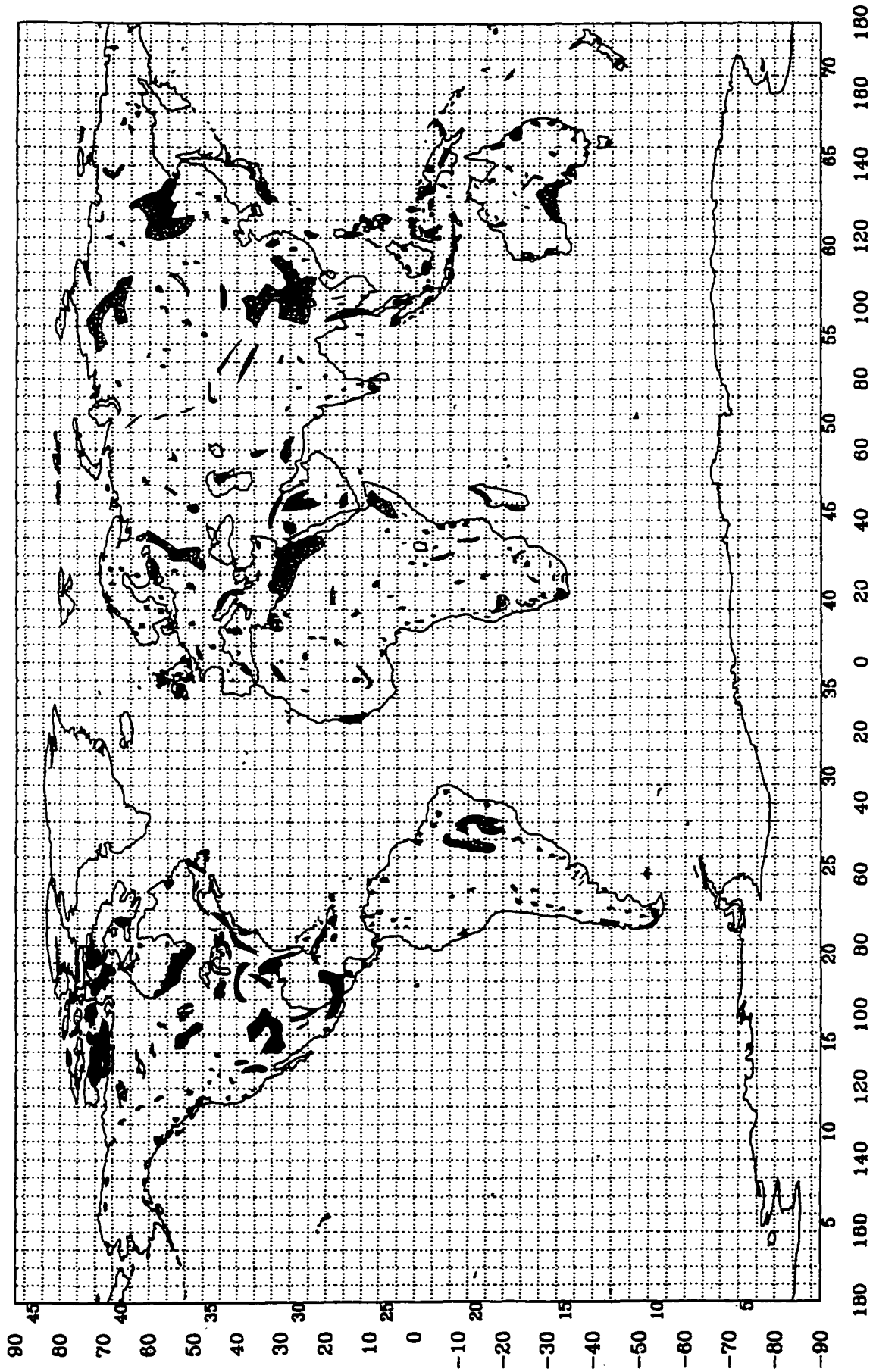

FIG. 5 Giss 4x5 GCM gridded global karst map

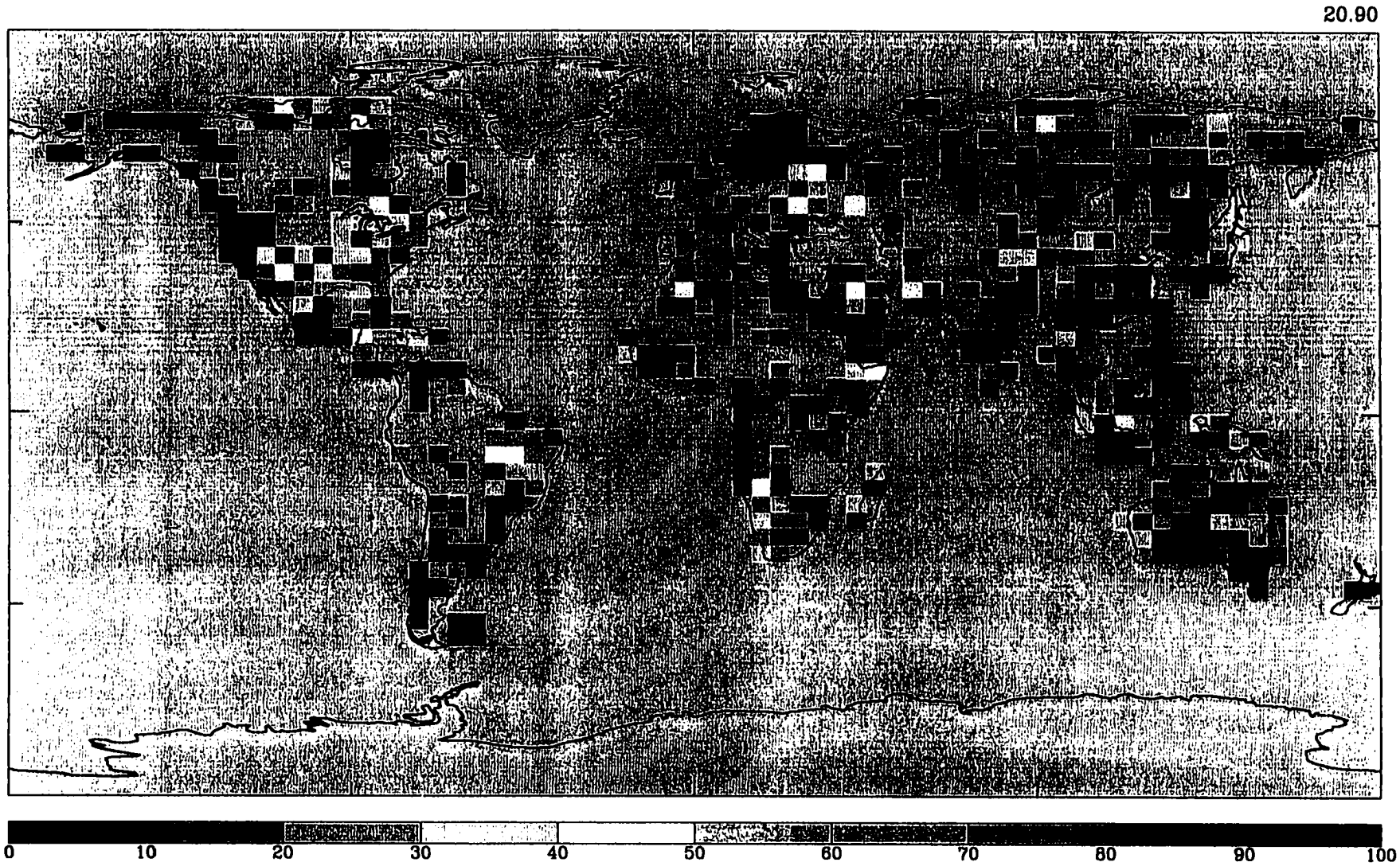

FIG. 5a . Digitized Karst Map

4.3 Groundwater Hydrology and Karst Hydrology

General groundwater hydrology theory explains that the process of infiltration, and the subsequent movement of water through the soil (percolation) are both the result of matric, or capillary, forces and gravity. The capillary force represents the physical attraction of soil and rock particles to water; water flows from wetted particles (high-energy potential) to drier particles (low-energy potential). The drier the soil, the more dominant is the matric force. However, as the voids in the soil become filled with water, the gravity force dominates. As the field capacity (the maximum amount of water that a given soil can retain against the force of gravity) of a well-drained soil is exceeded, a rapid flow of water begins in the direction. This downward movement of water continues through pores in the soil. In general, the number of pores and the sizes thereof, decrease with increasing depth, thus increasing resistance to flow. Furthermore, as water moves into deeper soil it becomes less available to both evaporation and transpiration. Consequently, a zone of saturation (the phreatic zone) is formed.

The first portion of the aquifer between the soil surface and the top of the saturated zone is called the zone of aeration or the unsaturated zone, where the pore spaces are partially filled by either air or water. The zone of aeration

consists of the soil water zone, which extends through the rooting zone; the vadose zone, which extends from the soil water zone to the capillary fringe; and the capillary fringe. The top of the zone of saturation is characterized by a pressure that is equal to the atmospheric pressure and a water potential that is zero. This surface is called the water table. Directly above the water table is the capillary fringe, a zone which is characterized by a pressure that is sub-atmospheric and a water potential that is negative. These conditions allow capillary forces to pull water upwards from the zone of saturation into the zone of aeration. The water table is not a static surface. It moves up and down in response to precipitation and evapotranspiration changes. Flow in the aquifer's porous medium is governed by Darcy's law. This law stipulates that flow in the porous medium moves down the head gradient and is directly proportional to both the gradient and the medium's hydraulic conductivity. To completely describe groundwater flow, Darcy's equation is expanded and written for the general case of three-dimensional flow with anisotropic hydraulic conductivity

$$q = -K\nabla\phi \tag{5}$$

where q is flux, κ is hydraulic conductivity and ϕ is head. This equation can be combined with a mass balance or continuity equation to give

$$\frac{d}{dx}\left[K_x \frac{d}{dx}\phi\right] + \frac{d}{dy}\left[K_y \frac{d}{dy}\phi\right] + \frac{d}{dz}\left[K_z \frac{d}{dz}\phi\right] = 0 \qquad (6)$$

for the steady state case.

Karst's unique geomorphologic features complicate its hydrology, especially its groundwater component. The validity of applying the general groundwater hydrology concepts to karst 'aquifers' has been questioned from the very inception of karst research. Beginning with Martel (1910), karst geomorphologists had always known that the distribution of water in karst regions was far different than that in other areas.

In karst regions water moves through caves, holes, joints, fissures and vertical shafts among a variety of other surface and sub-surface cavities. That is, the assumption of flow through a porous medium which underlies traditional dynamic equations and methods for studying groundwater are violated. An alternative description must be applied. Karst regions are distinguished by the

following hydrologic features:

(1) Diverse forms and sizes of surface openings result in very large infiltration and percolation rates. Consequently, karst regions may be rich in groundwater but poor in surface water resources.

(2) Sub-surface drainage systems such as karst caves and underground rivers are well developed. Karst water flows at high speeds in both the horizontal and vertical directions. Jianyun and Yiling (1990) contend that water movement in karst can even be divided into three categories: rapid flow, medium flow and slow flow.

(3) In many karst areas surface streams and underground rivers develop simultaneously, and surface runoff can become groundwater and vice-versa over a range of spatial and temporal scales. Additionally, when the exchange between surface and groundwater occurs, not all the surface runoff returns within the watershed. Some of it resurface as springs in other watersheds (White, 1988) while some may be lost to all watersheds and flow to the sea as submarine springs (Ford and Williams, 1989). This increases the complexity of karst hydrology.

(4) Poor vegetation, exposed rocks and thin soil cover limit evapotranspiration.

(5) No definable water table exists (Tratman, 1969 ; Sweeting, 1972).

As stated above, aquifers are usually treated as porous media in conventional groundwater hydrology. Karst, however, is fundamentally different from other 'soils' and cannot be classified as a porous medium. Flow in karst is not a capillary, diffusive process. Traditional groundwater concepts of matric potential, diffusivity and hydraulic conductivity have little or no significance in karst hydrology. Ford and Williams (1989), and their predecessors, questioned the applicability of the normal laws of groundwater hydrology to the fractured rocks perforated by large solution pipes that characterize karst. Of major concern is the appropriateness, or lack thereof, of applying Darcy's law to karst hydrology.

Darcy's law, as expressed in three dimensional form, equation (5), is an empirical relation for the specific discharge in terms of the hydraulic conductivity and a head gradient. The law is applicable strictly to laminar (no mixing , no transverse component in motion, no tortuosity), rectilinear flow (average flow in one direction) of a homogeneous liquid, and it is restricted to specific discharges less than a certain critical value. This critical value is described by the dimensionless Reynolds number, N_R, equation (7)

$$N_R = \frac{D\rho}{\mu} q \qquad (7)$$

where D is the average grain size diameter (m), ρ is the density (kg/m^3), and μ is the dynamic viscosity ($N\ s\ /\ m^2$) of water. Darcy's law is valid only when $N_R \leq 1$.

If the Reynolds number is greater than 1, other more complex equations of motion must be employed. Figure 6, adopted from Freeze and Cherry (1979), illustrates the range of Reynolds number for which Darcy's law is valid and the range for which it is inappropriate. It is clear that the linear relationship breaks down for relatively high rates of flow.

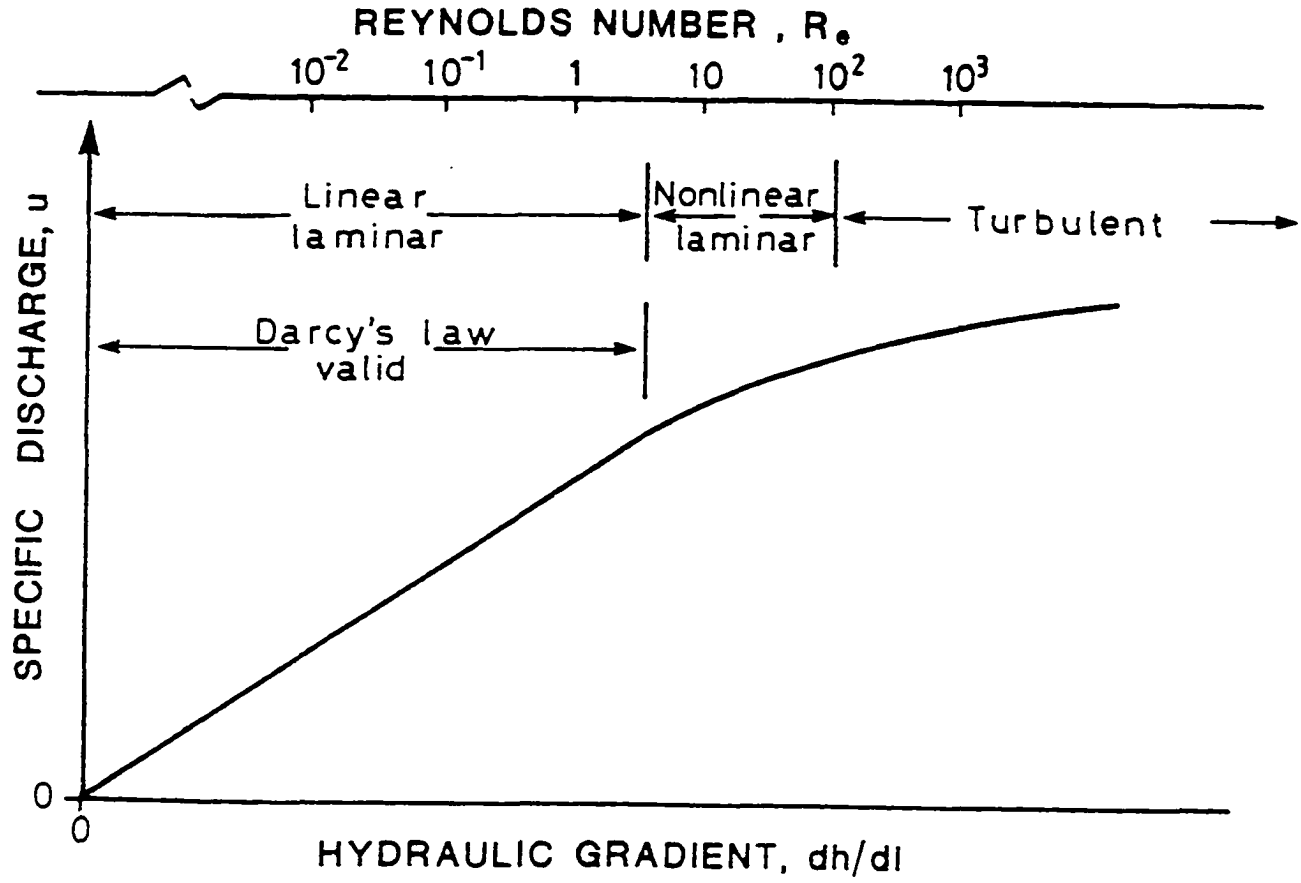

FIG. 6 APPLICABILITY OF DARCY'S LAW

To apply Darcy's law, the hydraulic conductivity for the porous medium is necessary. Figure 33 from White (1988) shows that for karst, the concept of a hydraulic conductivity is at least to be questioned. Note the question mark on the

figure next to karsted limestone.

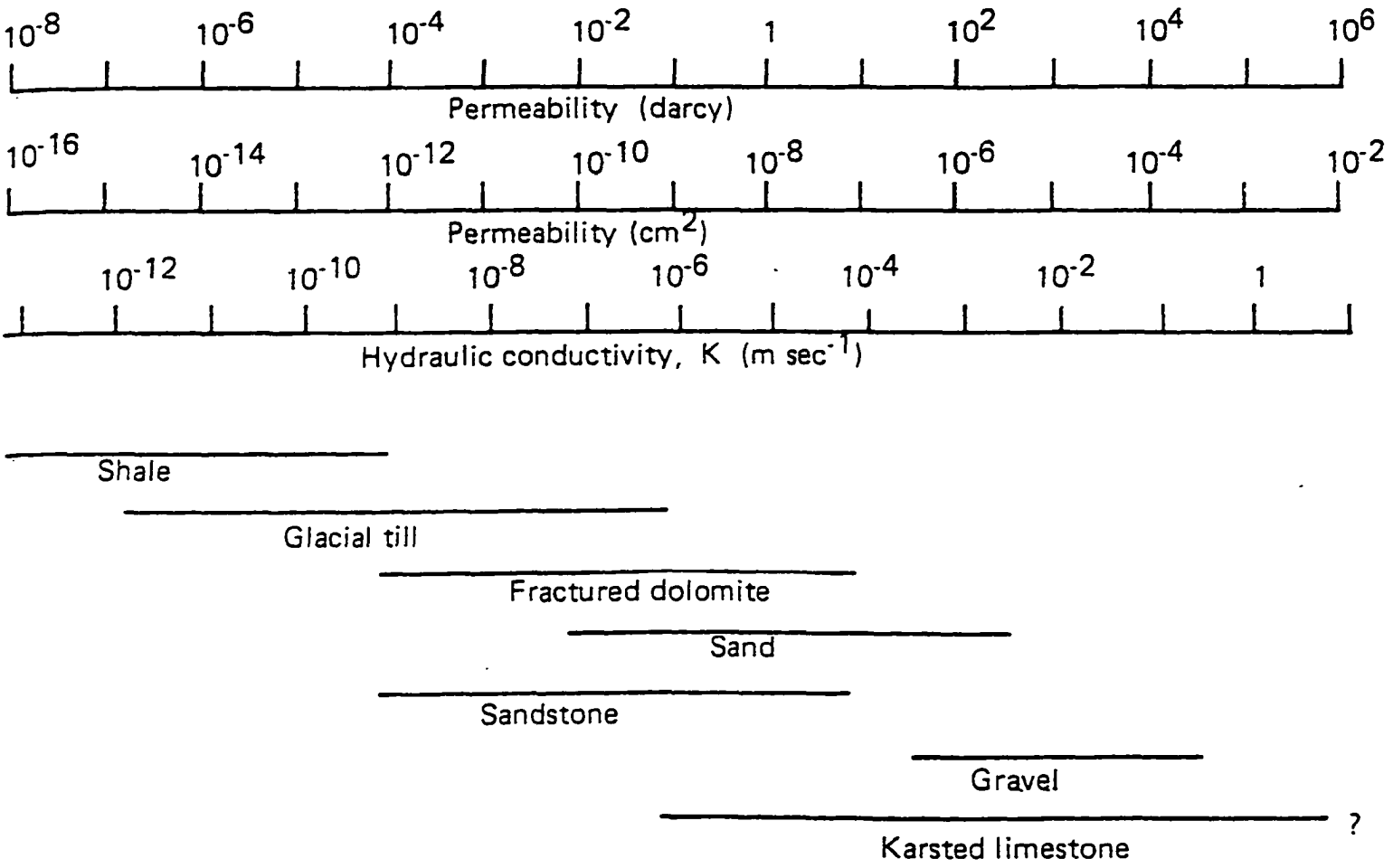

FIG. 7 Ranges of permeability found in various types of aquifer materials. The hydraulic conductivity is for water at 25°C.

Karstic 'aquifers' are unique in that they contain integrated systems of large solution cavities and pipelike conduits that behave as drains and

underground bypasses to transport water from the surface through the subsurface. In karst hydrology, flow is rarely laminar. It is usually turbulent, tortuous and of high speeds. Therefore, an alternative to the Darcian-based approach of aquifer analysis is needed to understand and to model the heterogeneous nature of a karst 'aquifer'. Pipe flow theory will be applied to treat the interconnected karst conduit system. This method is closer to the Hagen-Poiseuille approach in which the hydraulics of flow in individual fractures and pipes are considered. This concept of aquifer analysis takes a dynamic input-output systems perspective and focuses particularly on the transport of surface flow to and through the subsurface.

Part 2. Analyses

5. Sacramento Model and GISS Land-Surface Model Simulations of Rio Cobre's Runoff

5.1 Jamaica and the Rio Cobre Watershed

The island of Jamaica (Figure 8) is the largest of the English speaking Caribbean islands, and it is the third largest island in the region after Cuba and Hispaniola (Haiti and the Dominican Republic). It is located in the northern

portion of the Caribbean sea in the Greater Antilles approximately 145 km south of Cuba, 850 km south of Miami and 1000 km north-north east of the Panama Canal. Jamaica is elongated in an east-west direction. It is approximately three times as long as it is wide, and has a surface area of approximately 11,000 sq km. Approximately two-thirds of the island is covered by karstic limestone, see Figure 9 and White (1985). Sweeting (1955, 1958), Zans (1958), Versey (1962) and the FAO (1971, 1972, 1974) have all documented the island's unique, complex, karstic drainage system. The principal mountain chain stretches from the WNW to the ESE portions of the island. The highest elevation on the island is 2,257 m and is located at the peak of the famous Blue Mountains of eastern Jamaica. Jamaica's climate is classified as maritime tropical with a mean daily temperature of 27°C. The rainy season lasts from May to November, while the dry season dominates the other months of the year. Mean island-wide rainfall is approximately 350 cm/yr.

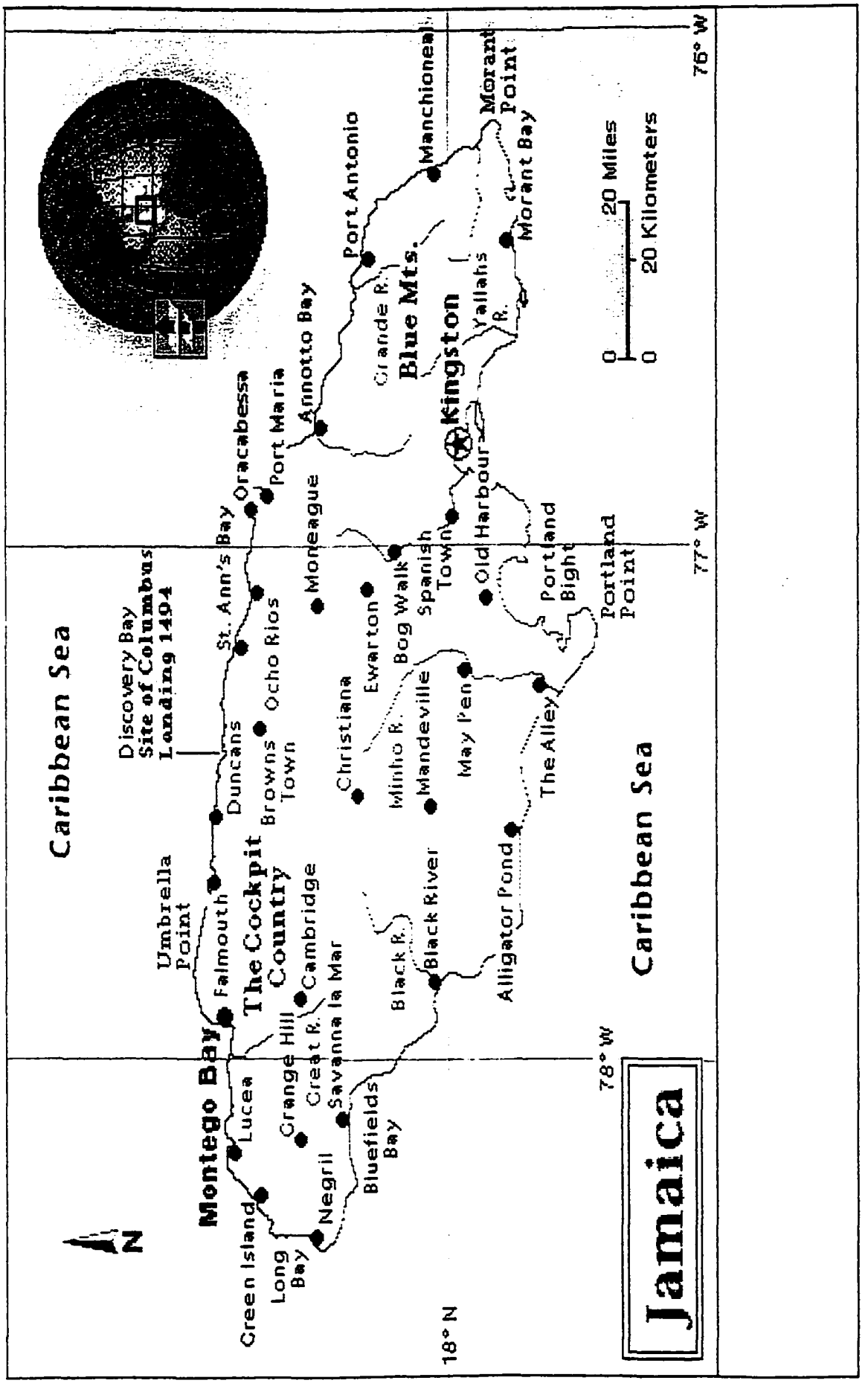

FIG. 8 Map of Jamaica

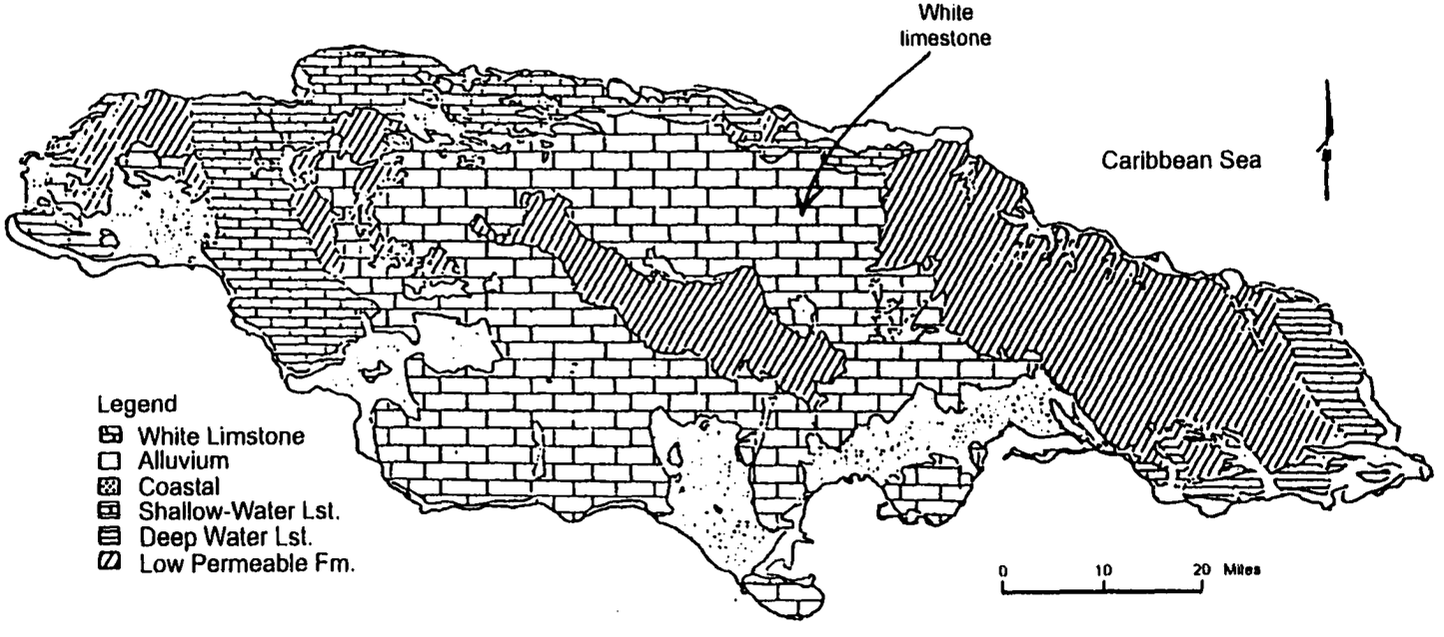

FIG. 9 Simplified geology of Jamaica

To facilitate this research, one of the island's major river basins, the Rio Cobre River basin, was chosen as a case study basin to assess the possible impacts of climate change on Jamaican water resources. This basin was selected because of data availability and its key role of augmenting the island's domestic water supply. The Rio Cobre is also the largest river basin in Jamaica.

The Rio Cobre basin (Figures 10 and 11) is located in the south-east region of central Jamaica where annual rainfall is slightly below the island average. The basin's average slope is reported by Nkemdirim and Jones (1978) to be 17%. It rises some 650 m in the relatively flat central regions of the island. As the river snakes south-ward to the Caribbean Sea, it meanders through a series of low north-south limestone ridges. The basin's 524 sq. km. catchment area is comprised of white limestone aquifers. Its landscape displays classic karst features. Solution hollows, sinkholes, underground caves and underground rivers moving at speeds of 1 mile/day are regular features and popular tourist attractions. Subterranean drainage is widespread. Eyre (1988) described the basin as being "cavernous like a thick, flat block of Swiss cheese."

According to White et al., (1983), over 66% of the watershed is comprised of tertiary white limestone . This white limestone group ranges in age from the mid-Eocene to the upper-Miocene, and it consists of white to pink

colored micritic, spartitic and bioclastic limestones (karst). Karstification is believed to have begun in this white limestone group some 12 million years ago. In portions of the watershed, three-terraced, subterranean levels are clearly discernable. Fincham and Ashton (1967) and the Water Resources Authority of Jamaica (personal communication), agree that runoff from main tributaries (example, Pedro River and Lluidas Vale) of the basin sinks in the limestone, and is lost to the main channel. Indeed, White et al., (1983) reports that the Murmuring Brook tributary during normal rainfall periods sinks in its bed on reaching the limestone outcrops. The basin, therefore, is characterized as a losing stream.

However, unlike certain parts of the island's karstic terrain where surface flow is almost non-existent (for example, the Cockpit Country region which has a kegel karst terrain) annual precipitation and runoff in the Rio Cobre average about 178 cm and 65 cm respectively. Maximum streamflow coincides with maximum rainfall in October, and a secondary peak flow in June lags the secondary rainfall peak by one month. The basin's gaging station is located at Bog Walk in St. Catherine, and it has been operational since 1955. Despite not being the river with the greatest quantity of runoff on the island, this river is of extreme importance, especially in the dry season, since it is a major contributor

to the domestic water supply of Jamaica's capital city. Kingston is the dwelling place for at least 25% of the country's population. The river also supplies domestic and irrigation water to St. Catherine, the largest parish in Jamaica.

Undoubtedly, the livelihoods of the people who live in the vicinity of the river may be in jeopardy if the Rio Cobre's flow and storage subside substantially below their present levels in a $2xCO_2$ climate. People in the parish of St. Catherine, and especially those in the former capital city of Spanish Town, are almost completely dependent on the water resource that the river provides. Although the region that the river supplies in St. Catherine and Spanish Town, has undergone substantial development and transformation since 1950 with the introduction of industries and factories that manufacture textiles, and steel, cigarettes and ceramics, cereals and electrical switchgear, steel shipping containers and batteries, underwear and buttons, agriculture still remains its most important sector in terms of the number of people it employs and the amount of revenue it generates for the region and the country. Crops are cultivated in the region for both domestic use and exportation. The crops cultivated in and around the watershed area of the Rio Cobre are : Sugarcane, Bananas, Citrus, Yams, Sweet potatoes, Irish potatoes, Pumpkins, Mangoes, Cassava, Tomatoes, Corn, Tobacco, Rice, Pimento, Cocoa and Coffee. Insight as to the future state of this

important river is, therefore, a national imperative.

Managers of the island's water resources (the Water Resources Authority of Jamaica and the National Water Commission) and researchers at the University of the West Indies in Kingston believe that the river basin has undergone climatic change due to environmental abuse: deforestation, fires, poor agricultural practices and the exploitation of fragile ecosystems. They argue that the environmental abuse has caused Köppen's Aw climate (tropical wet-and-dry) to gradually displace the basin's Ar climate (tropical wet). Thus, the basin is drier than it was. Changes in vegetation type may support their claim of a drier basin. Dry season flow has steadily declined, streams and springs have dried up and perennial streams have become seasonal. With the basin apparently already environmentally stressed, expected climate change may seriously jeopardize the future supply of domestic and irrigation water to both Kingston and St. Catherine. This could have severe implications for these over-populated areas, especially in the dry season.

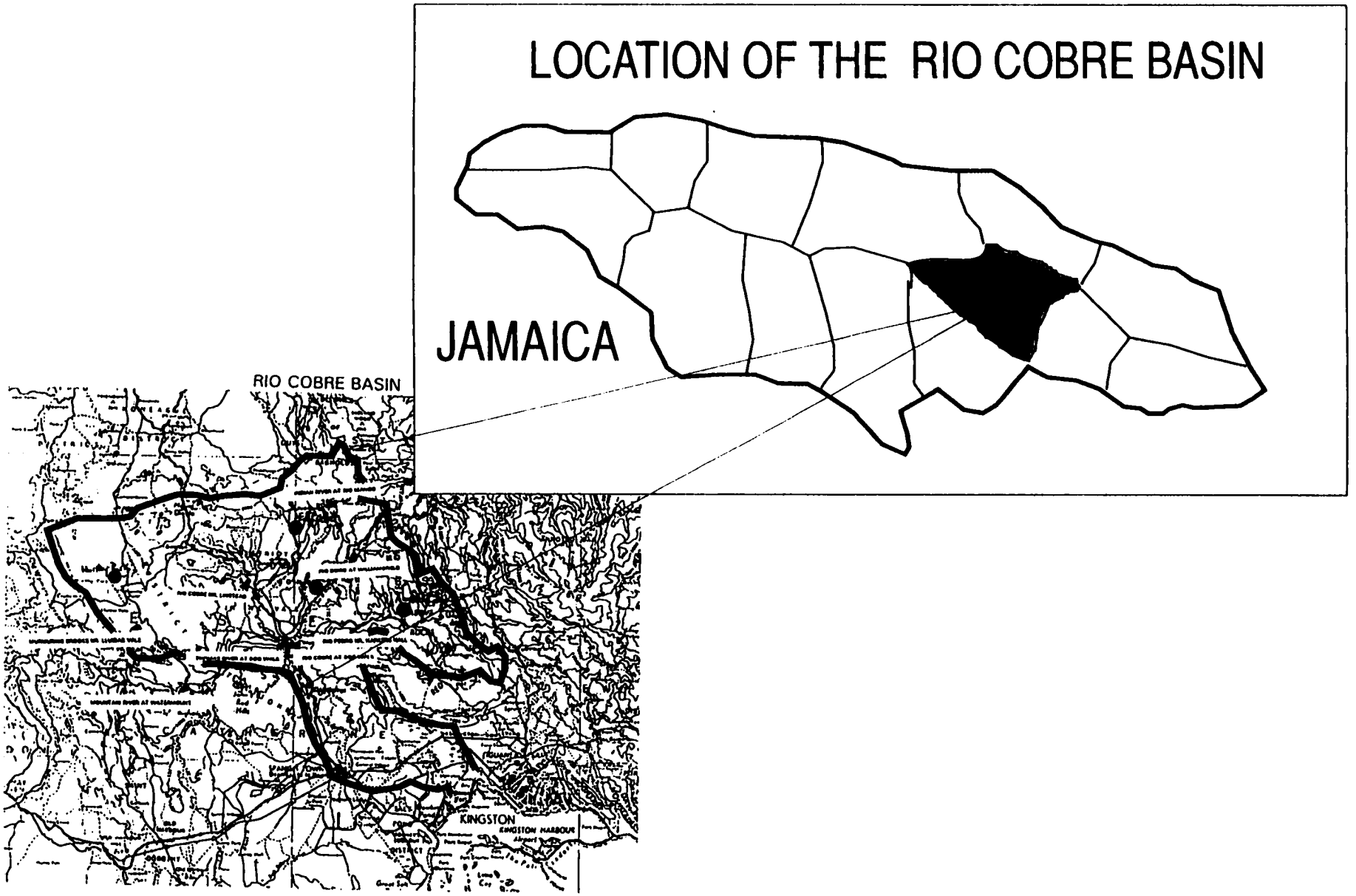

FIG. 10 Location of the Rio Cobre basin

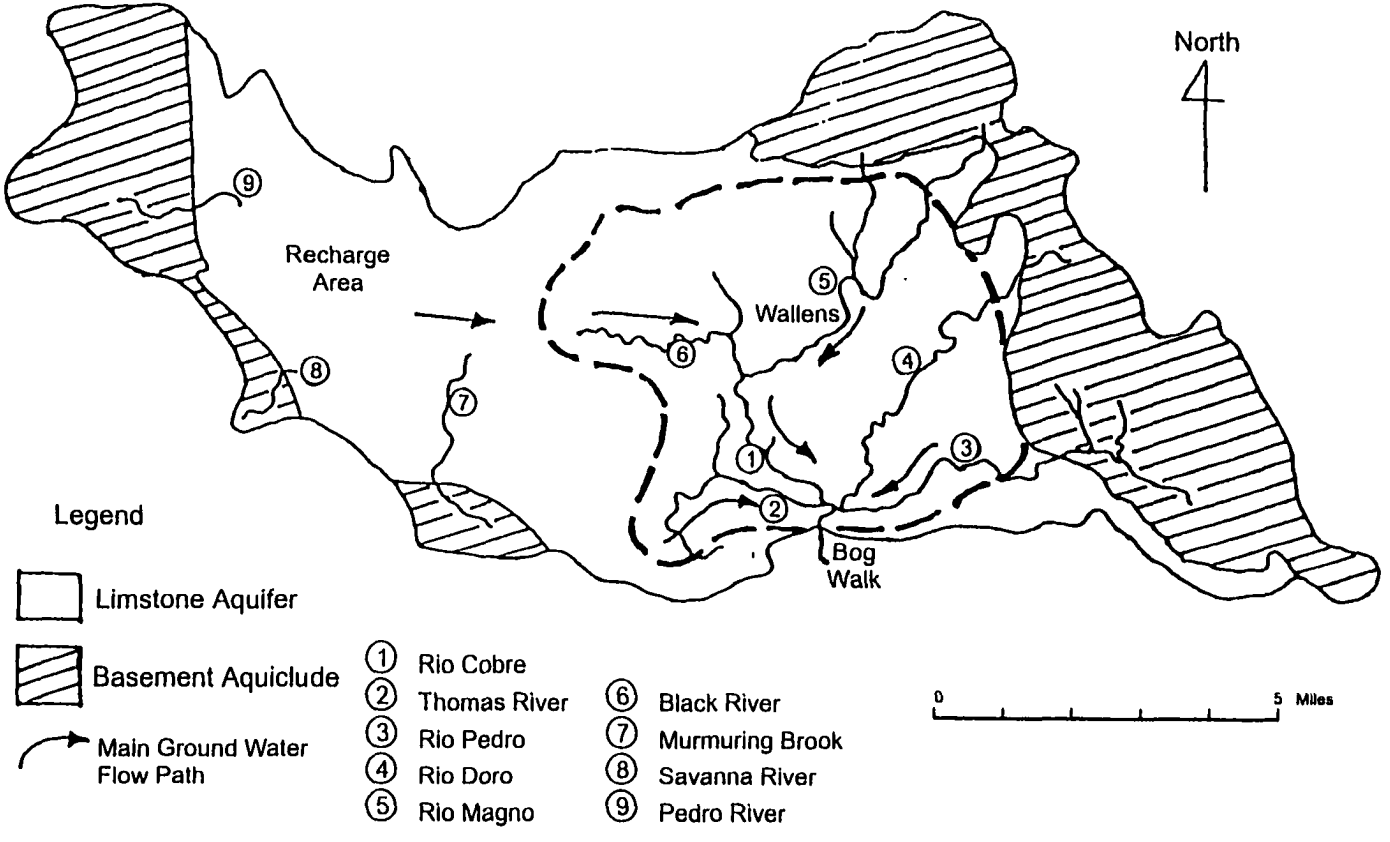

FIG. 11 Simplified Hydrogeological map of the Rio Cobre Basin

5.2 Sacramento Watershed Model Application

The Scaramento Watershed model is the hydrological model currently being used by the Water Resources Authority of Jamaica to aid in its management of Jamaica's water resources. It is, therefore, appropriate that this model be included in this study. Schematics of the model are shown in Figures 12 and 13. Figure 12 highlights the basic components of the model. The figure shows how the model utilizes a set of storages of determinable capacities which are linked by processes which allow the system to approximate many of the soil moisture conditions which control the production of streamflow. The storages are filled if sufficient rain should occur, and they are depleted by vertical percolation, evapotranspiration and lateral drainage. Figure 13 depicts the model at the onset of computing runoff from a rain event after a prolonged dry spell which left the base flow low and its supporting aquifer almost empty. The model works best when the initial conditions are typical of the scenario in the figure.The model would then compute runoff through the sequence beginning with the very dry conditions through to a seasonal wetting cycle and then to the return of dry conditions.

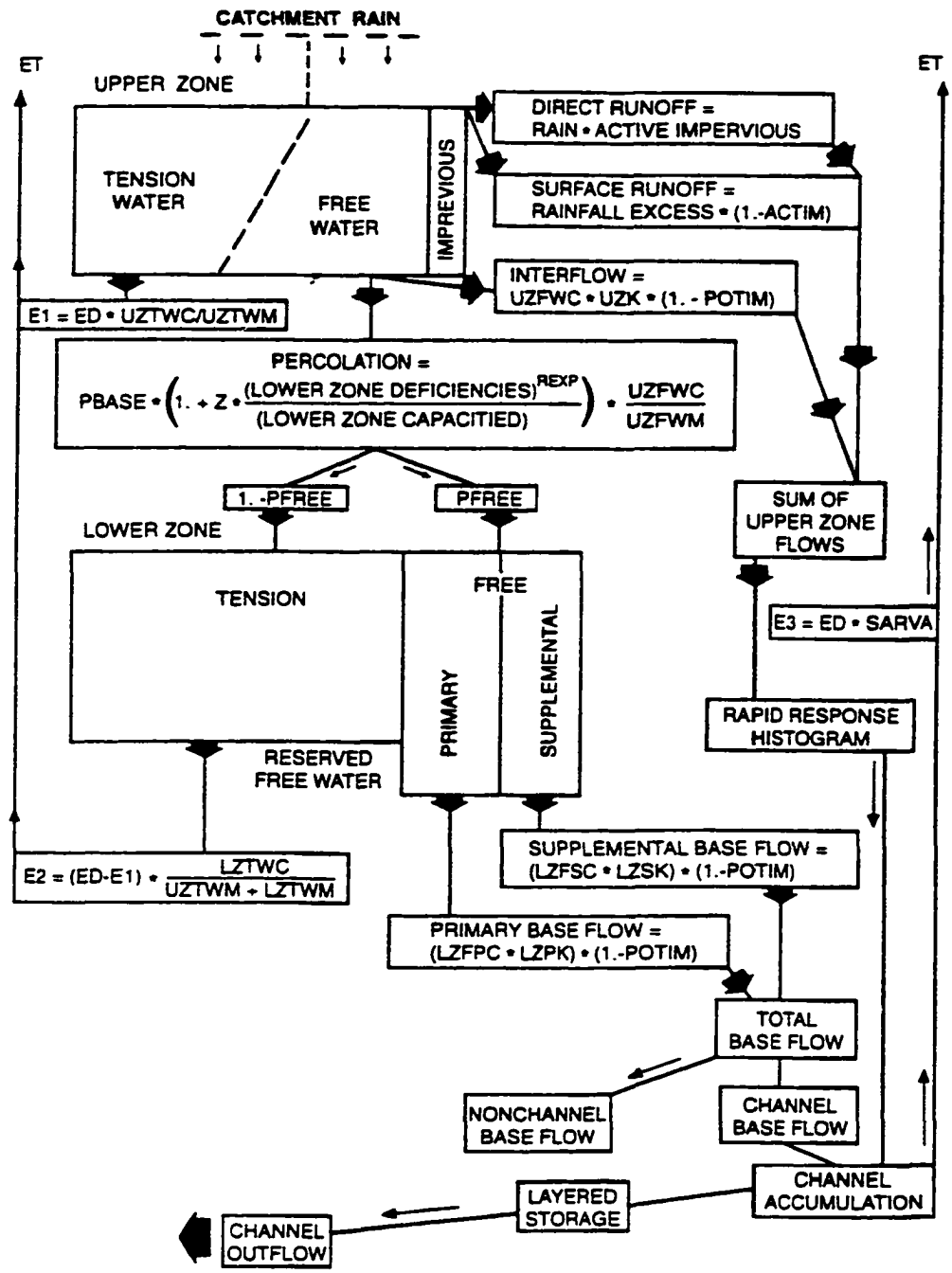

FIG. 12 **Components of the Sacramento Catchment Model.**

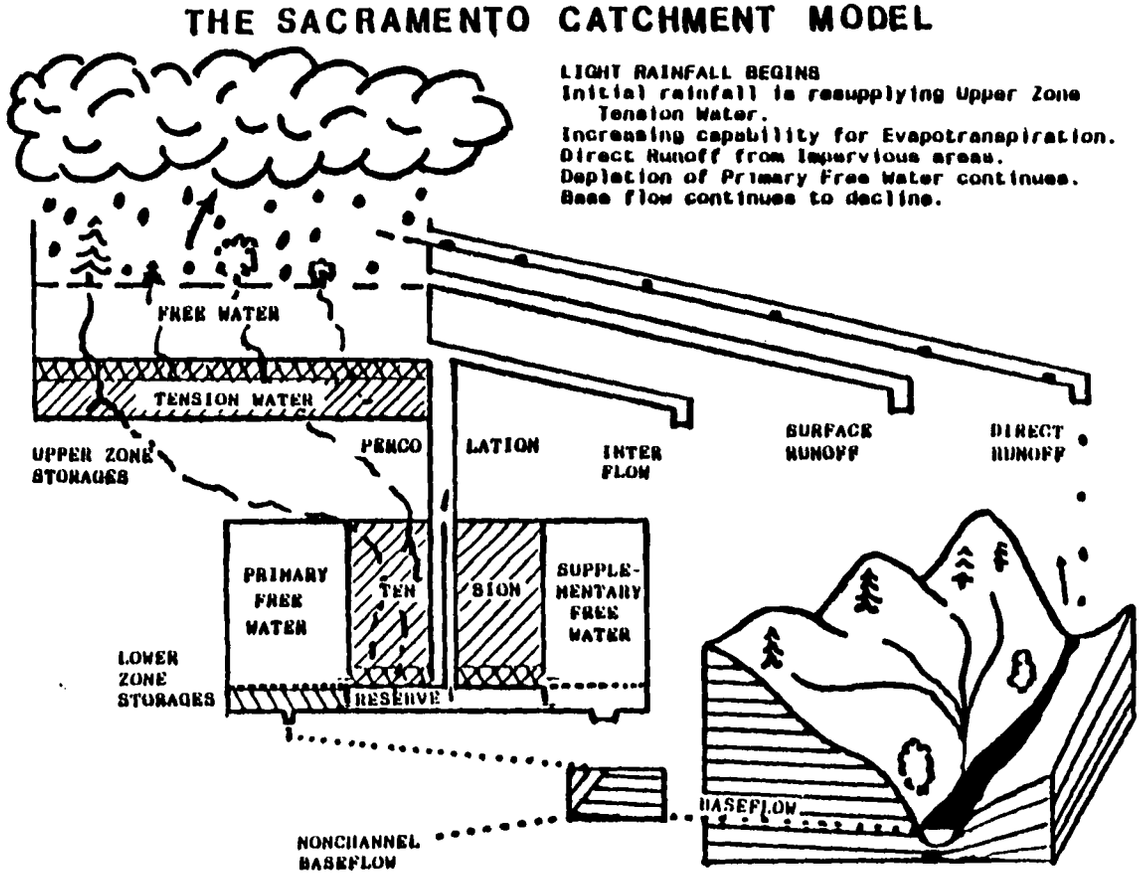

FIG. 13 **The Sacramento Catchment Model after light rainfall begins.**

The model will be used to simulate runoff under climate change conditions for the Rio Cobre. However, before it is used for climate change assessment for the basin, it was first calibrated and verified. Eleven years of hydrometeorological data (1980 - 1990) for the Rio Cobre watershed were obtained from the Water Resources Authority of Jamaica and the Jamaica Meteorological Office. The eleven years of observed rainfall and runoff data from the Rio Cobre basin were used in this calibration/verification process. Eight years - 1980 to 1987 - were used for calibration (see Figure 14), and the remaining three years were used for verification (see Figures 15 - 17). In Figures 15 - 17, the runoff error is the simulated Sacramento model runoff minus the observed runoff. If the model were perfect, the runoff error would be zero, and all the points would lie on the 45° line. A positive runoff error means that the model over predicts runoff, and the points would lie above the 45° line. A negative runoff error means that the model under predicts runoff, and the points would lie below the 45° line. The figures also indicate both the distribution of runoff error in relation to the total rain and to the wet and dry seasons.

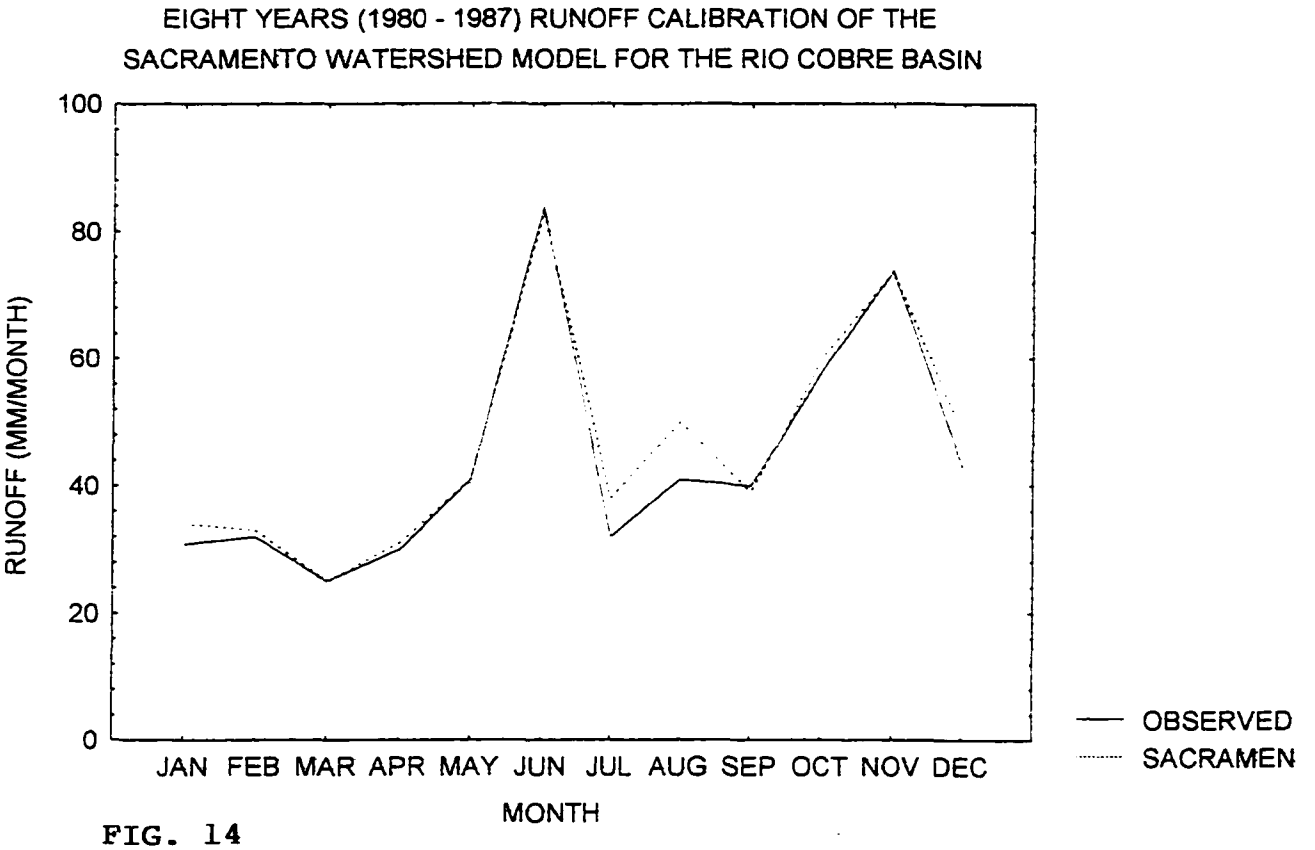

FIG. 14

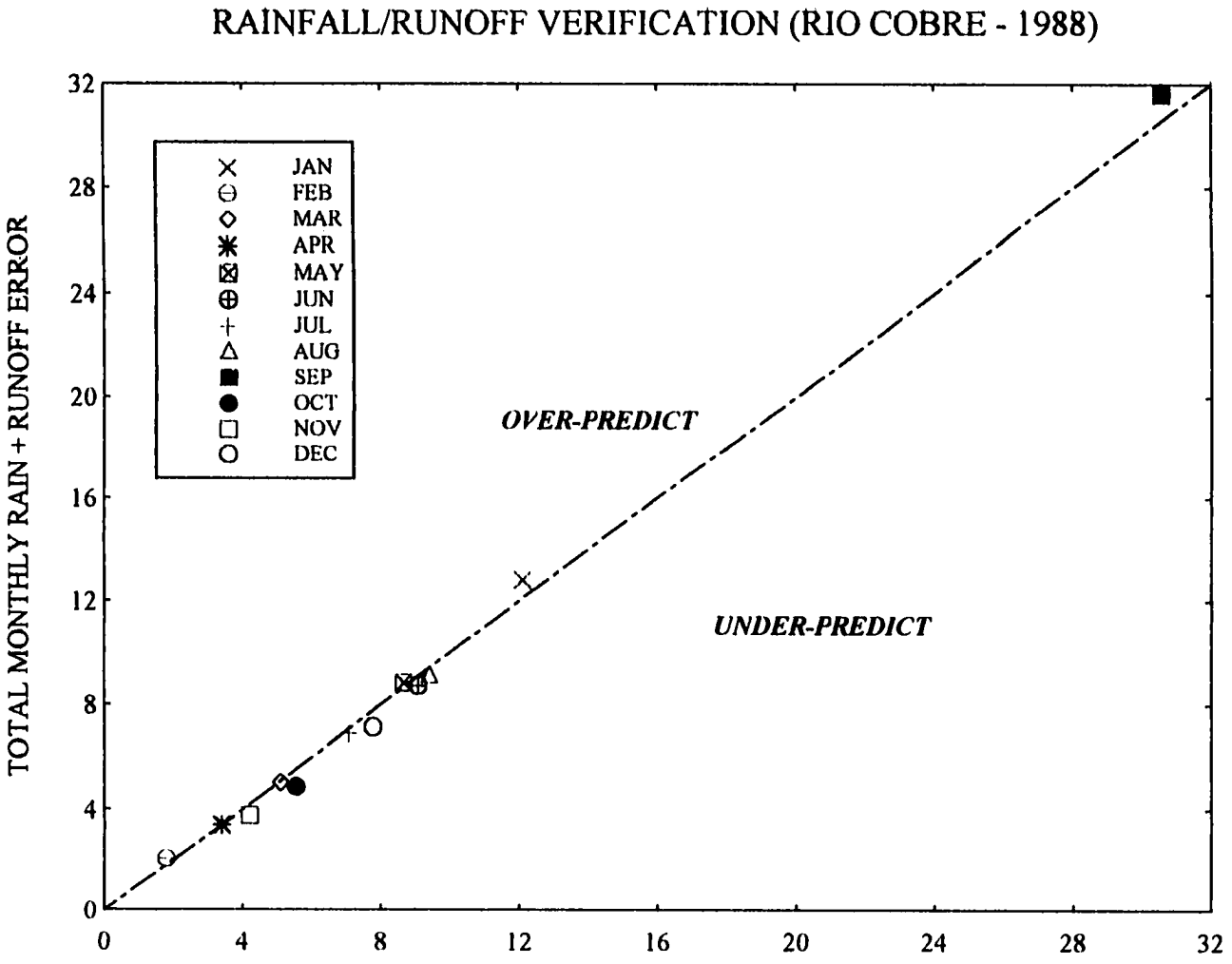

FIG. 15

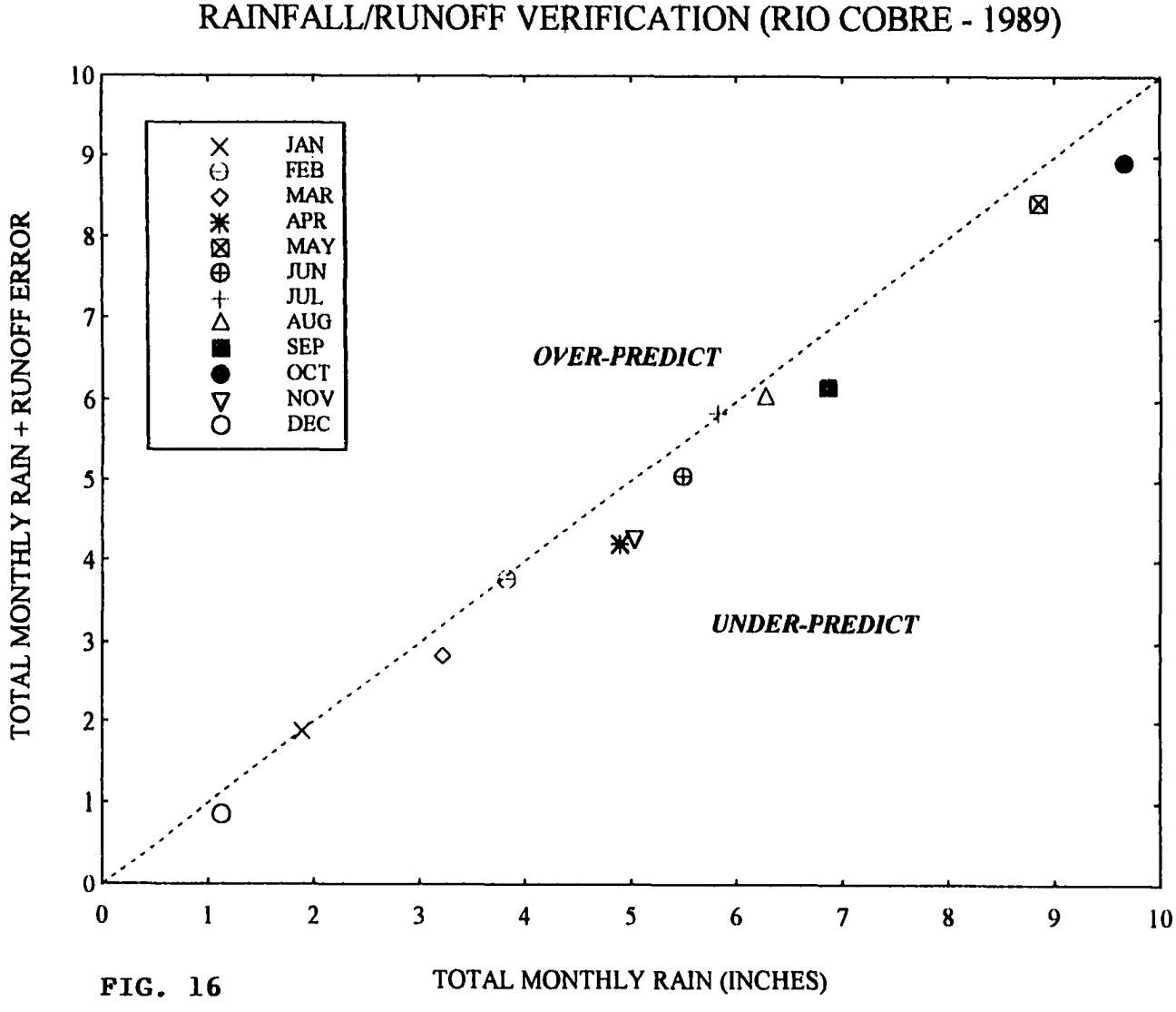

FIG. 16

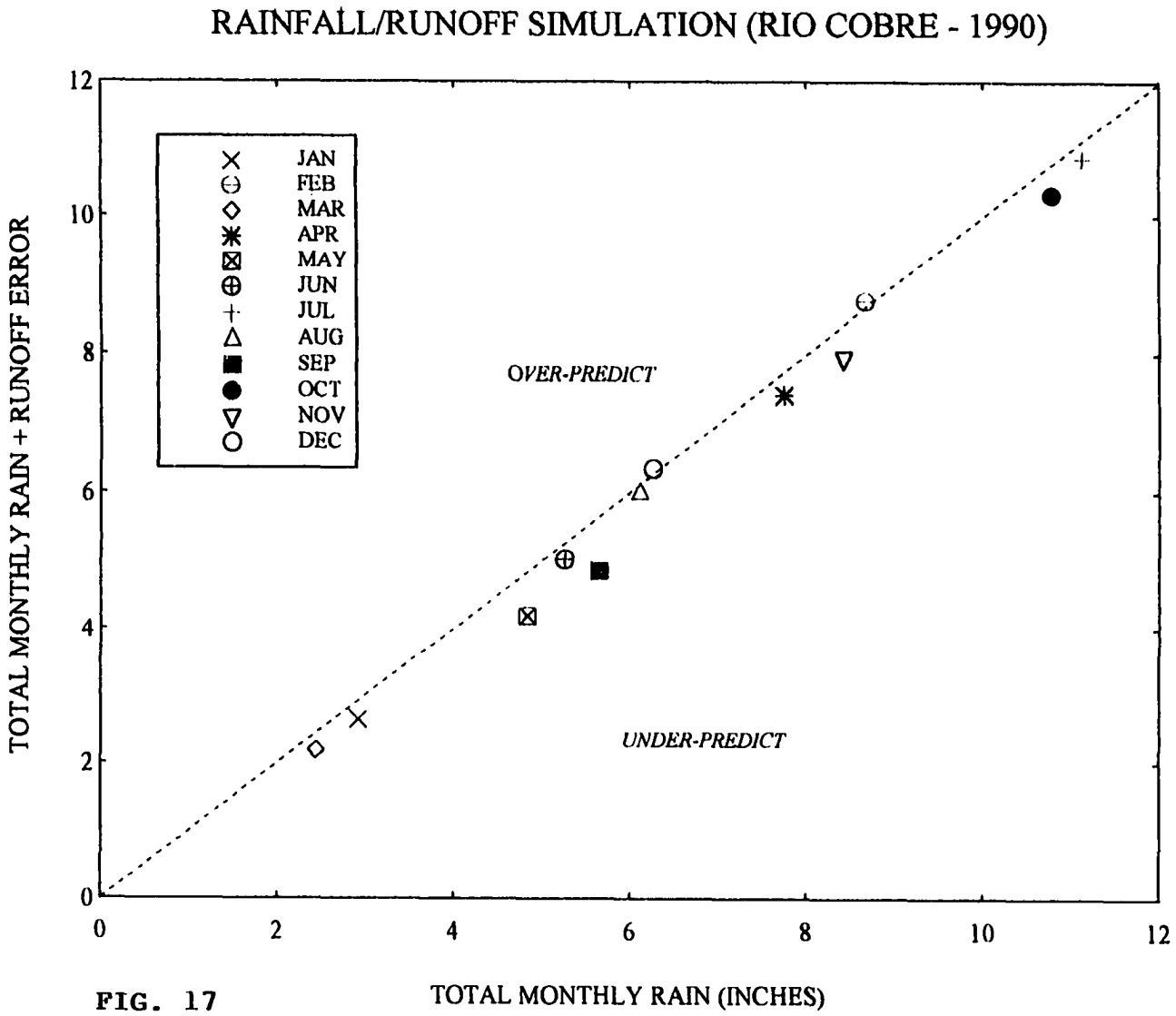

FIG. 17

5.3 GISS Land-Surface Model Application/Deficiency

The Rio Cobre data were used to drive the off-line GISS land-surface hydrological model so as to ascertain how well the model simulates the observed runoff from this karstic watershed. The following, then, are analyses of observed versus modeled runoff and sensitivity analyses of key model parameters which can be calibrated to improve model performance.

Figures 18, 19, and 20 highlight the model's runoff, the observed runoff and the observed rainfall within the Rio Cobre watershed for each year from 1980 - 1990. Figure 18 covers 1980 - 1983, Figure 19 shows 1984 - 1987 while Figure 20 depicts 1988 - 1990. For each year, the monthly total for each of the three variables is plotted. The modeled runoff is in red while the observed runoff shown in green. It is very evident that in each of the years, for the given watershed rainfall, the runoff predicted by the model greatly exceeds the observed runoff.

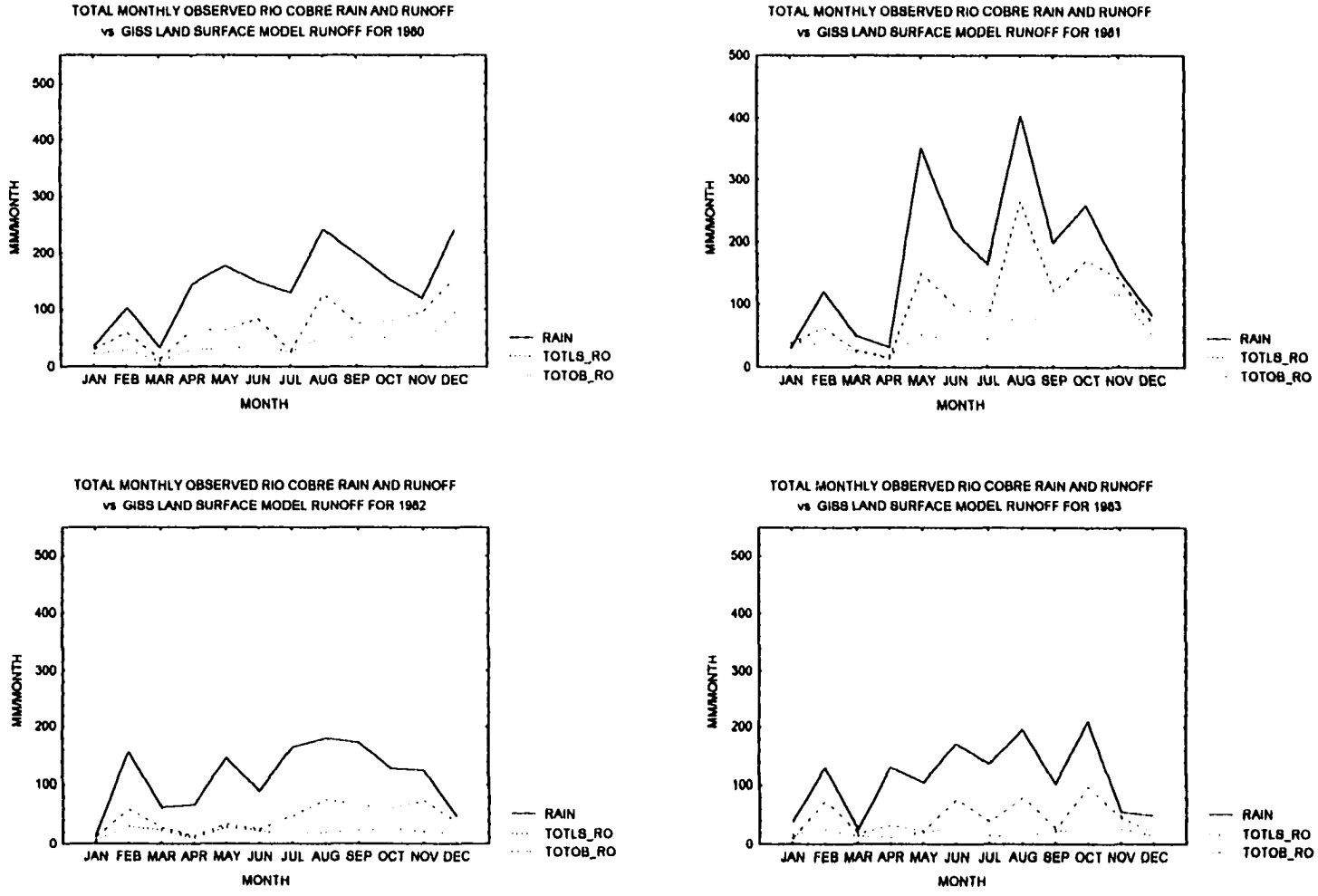

Fig. 18 Total monthly rain, observed and modeled runoff 1980 - 1983

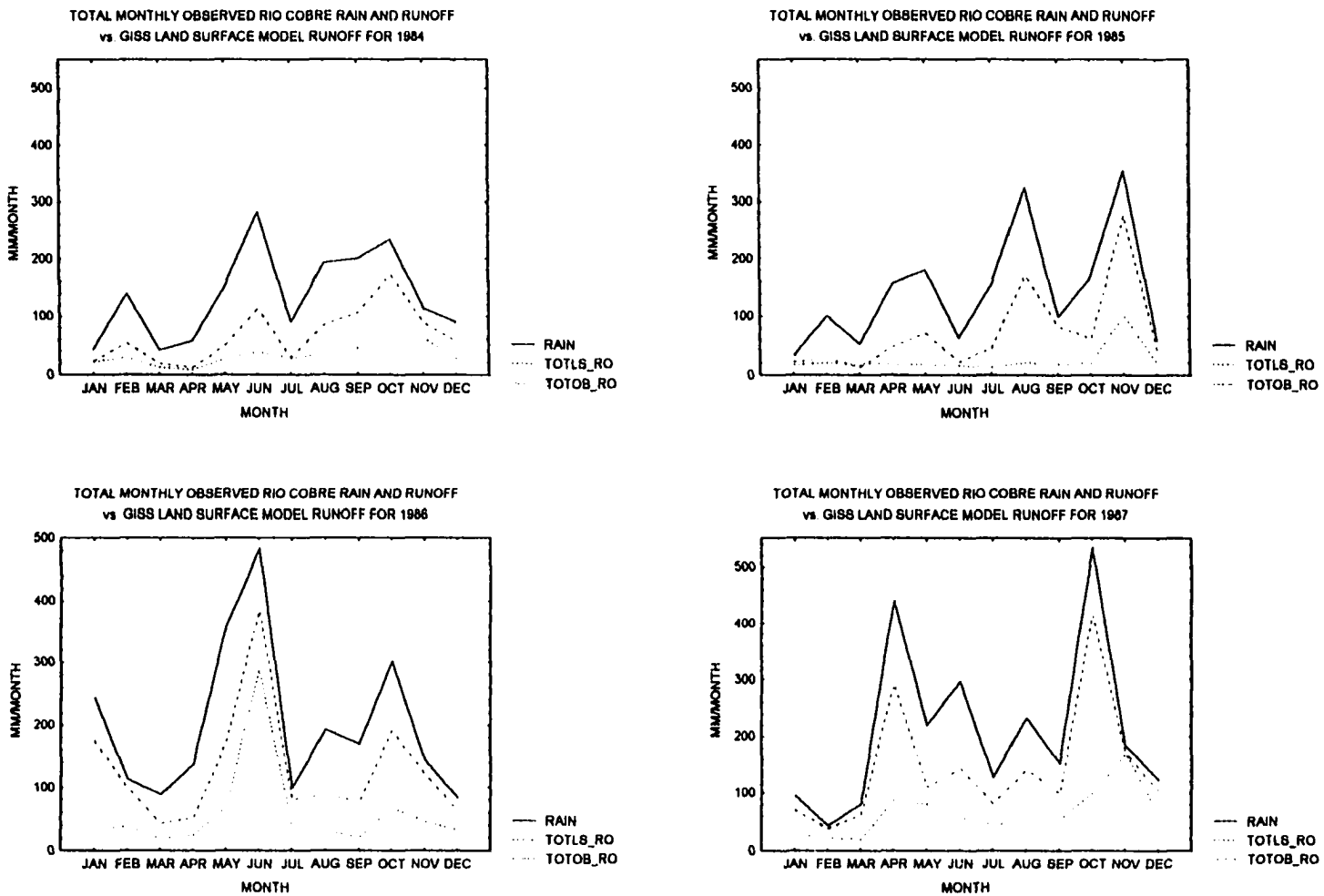

FIG. 19. Total monthly rain, observed and modeled runoff [1984 - 1987]

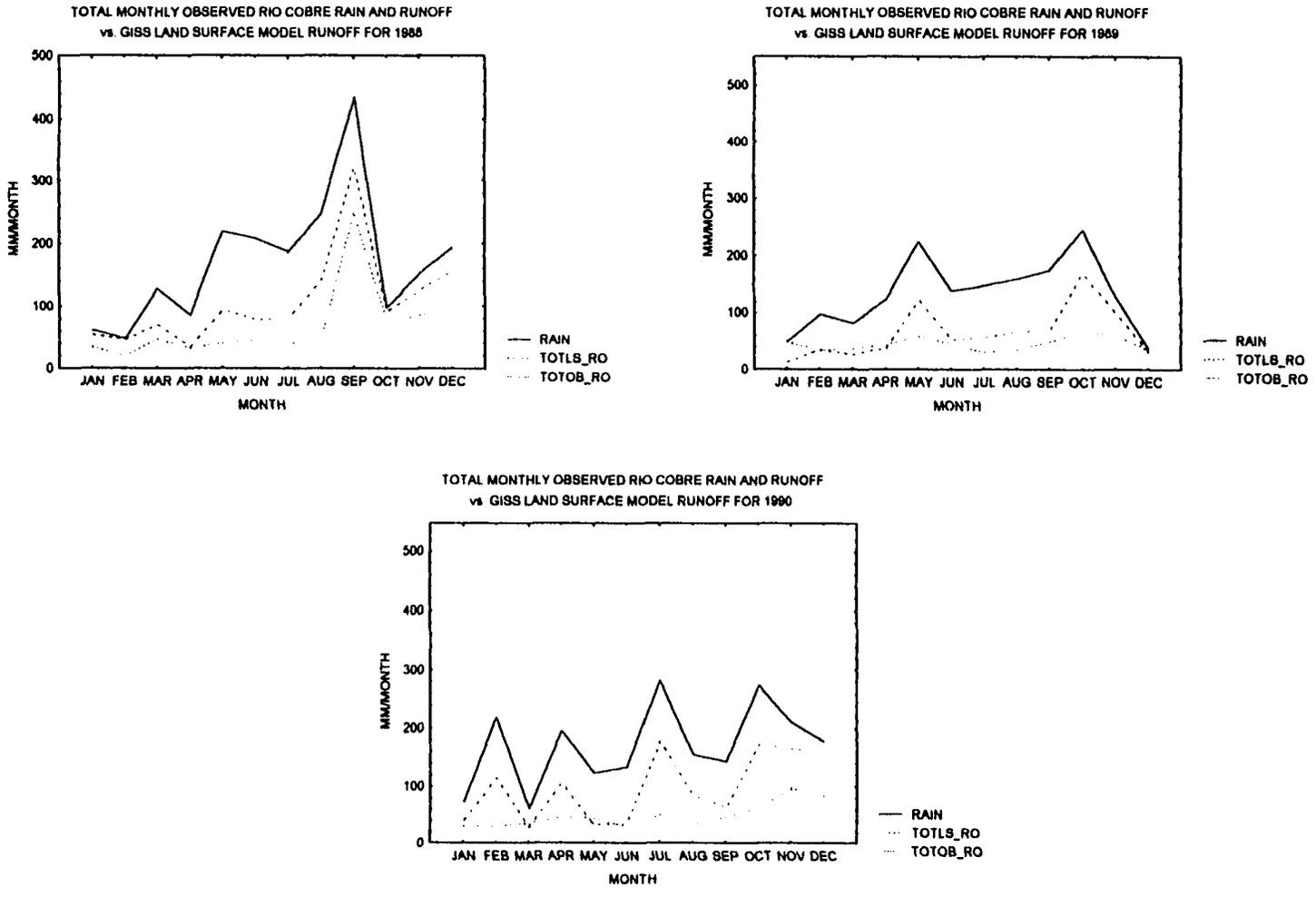

FIG. 20. Total monthly rain, observed and modeled runoff [1988 - 1990]

Taking a slice of the data from 1980 - 1985 and examining two different temporal scales for the same three variables, Figures 21 and 22 give another perspective of the model's over-prediction of watershed runoff. In Figure 21, the mean monthly values of these variables for the six year span show that the model over-predicts the runoff in every month except January and March. In those two months the model underpredicts the mean runoff. However, some time in early January and in late March, the model does in fact reproduce the mean runoff. When the yearly totals are analyzed, it is again quite clear (Figure 22) that for the given yearly total watershed rain, the model's yearly total runoff exceeds the observed.

The year 1981 was randomly selected from the eleven year data set to assess the model's performance in predicting daily runoff. Figure 23 shows the analyses for the first four months of the year, Figure 24 shows the model's performance for the days from May to August while Figure 25 covers the days from September to December. Although the pattern of over-prediction of the watershed's runoff by the model is consistent with the analyses done on other time scales, two new features have emerged from this analyses done on the daily time scale. The model modestly under-predicts the runoff when rainfall is not occurring or when the rainfall intensity is low. However, the model grossly

MEAN MONTHLY TOTAL RAIN AND RUNOFF - RIO COBRE
vs. MEAN MONTHLY TOTAL RUNOFF - GISS LAND SURFACE
MODEL : (1980 - 1985)

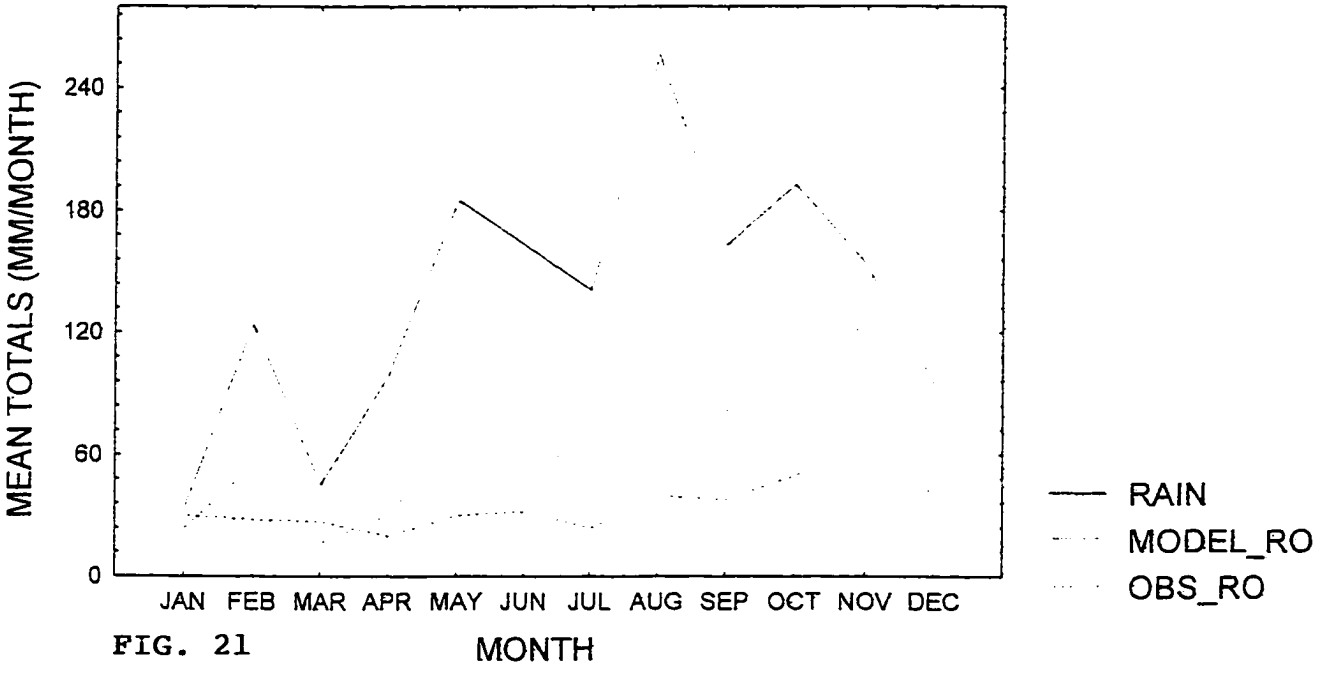

FIG. 21

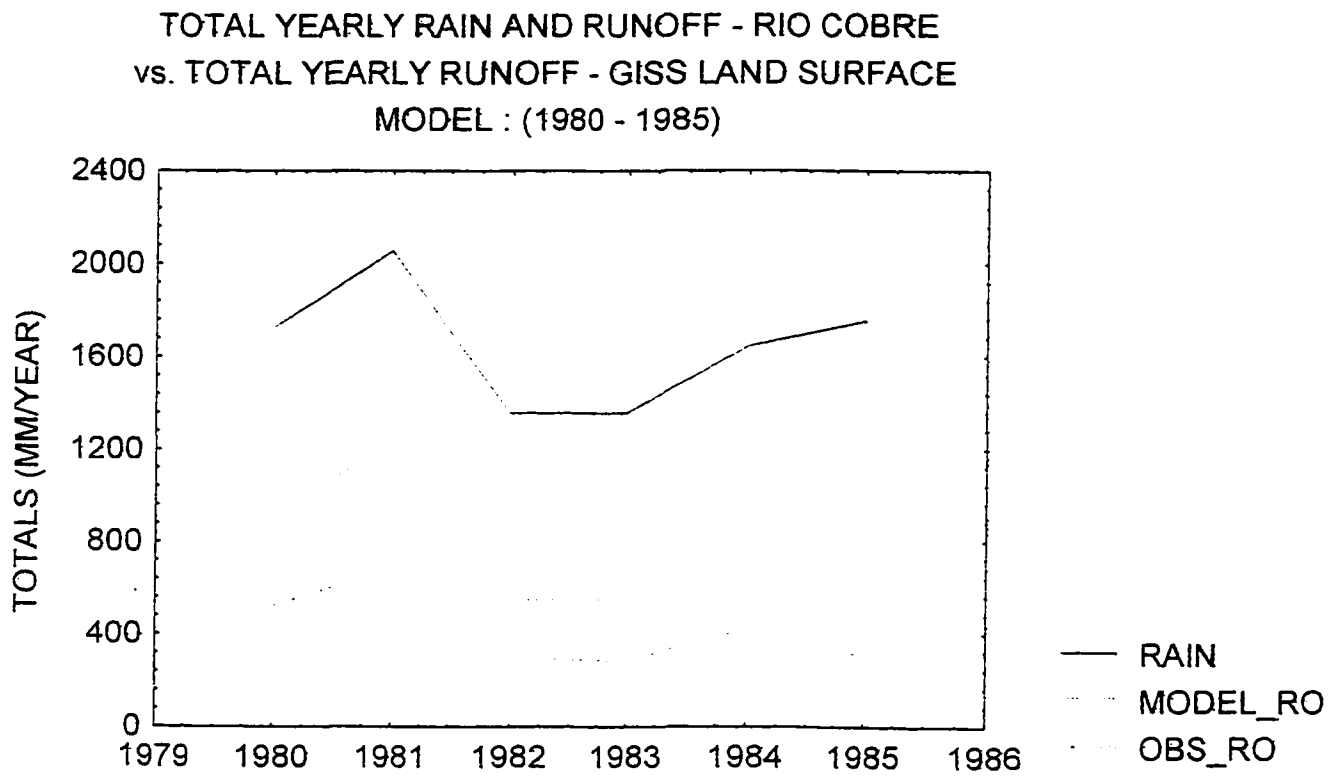

FIG. 22

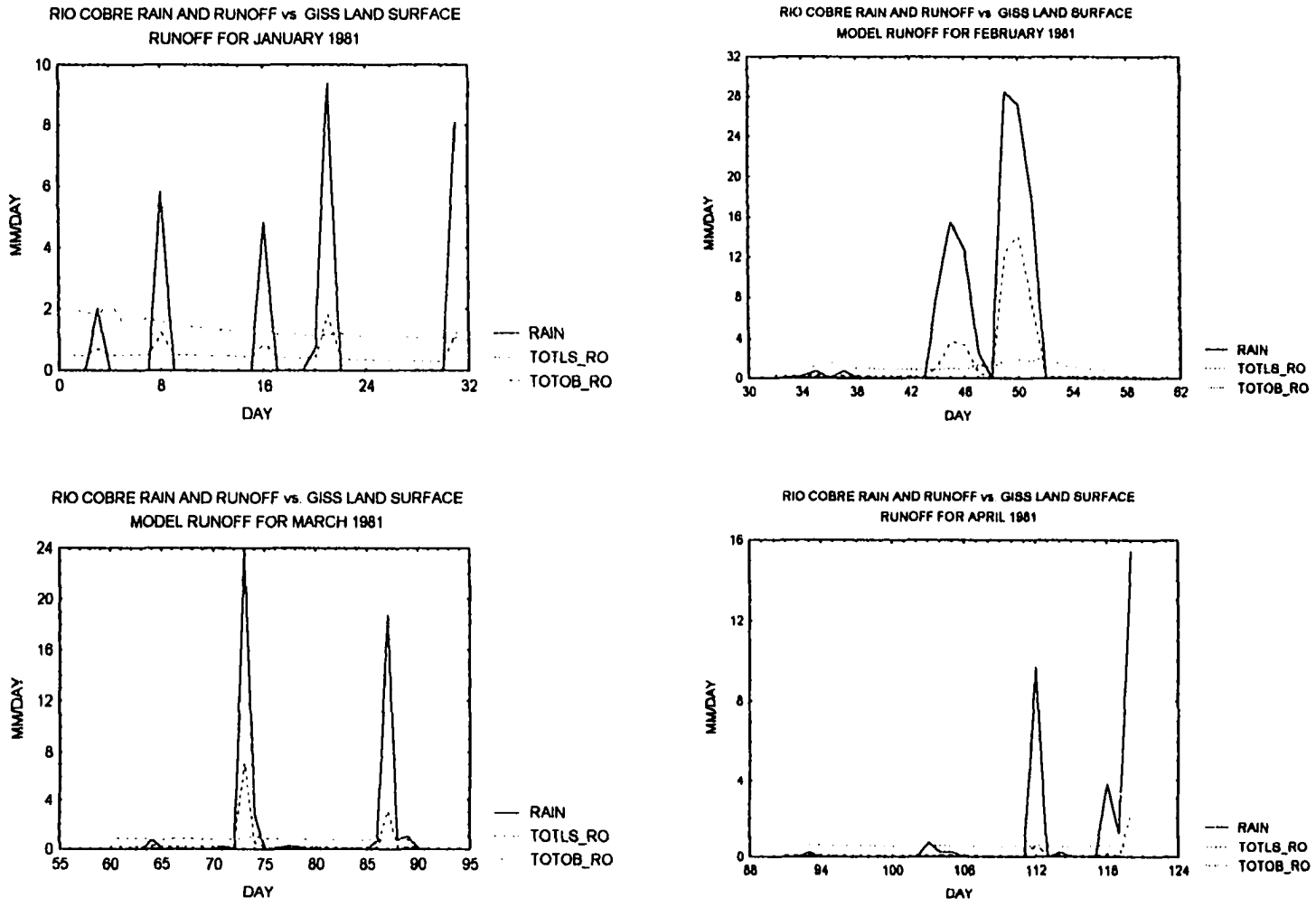

FIG. 23. Daily rain, observed and modeled runoff [Jan. - Apr., 1981]

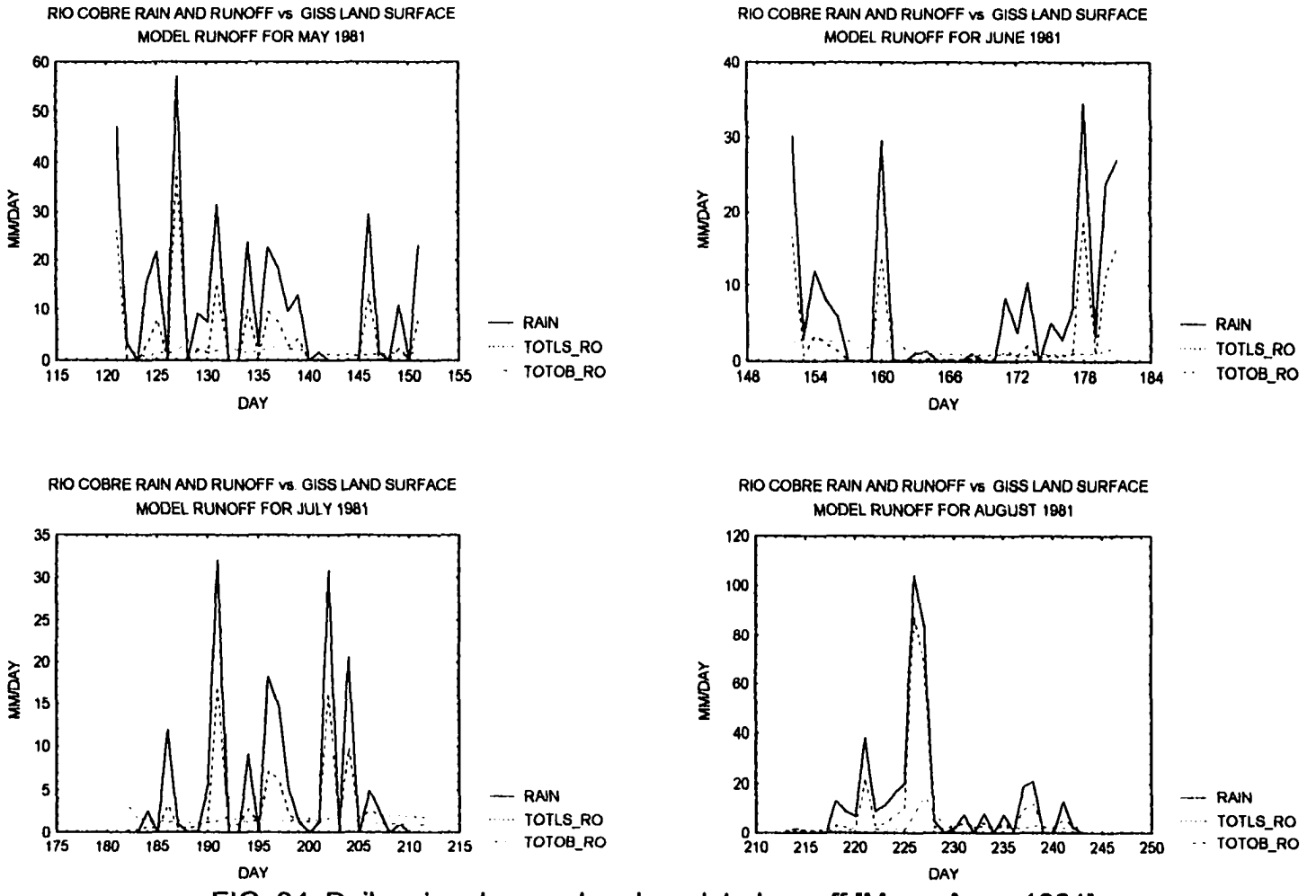

FIG. 24. Daily rain, observed and modeled runoff [May - Aug., 1981]

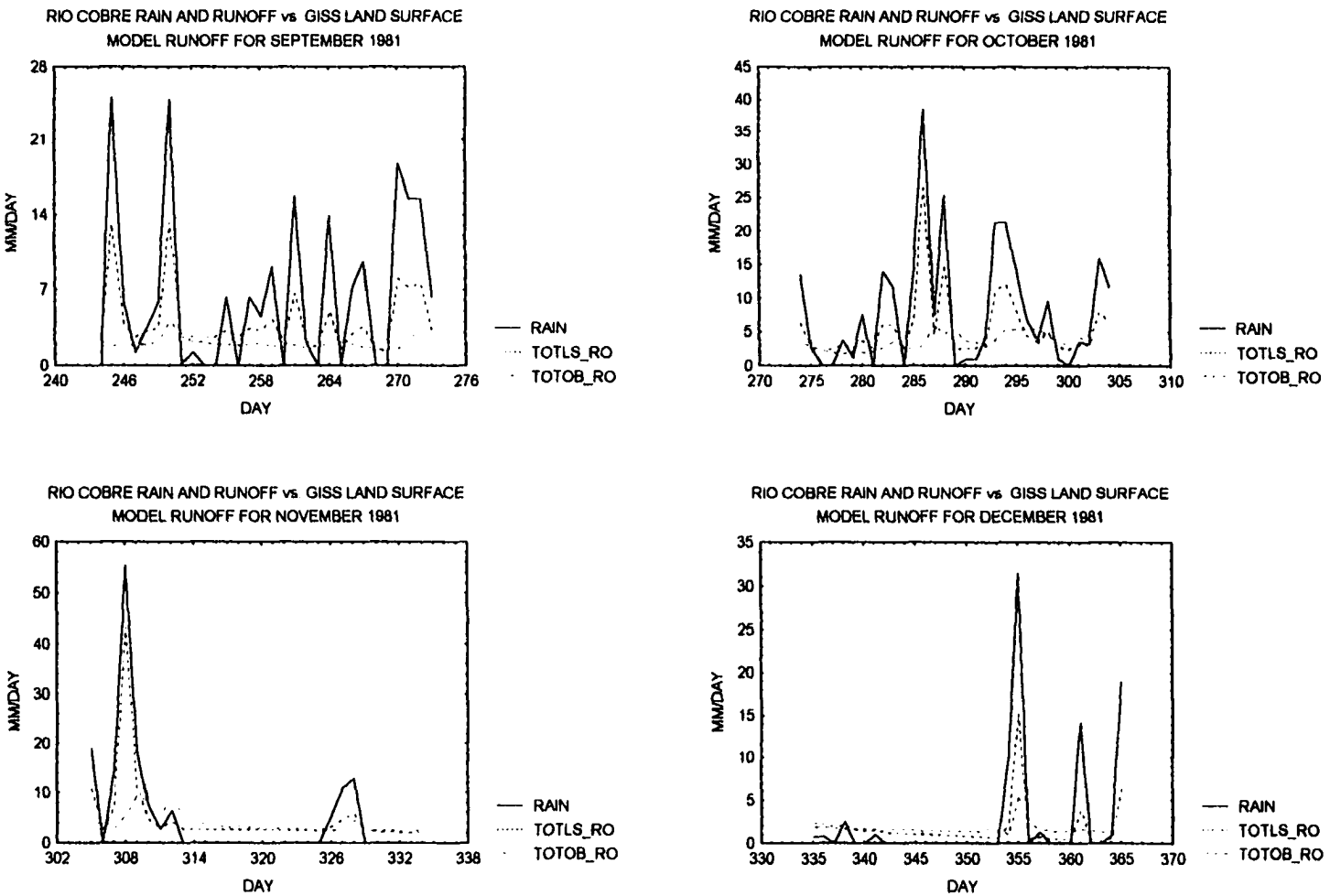

FIG. 25. Daily rain, observed and modeled runoff [Sep. - Dec., 1981]

over-predicts the runoff whenever the rainfall intensity is high. Since high intensity rainfall events occur often in the watershed, the model has a tendency to over-predict the runoff. January 1981 seems to be an anomalous month.

Comparing predicted and observed mean monthly runoff and the +/- 1 standard deviation range of that runoff for 1981 is yet another method of interrogating the data. In Table 1, the observed and modeled mean and the standard deviation range for each month of 1981 are shown. The standard error of the difference between two means is used to determine if the difference between the observed and the modeled monthly mean for each month is significant or merely due to chance.

Table 1. Mean Monthly Rio Cobre Runoff (mm/day) and its +/- 1 Standard Deviation Range for 1981: Observed (O) and GISS Land Surface (LS) Model

Month	O_Mean (x)	O_STD. Range	LS_Mean (t)	LS_STD. Range
* Jan	1.40	$1.09 \leq x \leq 1.71$	0.56	$0.23 \leq t \leq 0.89$
Feb	1.20	$0.83 \leq x \leq 1.57$	1.71	$-1.99 \leq t \leq 5.41$
Mar	0.80	$0.73 \leq x \leq 0.87$	0.54	$-0.76 \leq t \leq 1.84$
* Apr	0.60	$0.57 \leq x \leq 0.63$	0.19	$-0.21 \leq t \leq 0.59$
* May	1.70	$1.04 \leq x \leq 2.36$	5.10	$-3.60 \leq t \leq 14.80$
Jun	1.50	$0.74 \leq x \leq 2.26$	3.20	$-2.50 \leq t \leq 8.90$
* Jul	1.40	$0.94 \leq x \leq 1.86$	3.10	$-1.10 \leq t \leq 7.30$
Aug	2.80	$-0.20 \leq x \leq 5.80$	9.30	$-9.80 \leq t \leq 28.40$
* Sep	2.10	$1.51 \leq x \leq 2.69$	4.20	$1.10 \leq t \leq 7.30$
* Oct	3.60	$2.40 \leq x \leq 4.8$	5.70	$0.60 \leq t \leq 10.80$
Nov	3.80	$1.80 \leq x \leq 5.80$	5.00	$-2.60 \leq t \leq 12.60$
Dec	1.70	$0.95 \leq x \leq 2.45$	1.80	$-1.00 \leq t \leq 4.60$

* Monthly standard error statistic at the $\alpha = 0.05$ level indicates that the difference in means for this month is not due to chance; therefore, it is significant.

Figure 26 is a graphical representation of the data in Table 1. Both the table and the figure show that though the model may sufficiently capture the monthly mean runoff for six of the months in 1981, it fails to reproduce the variability therein.

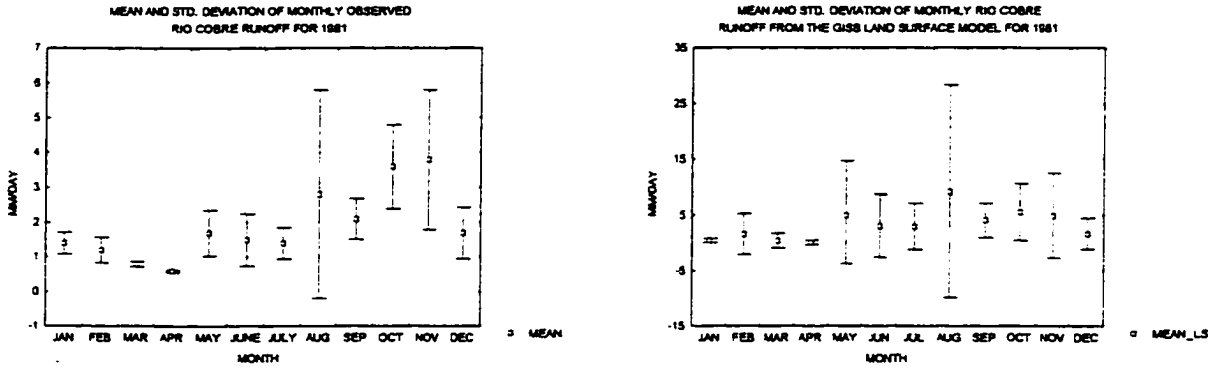

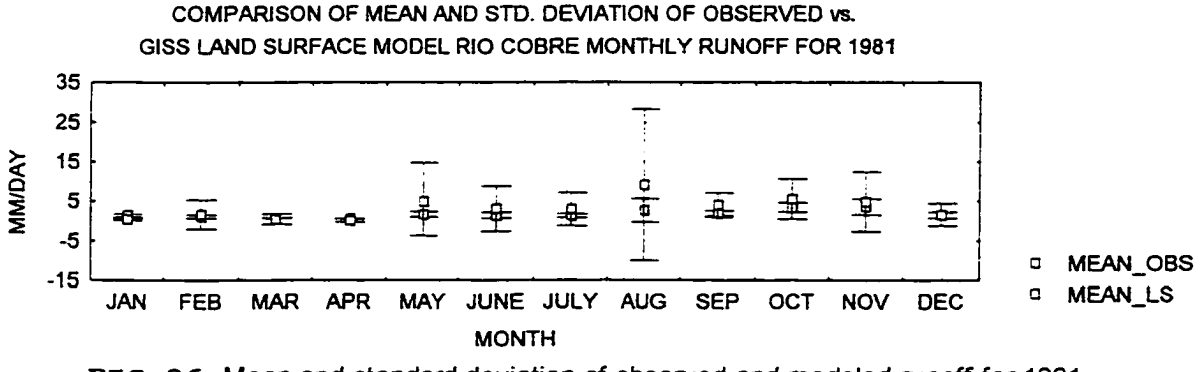

FIG.26 Mean and standard deviation of observed and modeled runoff for 1981

5.4 GISS Land-Surface Model's Sensitivity Analyses

In order to optimize the model's performance, sensitivity analyses were carried out for the primary parameters that affect runoff. These parameters are: root depth, root density, soil depth, vegetation type, the runoff soil moisture parameter and the interstream distance. The objective was to ascertain if variations in any of these parameters, or in some optimum combination thereof, would allow the model to better simulate the observed runoff. The following, then, are the sensitivity analyses for the above parameters.

Vegetation can affect watershed runoff by altering the watershed's water balance via evapotranspiration. Water is extracted from the soil by the root system of plants and passes through their vascular system and is ultimately released into the atmosphere through the stomata. The uptake of water by the root system depends on, among other things, the plant's root depth (for roots absorb water from soils at different depths) and the density distribution of the roots with depth, Taylor et al., (1978). Figure 27 illustrates the model's runoff sensitivity to root depth for (a) a uniformly distributed root system and (b) a non-uniformly distributed root system. On the figure's legend, BASE represents runoff when the root depth is 3m for both the uniform and non-uniform root distribution cases. The root depth of 3m. is the assumed root depth for the basin.

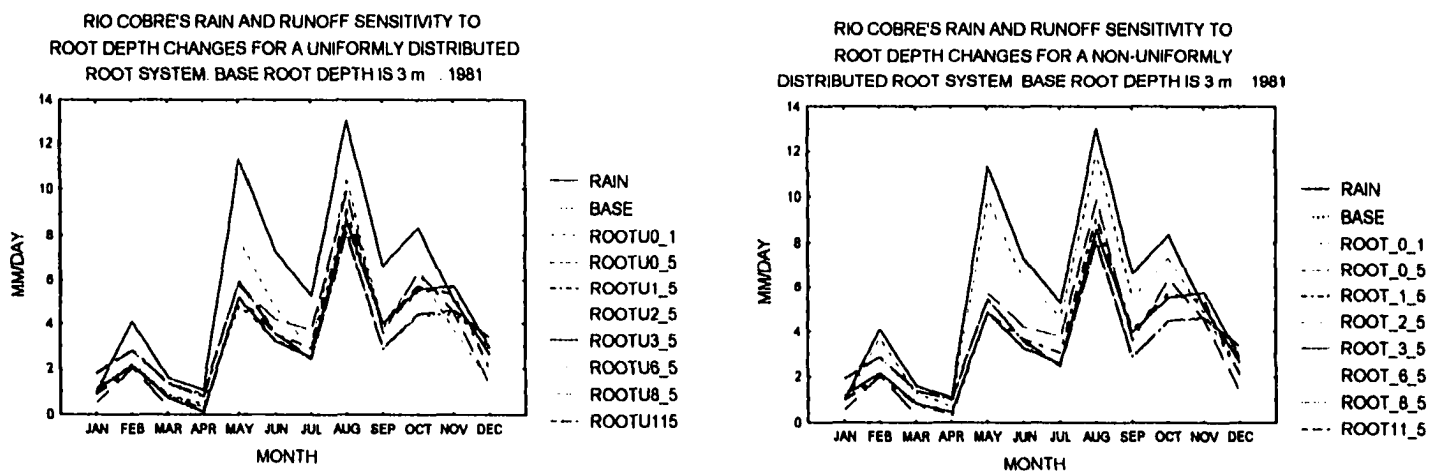

FIG. 27 Runoff sensitivity to uniform and non-uniform root system

The legend's ROOTU0_1 through ROOTU115 represent increases in the uniformly distributed root depth system from 0.1 to 11.5 meters while ROOT_0_1 through ROOT11_5 represent the same depth changes for the non-uniformly distributed root depth system. The figure also shows the model's runoff sensitivity to root density for a specific root depth. Overall, the model's runoff seems to be slightly more sensitive to the non-uniform root density distribution than it is to the uniform distribution especially for shallow soil depths. The indication, however, is that as the root depth increase and more water becomes available for transpiration, the watershed runoff decreases. In general, the model seems to be insensitive to root density. It is evident that the model's sensitivity to the root system is insufficient to account for its over-prediction of the Rio Cobre's runoff.

Another way in which vegetation can affect the water balance of a watershed, and thus it's runoff, is to intercept and withhold water that would otherwise reach the soil. Therefore, the water holding capacity of the canopy can alter runoff. In general, the bigger the water holding capacity of the canopy - the bigger the leaf area - the less the runoff. Additionally, with bigger or more leaves the canopy's active evaporating surface at the leaf-atmosphere interface increases. This enhances transpiration, and more transpiration would also lead

to less runoff. A grass-land vegetation area should, therefore, have more runoff than a forested area. Figure 28 shows the sensitivity of the model's runoff to vegetation type. Although some degree of runoff sensitivity is seen, it is not nearly enough to account for the discrepancy between simulated and observed runoff in the Rio Cobre watershed.

Figure 28 also depicts the sensitivity of the model's runoff to changes in soil depth for a constant root depth. In the figure, ZMAX [1, 3, 7, 10], represent maximum soil depths of 1m, 3m, 7m and 10m. For the most part, the model's runoff is insensitive to changes in soil depth. This may be so since at equilibrium the moisture in the soil will remain at the same level irrespective of the soil depth. Runoff sensitivity to changes in soil depth may be more pronounced and more seasonally dependent in climatic zones outside the tropics.

In the model, the slope of the soil surface is directly proportional to the underground runoff, one of the three components of total runoff. Runoff within the root zone and surface runoff are the other two components of total runoff. However, as Figure 29 illustrates, the model's total runoff is completely insensitive to changes in surface slope. This may be due to the incapacity of the model to appropriately simulate underground runoff in a karstic domain where the flow is not Darcian.

SENSITIVITY OF GISS LAND SURFACE MODEL'S RUNOFF TO VEGETATION TYPE. (RIO COBRE 1981 OBSERVED RAIN AND RUNOFF)

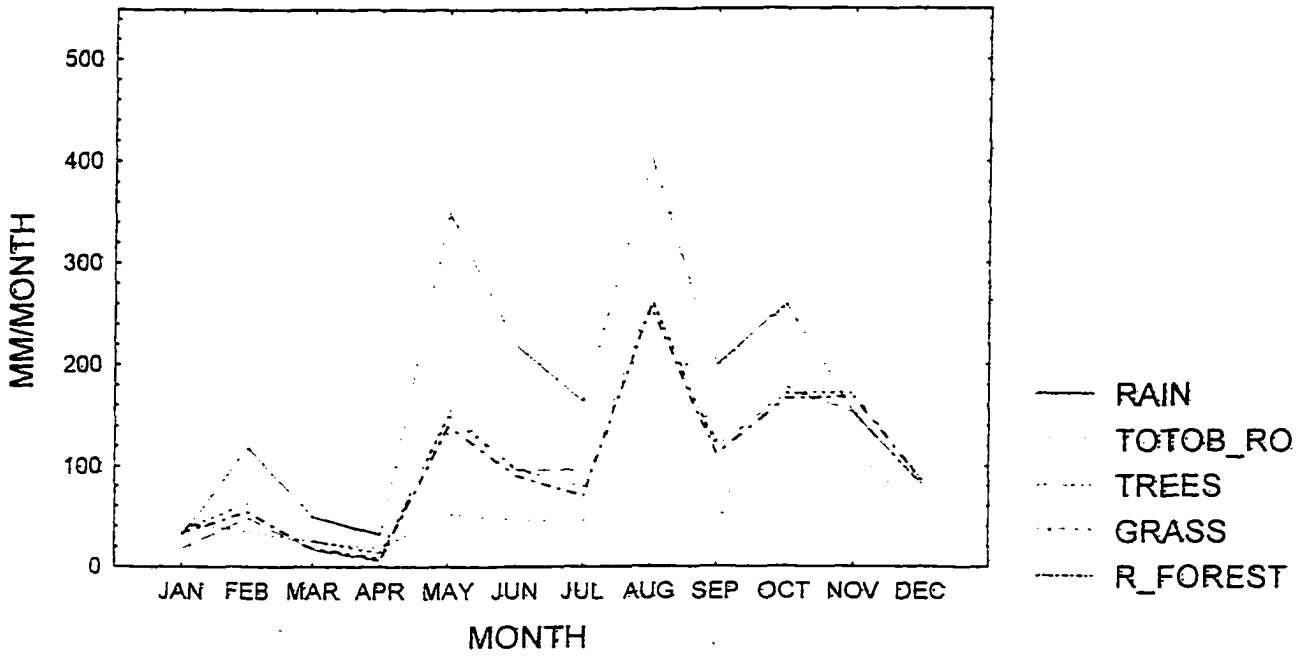

RIO COBRE'S MEAN MONTHLY RAIN AND MEAN MONTHLY RUNOFF SENSITIVITY TO CHANGES IN SOIL DEPTH: 1981 BASE ZMAX IS 3.5 m AND ROOT DEPTH IS 3.0 m IN ALL CASES

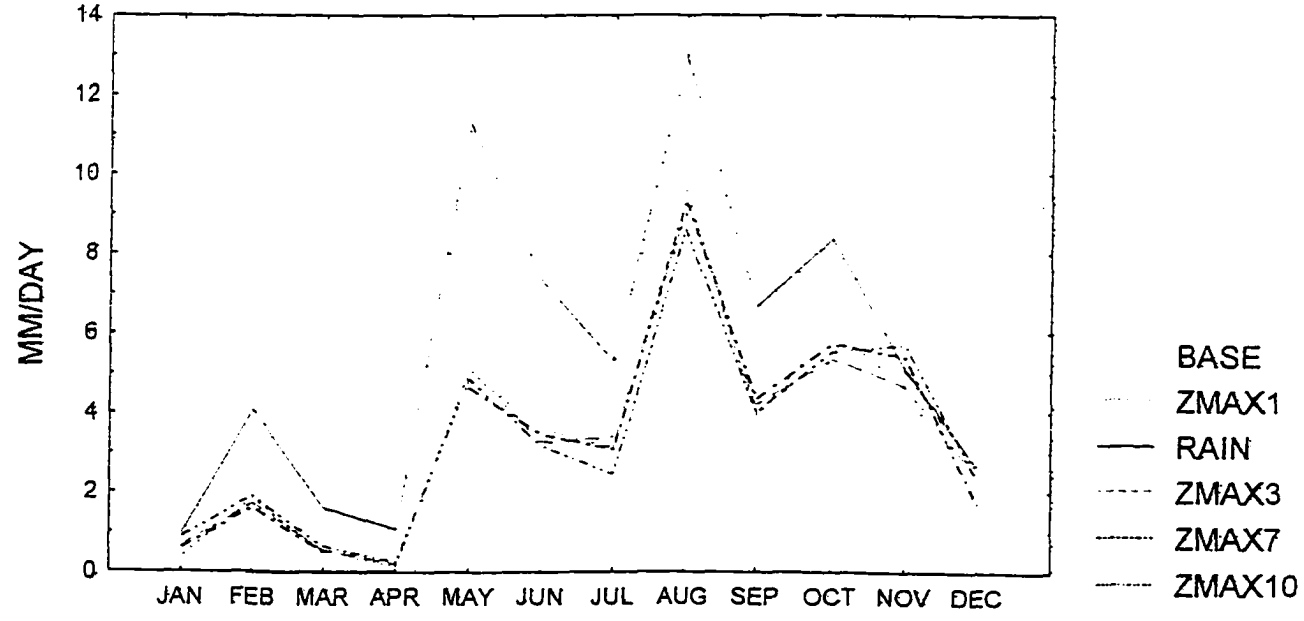

FIG. 28

RIO COBRE'S MEAN MONTHLY RAIN AND MEAN MONTHLY RUNOFF SENSITIVITY TO CHANGES IN BASIN SLOPE: 1981. BASE SLOPE IS 14 DEGREES

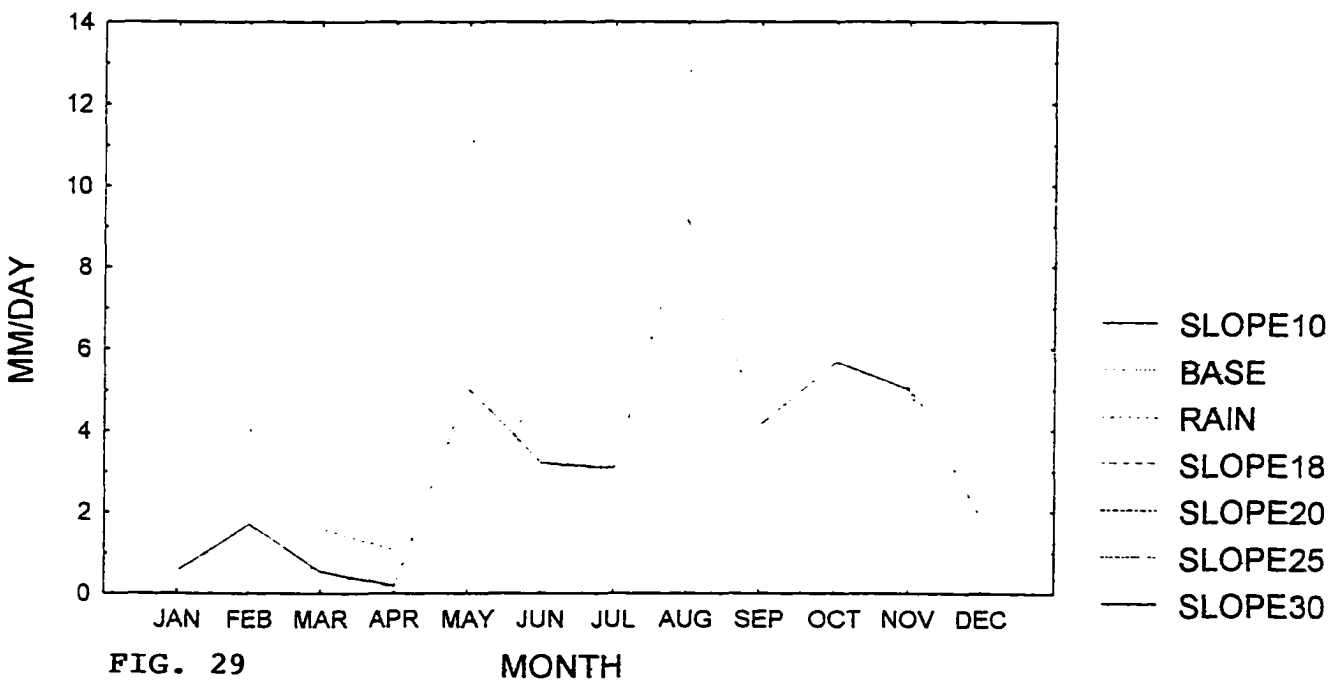

FIG. 29

The runoff soil moisture parameter (ROSMP) of the land-surface model is designed to reflect the Dunne type of runoff, i.e., runoff from a saturated or impermeable ground surface. Whenever the soil surface is impermeable or the first soil layer is saturated, all incoming rainfall should become runoff. Figure 30 shows how this parameter can be used to alter surface runoff. If the first soil layer is dry, then the fraction of soil that will produce runoff is zero, and if the first soil layer is saturated then the fraction of soil that will produce runoff is one. The ROSMP is designed, then, to alter the fraction of the soil that produces runoff when the relative saturation of the first soil layer is between zero and one. Admittedly this parameter is not physical, but it is an artifice used in the model to affect surface runoff. In Figure 30, yellow, green and red represent ROSMP values of 8, 32 and 64, respectively. Therefore, the higher the ROSMP value the lesser is the runoff fraction and thus the lesser the surface runoff.

The usefulness of the ROSMP is illustrated in Figures 31 - 36. In the figures the increase in the ROSMP is used to reduce the daily Rio Cobre runoff for 1981. Although the month of January is an anomalous month, three features emerge from these figures. First, increasing the ROSMP can be used to decrease predicted runoff. Second, ROSMP's effect on predicted runoff seem to peak at a value of 32, and third, the decrease in runoff which follows increases in

ROSMP is insufficient to bring the model's over-predicted runoff down to appropriate levels.

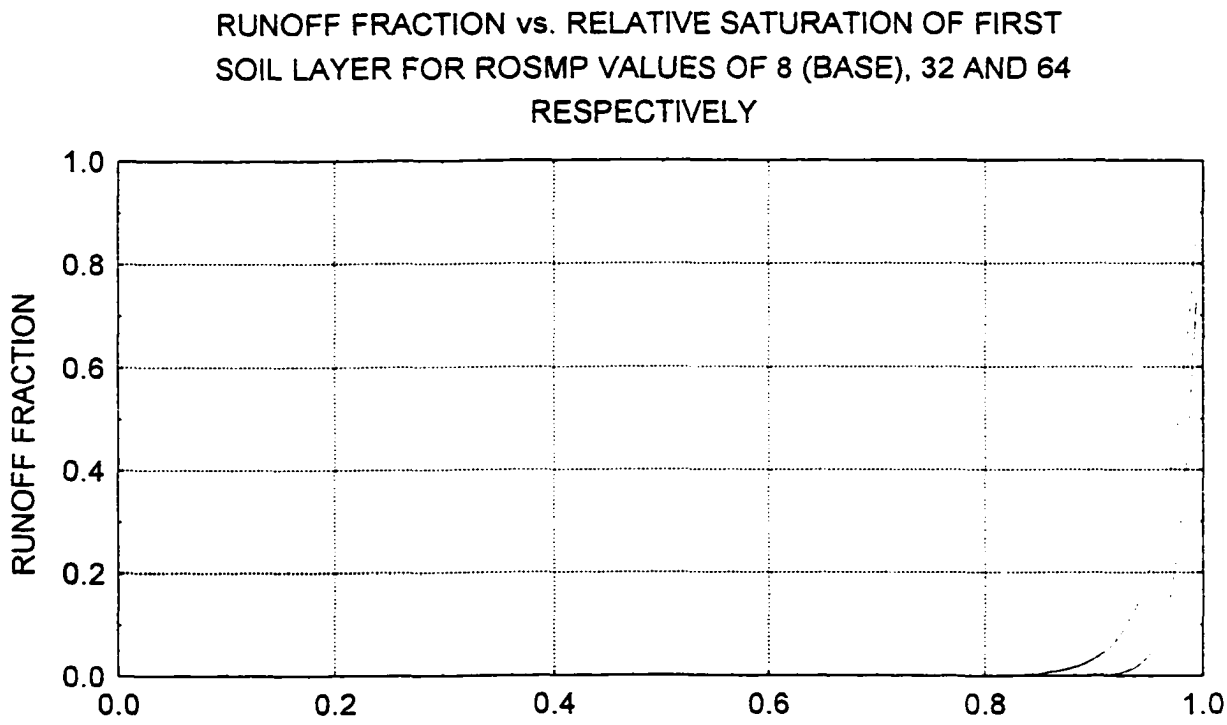

FIG. 30

RIO COBRE RAIN AND RUNOFF vs. GISS LAND SURFACE MODEL
RUNOFF SENSITIVITY TO ROSMP VALUES OF 8 (BASE), 32 AND 64
FOR JANUARY 1981

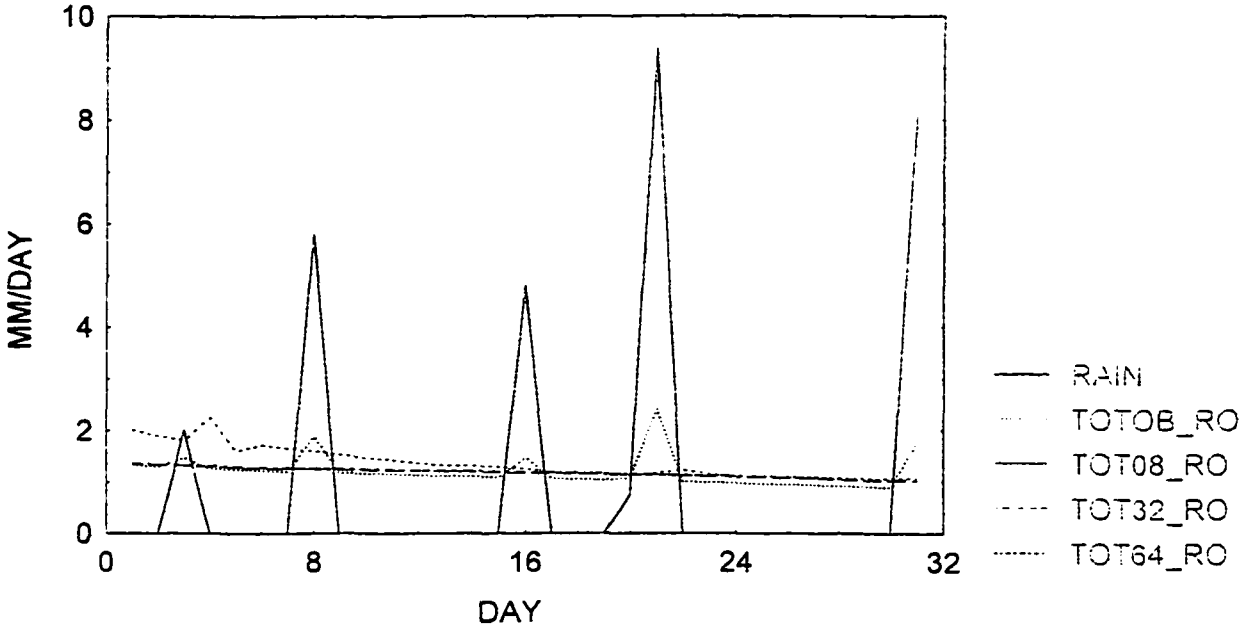

RIO COBRE RAIN AND RUNOFF vs. GISS LAND SURFACE MODEL
RUNOFF SENSITIVITY TO ROSMP VALUES OF 8 (BASE), 32 AND 64
FOR FEBRUARY 1981

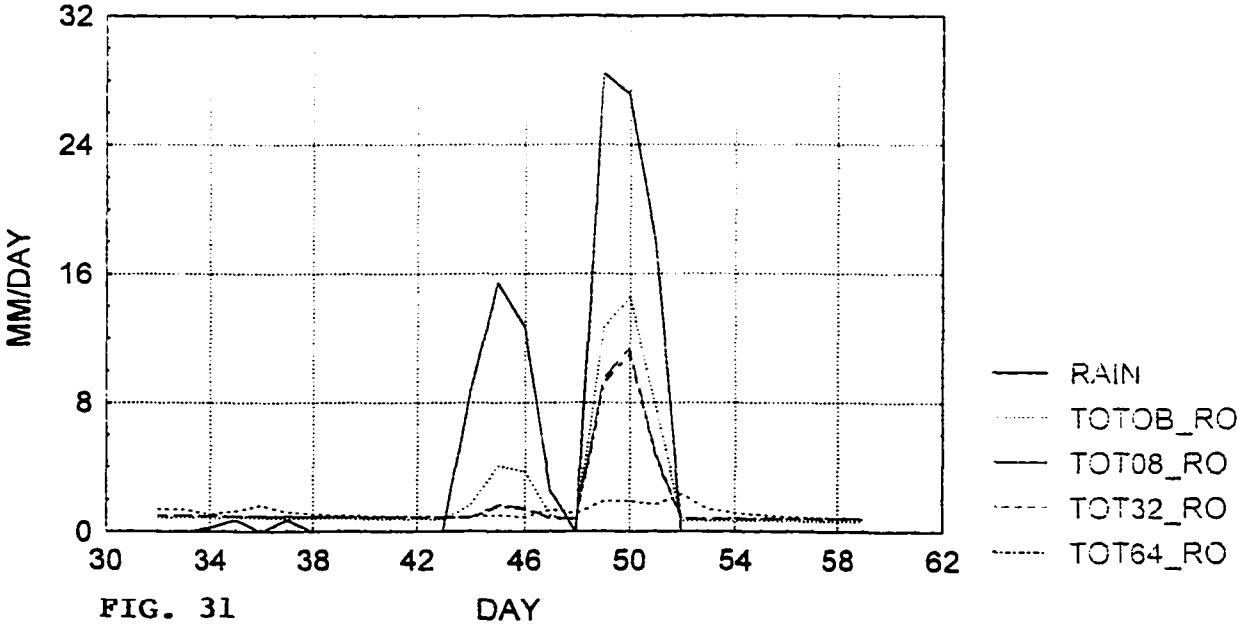

FIG. 31

RIO COBRE RAIN AND RUNOFF vs. GISS LAND SURFACE MODEL
RUNOFF SENSITIVITY TO ROSMP VALUES OF 8 (BASE), 32 AND 64
FOR MARCH 1981

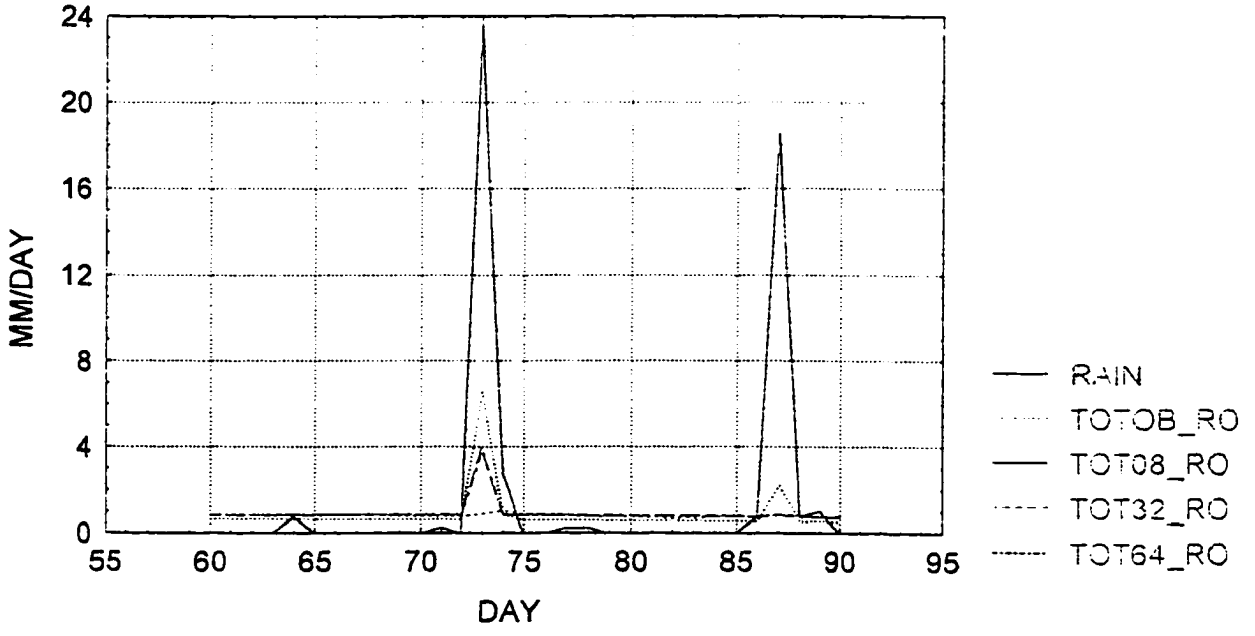

RIO COBRE RAIN AND RUNOFF vs. GISS LAND SURFACE MODEL
RUNOFF SENSITIVITY TO ROSMP VALUES OF 8 (BASE), 32 AND 64
FOR APRIL 1981

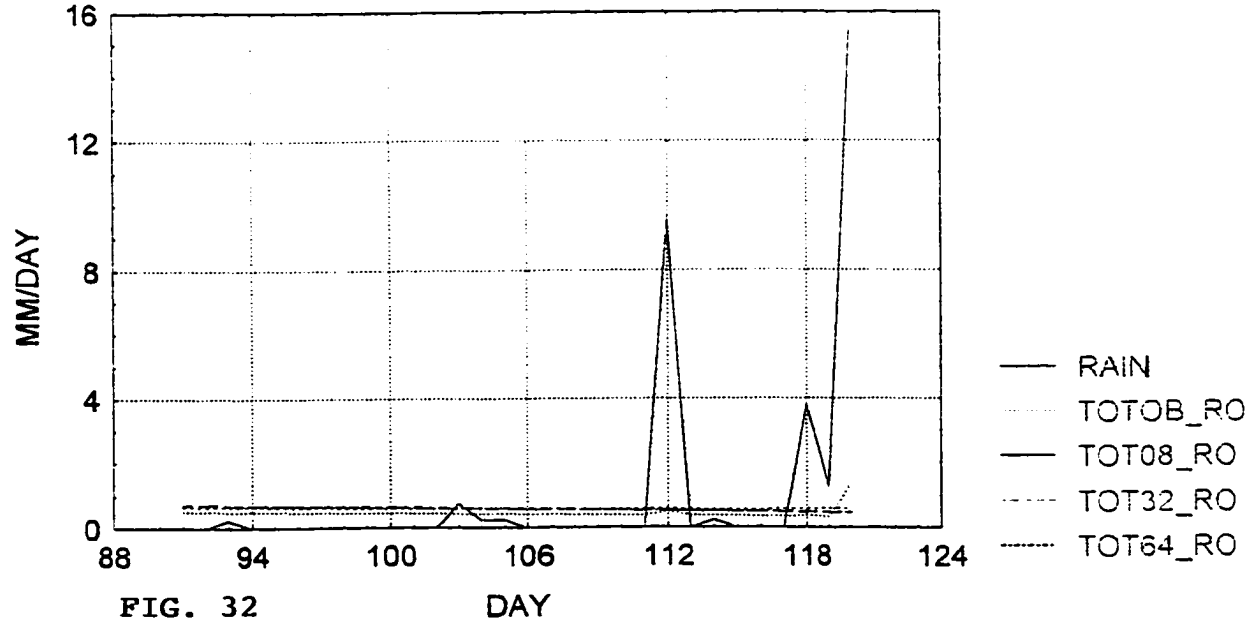

FIG. 32

RIO COBRE RAIN AND RUNOFF vs. GISS LAND SURFACE MODEL
RUNOFF SENSITIVITY TO ROSMP VALUES OF 8 (BASE), 32 AND 64
FOR MAY 1981

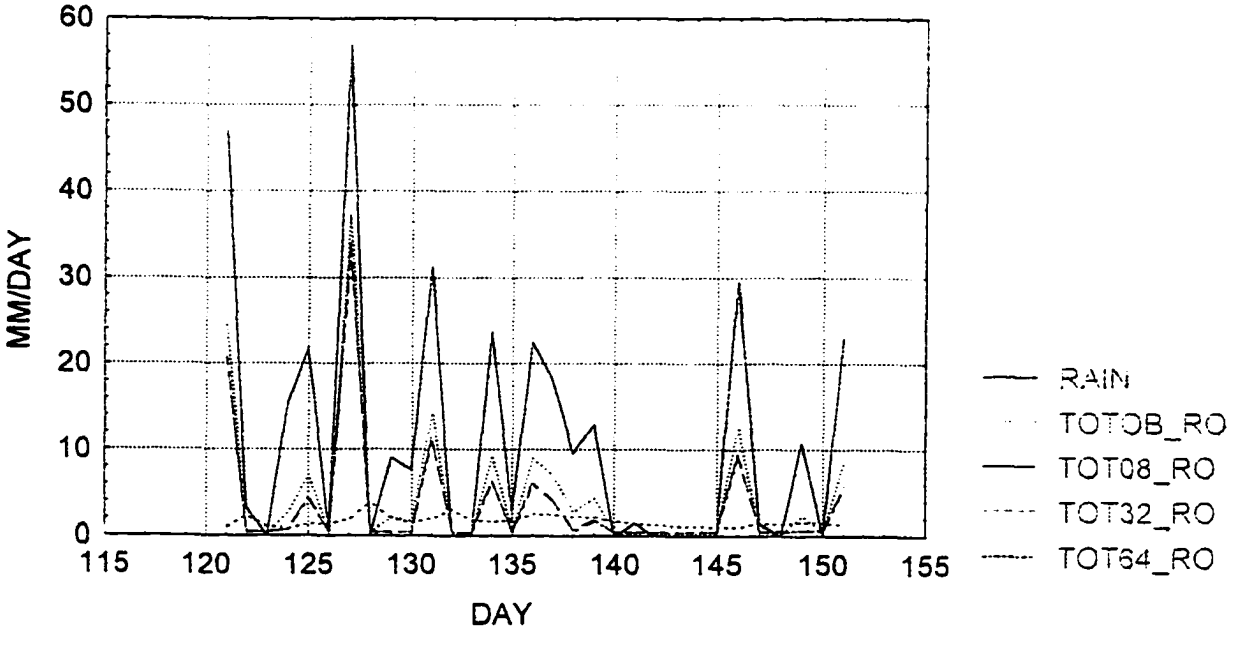

RIO COBRE RAIN AND RUNOFF vs. GISS LAND SURFACE MODEL
RUNOFF SENSITIVITY TO ROSMP VALUES OF 8 (BASE), 32 AND 64
FOR JUNE 1981

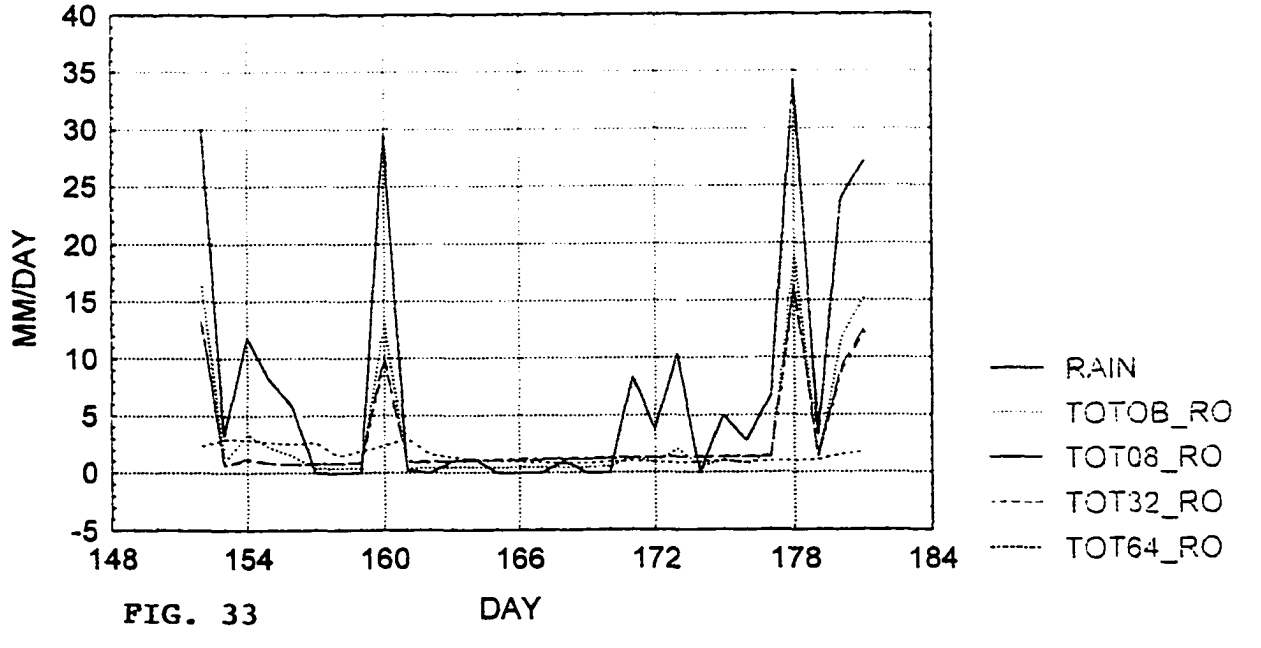

FIG. 33

RIO COBRE RAIN AND RUNOFF vs. GISS LAND SURFACE MODEL
RUNOFF SENSITIVITY TO ROSMP VALUES OF 8 (BASE), 32 AND 64
FOR JULY 1981

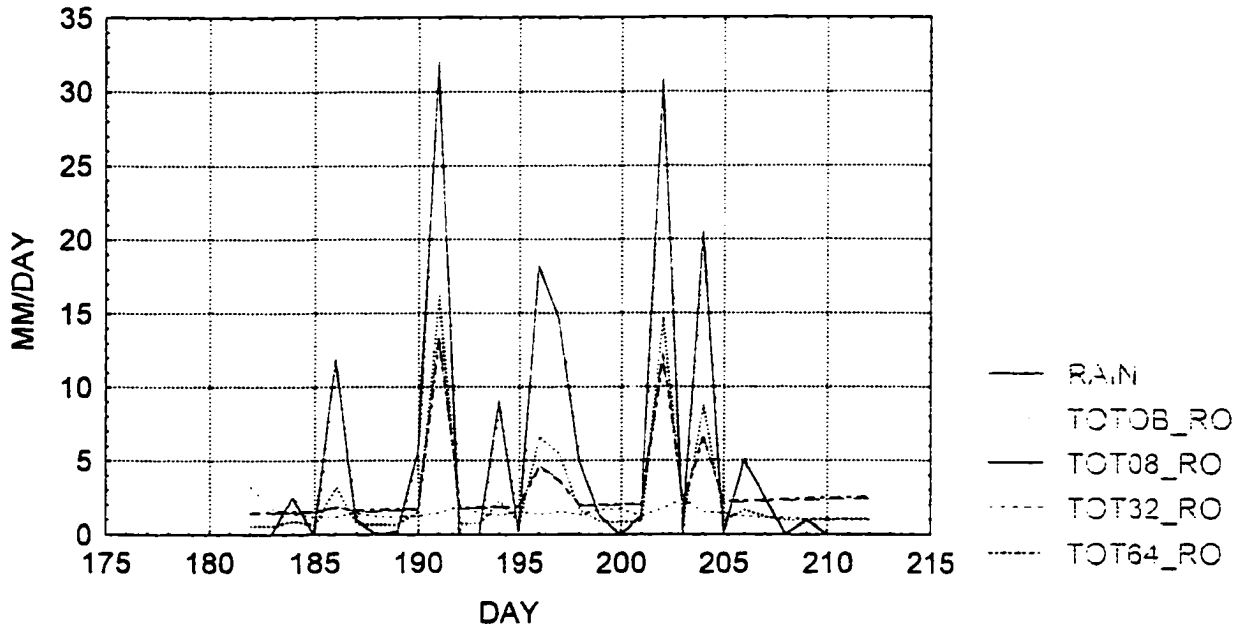

RIO COBRE RAIN AND RUNOFF vs. GISS LAND SURFACE MODEL
RUNOFF SENSITIVITY TO ROSMP VALUES OF 8 (BASE), 32 AND 64
FOR AUGUST 1981

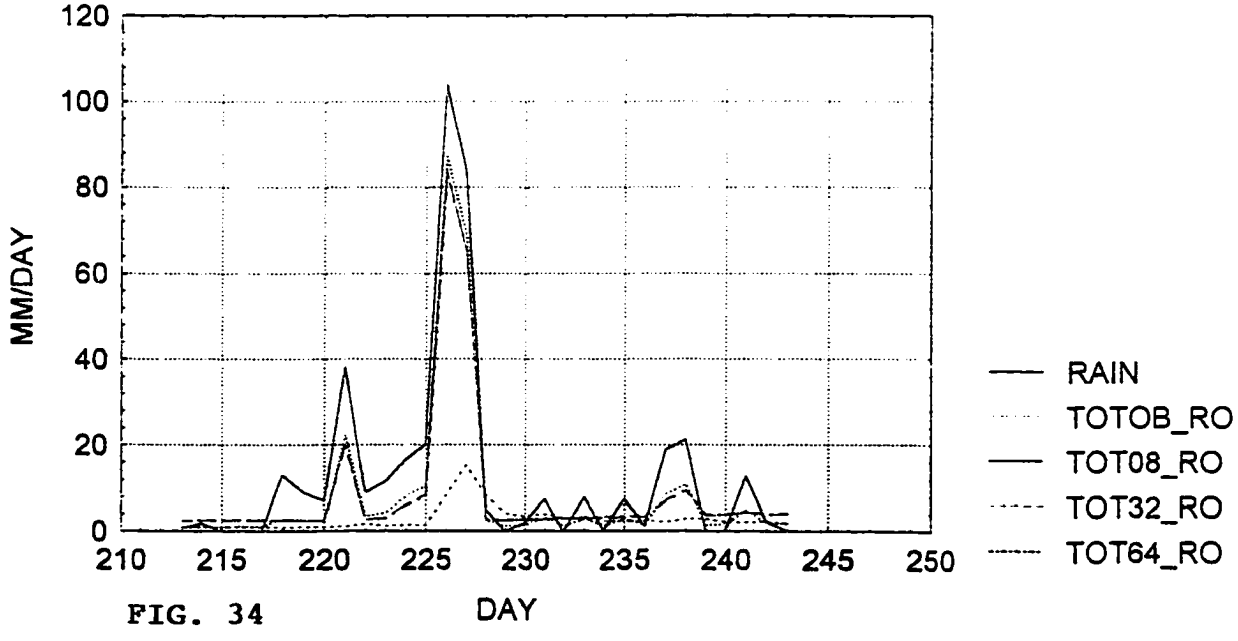

FIG. 34

RIO COBRE RAIN AND RUNOFF vs. GISS LAND SURFACE MODEL RUNOFF SENSITIVITY TO ROSMP VALUES OF 8 (BASE), 32 AND 64 FOR SEPTEMBER 1981

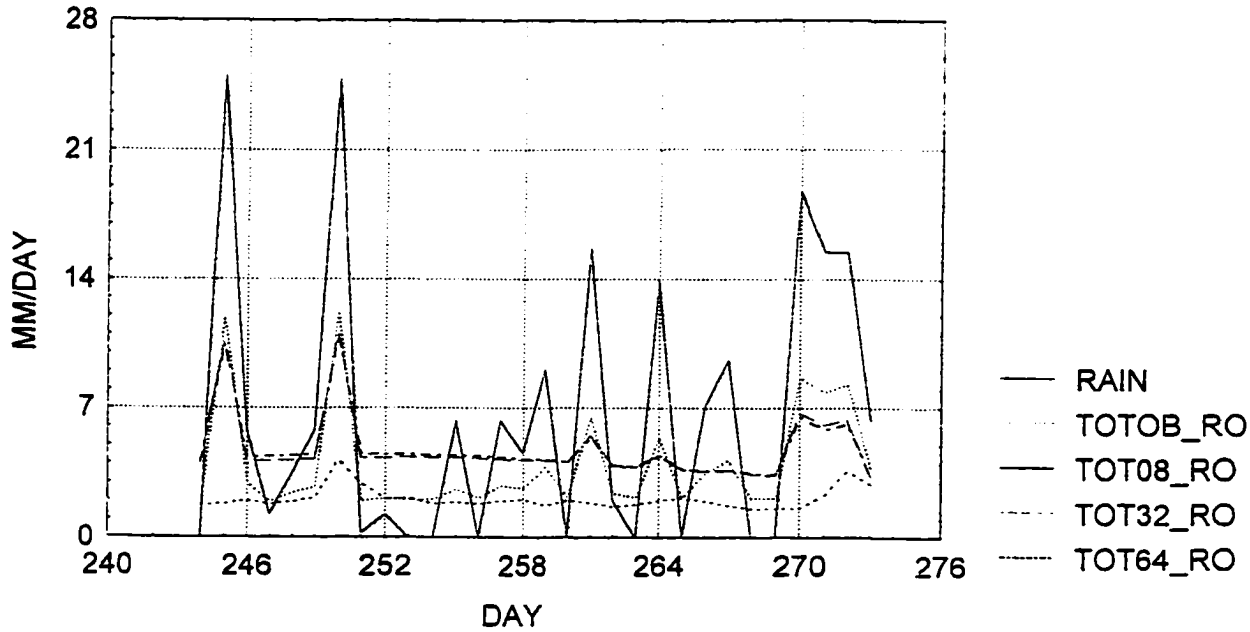

RIO COBRE RAIN AND RUNOFF vs. GISS LAND SURFACE MODEL RUNOFF SENSITIVITY TO ROSMP VALUES OF 8 (BASE), 32 AND 64 FOR OCTOBER 1981

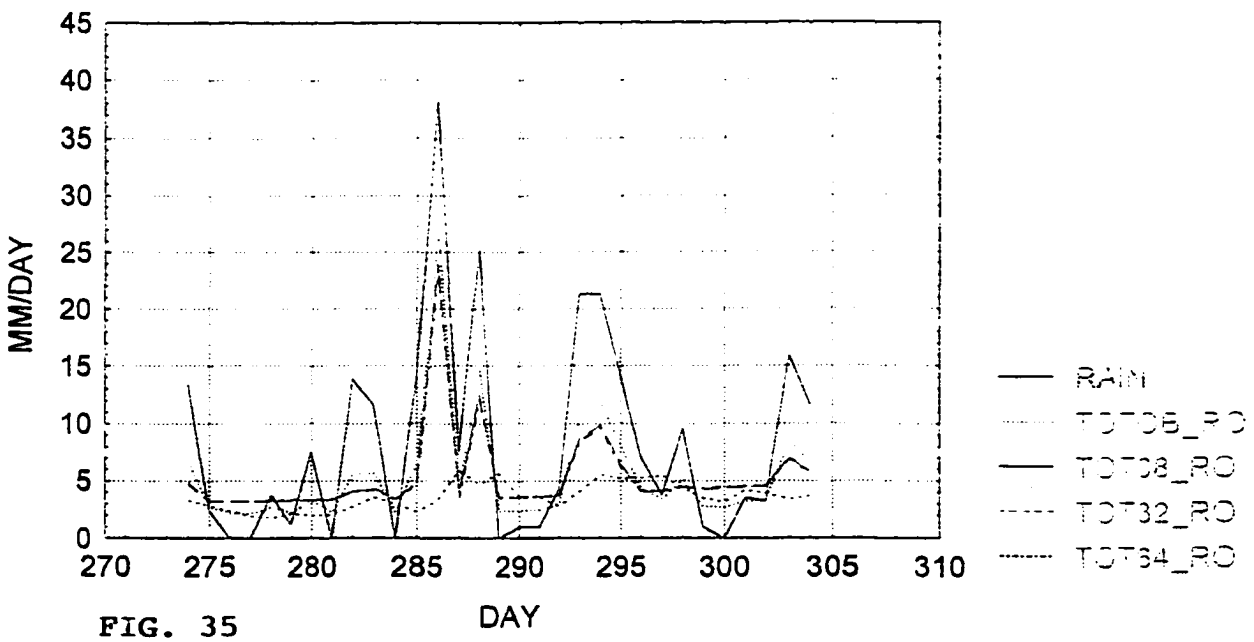

FIG. 35

RIO COBRE RAIN AND RUNOFF vs. GISS LAND SURFACE MODEL RUNOFF SENSITIVITY TO ROSMP VALUES OF 8 (BASE), 32 AND 64 FOR NOVEMBER 1981

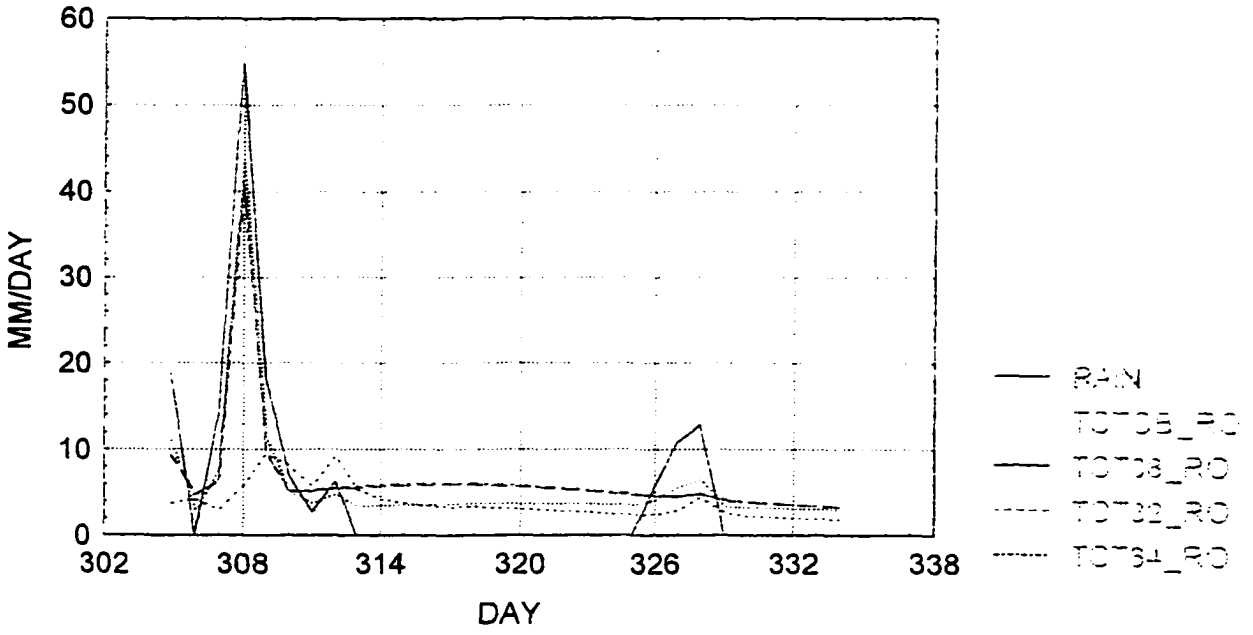

RIO COBRE RAIN AND RUNOFF vs. GISS LAND SURFACE MODEL RUNOFF SENSITIVITY TO ROSMP VALUES OF 8 (BASE), 32 AND 64 FOR DECEMBER 1981

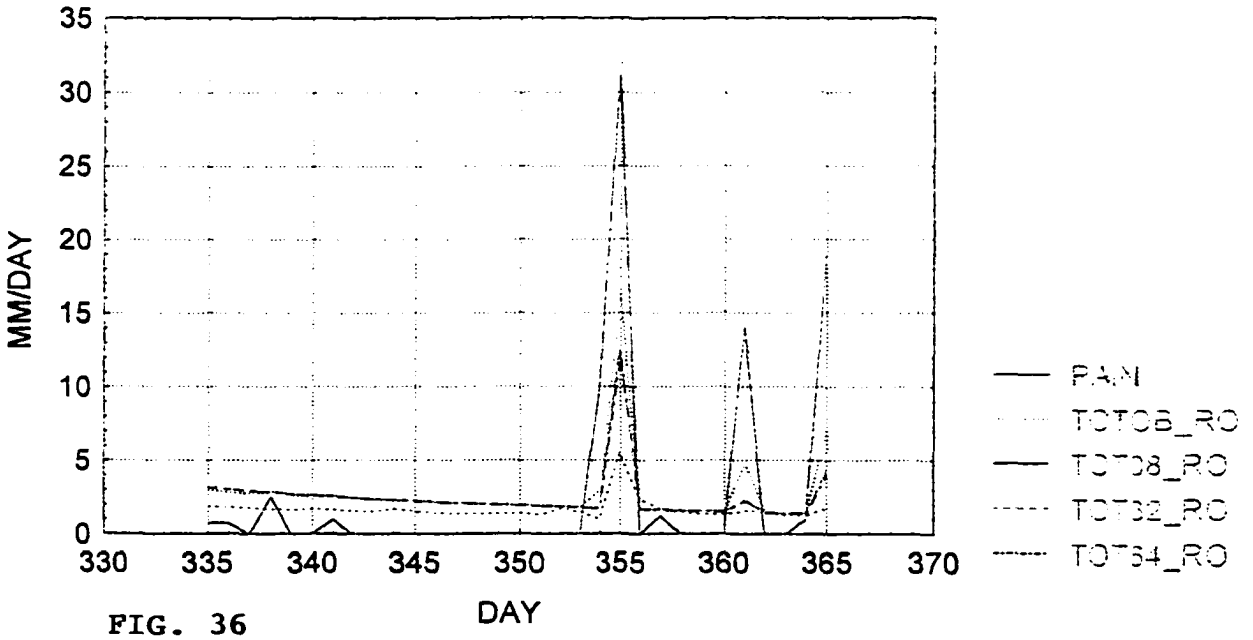

FIG. 36

The interstream distance can be interpreted as the distance over which the model removes the horizontal flux that is caused by the slope of the ground. It is the distance underground runoff must travel before it becomes a sink for the ground and a source for the main channel. The interstream distance is, therefore, inversely proportional to the runoff as can be seen in Figure 37. The figure shows the sensitivity of the model's runoff to this interstream distance and interstream distance coupled with ROSMP values. For the most part, Rio Cobre runoff is insensitive to the interstream distance.

After applying the GISS land-surface model to the Rio Cobre watershed, and after seeking model enhancement via sensitivity analyses of the model's key parameters, it is quite clear that the model in its present form cannot adequately simulate the runoff from this karstic landscape. Improvement in the model's performance can only be achieved by significant modification of the model. An additional hydrological component that represents the complex flow system of a karst terrain is required.

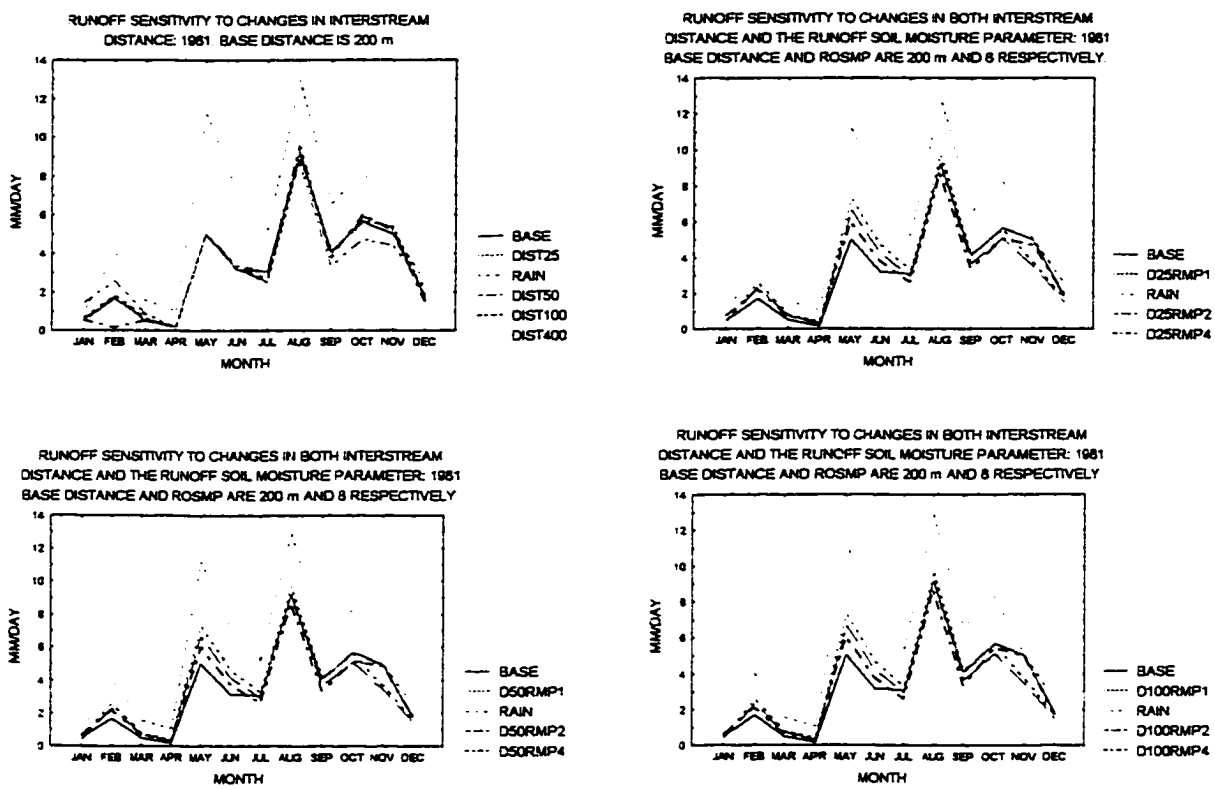

FIG. 37 Runoff sensitivity to interstream distance and ROSMP

6. GISS Land-Surface Model Improvement

The GISS GCM cannot accurately simulate the climate (past, present or future) of the approximately 12% of the earth that is karstic, where 25% of the world's population lives unless its land-surface component is able to improve the over-estimate of runoff from karstic watersheds. Armed with a better understanding of karst hydrology, three approaches toward model improvement will now be applied and discussed. The three approaches are: one, simulate runoff with the existing model but by using a permeable bedrock; two, simulate runoff with the existing model by using a coarse soil (sand) in conjunction with a permeable bedrock; and three, simulate runoff by modifying the existing model via adding a third column characterized by pipe flow theory.

6.1 Permeable Bedrock

The first step towards model improvement is to relax the model's constraint of a no mass flux at the bottom boundary of the column. That is, make the bedrock permeable. Figure 38 (a plot of September 1981 rain and runoff sensitivity to permeability and the ROSMP) indicates that greater reductions in runoff do occur with increasing ROSMP values and a permeable bedrock than with increasing ROSMP and an impermeable bedrock. To see more clearly how

sensitive the runoff is to changes in permeability, plots of 0%, 50% and 100% permeable bedrock with a ROSMP value of 32 were done for each month of 1981: Figure 39 [January - April], Figure 40 [May - August] and Figure 41 [September - December]. As expected, runoff is inversely proportional to permeability. However, the reductions that occur, especially for high rainfall rates, are still grossly inadequate to match the observed runoff. This indicates that a permeable bedrock, by itself, is insufficient to improve the model's runoff for a karstic watershed.

6.2 Sand and Permeable Bedrock

The soil textures that were used in the above experiments were those given by the Water Resources Authority of Jamaica as being most representative of the Rio Cobre watershed. They were: sand (5%), loam (40%) and clay (55%). The second step towards model improvement is to treat the watershed as if sand - the most permeable of the three textures - were the only soil texture. Runoff simulations were then done with an all sand watershed and a permeable bedrock.

RIO COBRE RAIN AND RUNOFF vs. GISS LAND SURFACE RUNOFF
FOR 100% PERMEABLE BEDROCK WITH ROSMP VALVES OF 8, 16, 32

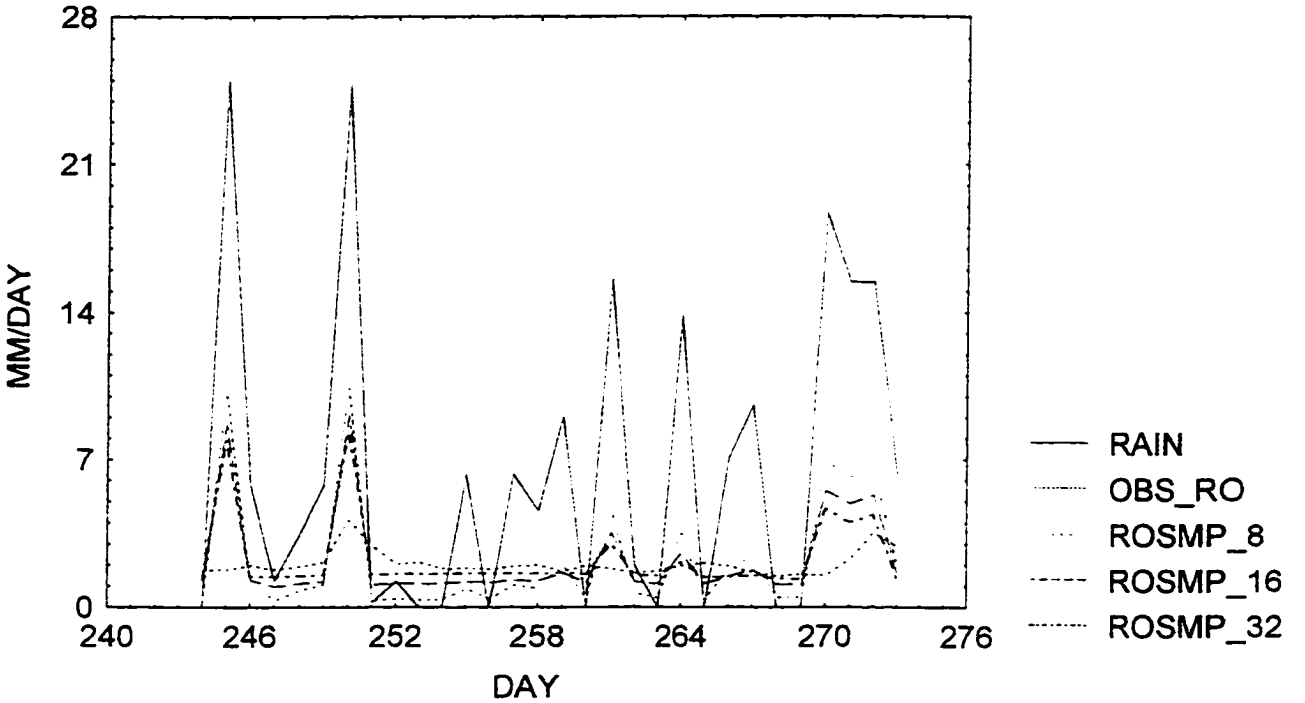

RIO COBRE RAIN AND RUNOFF vs. GISS LAND SURFACE RUNOFF
FOR IMPERMEABLE BEDROCK WITH ROSMP VALUES OF 8, 16, 32

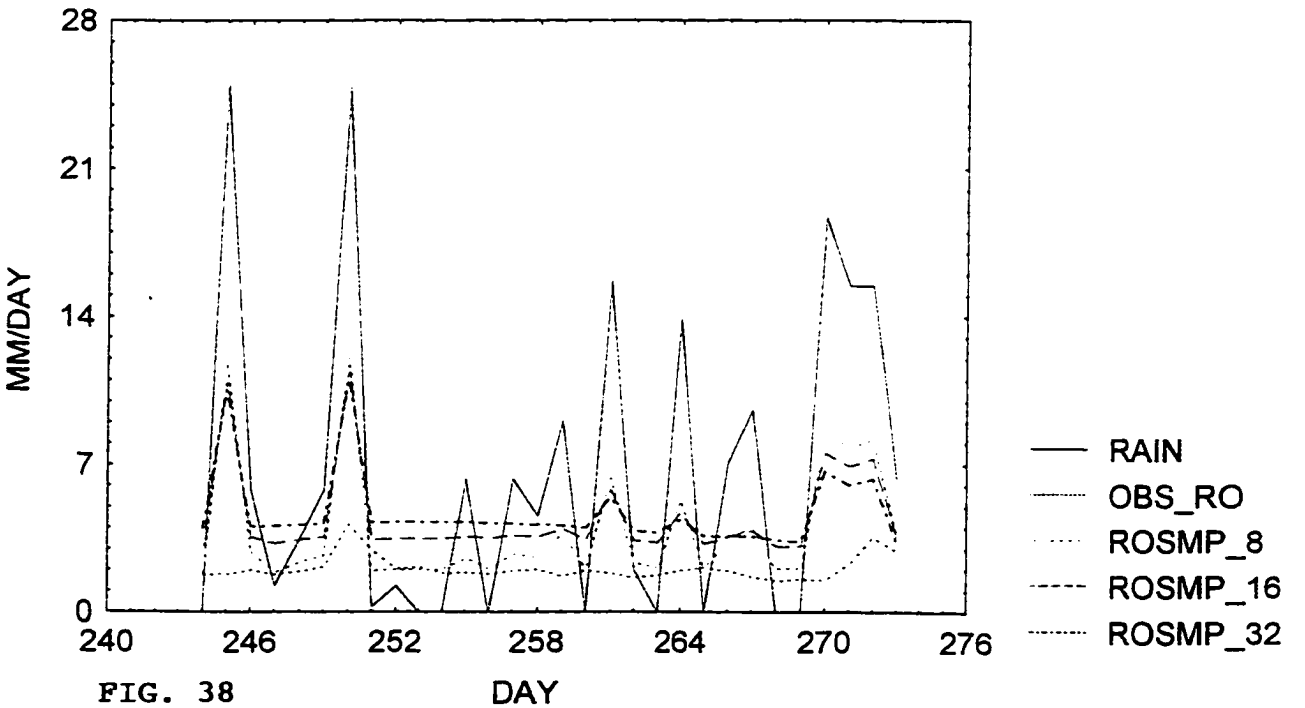

FIG. 38

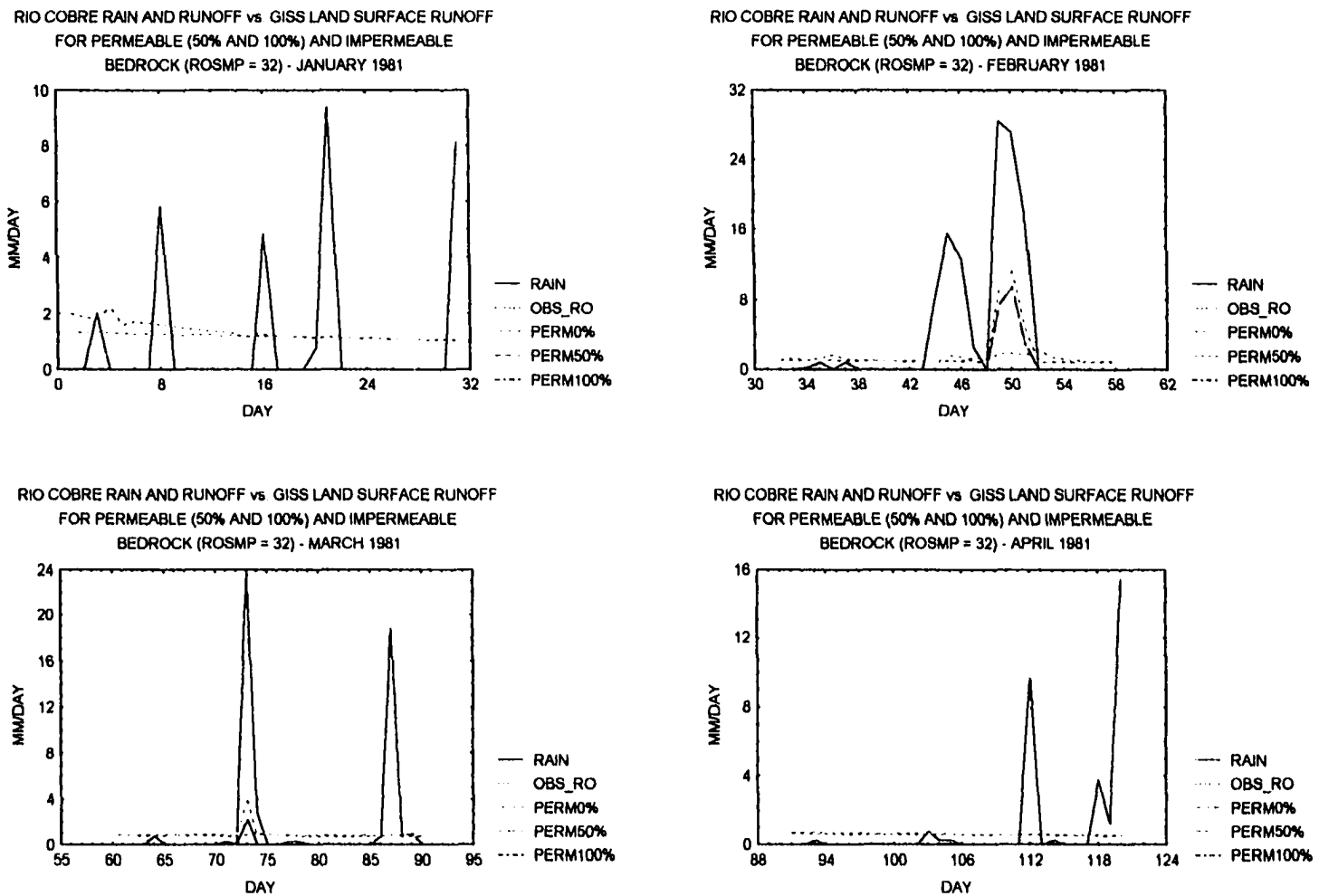

FIG. 39 Runoff sensitivity to permeable and impermeable bedrock [Jan-Apr., 1981]

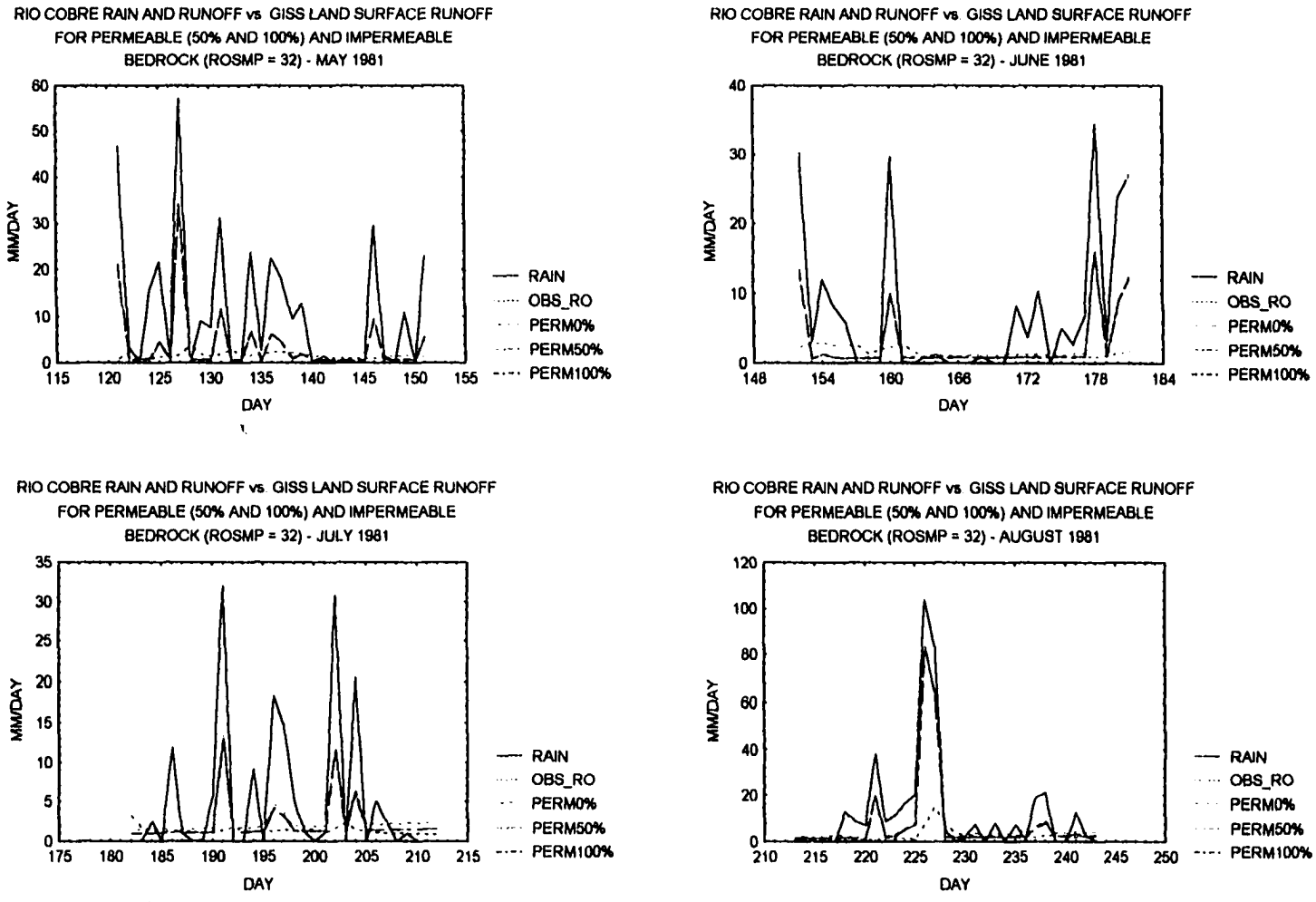

FIG. 40 Runoff sensitivity to permeable and impermeable bedrock [May-Aug., 1981]

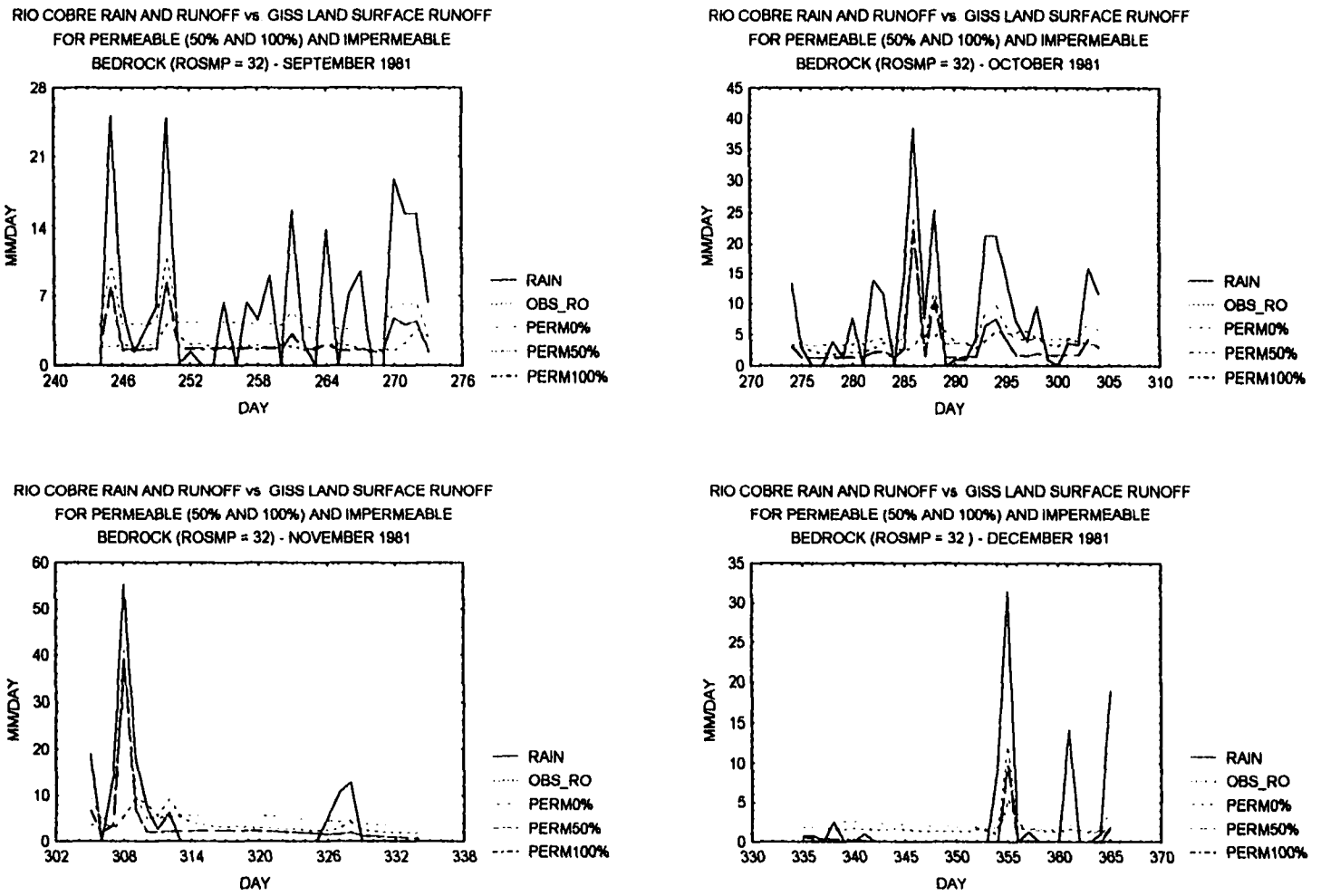

FIG. 41 Runoff sensitivity to permeable and impermeable bedrock [Sep-Dec., 1981]

Figures 42 - 44 show the results of this experiment. Comparing the all sand results to the three-textured soil results, there is a slightly greater reduction in runoff when the watershed is treated as if sand were its only soil texture. However, the reductions achieved via an all sand column with a permeable bedrock are inadequate to match the observed watershed runoff. This result may be indicative of the inappropriateness of applying Darcian flow theory to karst.

6.3 Third Column with Pipe Flow

The third step in model improvement involves the creation of a third "karst" column. This is achieved by dividing the model's gridbox into three separate columns - vegetated, bare and karst - instead of the previous two. The vegetated and bare soil columns are the same as they were before, except that the bedrock in both is now permeable. The karst column is characterized by: (a) no watertable; (b) non Darcian flow; (c) a high infiltration rate; (d) permeable bedrock; (e) no Gardner-Hillel diffusion type parameterization for maximum evaporation; (f) no lateral underground runoff; (g) vertical pipes from the soil surface down and turbulent pipe flow. Figure 45 illustrates the three-columned model with the relevant fluxes.

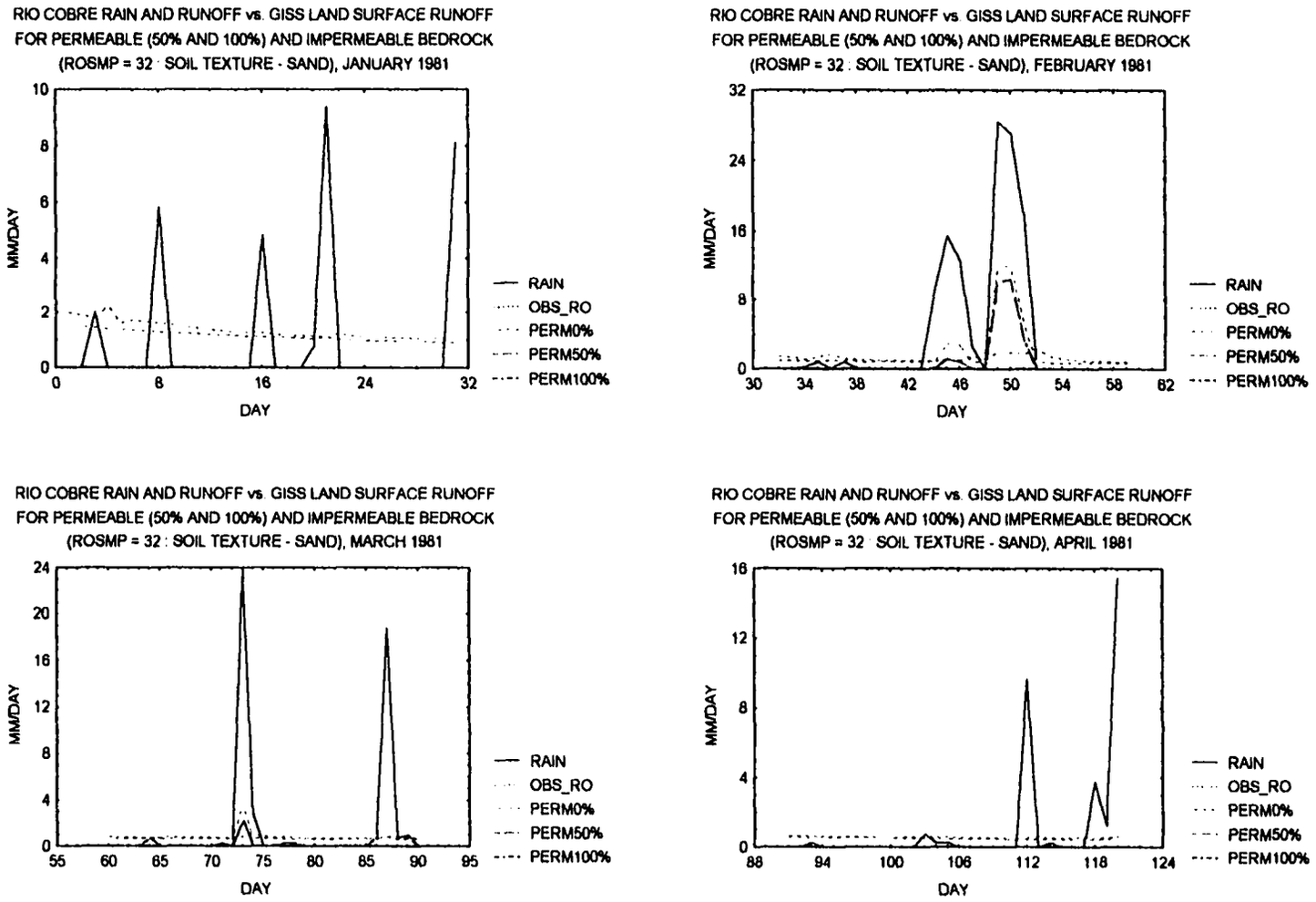

FIG. 42 Runoff sensitivity to perm. and imperm. bedrock: SAND: Jan-Apr, 1981

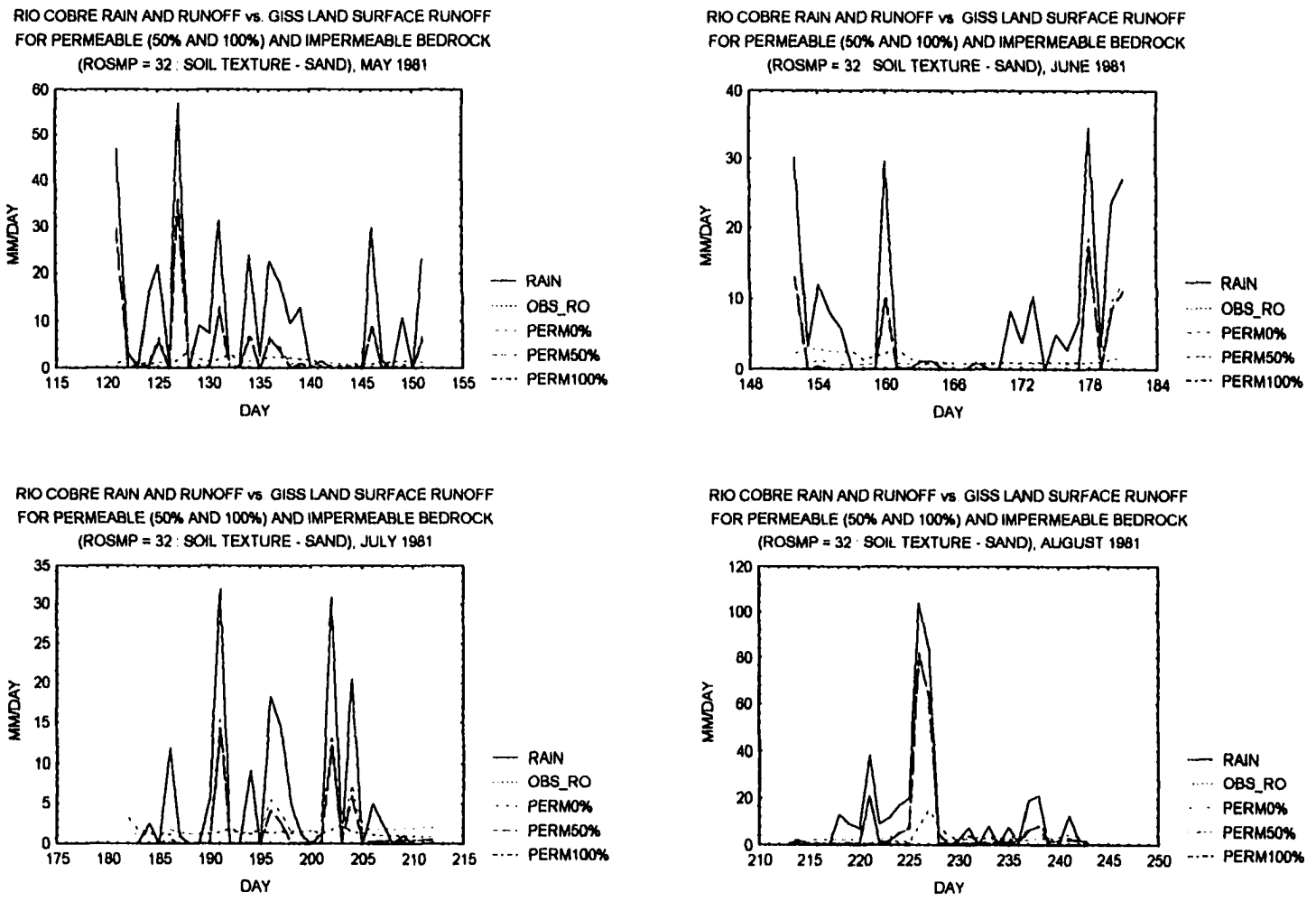

FIG. 43 Runoff sensitivity to perm. and imperm. bedrock: SAND: May-Aug, 1981

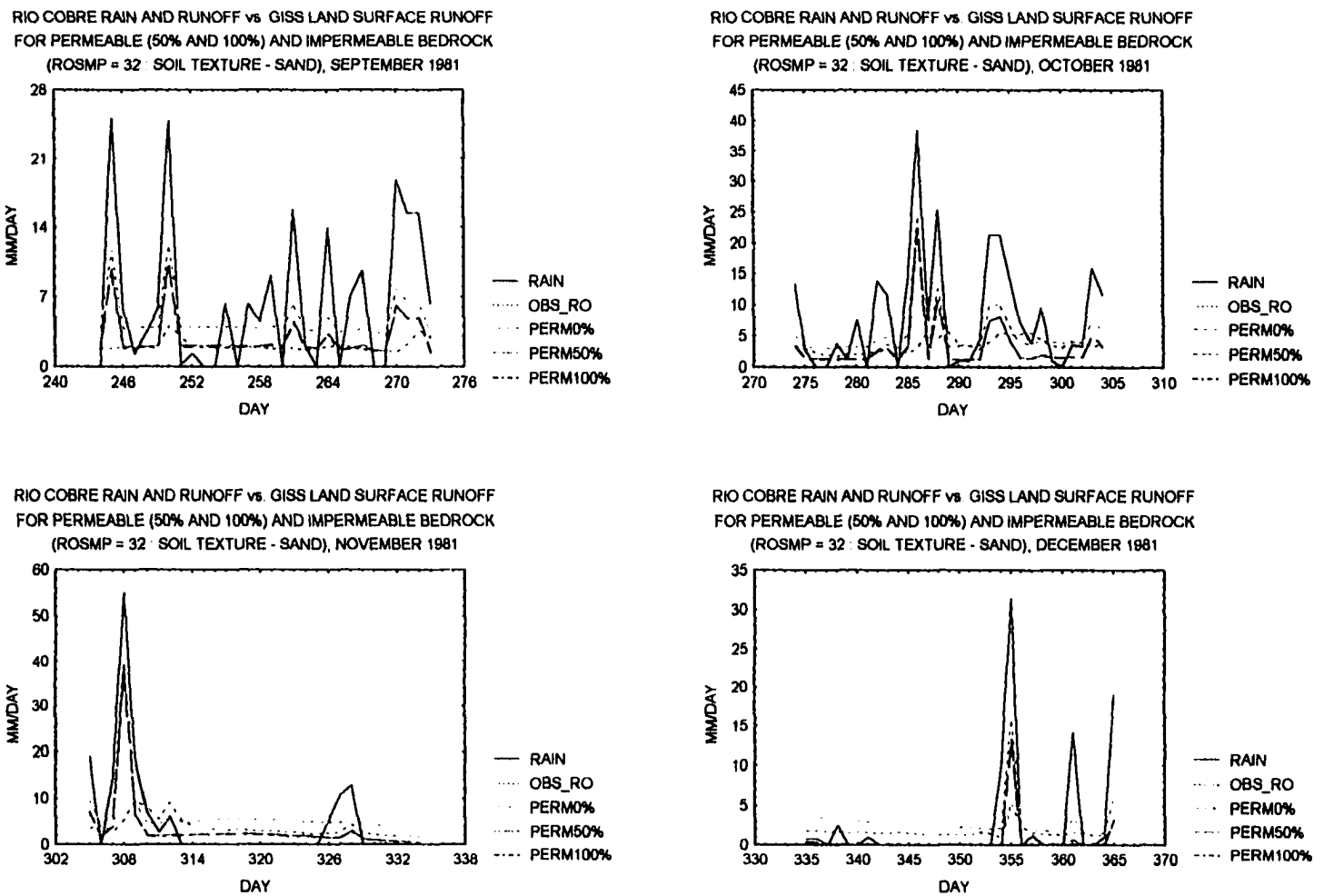

FIG. 44 Runoff sensitivity to perm. and imperm. bedrock: SAND: Sep-Dec, 1981

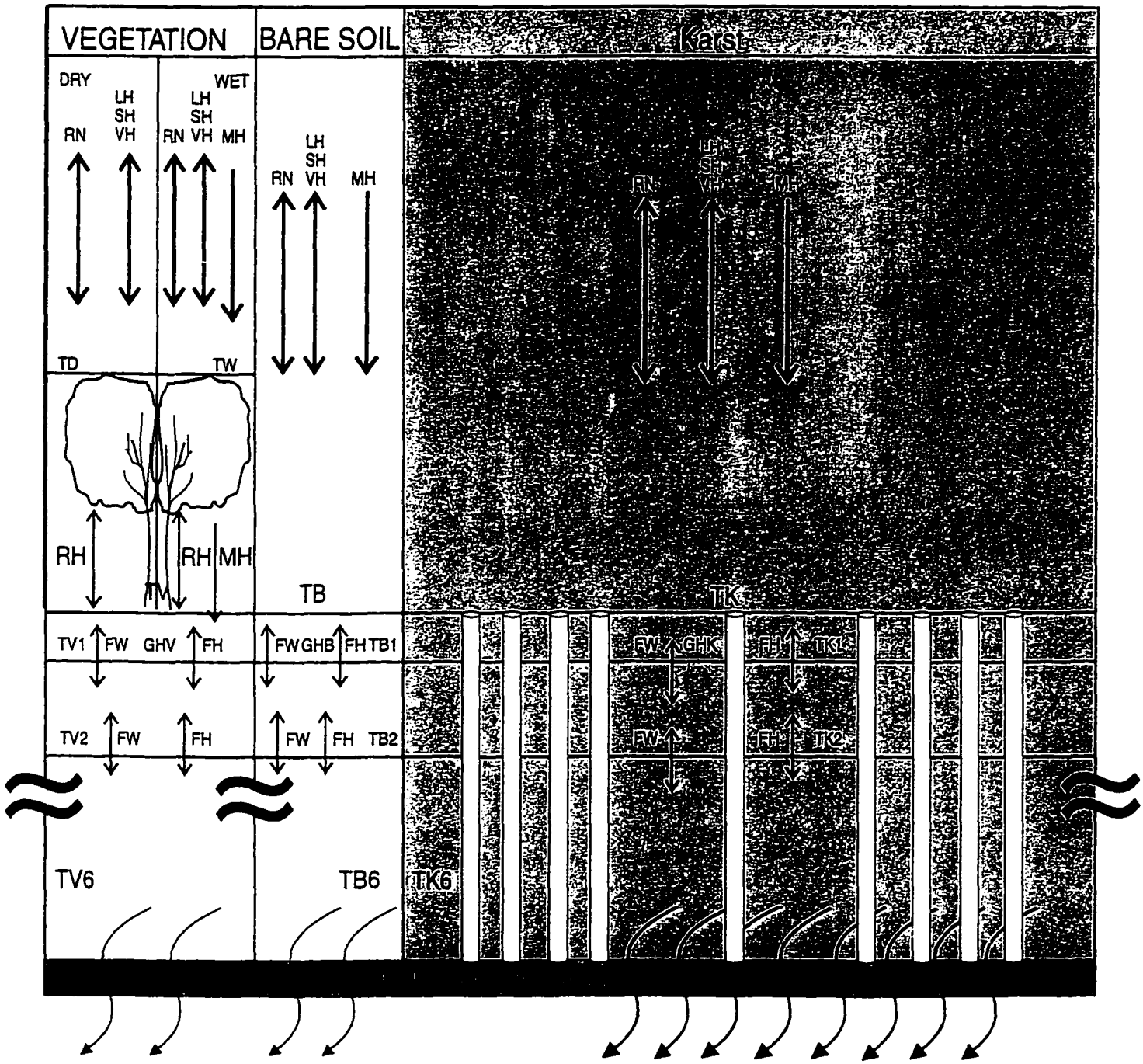

FIG. 45 Third column with karst (66%), pipe flow features

Flow in karst is usually sinuous and turbulent. Therefore, if pipe flow is used to simulate karst flow, the Darcy-Weisbach equation for turbulent pipe flow is appropriate for calculating the volumetric flow rate through a pipe. The equation is

$$Q = ((2\, d\, g\, a^2) / f)^{0.5} \bullet (dh/dl)^{0.5} \qquad (8)$$

where Q is the volumetric flow rate (m^3 / s), d is the pipe's diameter (m), g is gravity (m/s^2), a is the cross-sectional area of the pipe (m^2), f is the friction factor and dh/dl is the head loss over a unit length of the pipe. For turbulent flow, the friction factor can be approximated by the Haaland's (1983) equation

$$f(N_R, \epsilon/d) = [1.8 \log_{10} [(\epsilon/d)^{1.11} + (6.9 / N_R)]]^{-2} \qquad (9)$$

where ϵ is the effective sand grain roughness.

The standard pipe flow iterative technique for calculating Q is used. To compute Q, a value for f is first assumed and used in equation (8). The Reynolds number, N_R, is then computed and used in equation (9) to get a better estimate of f, and so on, until Q converges. This is tantamount to computing Q via the well-known Moody diagram. In this case, however, equation (9) is substituted for the Moody diagram; see (Roberson and Crowe, 1990) for this standard pipe flow

procedure.

This pipe flow approach is used to produce the experimental results shown in Figures [46 - 51]. In Figures [46 - 48], simulated Rio Cobre runoff from the non-karstic, two-columned model is plotted against simulated Rio Cobre runoff from the karstic, three-columned model for pipes with a constant diameter of 0.2 cm but with pipe densities of 2, 4, 6, 8 and 10 pipes / m^2. In Figures [49 - 51], a similar set of plots were made. However, in these latter plots, the pipe density was kept constant at 1 pipe / m^2 while the pipe diameter varied. In either set of plots dramatic reductions in the model's runoff were achieved. The pipes were able to even reduce the runoff in some cases down to zero. Finding the right combination of pipe diameter and pipe density for the watershed may then provide the means to appropriately match the observed runoff from the karstic watershed by that predicted by the model.

Figures 52 and 53 show in dramatic fashion the sensitivity of runoff to percentage of karst area for a pipe density of 10 pipes / m^2 and a pipe diameter of 2 cm. In Figure 52, a fictitious, unperturbed, constant rain falls, and it is clear that a karst ground-cover has a major influence on runoff. As the percent of karst increases the runoff greatly decreases. The same conclusion is reached from Figure 53 when actual observed Rio Cobre rain is used.

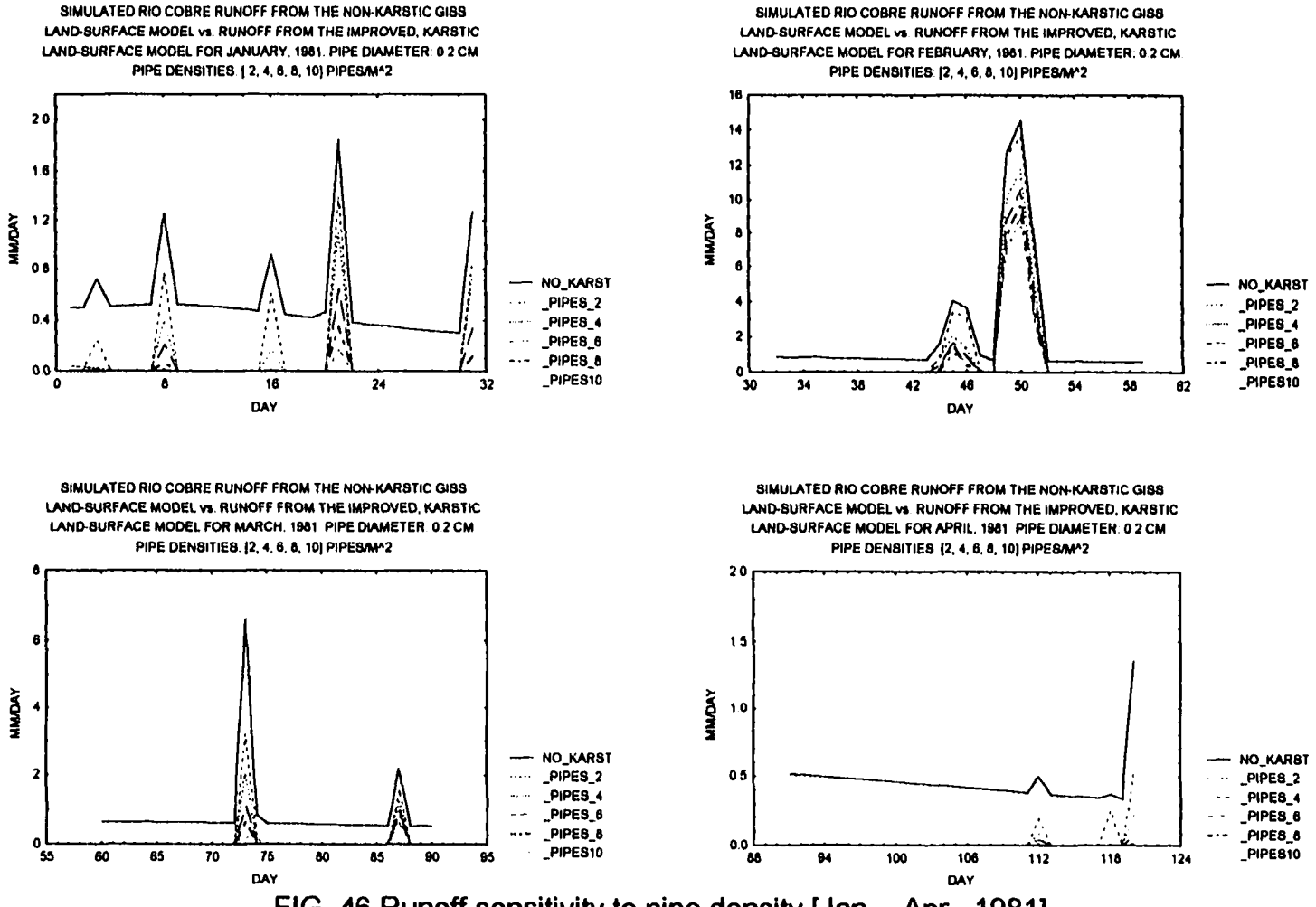

FIG. 46 Runoff sensitivity to pipe density [Jan. - Apr., 1981]

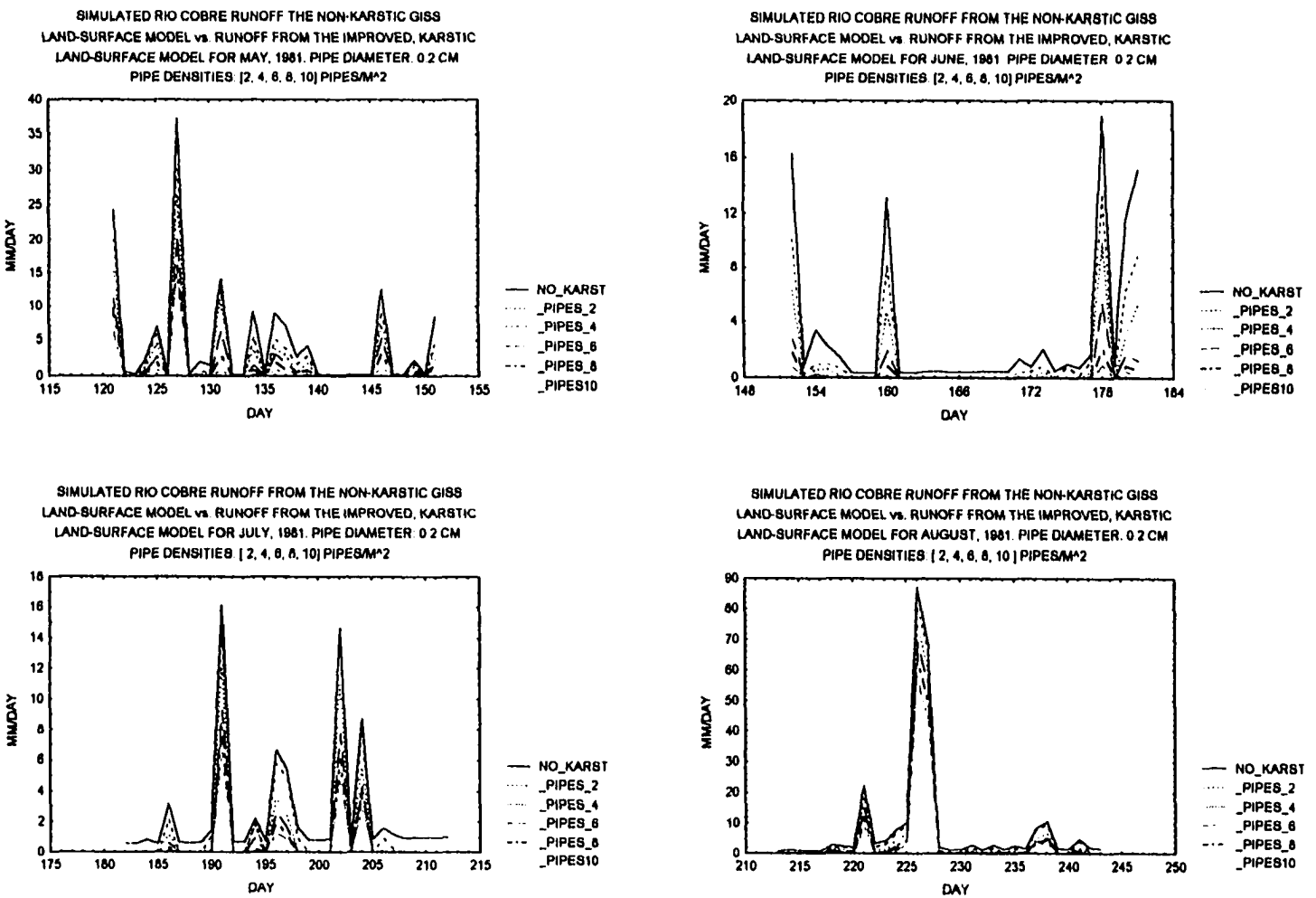

FIG. 47 Runoff sensitivity to pipe density [May - Aug., 1981]

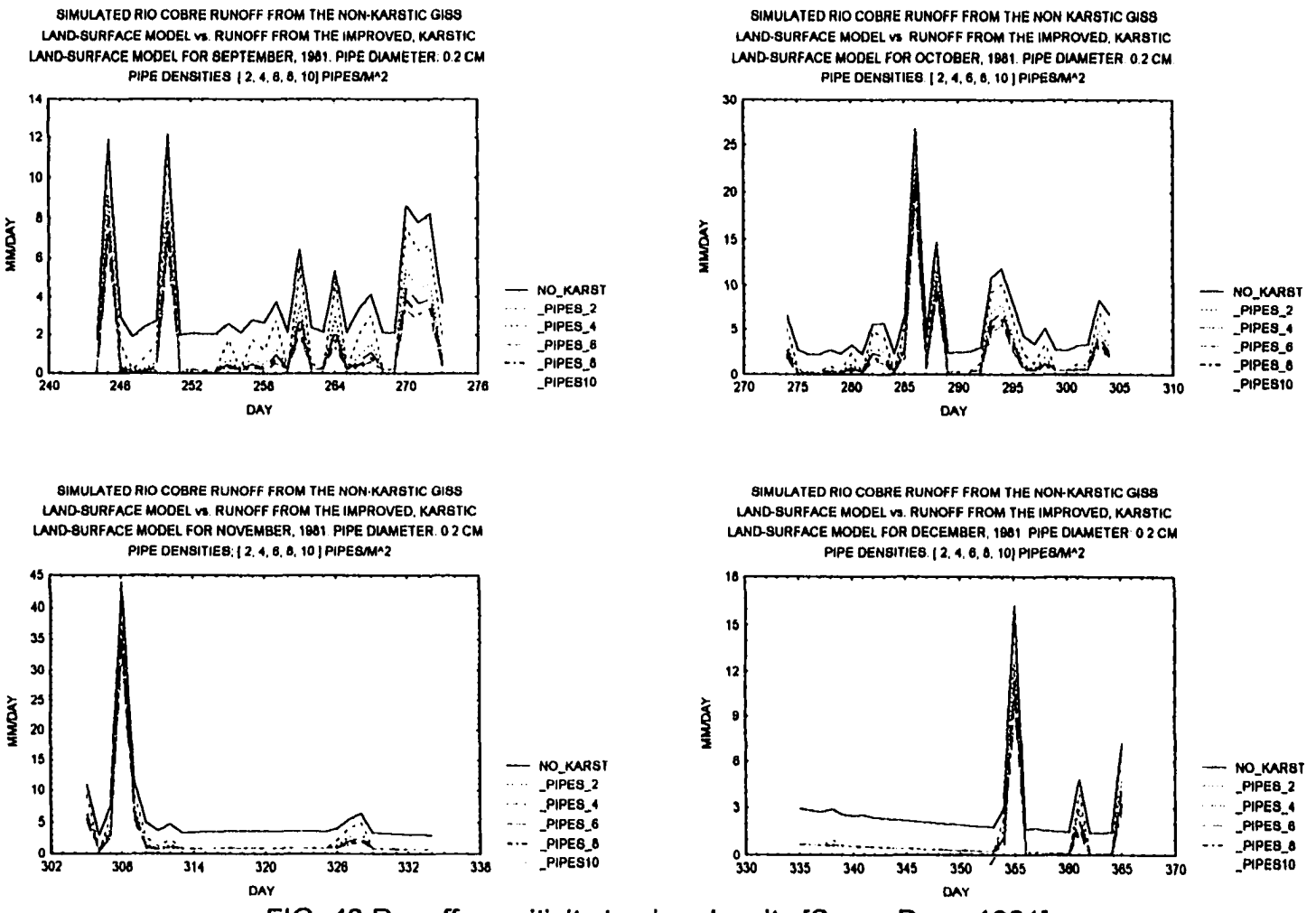

FIG. 48 Runoff sensitivity to pipe density [Sep. - Dec., 1981]

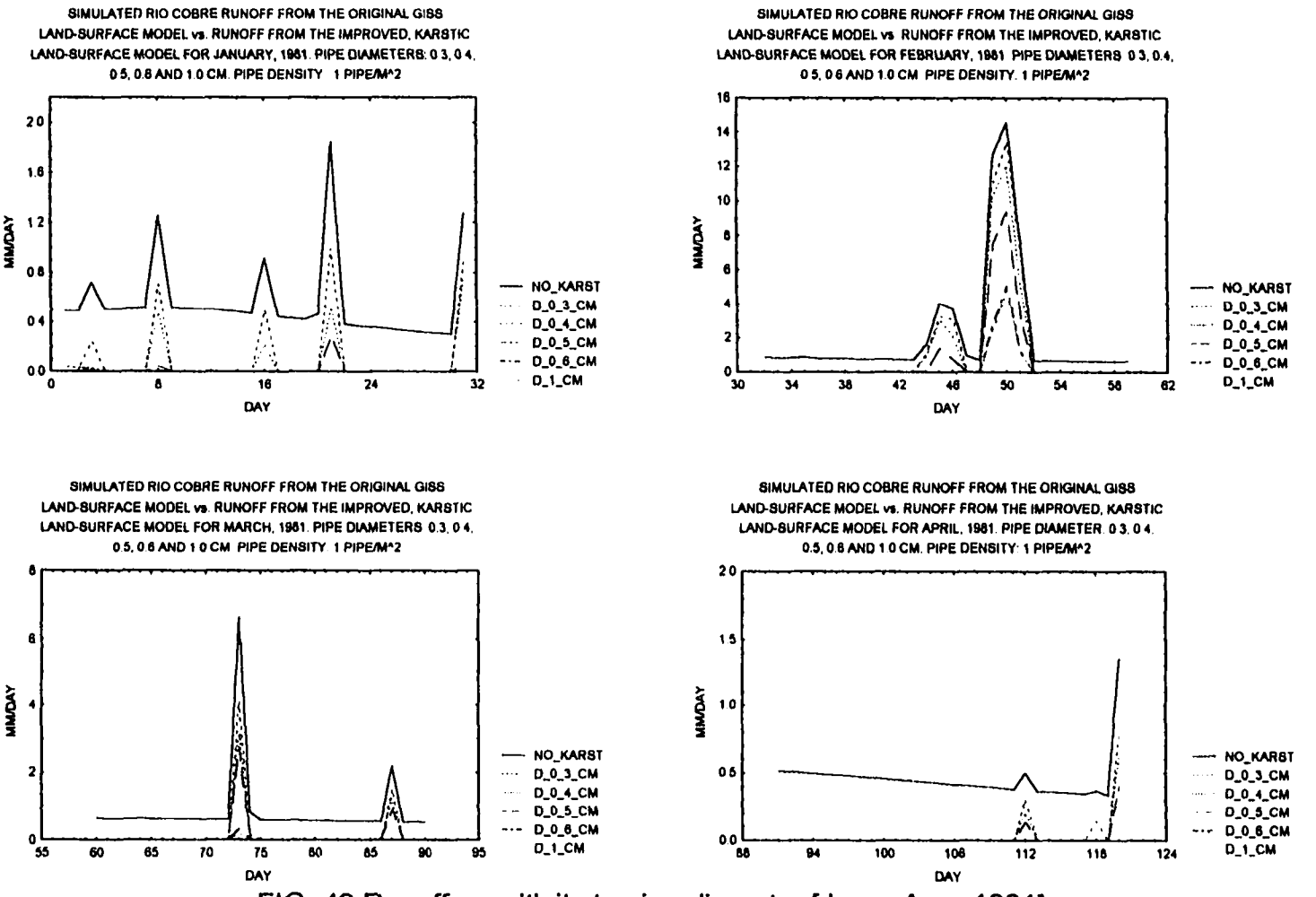

FIG. 49 Runoff sensitivity to pipe diameter [Jan. - Apr., 1981]

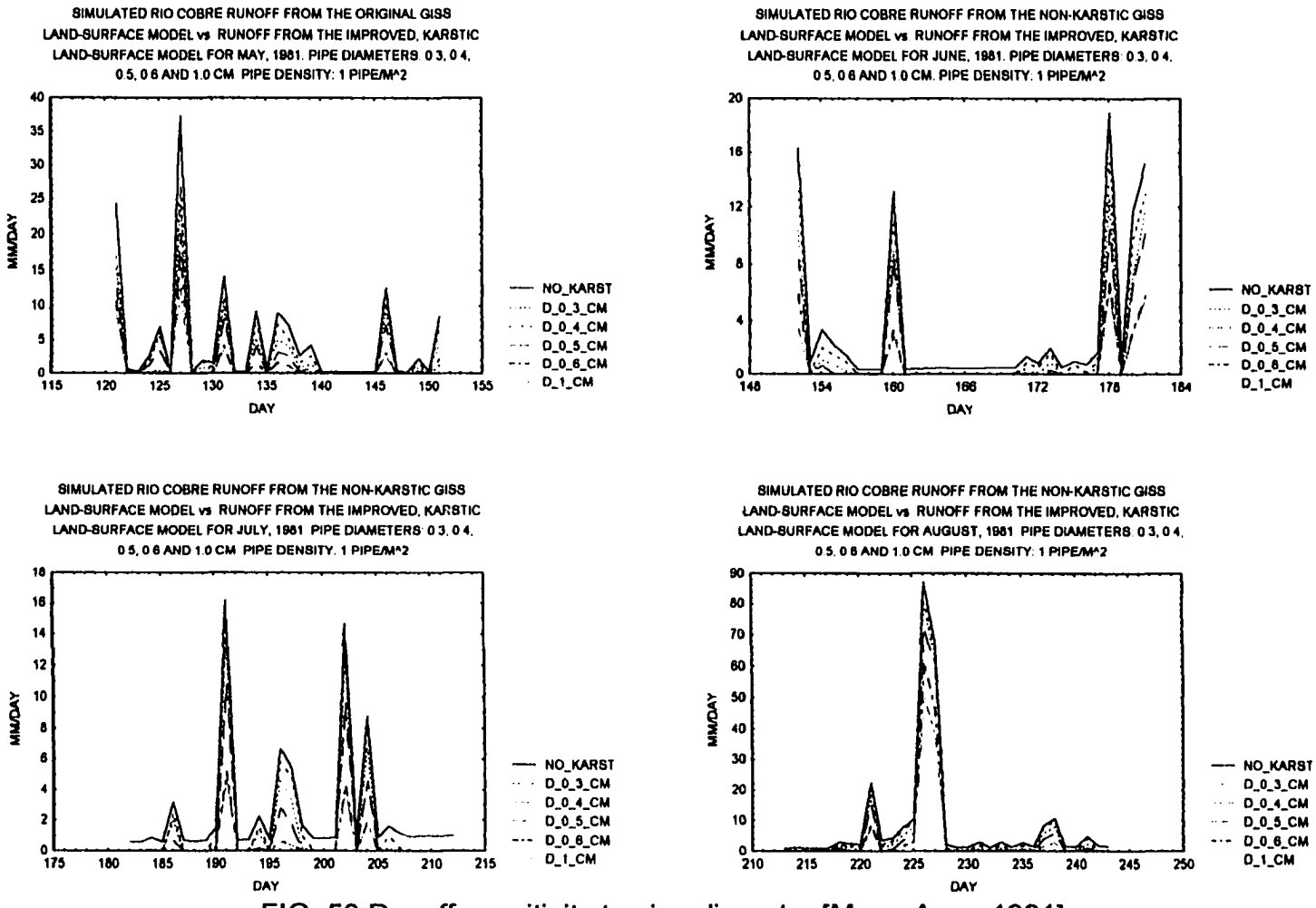

FIG. 50 Runoff sensitivity to pipe diameter [May - Aug., 1981]

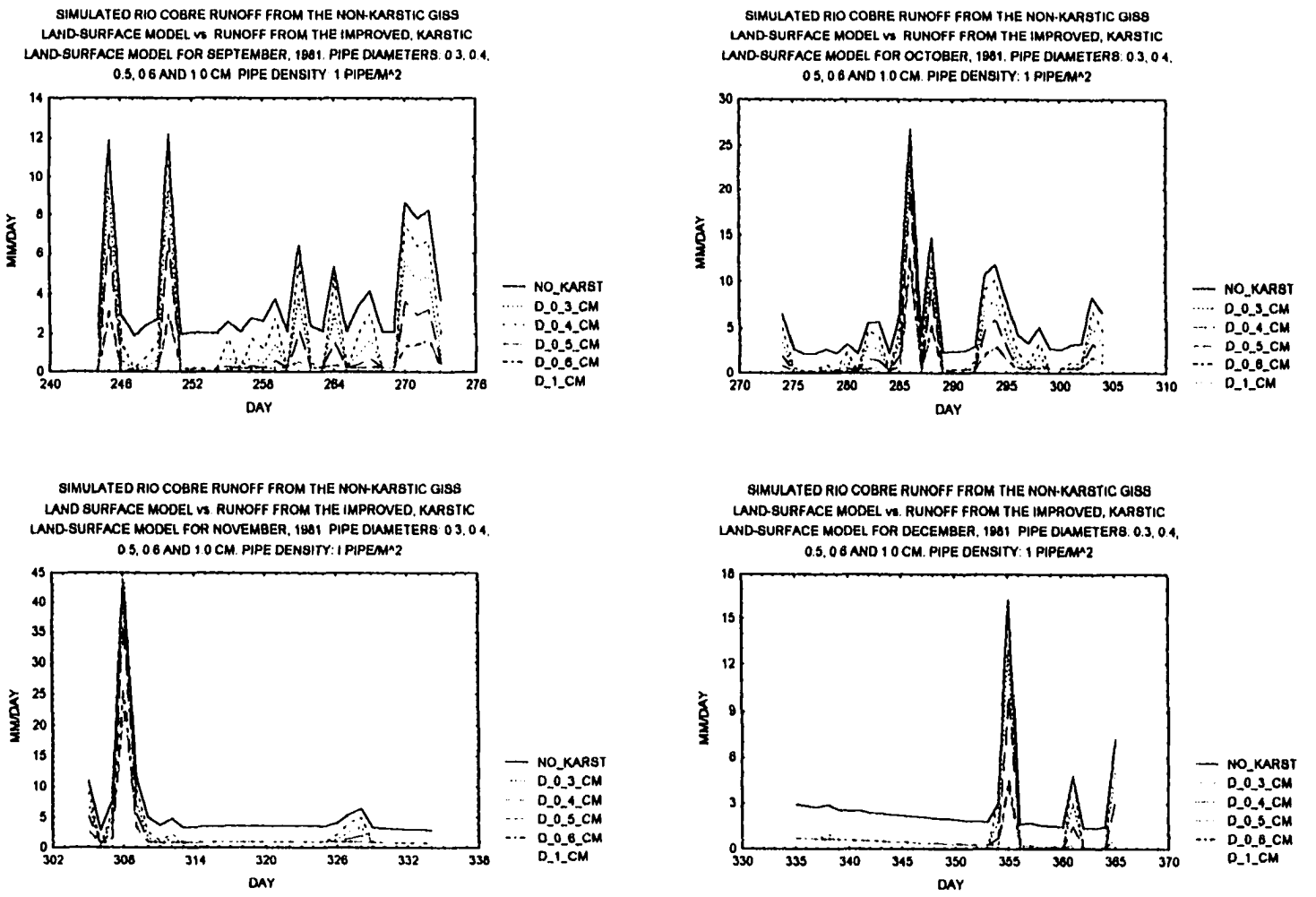

FIG. 51 Runoff sensitivity to pipe diameter [Sep. - Dec., 1981]

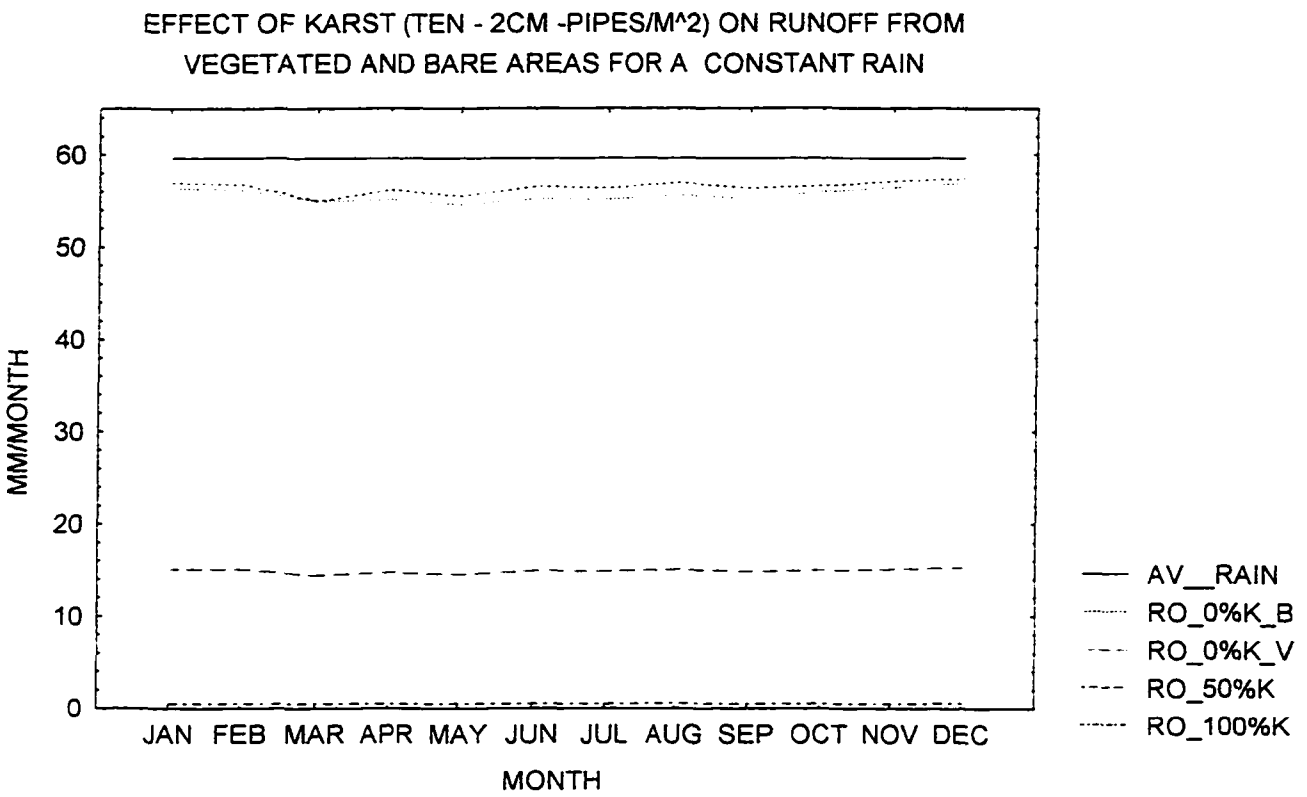

FIG. 52 Runoff sensitivity to areal % of karst for an average rain

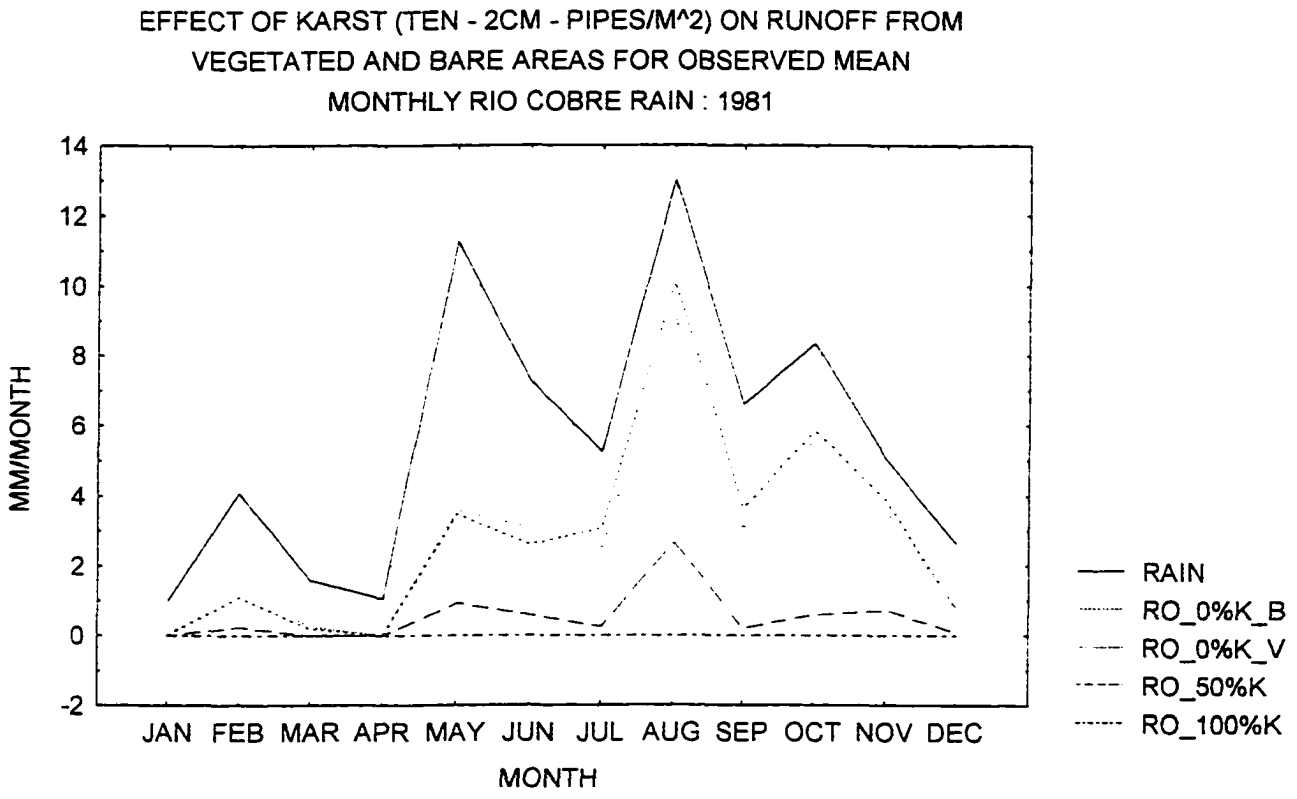

FIG.53 Runoff sensitivity to areal % of karst for observed Rio Cobre rain

6.4 Pipe Density and Pipe Diameter

In Figure 45, the karst portion of the watershed is represented as 66% of the basin area. However, this karst region also has vegetation in it. In fact, the type of vegetation there is the same as that in other parts of the basin. Since vegetation exists in the karst portion of the basin , it must be sustained by the same mechanism that exist in the vegetated portion of the watershed. According to the Water Resources Authority of Jamaica, approximately 12% of the watershed's karst area is vegetated. Therefore, the pipe flow approach should only be applied to a 54% karst area and not to a 66% area. This reduction in karst area and the corresponding increase in vegetated area are shown in Figure 54.

If there were no runoff from areas of 100% karst, then the karst column could be treated as one big equivalent pipe that takes in all the incident precipitation and produces no runoff. However, this is not the case, for there is runoff in karst areas. This runoff is called *autogenic* or *autochthonous* runoff. This runoff is produced from a portion of the watershed that is composed entirely of karst rocks and derives its water only from incident precipitation.

The manner in which the karst column treats autogenic runoff as a function of pipe density, pipe diameter and rainfall is shown in equations (10),

(11) and (12).

$$RO = R - I \tag{10}$$

$$I = Q \bullet \eta \tag{11}$$

$$\eta = N / A \tag{12}$$

where RO is the autogenic runoff rate (m/s), R is the actual rainfall rate (m/s), I is a limiting flux, an infiltration capacity (m/s), η is the pipe density (m^{-2}), N is the total number of pipes and A is the area of the karst portion of the basin (m^2). Therefore, up to a certain rainfall rate, the pipes are sufficient to prevent runoff. Runoff only occurs when the rainfall rate exceeds the pipe infiltration capacity.

Values of η and I are assumed. Equation (11) is then used to calculate Q. With an assumed value for friction factor, f, equation (8) is used to obtain a diameter of the pipe. A Reynolds number is calculated and equations (8) and (9) are then used in an iterative process until the pipe diameter converges. High rainfall rates are needed for karst runoff; therefore, the infiltration rate, I, could be set at some maximum rainfall rate for the watershed, or it could be set as the

average of the watershed's maximum and minimum rainfall rate. Whatever value is used it ought to reflect the watershed's rain. Since as N increases, I increases and runoff decreases, this method allows adjustments that will give an appropriate match for the observed runoff, and it allows η to control autogenic runoff. Figure 55 shows how the pipe diameter relates to the number of pipes. The average spacing, S, between pipes is given by

$$S = \eta^{-0.5} \tag{13}$$

The above approach to simulate autogenic runoff will now be applied to three karstic watersheds (the Rio Cobre, the Yangtze and the Rio Grande) for assessment of observed, and climate change scenarios.

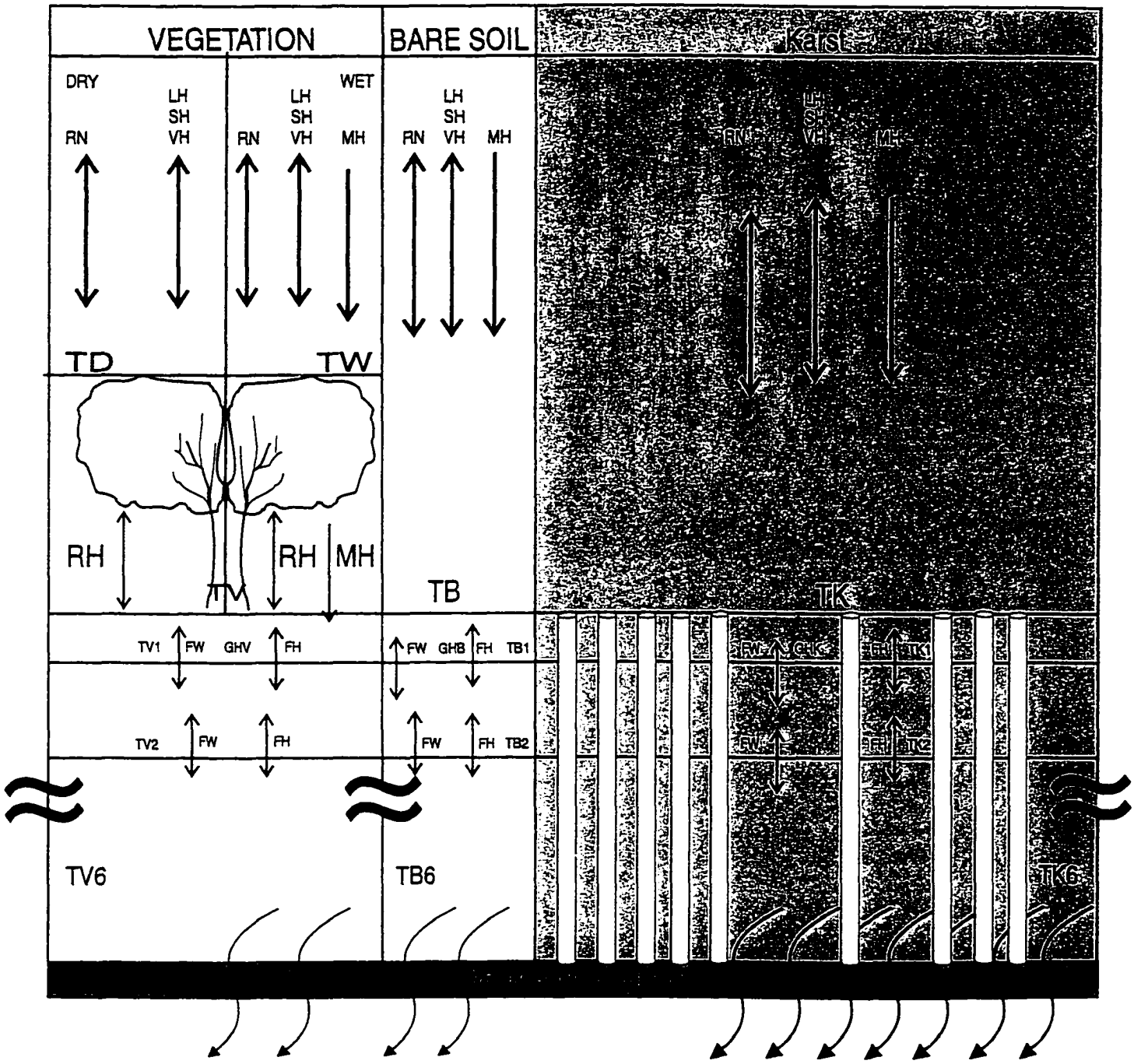

FIG. 54 Third column with karst (54%), pipe flow features

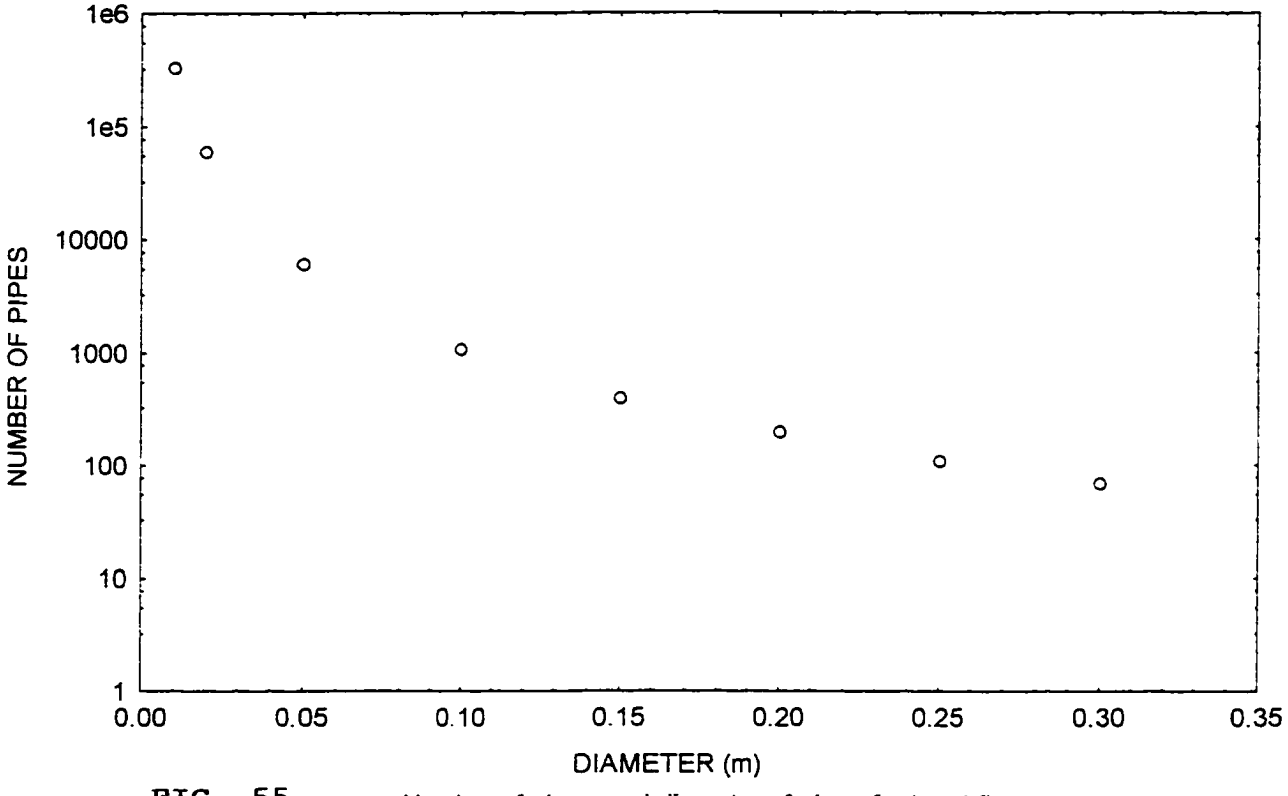

FIG. 55 Number of pipes and diameter of pipes for karst flow

7. Improved GISS Land-Surface Model Testing

7.1 Rio Cobre Runoff

The improved model was used to simulate runoff for the same time periods as the former model. For the yearly periods 1980 - 1990, Figures 56 - 58 show dramatic improvement in predicted runoff. In the figures, TOTLS_RO is the simulated runoff from the former model, TOTOB_RO is the observed runoff, RO_MAX4 and RO_MAX8 are simulated runoff from the improved model for pipe densities of 4 and 8 pipes / m^2, respectively. For each year, the infiltration rate was set equal to the maximum rainfall rate within that year. The figures also show that, as expected, autogenic runoff decreases with increasing pipe density. Figures 59 and 60 also show that the karst-component model does well in reducing the over-predicted runoff.

When the karst-component model is used to simulate daily runoff for the test year 1981, Figures 61 - 63 highlight the reductions in runoff that were achieved by the karst-component model. Figures 64 and 65 show the mean and the standard deviation for the observed runoff from the test year and the runoff from the karst-component model for pipe densities of 4 and 8 pipes / m^2. When these figures are compared to Figure 26, the improvement achieved for the inter-annual variability in runoff is quite evident.

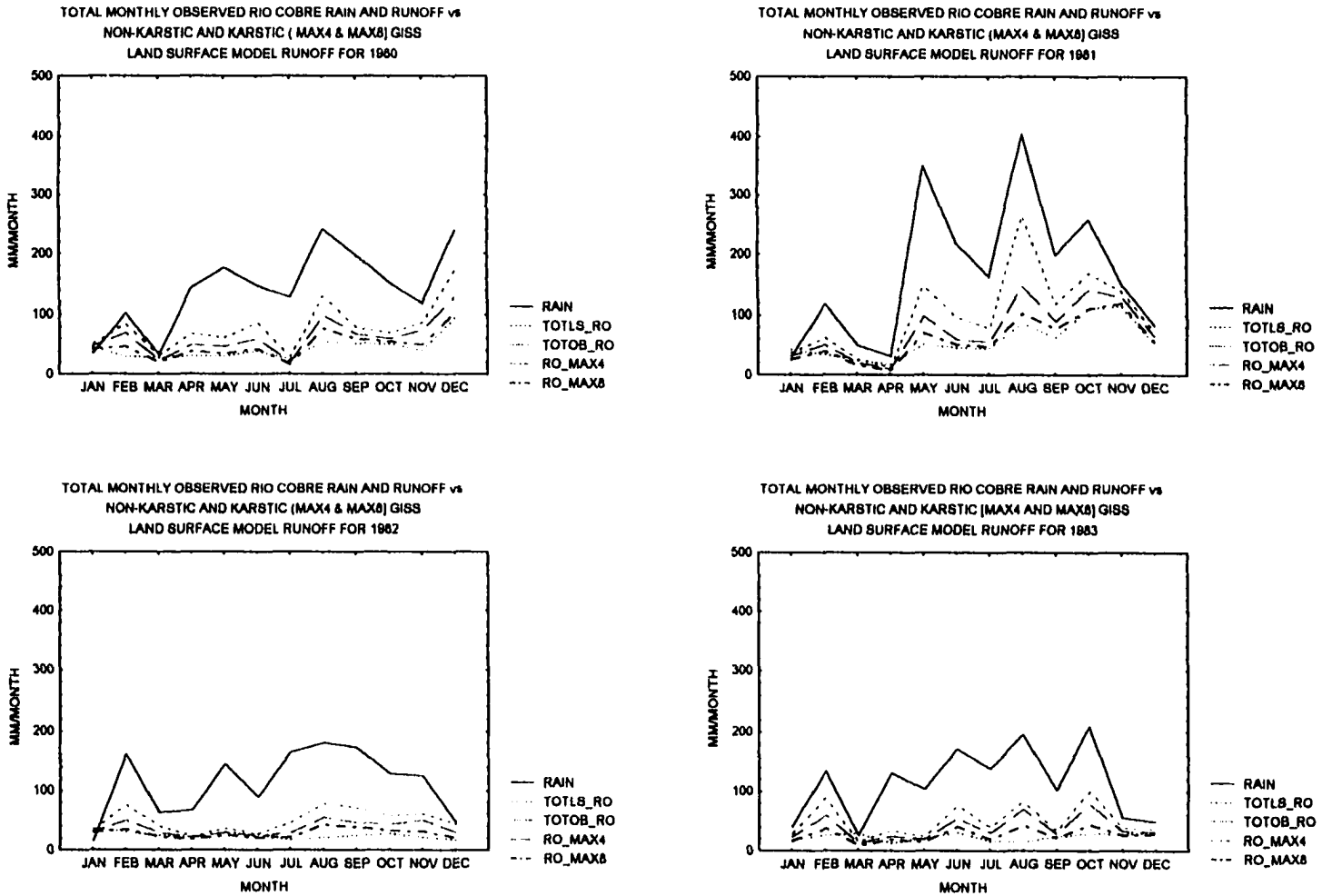

FIG. 56 Total monthly rain, observed and modeled runoff, 1980 - 1983

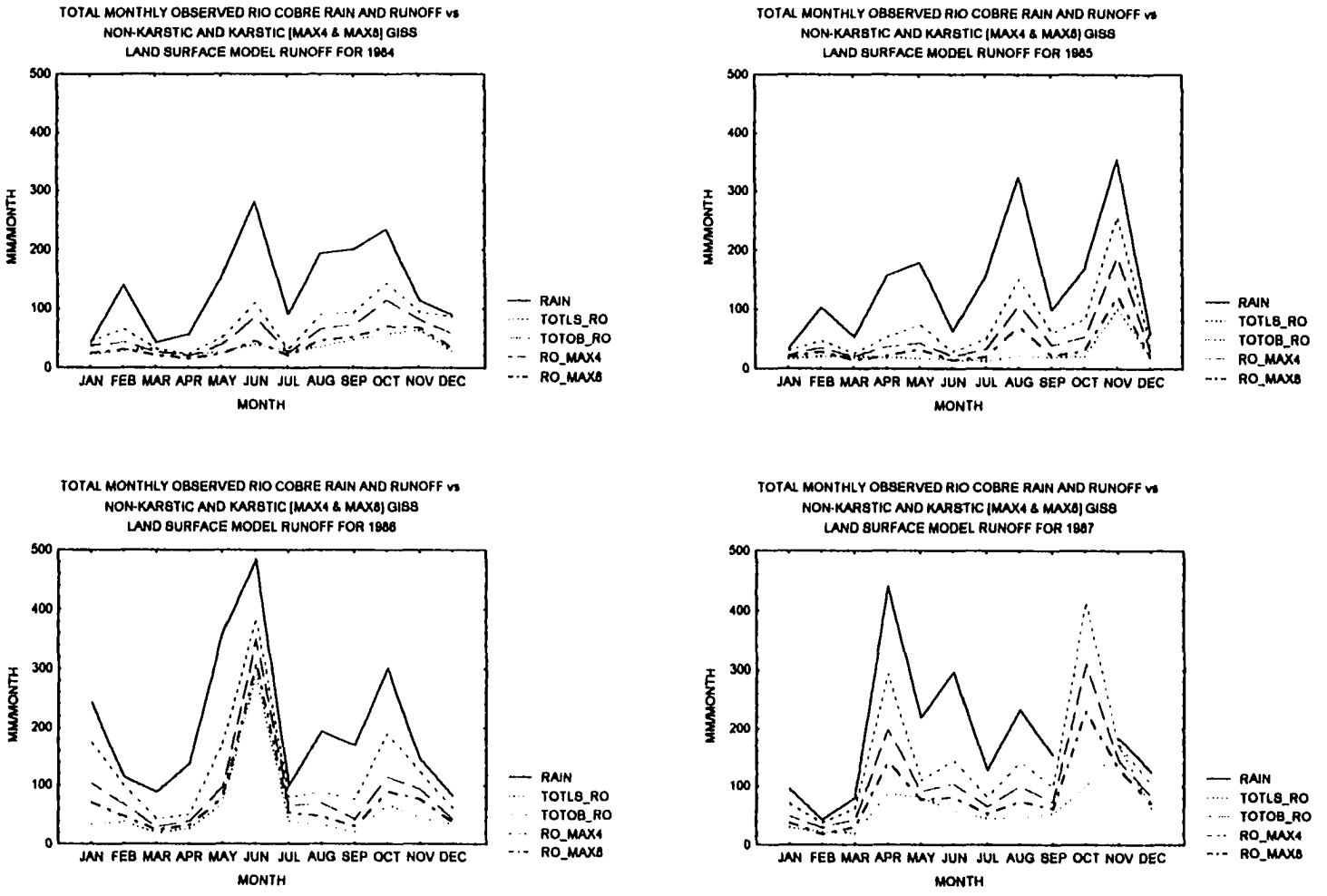

FIG. 57 Total monthly rain, observed and modeled runoff, 1984 - 1987

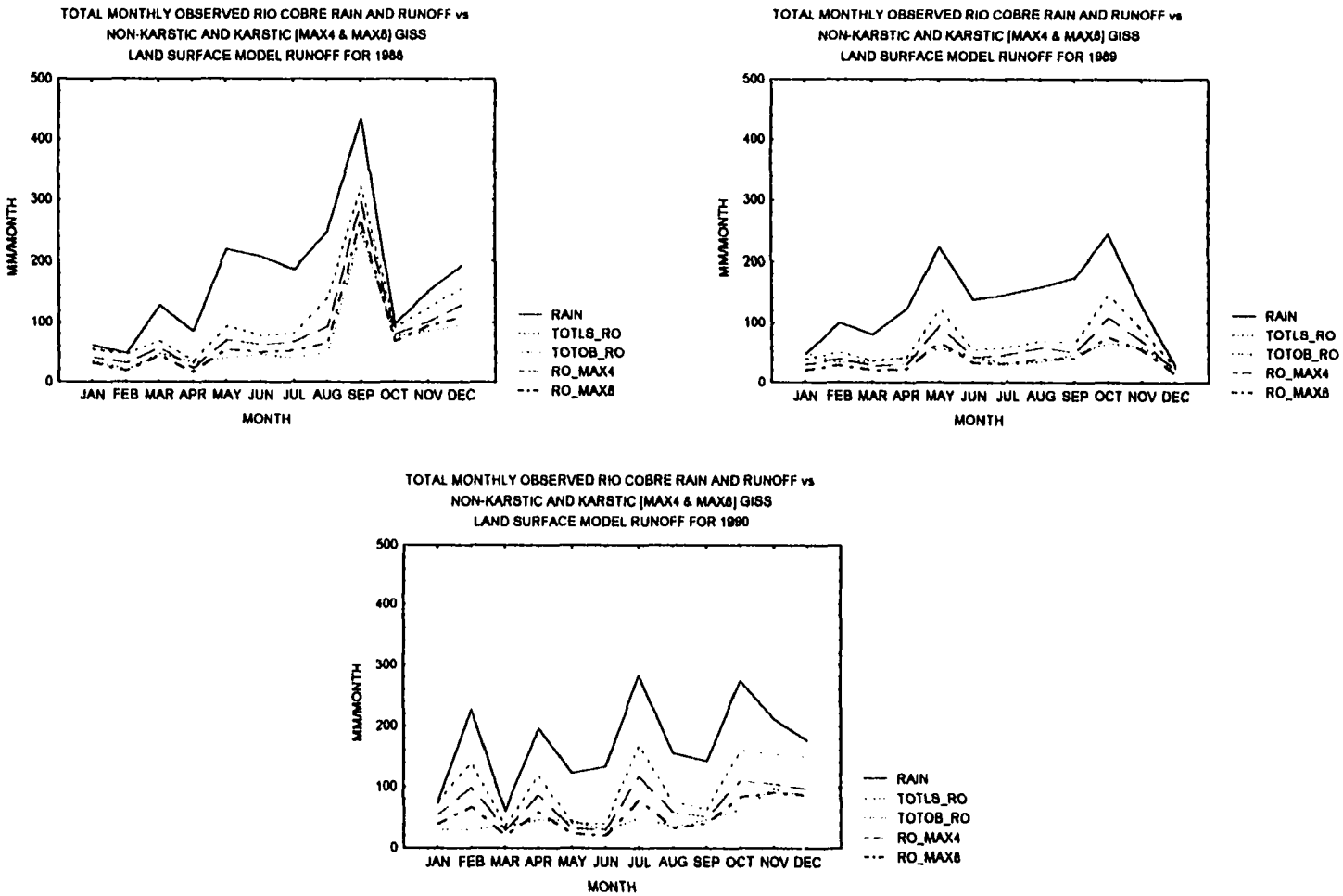

FIG. 58 Total monthly rain, observed and modeled runoff, 1988 - 1990

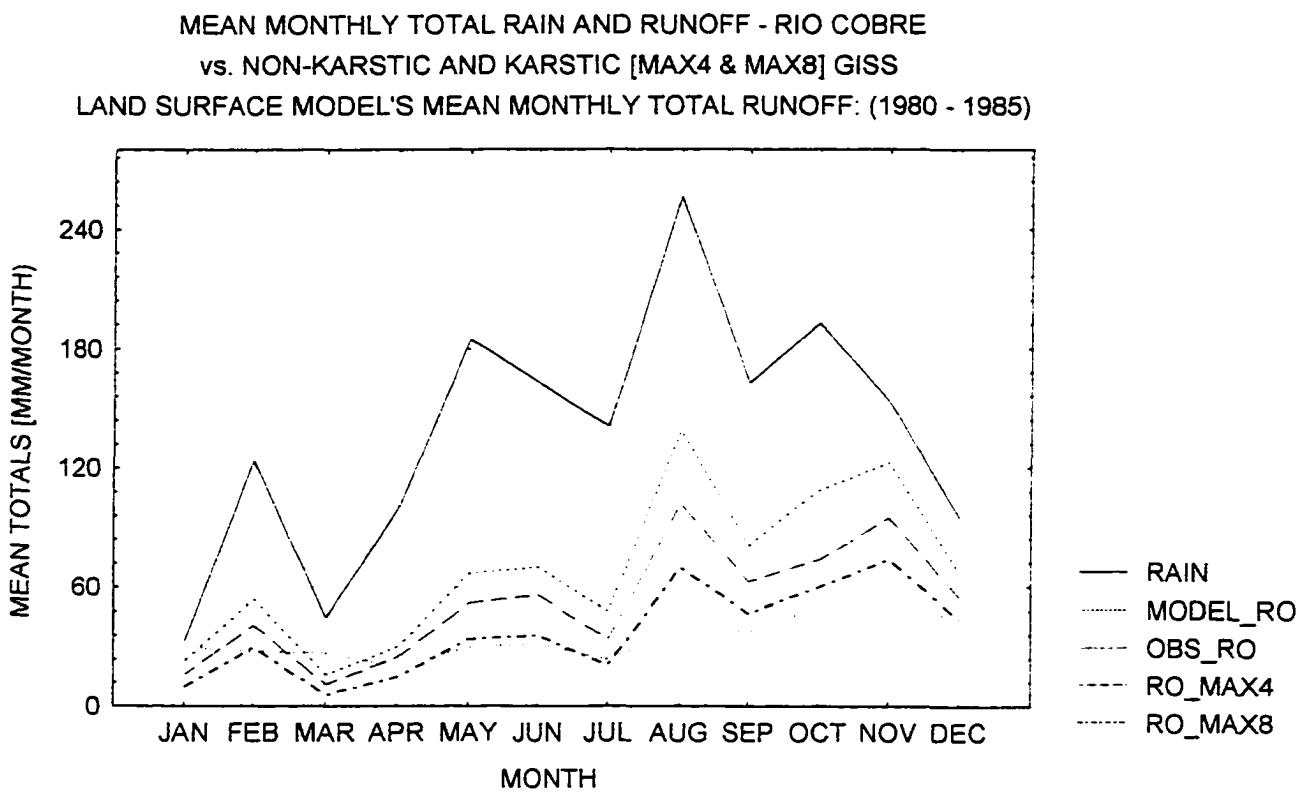

FIG.59 Mean monthly total rain, observed and modeled runoff [1980 - 1985]

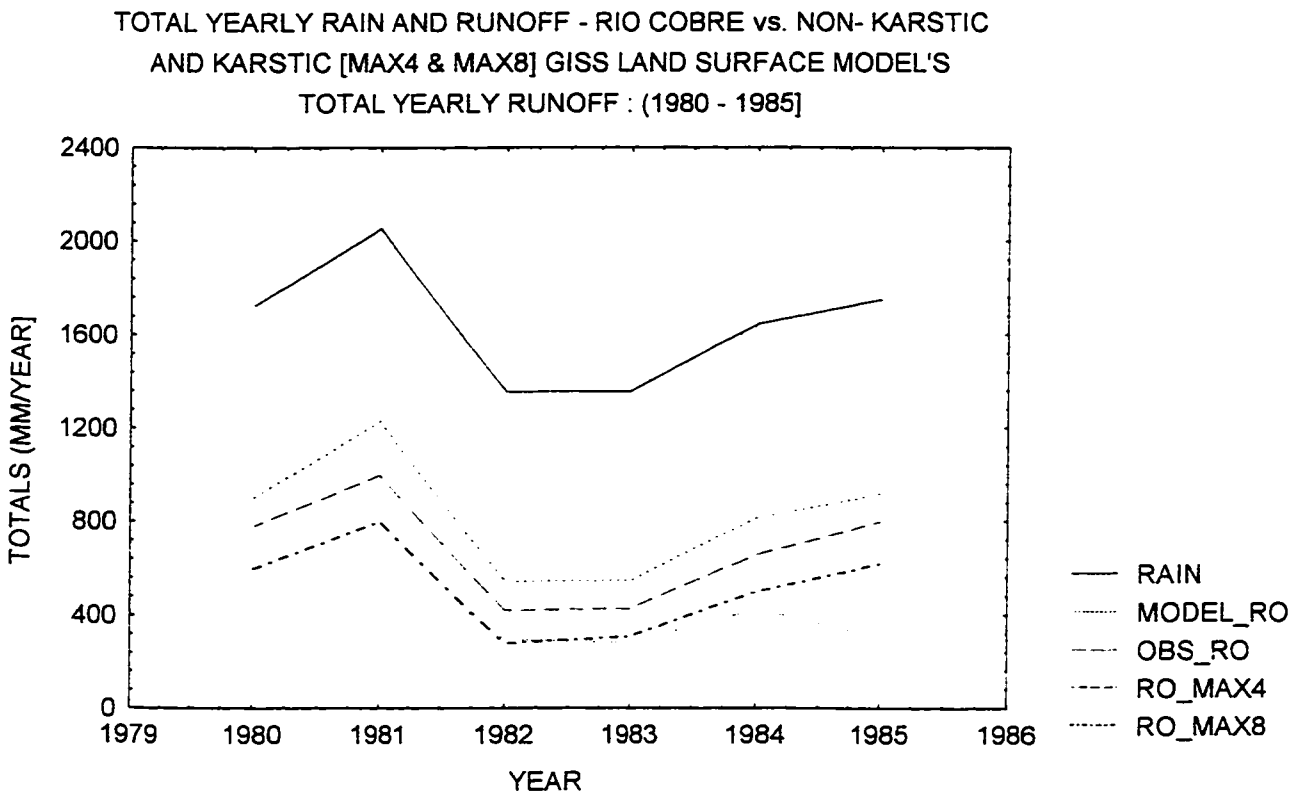

FIG. 60 Total yearly rain, observed and modeled runoff [1980 - 1985]

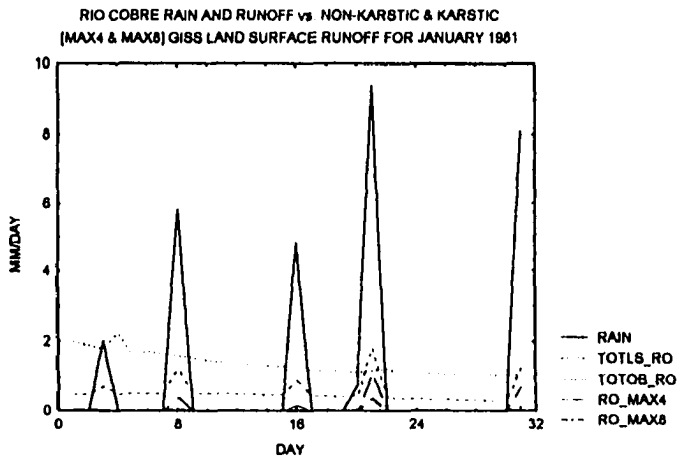

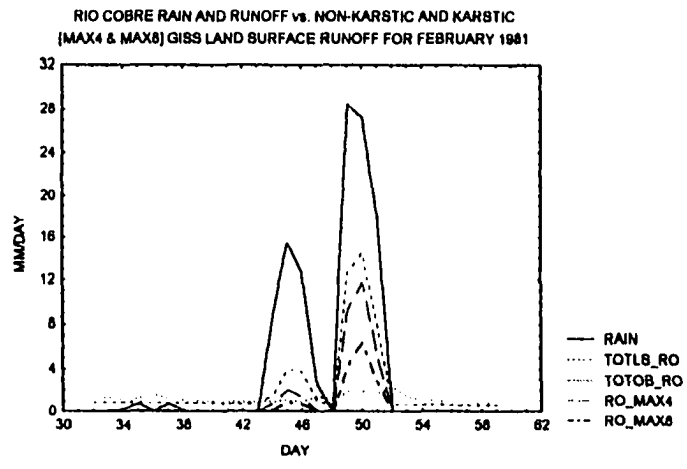

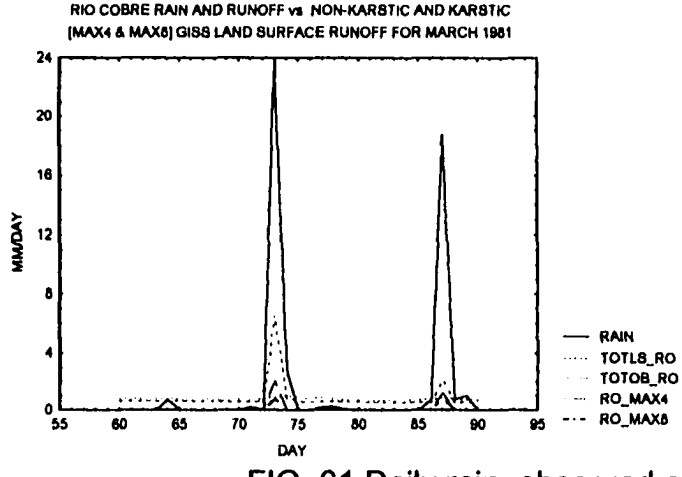

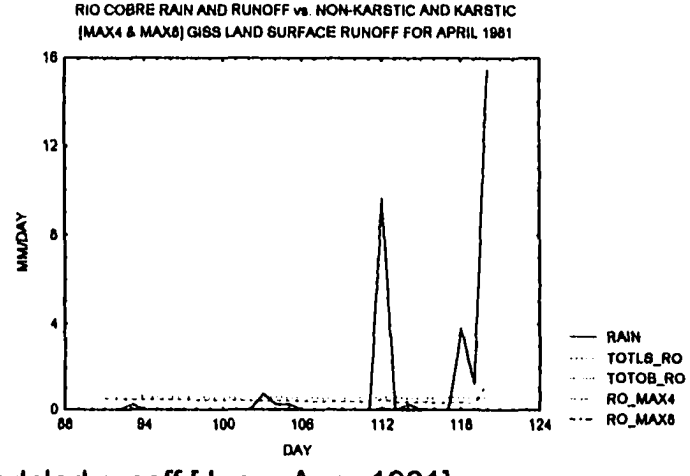

FIG. 61 Daily rain, observed and modeled runoff [Jan. - Apr., 1981]

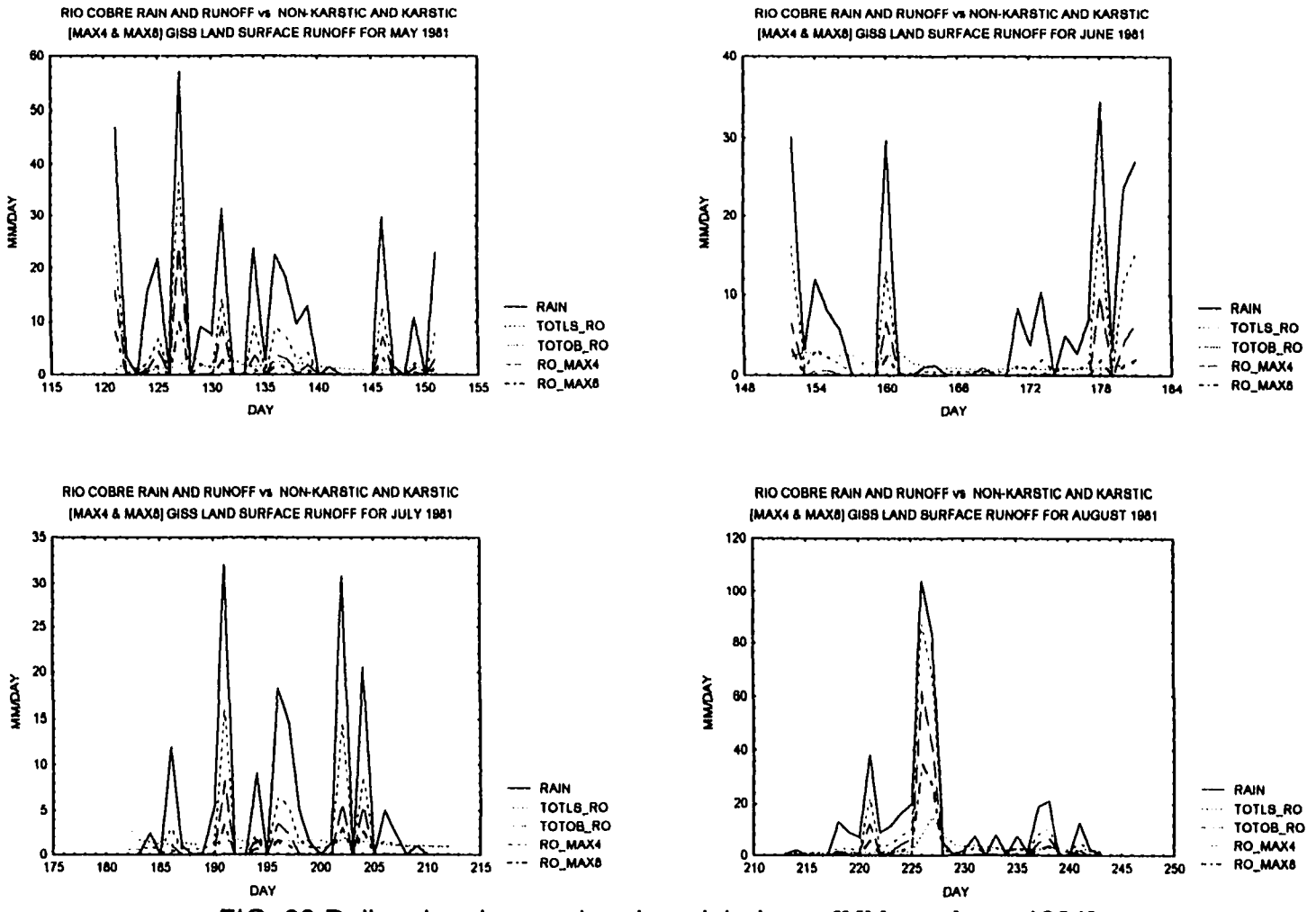

FIG. 62 Daily rain, observed and modeled runoff [May - Aug., 1981]

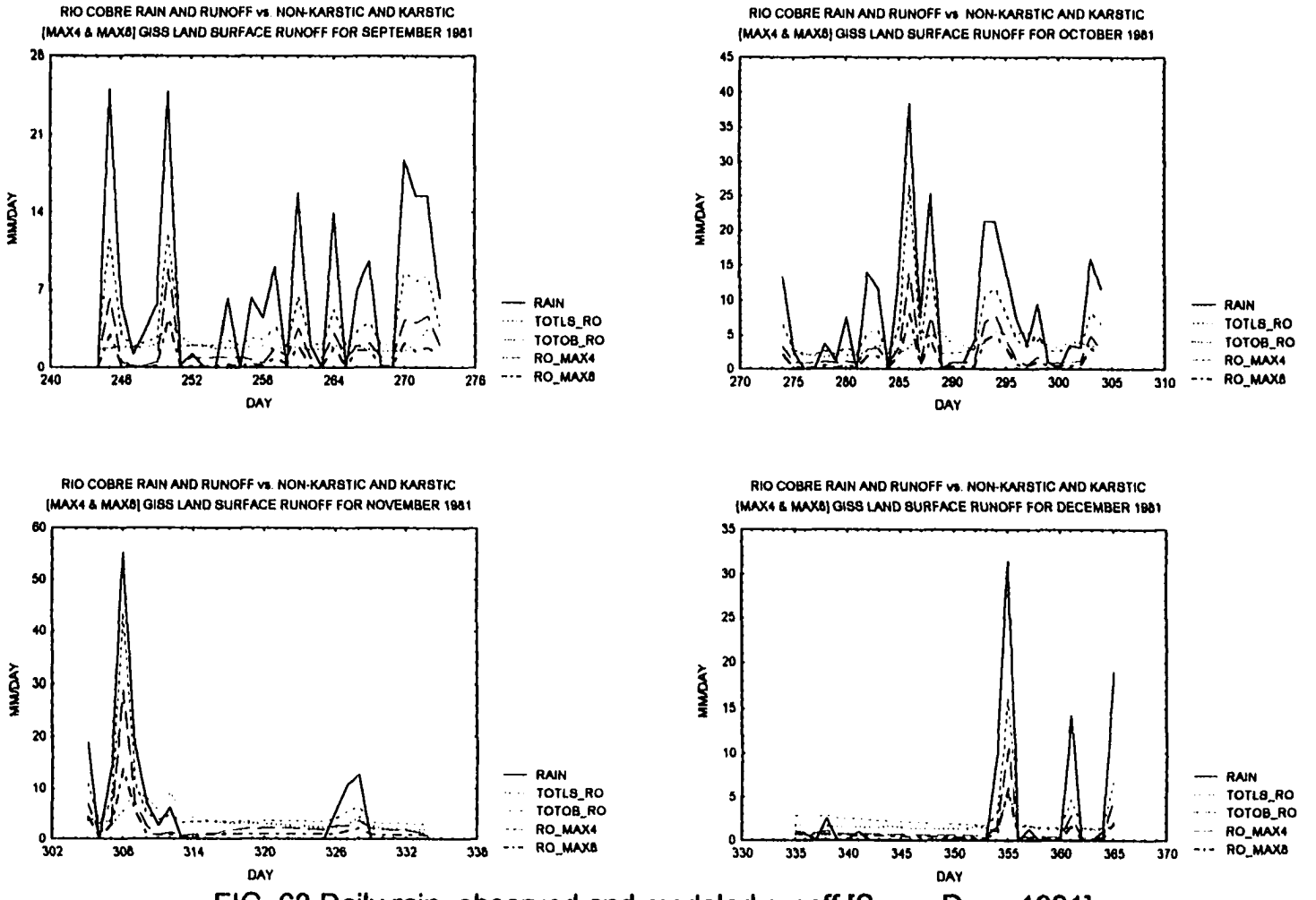

FIG. 63 Daily rain, observed and modeled runoff [Sep. - Dec., 1981]

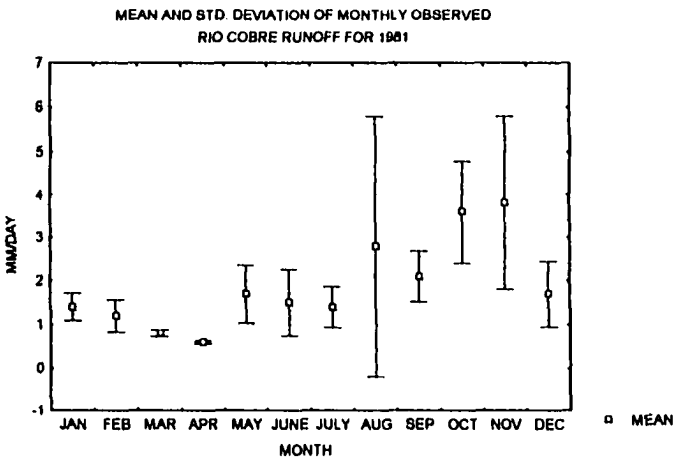

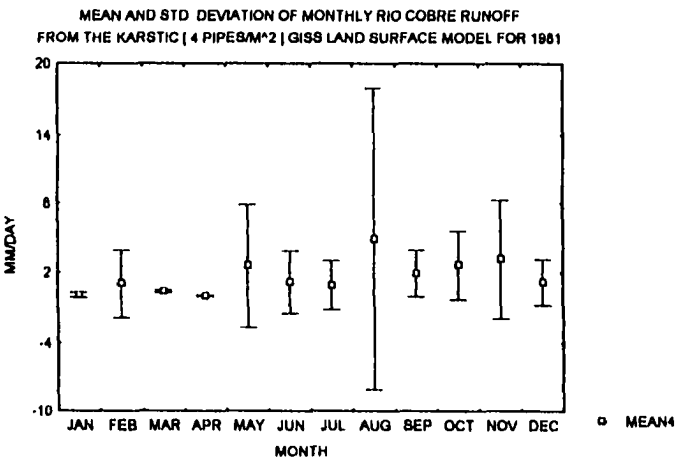

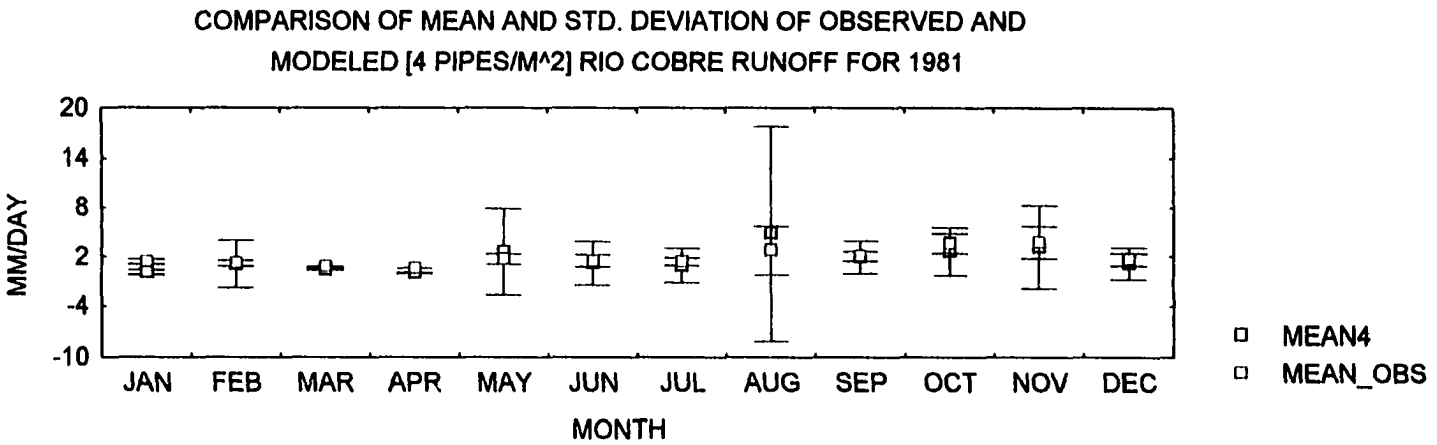

FIG. 64 Mean and standard deviation of observed and modeled (4 pipes/m^2) runoff

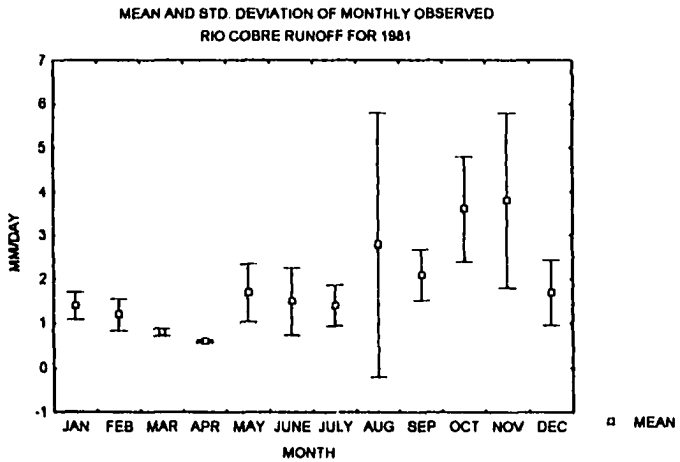

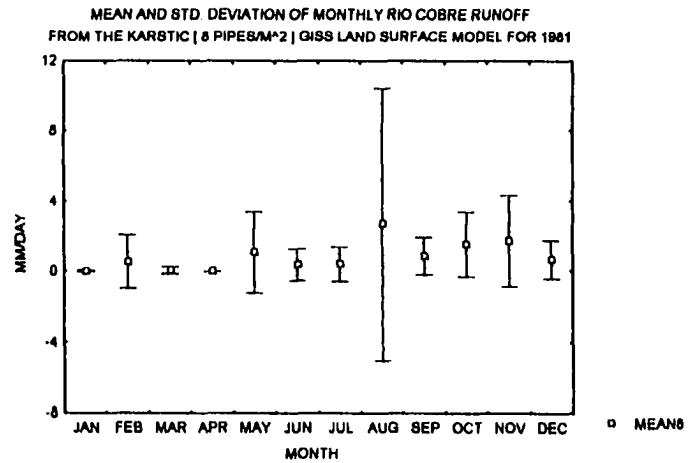

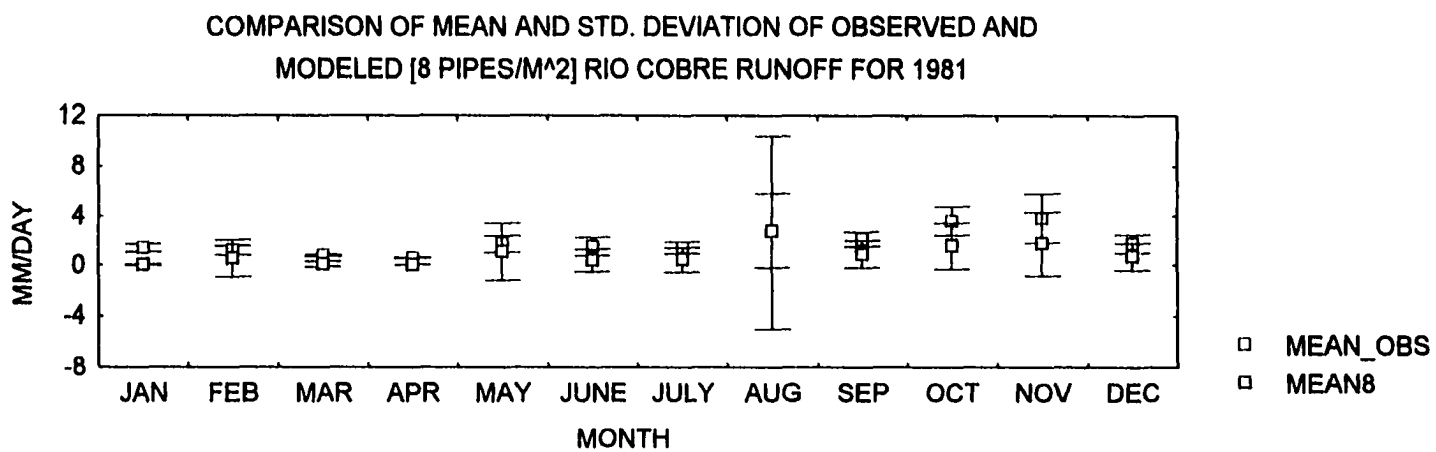

FIG. 65 Mean and standard deviation of observed and modeled (8 pipes/m^2) runoff

7.2 Yangtze and Rio Grande Runoffs

The validity of the karst-columned model is best confirmed by applying it to other karstic watersheds around the world. Two such watersheds, the Yangtze (China : GISS 4x5 grid-box 56, 31) and the Rio Grande (U. S. A. : GISS 4x5 grid-box 16,31) were selected as extended areas to test the model. Since the pipe density of 8 pipes/m^2 gave better results than 4 pipes/m^2 for a specified pipe diameter for the Rio Cobre, as a zeroth order approach, 8 pipes/m^2 is the pipe density used in the model application for these two other karst sites.

Figures 66 and 67 depict observed (Y_OBS and RG_OBS), non-karstic (Y_NO_KAR and RG_NO_KAR : former off-line model) and karstic (Y_KAR, RG_KAR : improved off-line model) runoff for the Yangtze and the Rio Grande rivers. The s show that similar to the Rio Cobre, the karst-columned model predicts the runoff better than the non-karst model. Table 2 quantifies the improvement of the karst-columned model (Karst) over the non-karst (N_karst) model. In the table, monthly ratios of runoff (observed and modeled : karst and no_karst) to observed evapotranspiration are shown for both rivers. Again, it is clear that the karst- columned model is an improvement over the non-karst model for predicting runoff from karstic watersheds.

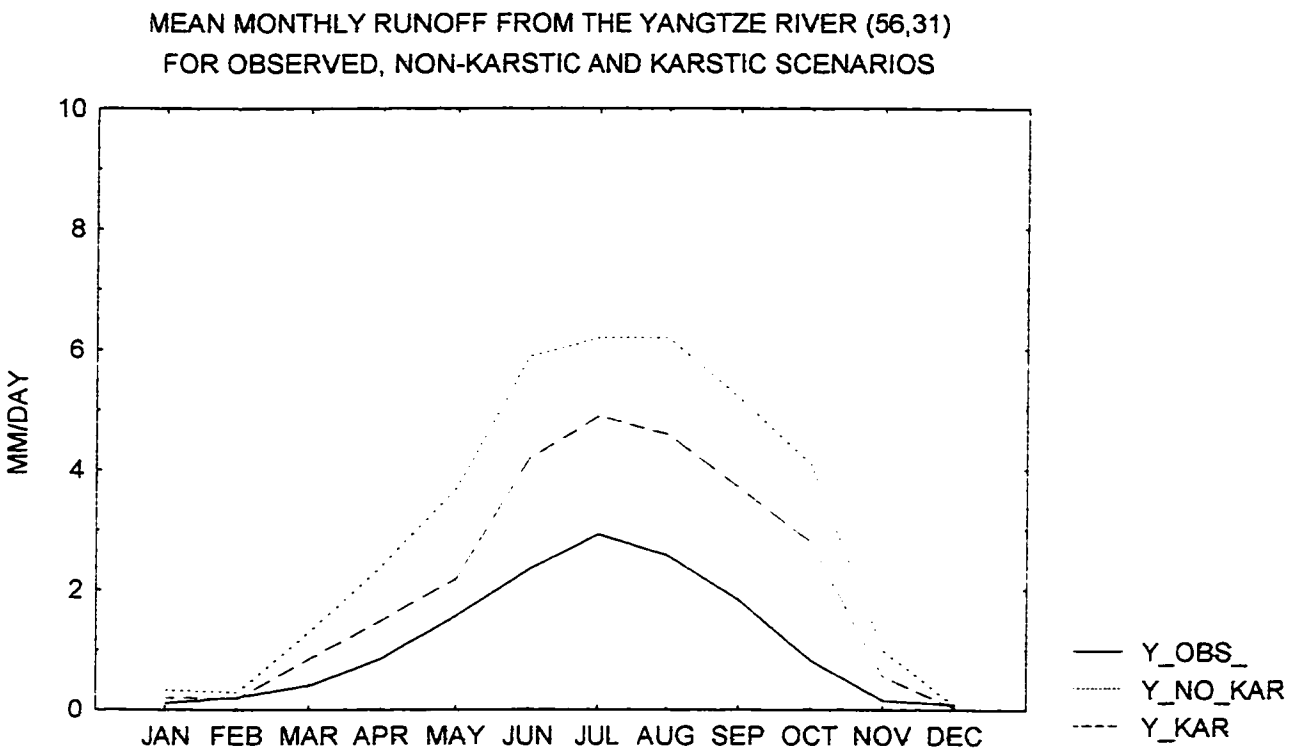

FIG. 66

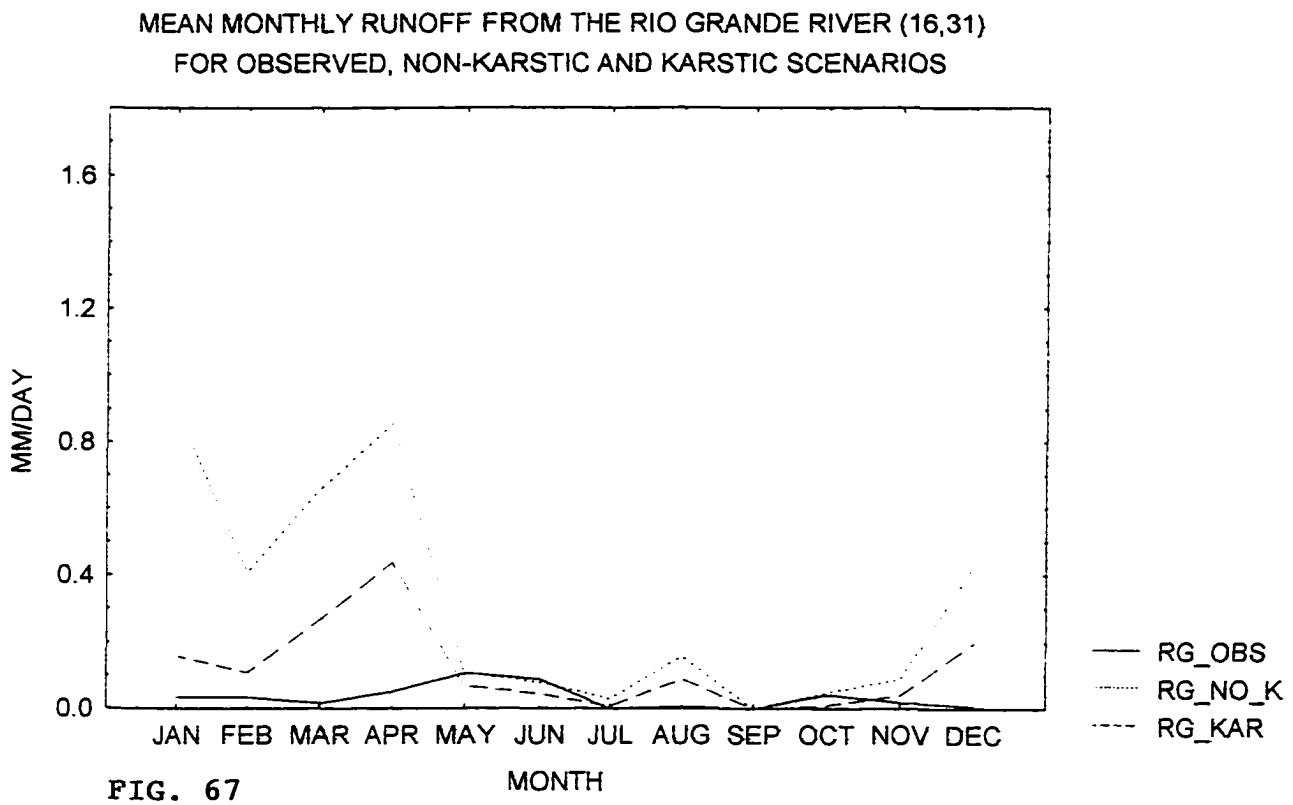

FIG. 67

Table 2. Ratios of mean monthly observed, no karst and karst runoff to observed evapotranspiration for the Yangtze (56, 31) and the Rio Grande (16, 31) rivers.

	Yangtze			Rio Grande		
	Obs.	N_karst	Karst	Obs.	N_karst	Karst
Jan	0.6452	2.4110	1.0753	0.1204	2.2200	0.5351
Feb	0.5854	1.1875	0.5149	0.0837	2.2120	0.2558
Mar	0.6375	2.8370	1.3438	0.0330	1.4941	0.4945
Apr	1.0047	5.4470	1.7442	0.0637	1.0812	0.5163
May	0.6351	2.2610	0.8821	0.0796	0.2331	0.0516
Jun	0.6341	2.1660	1.1357	0.0667	0.1244	0.0334
Jul	0.7194	1.9190	1.1989	0.0003	0.0063	0.0050
Aug	0.6898	2.3610	1.2299	0.0005	0.0558	0.0500
Sep	0.5936	2.8680	1.1962	0.0000	0.0000	0.0000
Oct	0.4714	3.1440	1.5713	0.0337	0.1251	0.0717
Nov	0.2777	3.2110	0.9256	0.0342	0.0911	0.0521
Dec	0.4229	0.6310	0.1762	0.0236	0.0522	0.3900

8. Climate Change Impacts on Water Resources - Model Simulations

8.1 Sacramento Watershed Model : Rio Cobre

After verifying that the Sacramento model does well in simulating the observed rainfall/runoff process within the basin, GISS GCM scaled climate change scenarios (further discussed in the next section) were used as inputs to the model to simulate the possible future changes to the runoff and soil moisture storage of the basin. These results are shown in Figure 68. From the figure, the indication is that the Rio Cobre basin may become severely stressed as substantial decreases in runoff and depletion of soil moisture are predicted. For most of the dry season, future runoff may be below its $1xCO_2$ amount. The dry month of August is predicted to have the greatest drop in runoff, a 25% decrease. However, March through June is expected to have favorable runoff. For the entire dry season soil moisture is expected to be depleted. The aquifer's depletion is expected to be at its worse, a - 40% , in August. Storage may be more favorable from January - March and again in November and December.

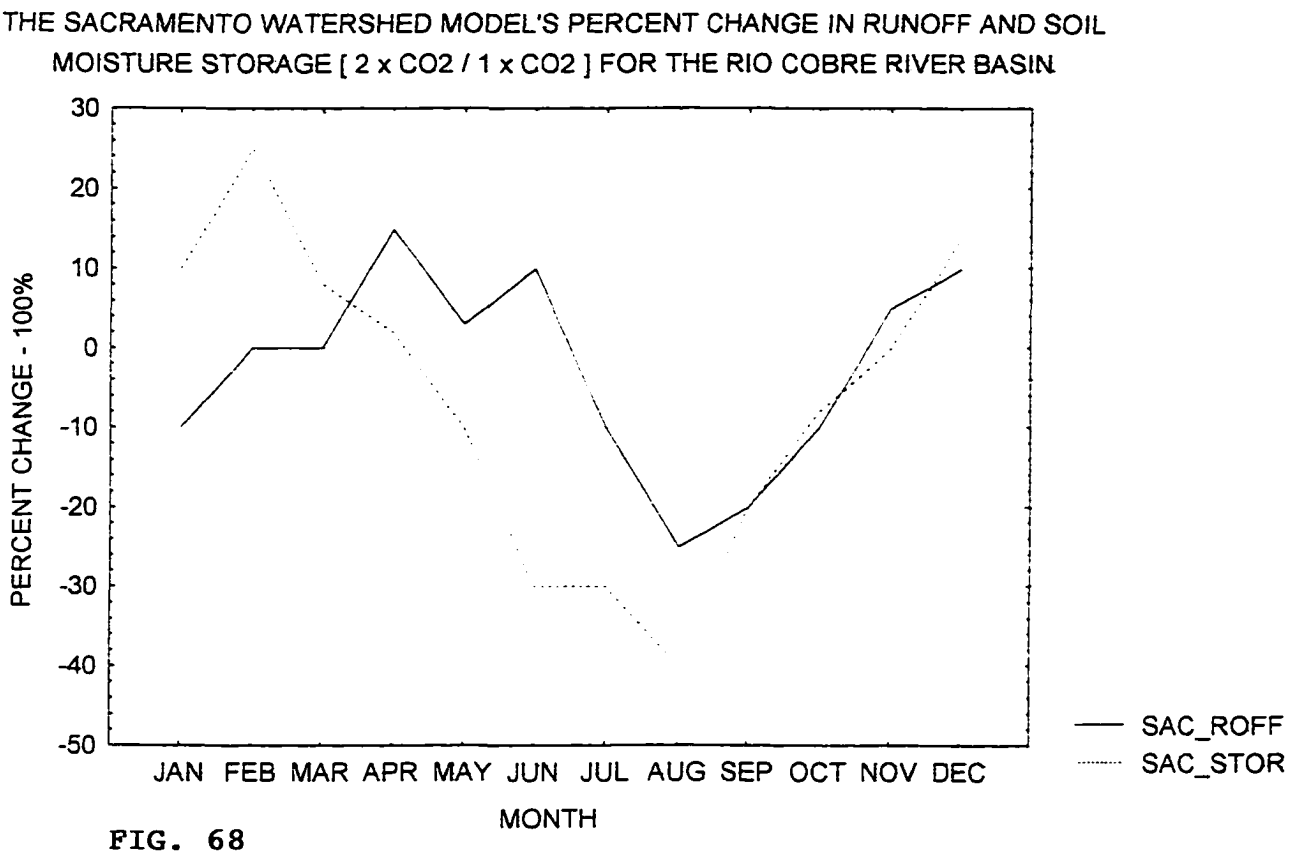

FIG. 68

8.2 Improved GISS Land-Surface Model : Rio Cobre

With the model doing better in predicting observed runoff from karstic watersheds, possible climate change impacts on the components of water balance (precipitation, runoff, evapotranspiration and soil moisture storage) can now be examined for the three sites - Rio Cobre, Rio Grande and Yangtze. However, before this can be done for the Rio Cobre watershed, the problem of scales must be addressed.

The GISS GCM gridbox that contains Jamaica is mostly occupied by the ocean. The island occupies a very small portion of the gridbox. Averaged, climatic variables that the GCM produces are apt for the larger gridbox and far less apt for the small land mass of Jamaica that lies within the gridbox. Therefore, any study of climate change for the island based on the scenarios produced by the GCM must first be scaled from the gridbox average down to the island average and then further down to the watershed average. The issue of scaling remains a major unresolved problem in the study of possible climate change impacts, via GCM scenarios, on small regional watersheds. There is no consensus within the climate change community as to how this scaling problem should be solved. An alternate approach is to nest a higher resolution model within the GCM gridbox, but this approach has flaws because of the inadequate

modeling of the boundaries between the two models. A very simplistic, zeroth-order, first estimate approach to this problem is used here. Since there must be some relationship between the gridbox averaged climate variables and the island averaged variables, a correction factor was used to scale the GCM climate variables down to the island averaged climate variables. Real world, gridboxed, observed data from the Legates global data set were used to develop the correction factor. The idea then is to make the relationship that exists between the Legates gridbox data and the island averaged data the same relationship that exist between the GCM gridbox data and the island averaged data (see Table 4). The percent change between the corrected GCM gridbox data and the island averaged data is then used to scale to the basin data. This is not the only way to get around this problem, and it may not be the best way, but it is far better than not to do any correction at all. The relationship may not hold for future climate, but it at least holds true now, and this is a straight, simple method of obtaining a zeroth order estimate. This method also captures the natural monthly climate variability as seen in Table 3.

Table 3 Linking mean Jamaican rainfall (mm/day) to GISS (4x5) GCM via a Legates correction factor.

MONTH	LEGATES	JAMAICA	CORRECTION FACTOR	GISS($1XCO_2$)	CORRECTED GISS($1XCO_2$)	GISS($2XCO_2$)	CORRECTED GISS($2XCO_2$)
JAN	1.3	3.5	2.7	1.6	4.3	1.6	4.3
FEB	1.1	3.1	2.8	1.8	5.0	1.5	4.2
MAR	1.2	3.1	2.6	1.9	4.9	1.4	3.6
APR	2.2	4.6	2.1	2.4	5.0	1.8	3.9
MAY	4.9	7.5	1.5	4.1	6.2	3.4	5.1
JUN	5.4	6.1	1.1	4.2	4.6	3.7	4.1
JUL	3.8	4.3	1.1	4.4	4.8	3.1	3.4
AUG	4.1	5.8	1.4	3.4	4.8	2.6	3.6
SEP	5.1	6.8	1.3	3.5	4.6	2.3	3.0
OCT	5.7	8.7	1.5	5.3	8.0	4.9	7.4
NOV	2.7	6.2	2.3	5.2	12.0	5.7	13.1
DEC	1.5	4.8	3.2	2.3	7.4	2.4	7.7

Figures 69 - 75 show climate change scenarios for the Rio Cobre basin. In the figures, the ordinate (percent change - 100%) is zero if the climate variable at $2xCO_2$ is the same as it was at $1xCO_2$. The ordinate is positive when the climate variable is greater at $2xCO_2$ than it is at $1xCO_2$, and it is negative otherwise. The percent changes in rainfall, as depicted in Figure 69, were obtained from the basin scaled GISS GCM scenarios. According to the model and the scaling approach, the Rio Cobre basin is expected to experience increased rainfall in a doubled CO_2 climate. The rain is expected to peak in April, but it then, abruptly at first, then steadily afterwards, decline throughout the year until November when it is expected to be at its normal amount for that month. Thereafter, it gradually increases.

Figure 70 shows how the components of the water balance (precipitation, runoff (RO), evapotranspiration (ET) and soil moisture storage (ST)) may vary in a doubled CO_2 climate according to simulations done with the karst-augmented, off-line GISS land surface model. The climate change data used to drive the model were obtained from the GISS GCM. The results from these simulations indicate that for the most part, except for April and December, RO, ET and ST will all decrease in a doubled CO_2 climate. However, these decreases are not expected to be too severe. It is also noteworthy from these

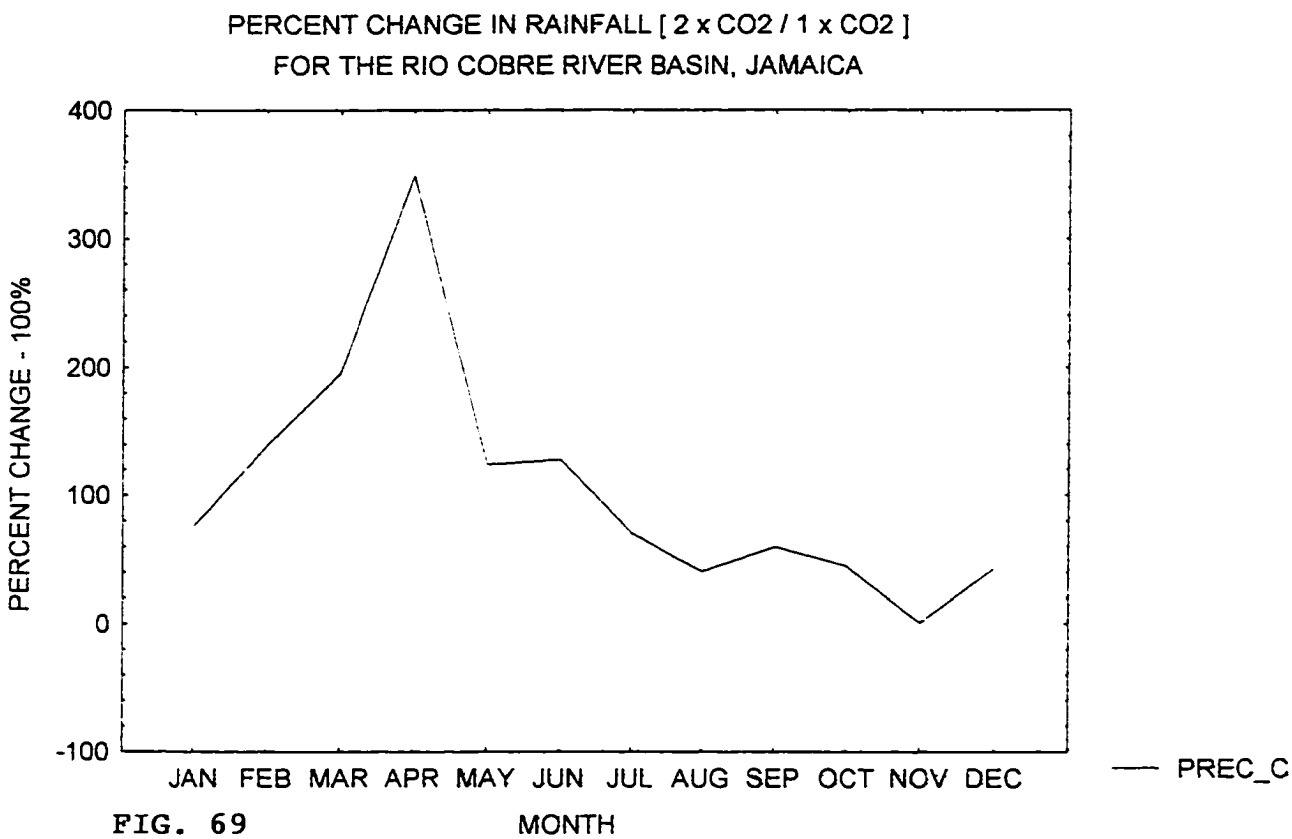

FIG. 69

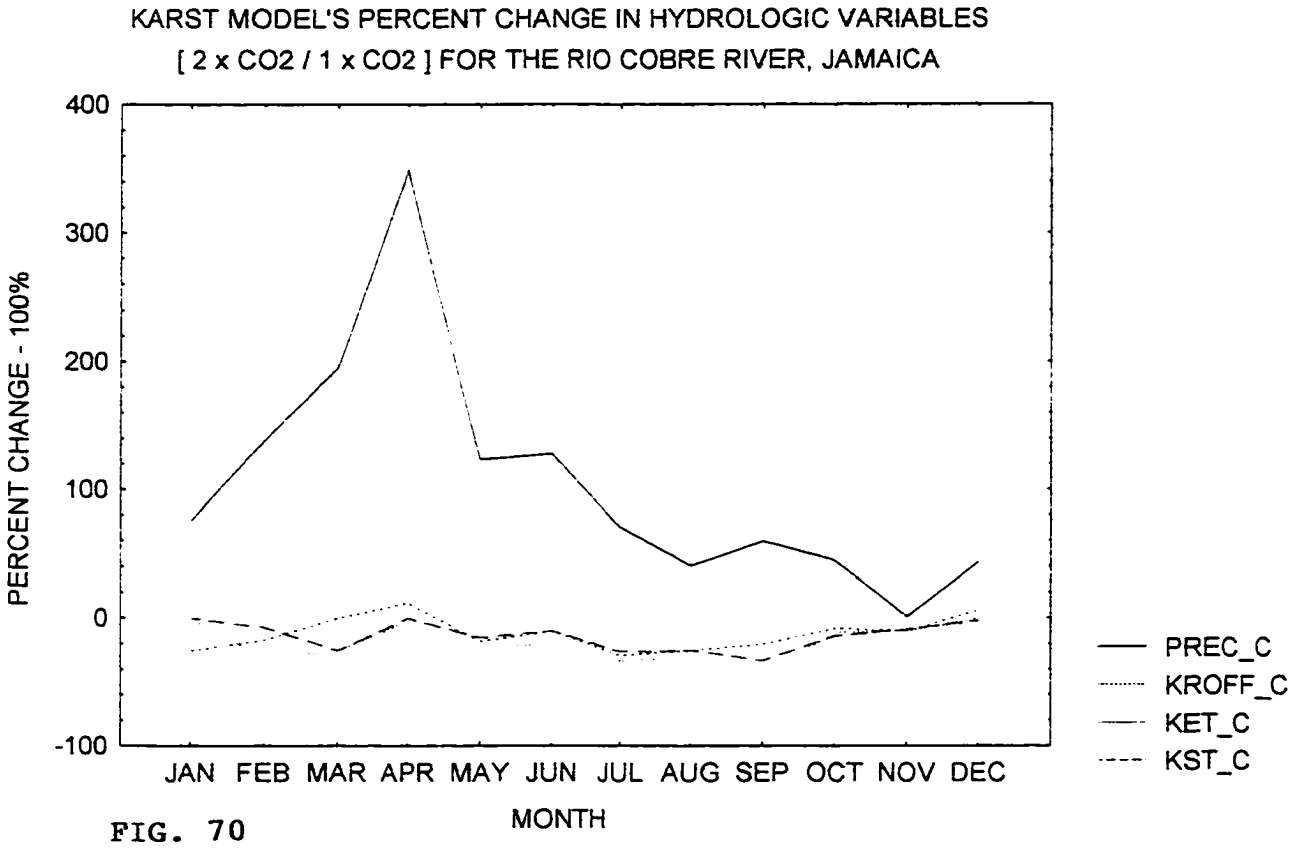

FIG. 70

karst model simulations that the response to rainfall changes by the other components of water balance is minimal. This may be due to the model capturing the karst features of the basin. Figure 71, like Figure 70, shows the hydrologic components and their possible percent changes in a doubled CO_2 climate for the Rio Cobre. The experiment setup is the same as that for Figure 70. However, these simulations were done with the original, no-karst, GISS land surface model. The figure indicates that on average the basin may experience slight increases in RO, ET and ST. Here, unlike in the previous figure, the water balance components are more responsive to changes in rainfall. However, ST seems to peak in February two months before the rainfall peaks. This may be due to the ET minimum at that time. Figure 72, unlike the two previous figures,was derived from simulations done only with the GISS GCM. No off-line, regional model was used here. The plots represent GCM scaled simulations for the Rio Cobre. The figure shows a possible positive trend for future ST, an overall increase in ET, and except for April when RO climbs to it 1 x CO2 level, it may decrease to an almost constant rate in a doubled CO_2 climate. Also, except for RO and especially for ST the components of water balance are responsive to changes in rainfall.

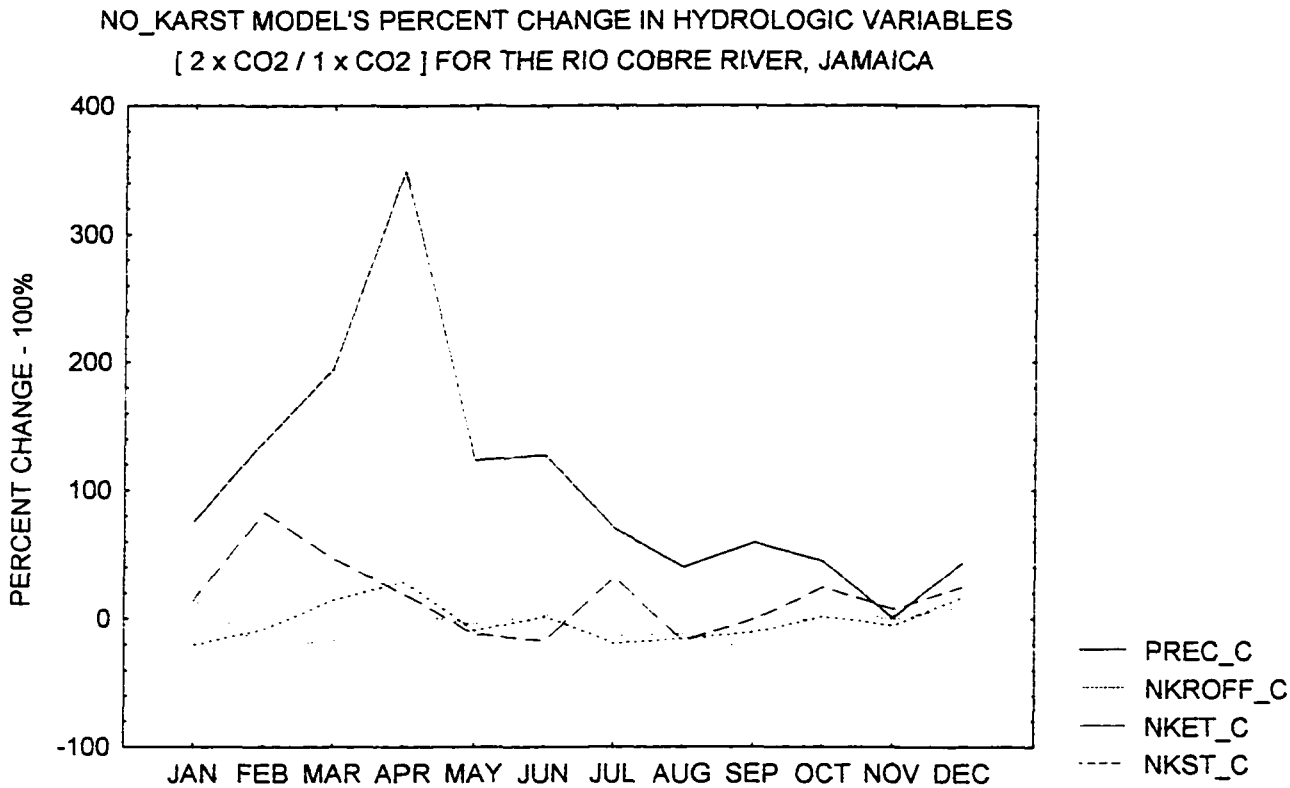

FIG. 71

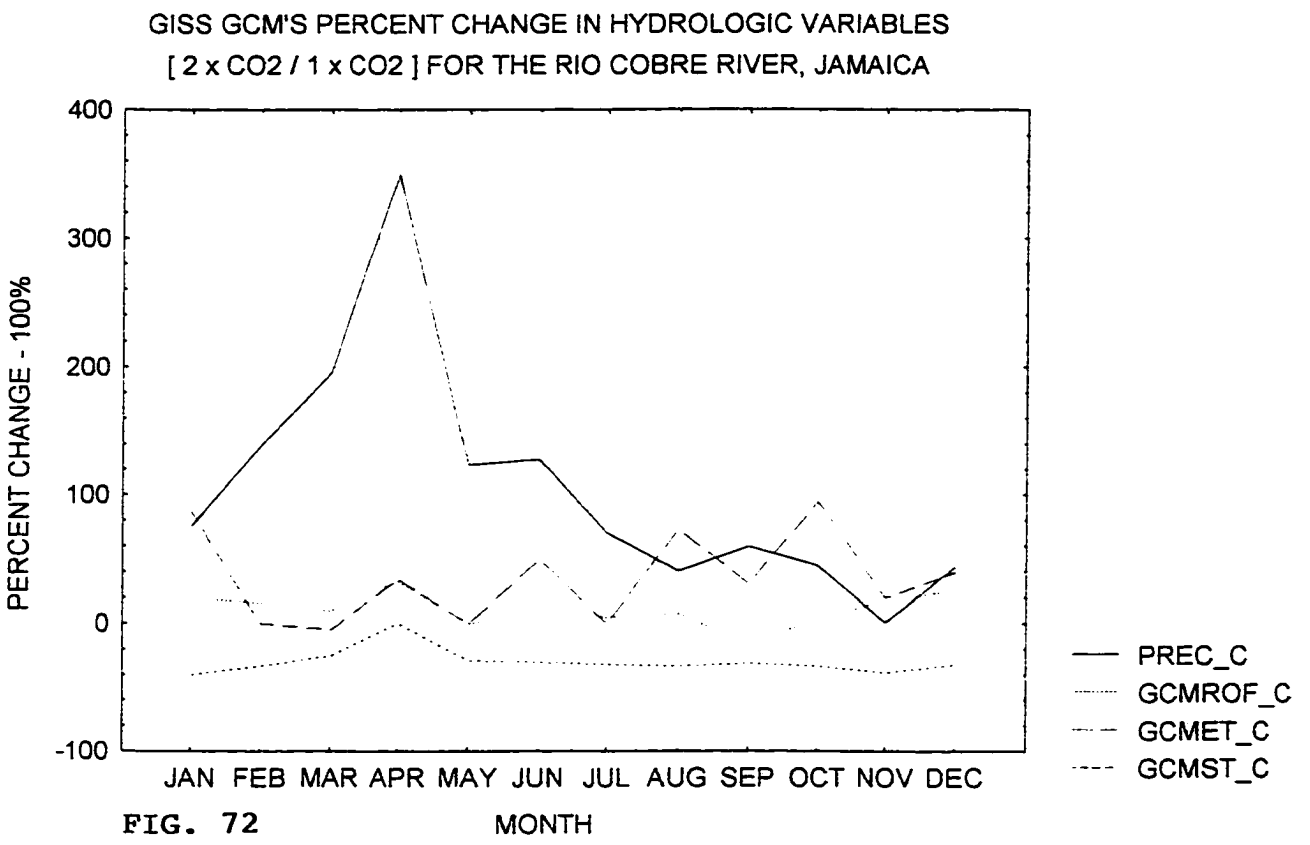

FIG. 72

Since three different models were used to assess the possible impacts of climate change on the hydrologic variables of the Rio Cobre, the range of possible changes for each variable may be best represented by Figures 73 - 75. In the figures, the karst simulation is blue, the no_karst simulation is red and the GCM simulation is green. Figure 73 illustrates the possible changes in RO for the three models used. All three models indicate that the basin may become severely stressed in terms of RO in a doubled CO_2 climate. The GCM gives the most woeful prediction while the no_karst model gives the least stressed possibility. The models also indicate that the stress on RO will be greatest during the usually hot, dry season which extends from May to October. Figure 74 shows the predictions of future ET for the basin from the three models. The greatest increase in ET is given by the GCM, and the greatest decrease is given by the karst land surface model. The karst model shows dramatic decreases in ET all year around but especially in September. Indeed, all three models show September to be the month of least ET. The no_karst model, for most of the year, shows decreases in future ET. In Figure 75, the three models' predictions of changes to future ST are shown. The karst model shows the greatest decrease in future storage while the GCM shows the greatest increase. The no_karst model, on an annual average, indicates an increase in future storage.

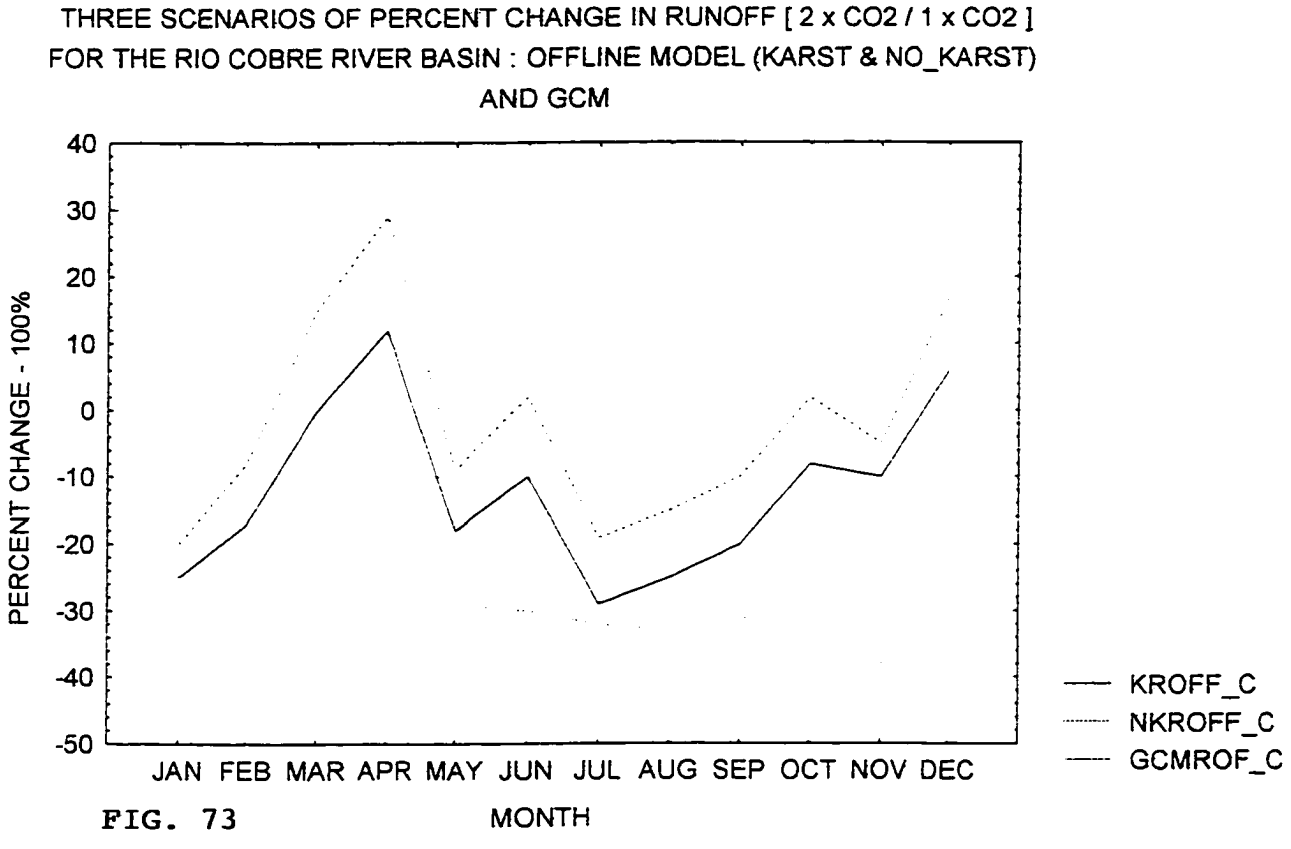

FIG. 73

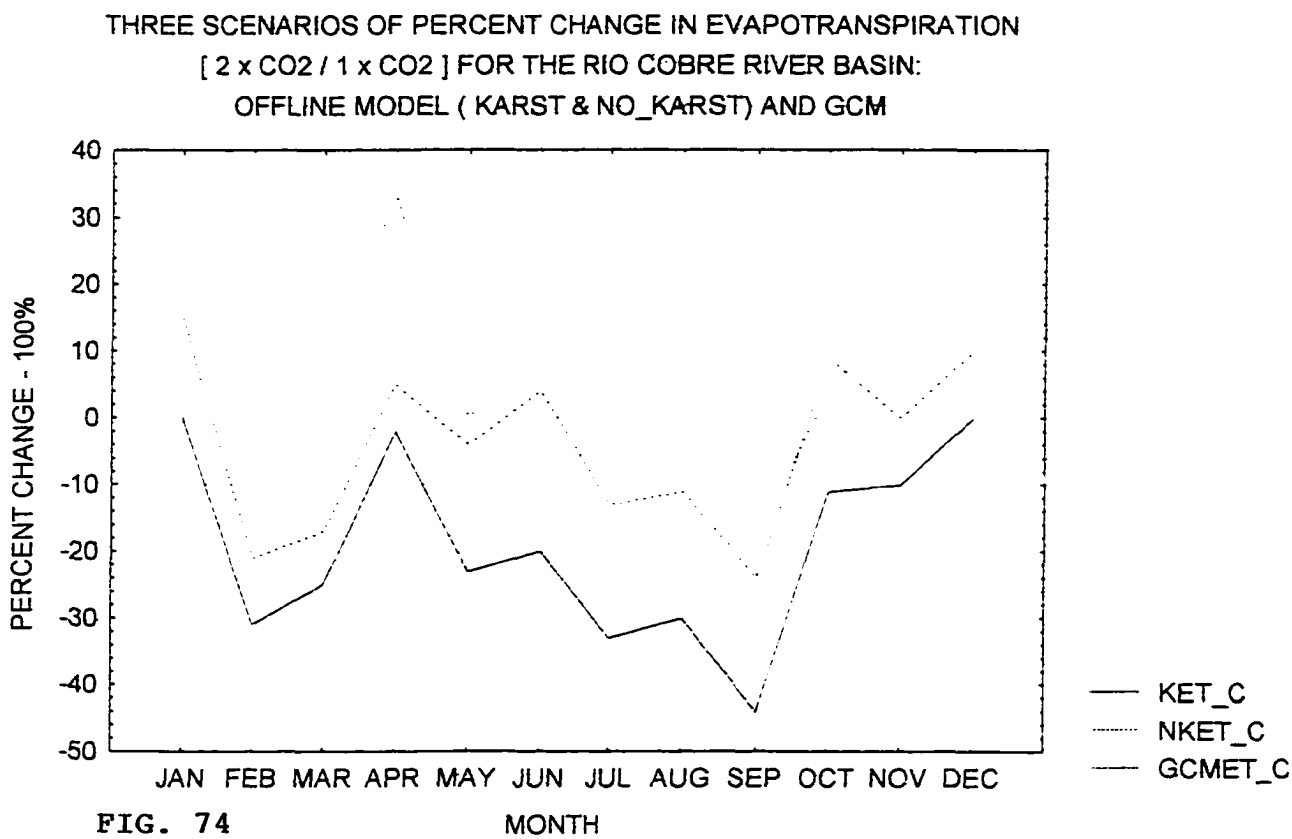

FIG. 74

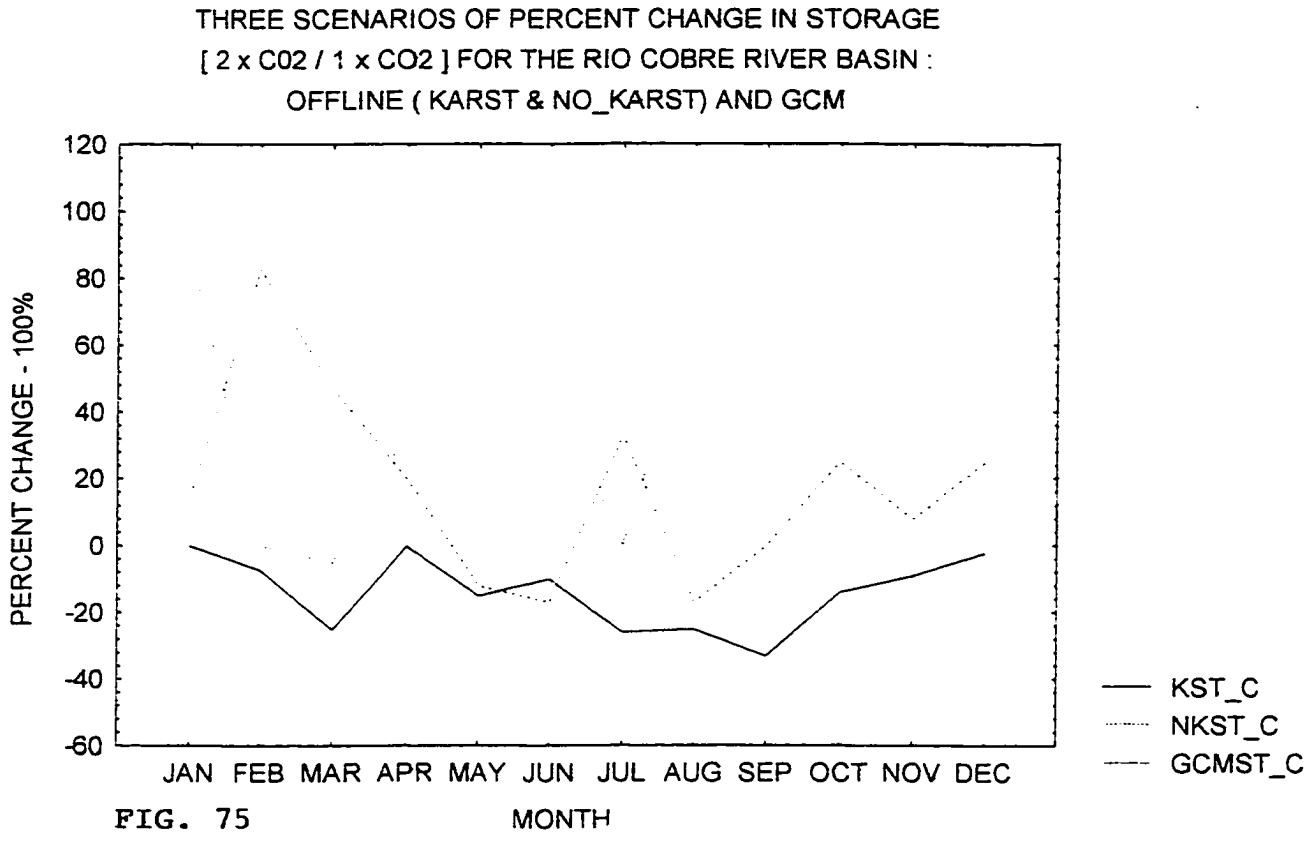

FIG. 75

Figure 76 and tables 4 - 7 examine possible climate change impacts on the runoff and rainfall in the Rio Cobre via observed and doubled CO_2 scenarios. The figure shows that with the exception of December, the future mean monthly runoff may be less than the current mean monthly runoff, and the months of March, April and August - October may experience the most severe reductions in runoff. In general then, the Rio Cobre watershed may become more stressed in a $2xCO_2$ climate.

The Kolmogorov-Smirnov statistical test for the normality of probability distributions was then implemented at the 0.05 significance level to aid in the determining of return periods for the extreme cases of annual minimum and annual maximum rainfall and runoff. The results are tabulated in Tables 5 -8. The tables indicate that the extremes in the basin's rainfall and runoff may become more extreme for all the considered return periods.

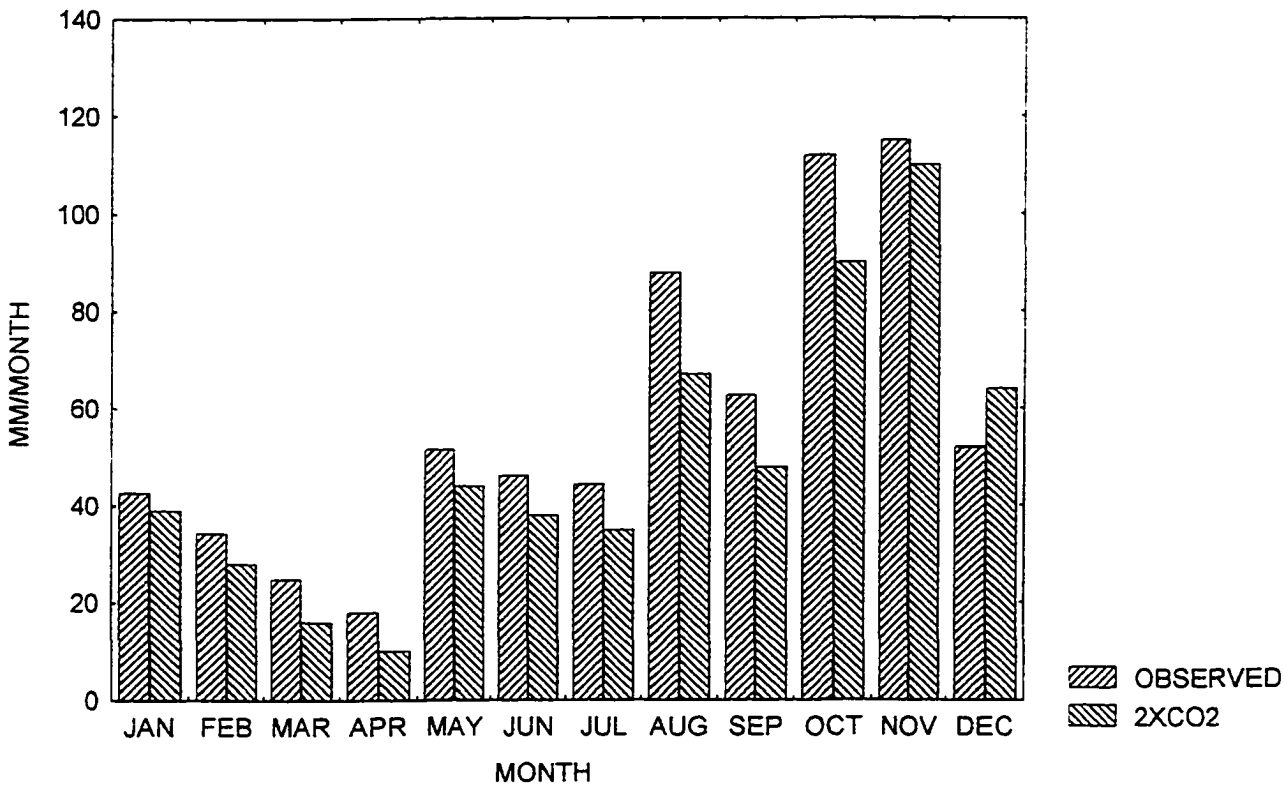

FIG. 76 Projection of Rio Cobre runoff at 2xCO2 scenario

Table 4. Return Periods for Rainfall (mm) of the Annual Minimum Series.

	Return Period (years)			
	10	20	50	100
Rio Cobre	129	154	187	211
GISS ($2 \times CO_2$)	104	123	146	165

Table 5. Return Periods for Rainfall (mm) of the Annual Maximum Series.

	Return Period (years)			
	10	20	50	100
Rio Cobre	676	796	947	1062
GISS ($2 \times CO_2$)	575	667	783	872

Table 6. Return Periods for Runoff (mm/day) of the Annual Minimum Series.

	Return Period (years)			
	10	20	50	100
Rio Cobre	1.58	1.74	1.94	2.09
GISS ($2 \times CO_2$)	0.88	0.94	1.02	1.08

Table 7. Return Periods for Runoff values (mm/day) of Annual Maximum Series.

	Return Period (years)			
	10	20	50	100
Rio Cobre	12.03	14.79	18.27	20.93
GISS (2 x CO2)	11.07	12.97	15.36	17.19

8.3 Improved GISS Land-Surface Model : Yangtze

As the Yangtze river meanders through the high mountains of China, cursory insight to possible climate change impacts on its RO can be obtained from Figures 77 - 79. Figure 77 shows RO from the karst model, Figure 78 shows RO from the no_karst model while Figure 79 depicts RO from the GISS GCM. In the figures, observed RO is blue, $1xCO_2$ RO is green and $2xCO_2$ RO is red. It is evident from the figures that quantitatively the models differ in peak and volumetric flows, and the control runs grossly over-predict the observed RO. However, qualitatively, and in general, the models all seem to indicate that future RO may, on average, be about the same volumetrically for the first half of the year, and then it slightly increases for the second half of the year. The karst model predicts substantial decreases in RO for the summer months from May to August. All three models predict decreases in future RO for the months of March and April. Deeper insights of possible future climate change impacts on the Yangtze river can be obtained from an analysis of the possible percent changes in the water balance components of the river.

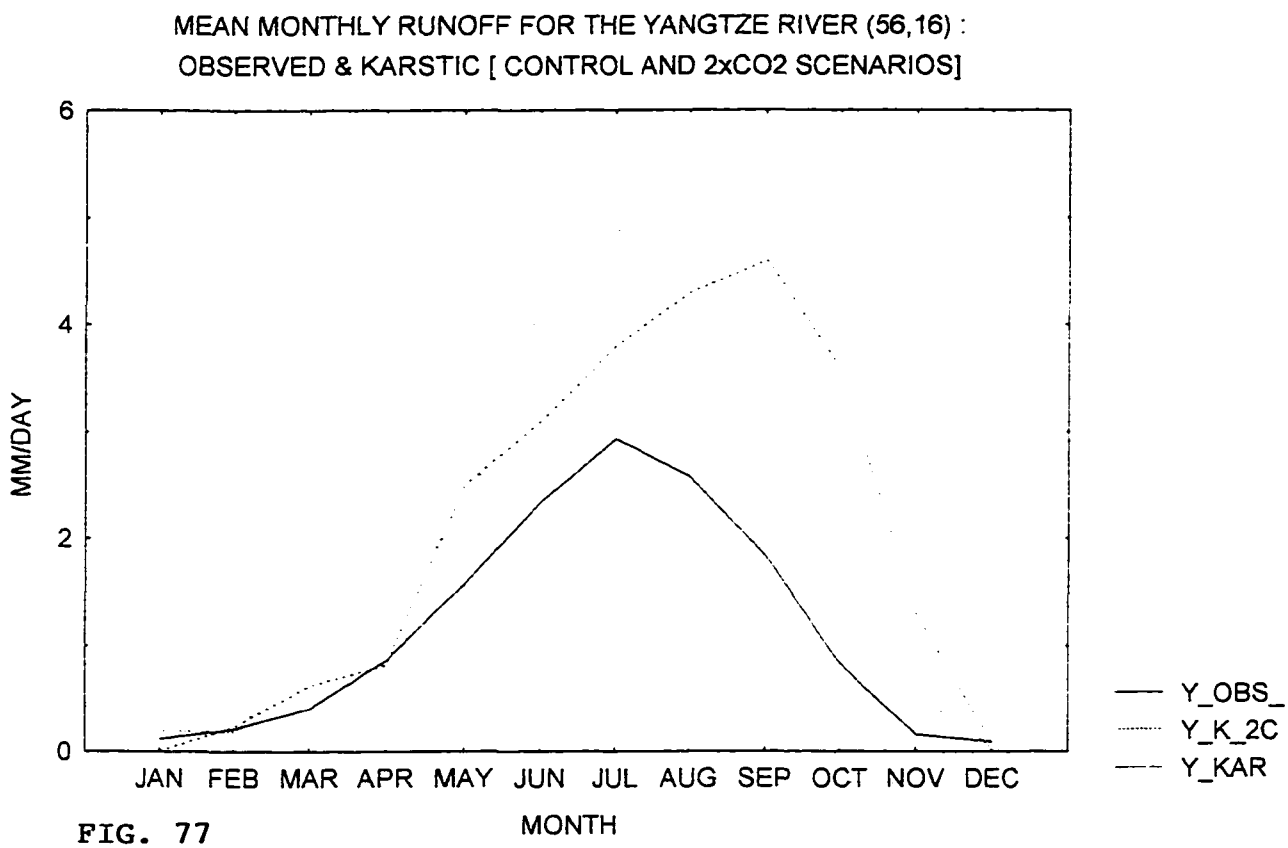

FIG. 77

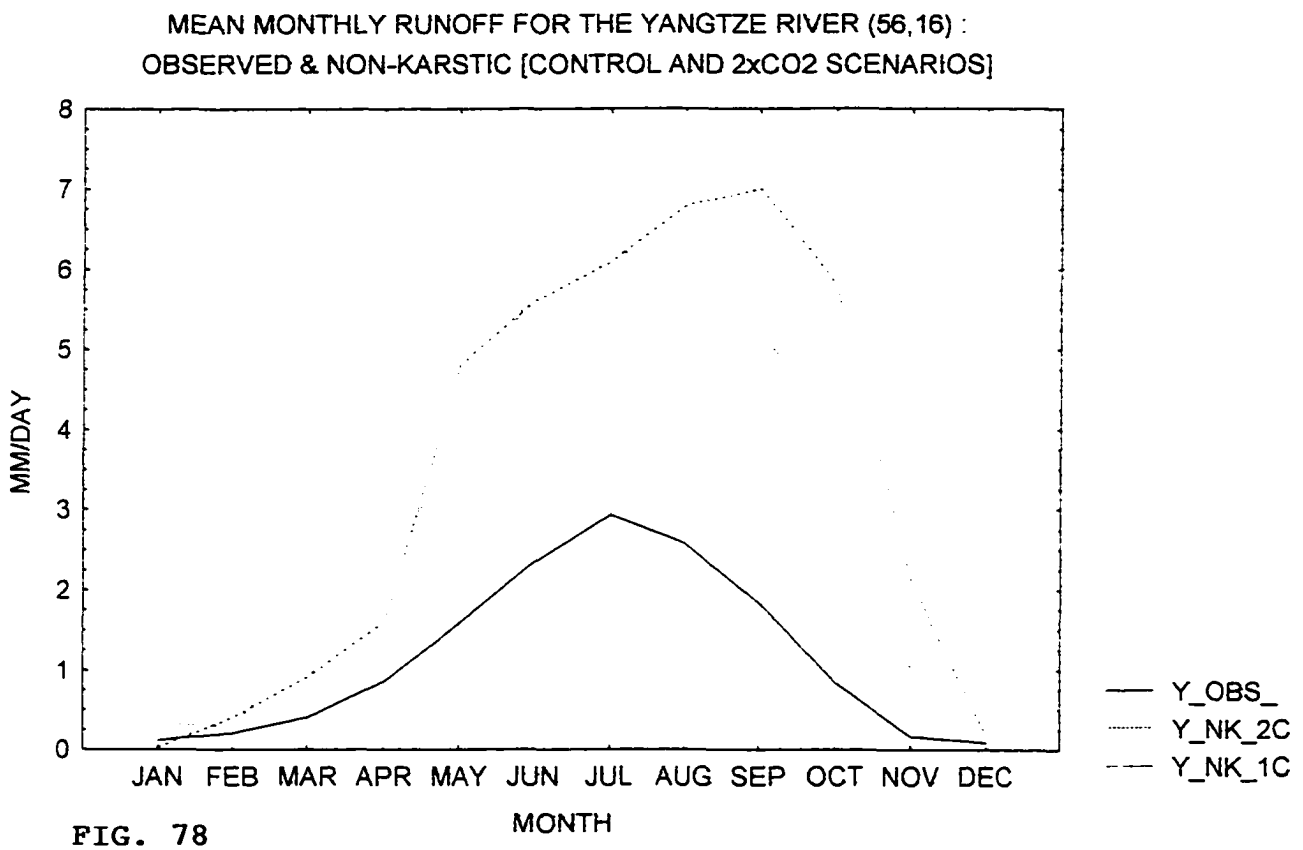

FIG. 78

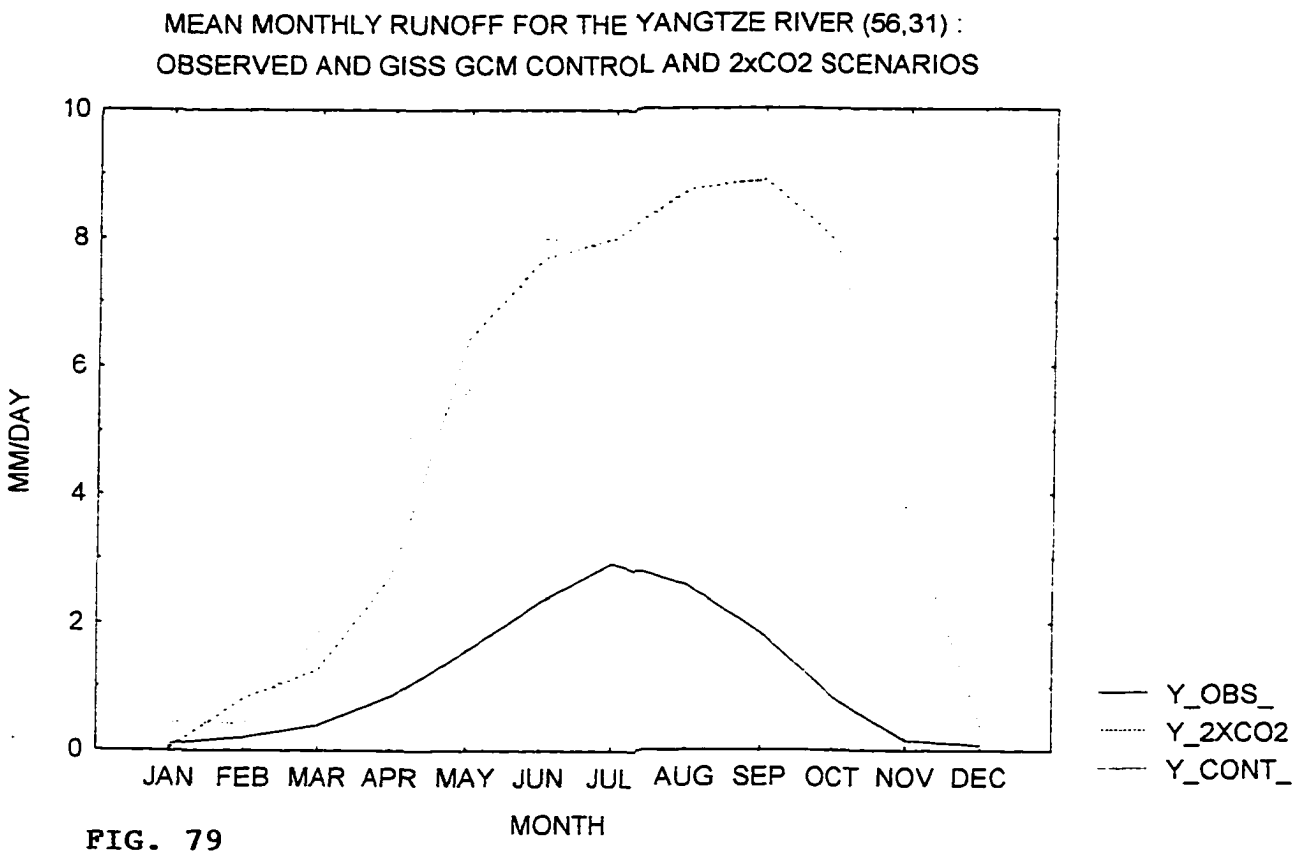

FIG. 79

Percent changes in precipitation between $1xCO_2$ and $2xCO_2$ scenarios for the Yangtze river are shown in Figure 80. These changes were calculated directly from GISS GCM output. The model indicates that decreases in future precipitation should occur only in the month of January. Maximum precipitation increase may occur in February, and a minor peak may occur in May. The months March, June - August may not experience any changes in precipitation. From September to December there may be a gradual increase in precipitation. Figure 81 depicts the probable changes to the hydrologic variables of the basin as simulated by the karst model. The model's output indicates that the basin's RO may decrease throughout the year until August. From August through December, the RO is expected to gradually increase. The period of greatest RO deficiency may occur in January. Under a doubled CO_2 climate regime, the ET for the Yangtze may increase. Maximum ET increases may occur in January and in December. For the remainder of the year, its increase may level off and become relatively constant. Depletion and deficiency of ST seems to occur throughout the year, and minima in ST occurs whenever ET is at its maximum. However, for almost steady ET throughout the year, fluctuations in ST do occur. This indicates that ST may then be responding more to the other components of the water balance during the year.

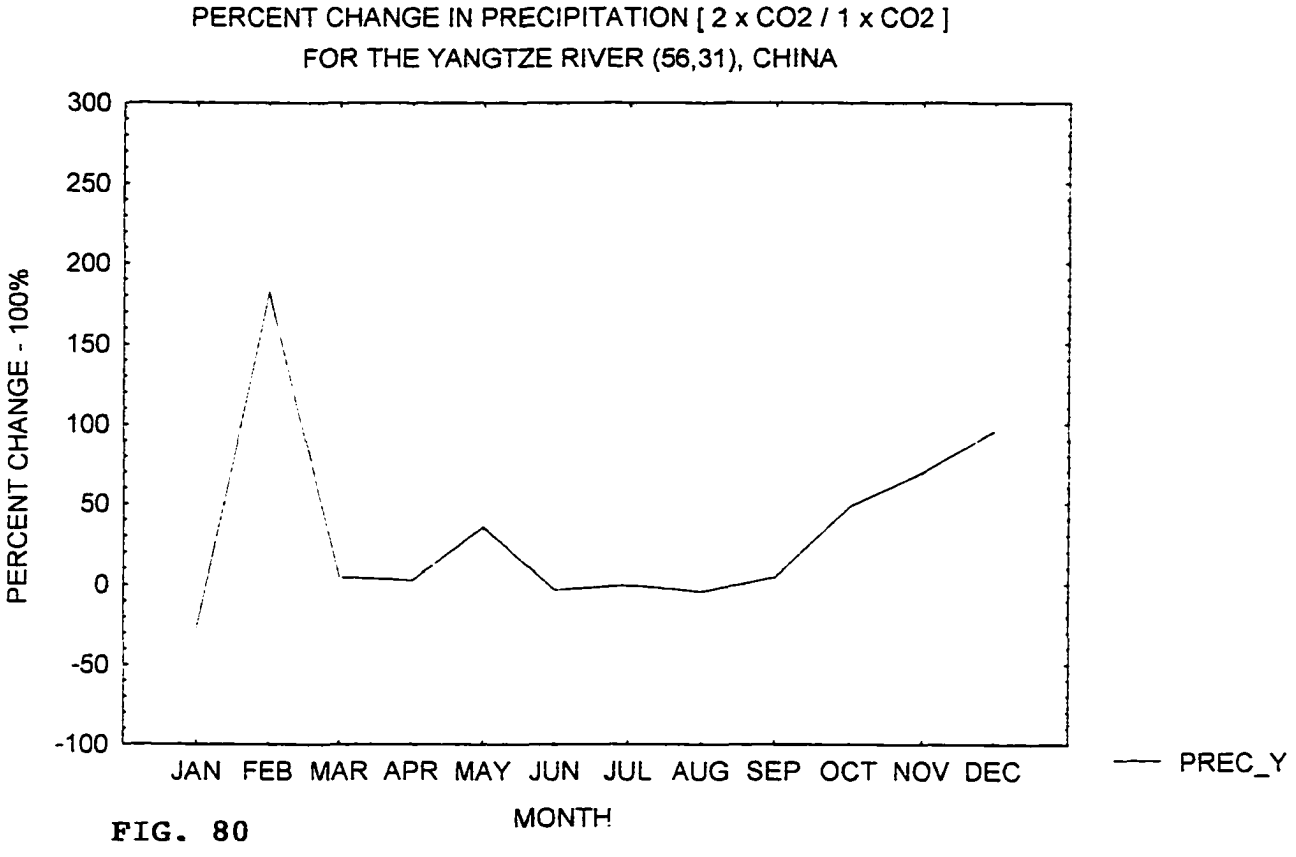

FIG. 80

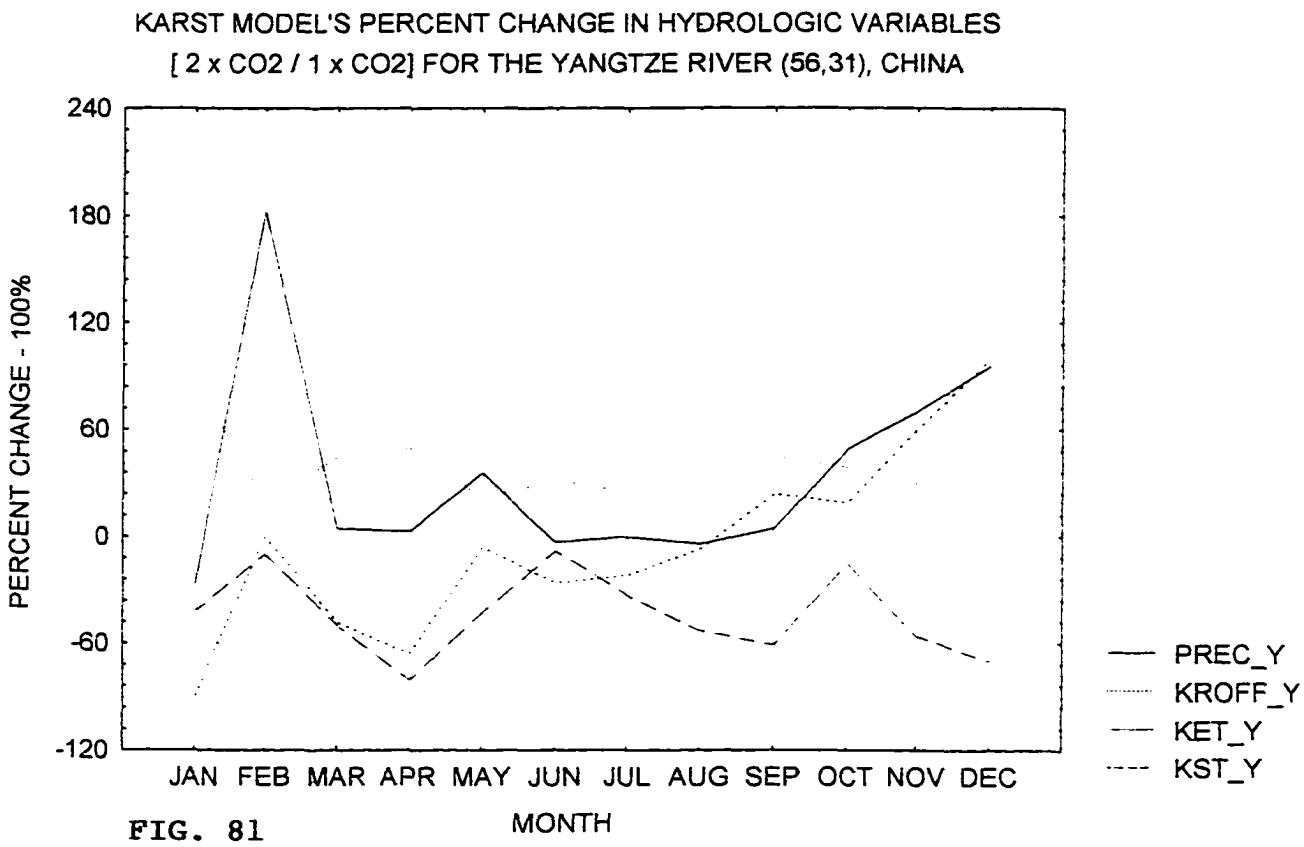

FIG. 81

Figure 82 depicts percent changes in the river's hydrologic variables via the no_karst model. It is quite apparent from the outset that the fluctuations in these variables are greater than the fluctuations in the variables simulated by the karst model - the previous figure. RO responds well to the precipitation and fluctuates with a positive trend from a state of deficiency in January to one of surplus in December. ET seems to increase throughout the year in a doubled carbon dioxide climate, but it may reach its minimum in July and its peaks in January and December. In the summer when ET is least, ST peaks, and maximum ET seems to coincide with minimum ST during January and December. Overall, the model predicts that ET and RO should be greater in a $2xCO_2$ climate than in a $1xCO_2$ climate. On an annual average, ST may be slightly decreased.

The probable percent changes in the Yangtze river's hydrologic variables as simulated by the GISS GCM for a climate richer in carbon dioxide are depicted in Figure 83. Apart from decreases in RO in January, March and April, the model predicts favorable increases in future RO for the Yangtze. Peak RO is shown to occur in December and lowest reduced flows may occur in January. Little or no change in flow is expected during the summer. The model expects the future RO to respond almost linaerly to the future precipitation. Substantial

increases in ET are expected for the river basin. The lowest percent increase is expected to be about 60% in June and October. ET is expected to peak in January and in December. The peak ET in January coincides with the lowest flows, the lowest precipitation and diminished ST while the December peak coincides with peak flows, substantial rainfall increases and lowest ST. According to the model, ST depletion will be occur rather steadily from May to December where its depletion may reach 60% of its $1xCO_2$ amount.

Figures 84 - 86 compare the three models' predictions for RO, ET and ST. In Figure 84, the RO comparison shows that, in general, all three models capture the same inter-annual variability in future RO. They all show a positive trend. The no_karst model and the GCM are more alike in their predictions than the karst model. All three models expect the lowest reduced flows to occur in January and the peak flows to take place in December. Minor peak flow reversals occur between the GCM and the no_karst models in February and May. For the first eight months of the year the karst model expects RO to be less than it is in a $1xCO_2$ climate, and the GCM expects little or no change in RO during the summer. All three models (see Figure 85) expect future Yangtze river ET to increase substantially. The karst model shows the least increase, and from January through September, the GCM increases exceeds those of the no_karst

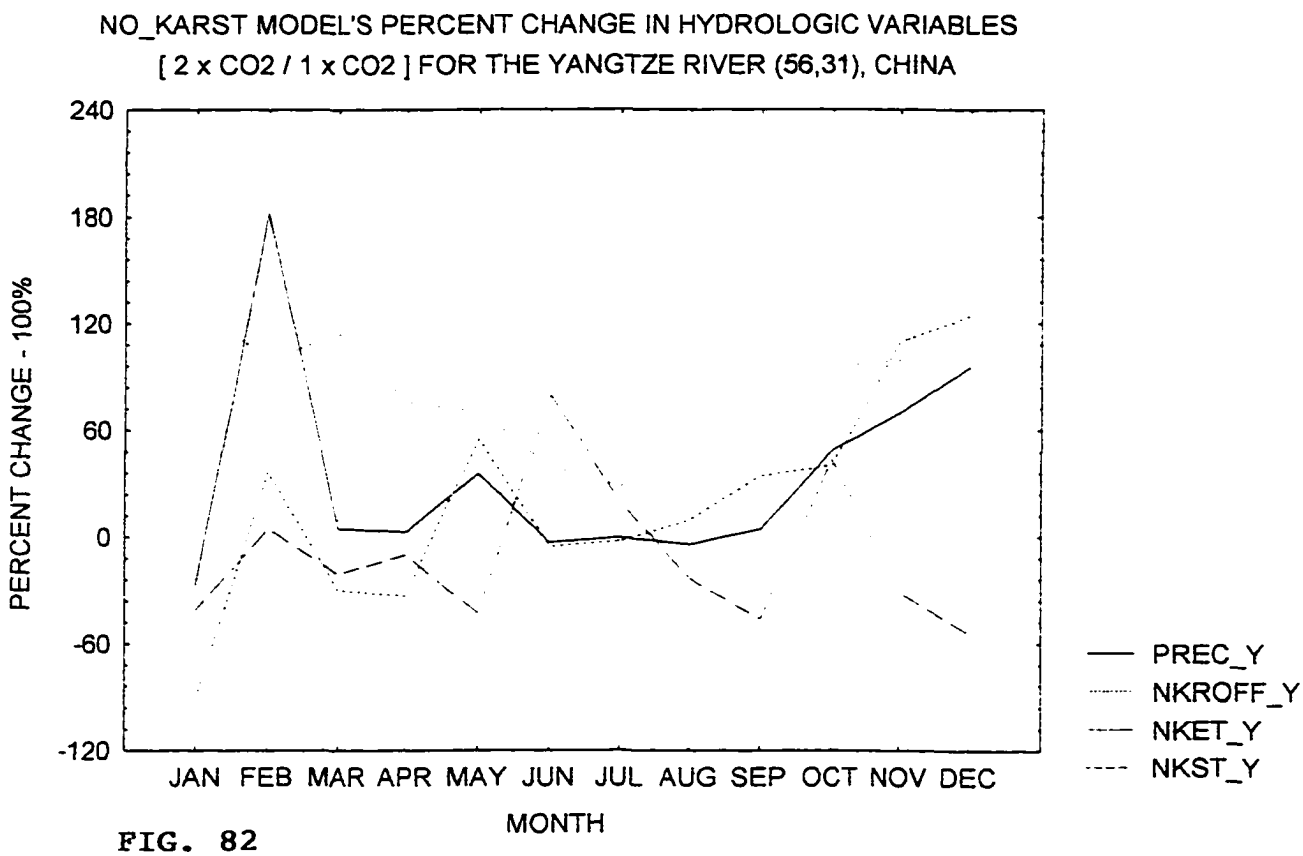

FIG. 82

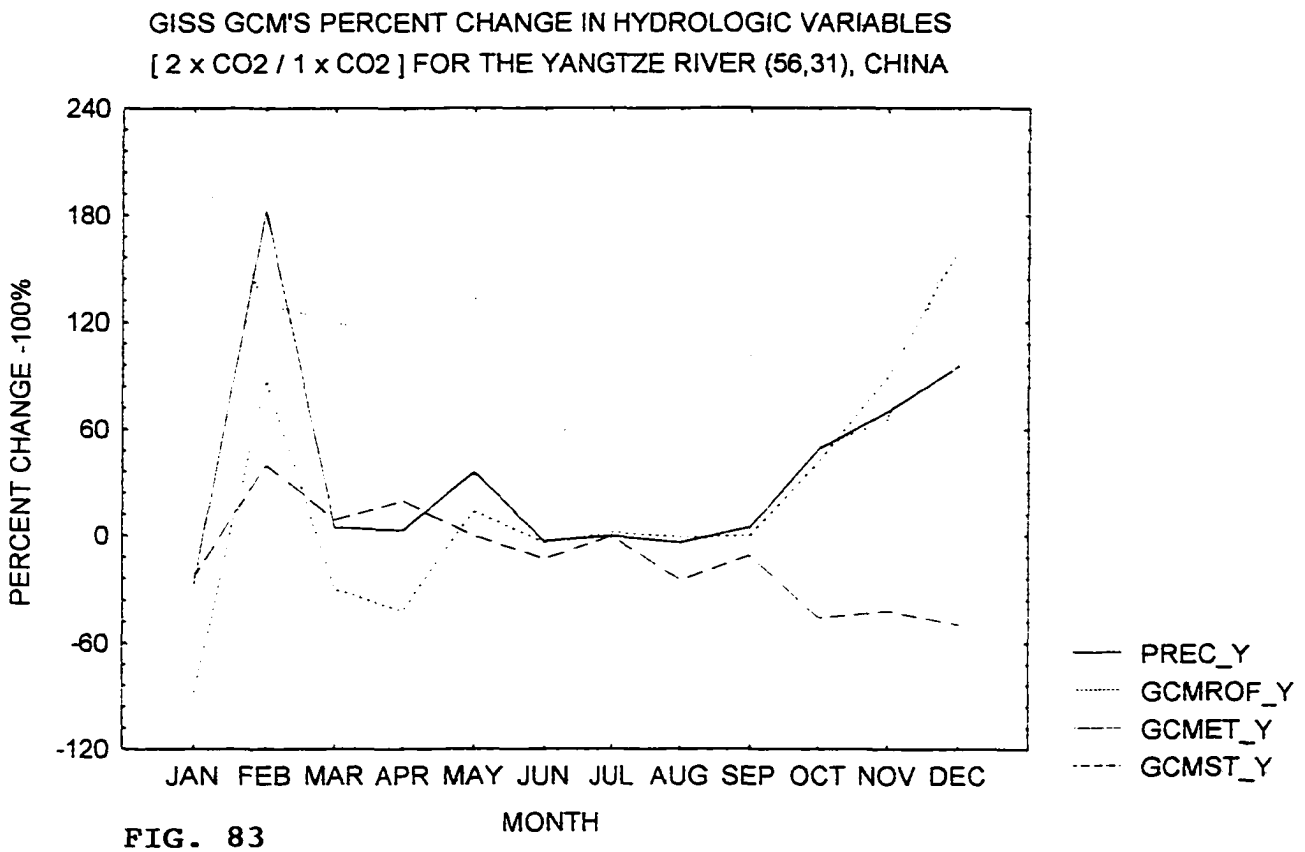

FIG. 83

model. From September through to December the no_karst model's expected ET change is greater than the GCM's expected ET change. Inter-annual peaks and lows in ET differ from model to model. Pronounced changes is ST are expected, irrespective of the model considered. However, each model's expectations are different from the other. Of the three models, the karst expects the worst decreases, and the no_karst expects the least. The karst model predicts that future ST will be severely depleted almost all year around with greatest depletion occuring in April. The GCM expects ST to peak in February at about 40% more than its $1xCO_2$ amount, but then it steadily decreases to about 50% of its $1xCO_2$ amount by December. After relatively minor fluctuations in ST from January through May, the no_karst model expects a substantial ST peak in June. This peak represent about an 80% increase in SM. After a sharp decline during the summer to about 50% of its $1xCO_2$ amount in September, the no_karst model expects the ST to rebound to above 40% of its $1xCO_2$ amount by October. From then there is a steady decrease to December. Taken all together, the models do not tell a consistent story with regards to the future SM of the Yangtze river.

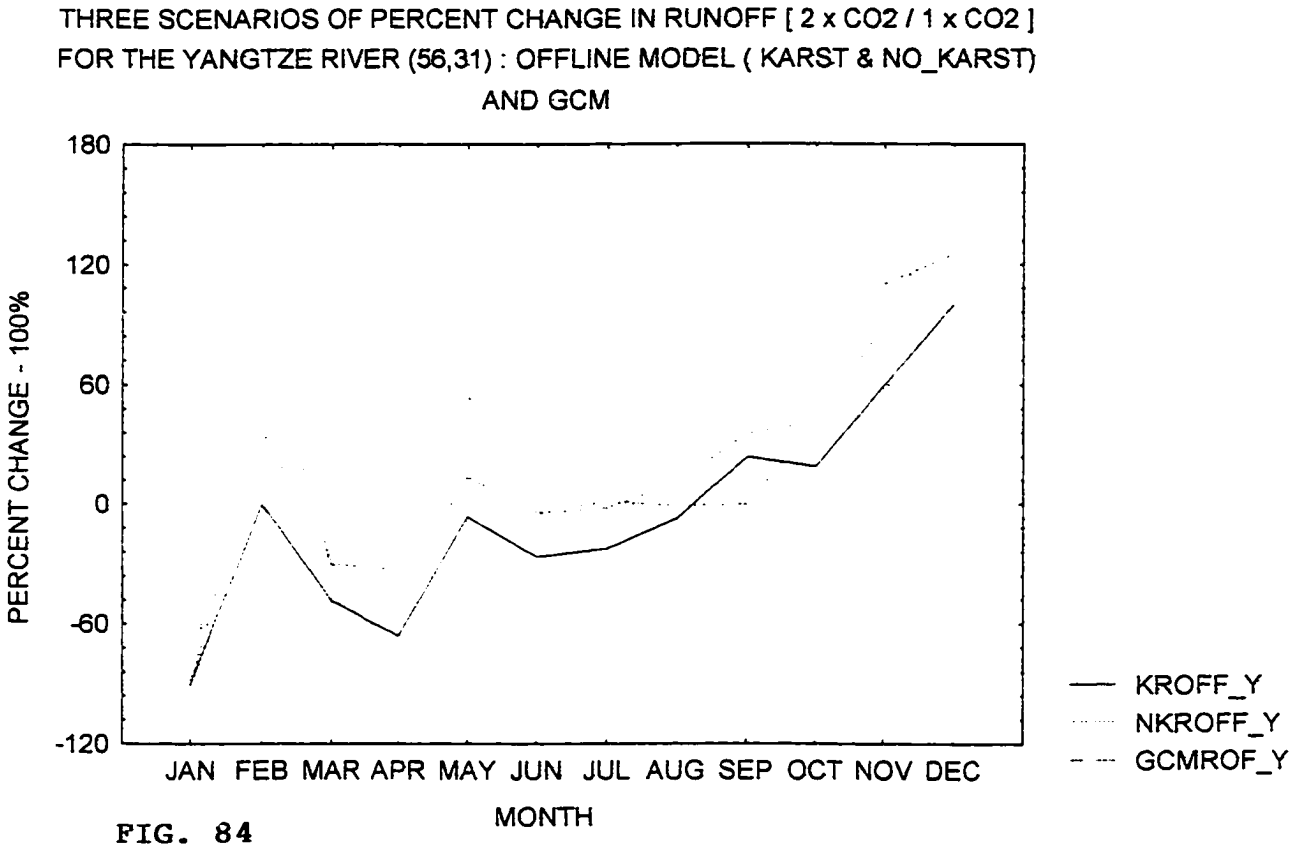

FIG. 84

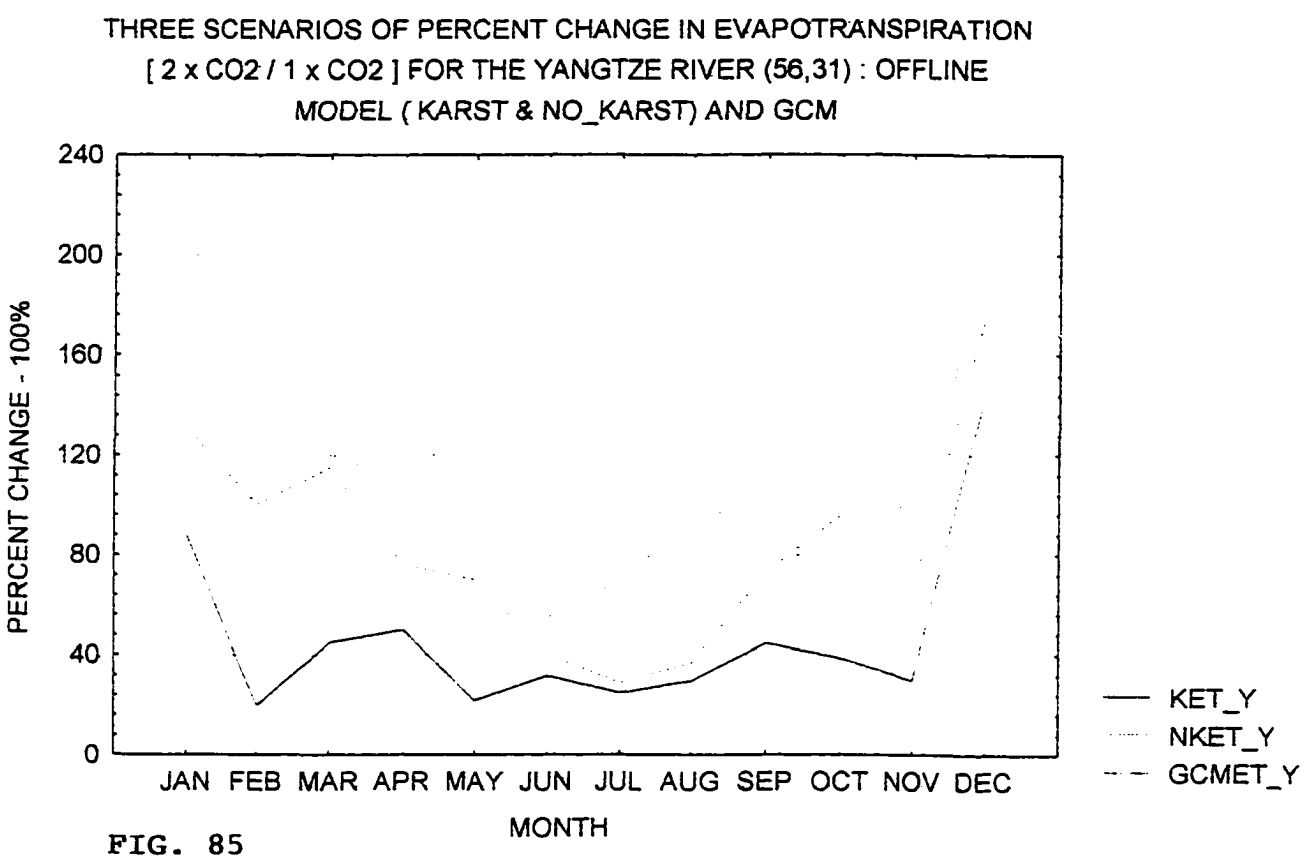

FIG. 85

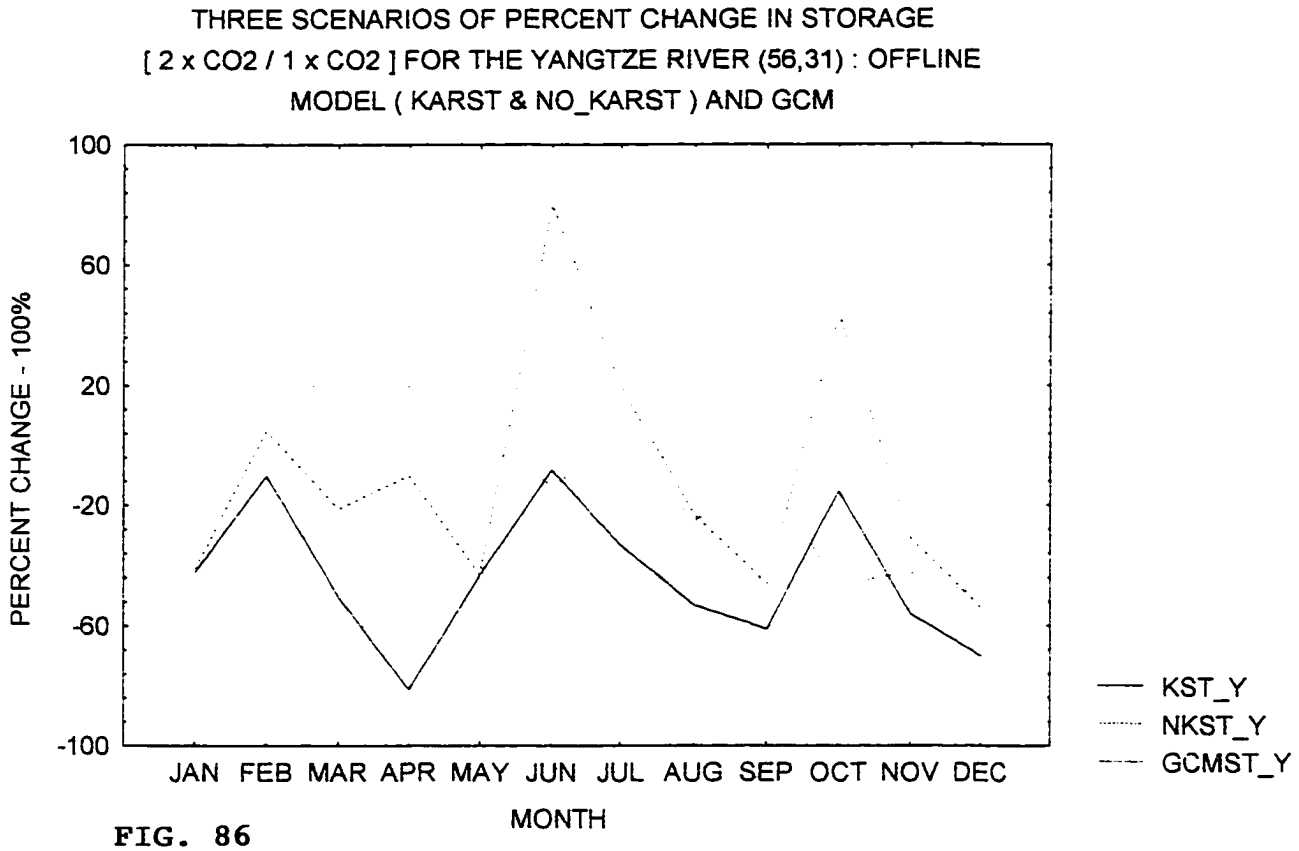

FIG. 86

8.4 Improved GISS Land-Surface Model : Rio Grande

Qualitative deductions about possible climate change impacts on RO from the Rio Grande river can be made from Figures 87 - 89. With its characteristic low flows in the desert regions of south-western U. S. A., the Rio Grande provides a good test site for the models. Figure 87 shows RO from the karst model, Figure 88 shows RO from the no_karst model while Figure 89 depicts RO from the GISS GCM. In the figures, observed RO is blue, $1xCO_2$ RO is green and $2xCO_2$ RO is red. For all three model assessments, the control runs over-predict the RO by much from January to May. From May on the predictions improve. The models' predictions of the river's future RO are all similar. They all indicate that as low as the river is now flowing, it may well ebb further in a $2xCO_2$ climate. Interrogation of all the river's water balance components is needed to provide a more holistic analysis of the possible impacts climate change may have on the Rio Grande.

Percent changes in precipitation between $1xCO_2$ and $2xCO_2$ scenarios for the Rio Grande river are shown in Figure 90. As with the Yangtze river, these changes were calculated directly from GISS GCM output. The figure indicates that the model expects Rio Grande precipitation to increase overall with maximum rainfall increase occuring in the summer month of July. Thereafter, the

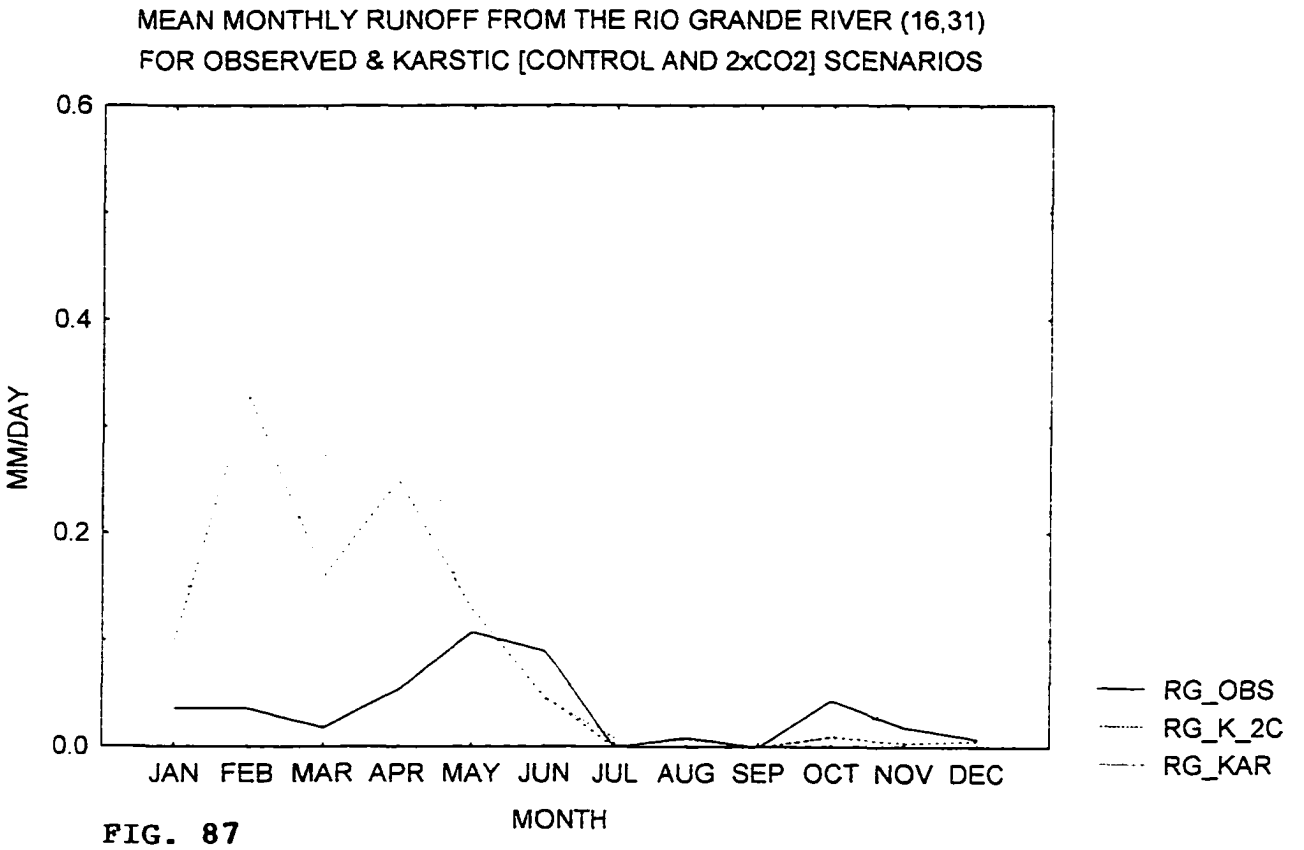

FIG. 87

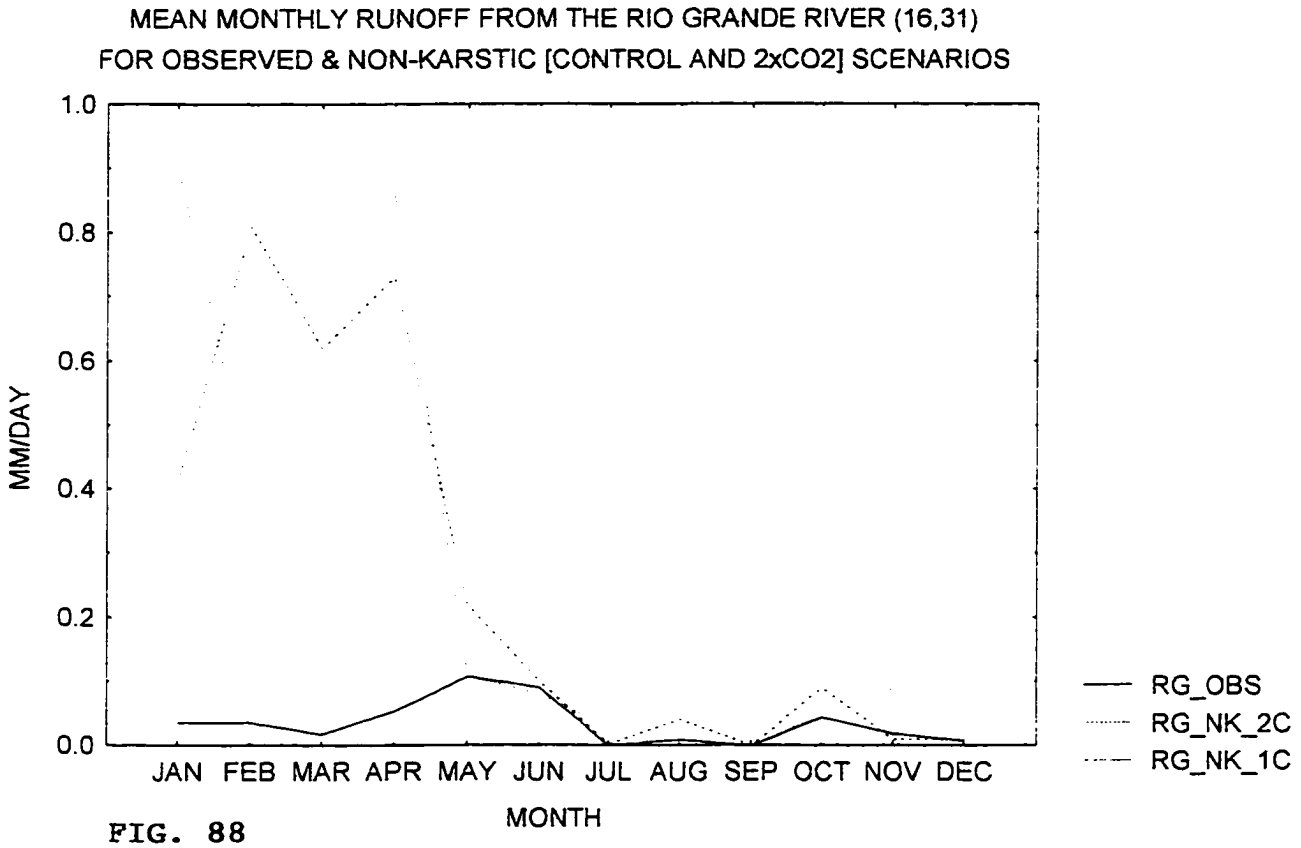

FIG. 88

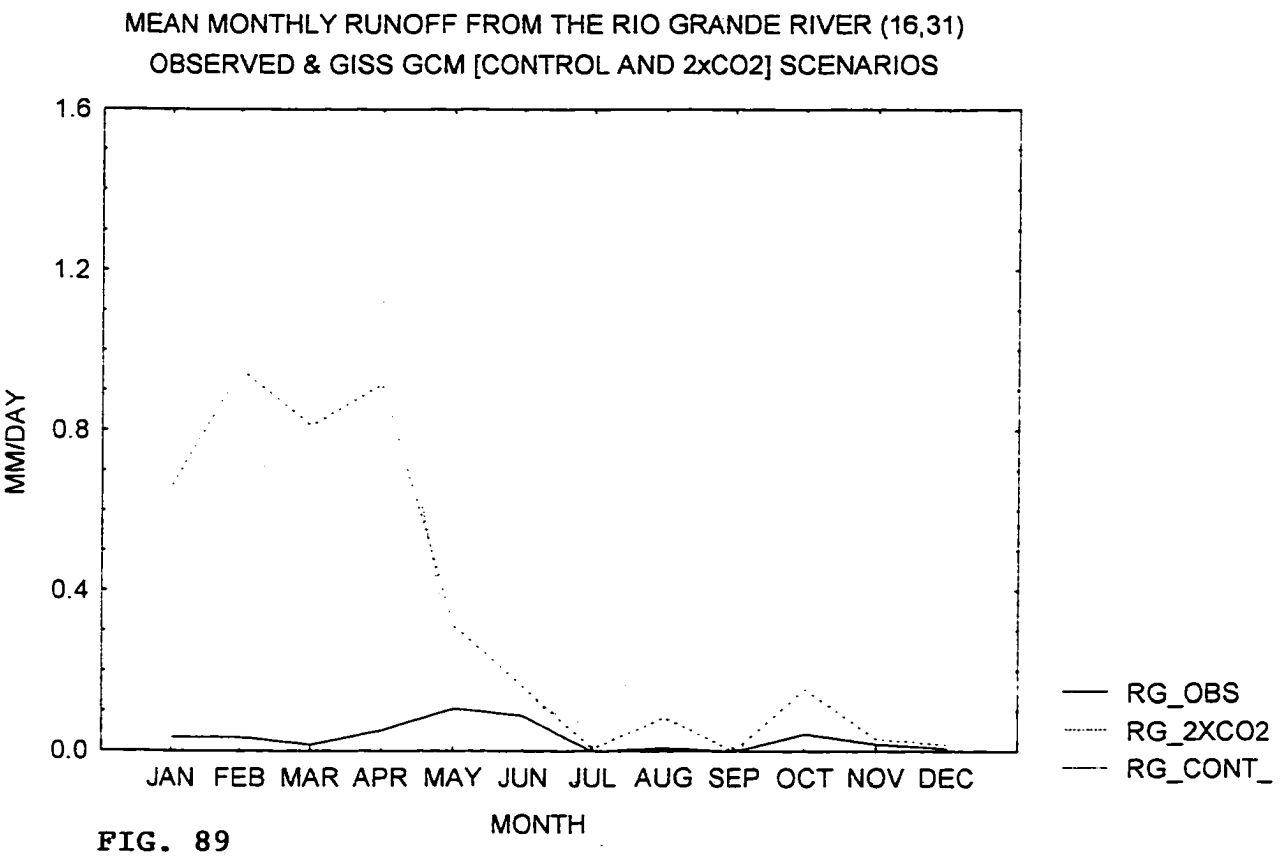

FIG. 89

rainfall sharply declines to its minimum, less than 50% of its $1xCO_2$ amount, by October. Figure 91 highlights the expected results that climate change may have on the hydrologic variables for the Rio Grande as predicted by the karst model. The model's predictions indicate that RO will diminish severly, and the river will become significantly stressed as the atmosphere extracts more water from it and thus depletes its storage.

The no_karst model's predicted changes to these variables for the Rio Grande are shown in Figure 92. This model predicts that on an annual average, RO may only slightly diminish. However, inter-annually, spring RO is expected to decrease, and summer RO, except for August, is expected to increase. As the atmospheric demand for water increases in a warmer climate, so does the Rio Grande's ET. Its projected minimum increase occurs in January, and its maximum increase is expected in December. Storage is predicted to significantly diminish, and it may be about 50% less throughout the year than it would be in a $1xCO_2$ climate.

Figure 93 depicts the GCM's version of how the hydrologic variables may change in a $2xCO_2$ climate. From the figure, the GCM expects increases in Rio Grande's RO except in May, November and December. Peak flows are expected

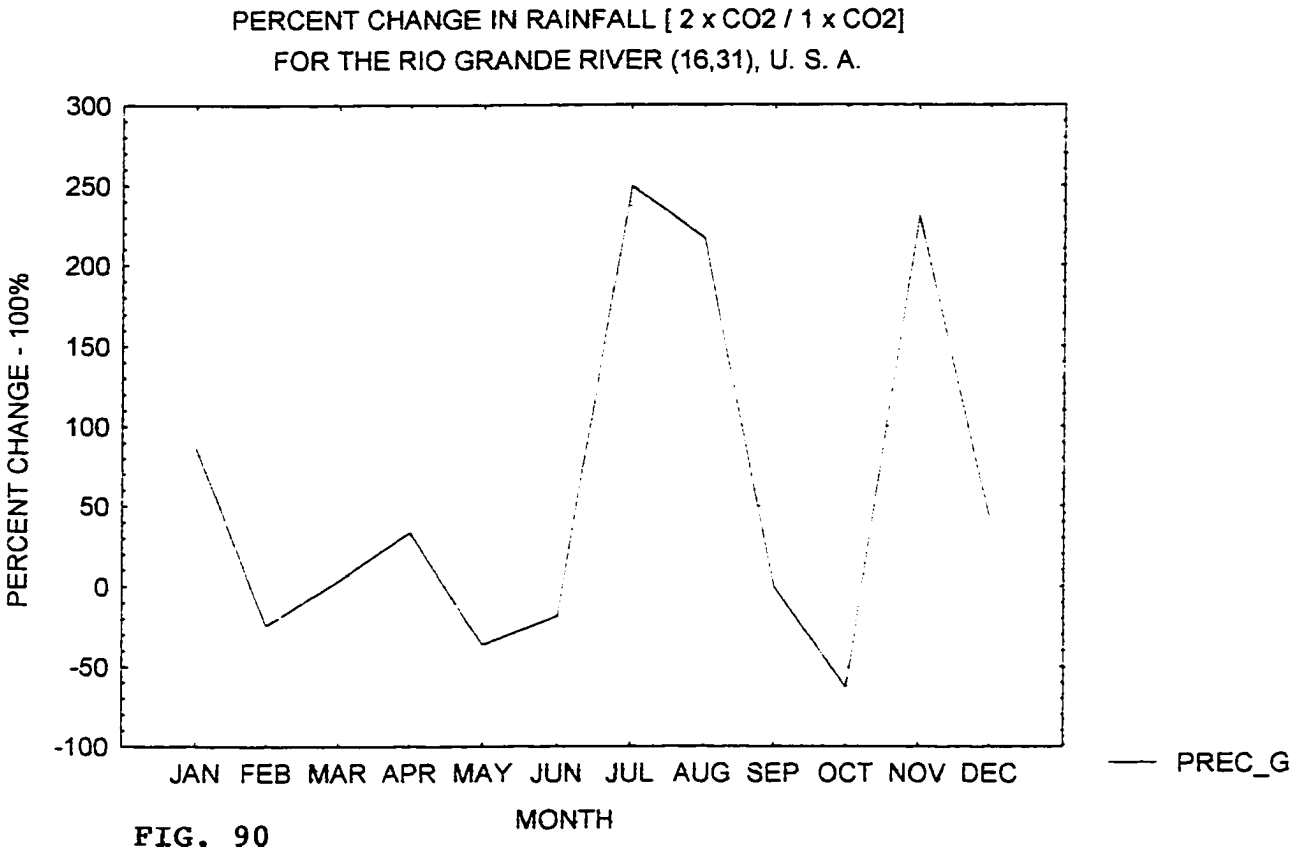

FIG. 90

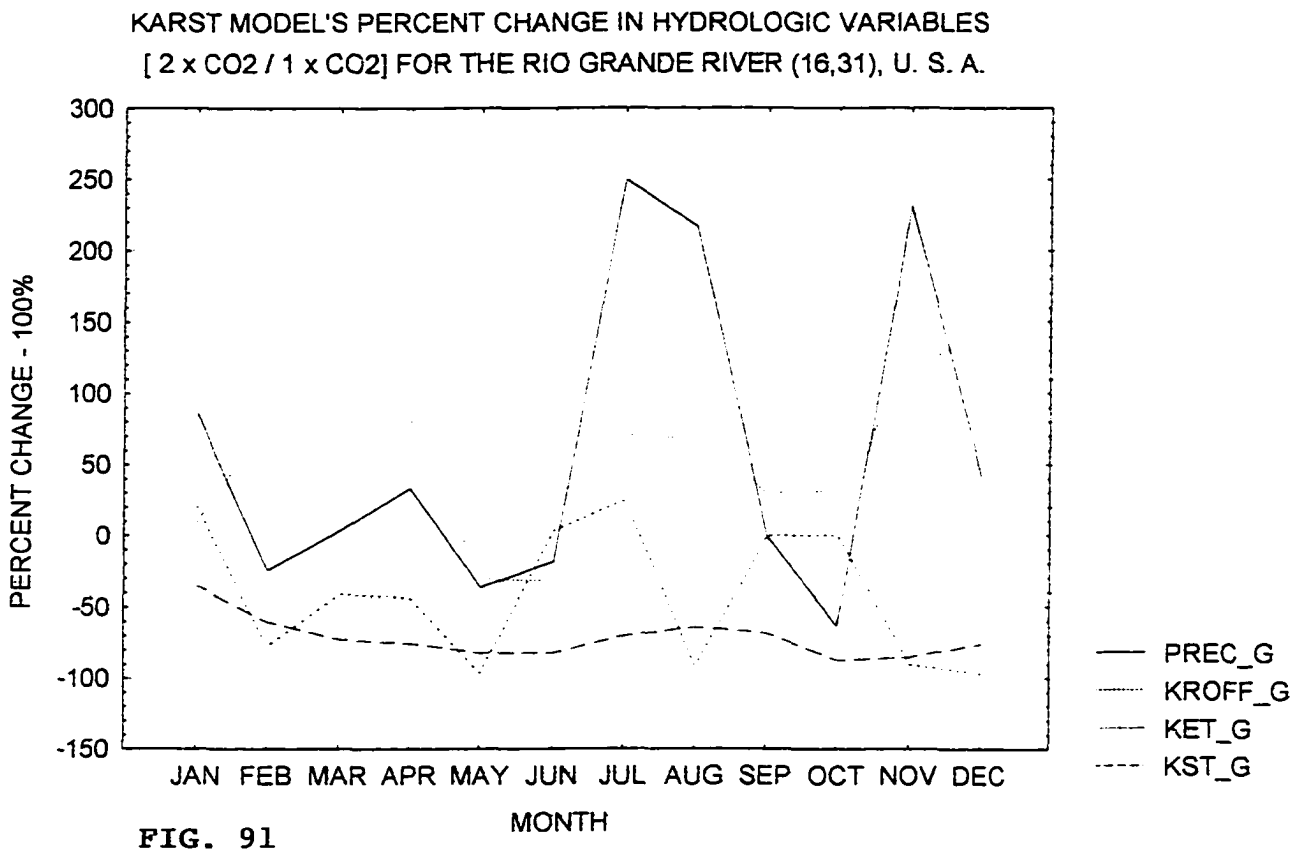

FIG. 91

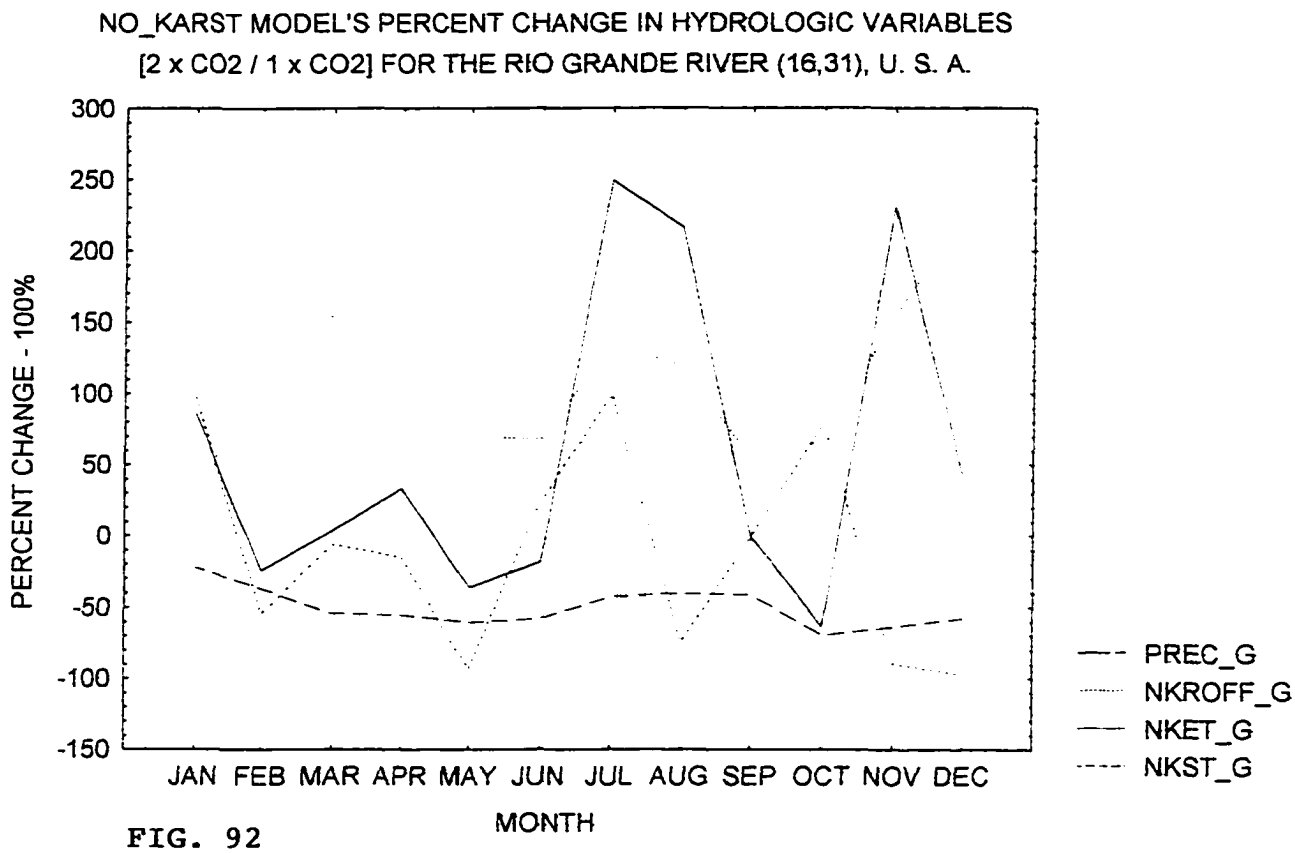

FIG. 92

in July and lowest flows in December. December's low flow coincides with December's maximum ET, and overall minor peaks in ET coincides with minor lows in RO and vice-versa. Evapotranspiration is predicted to increase and moreso in the winter than in the summer. On an annual average, the GCM does not expect much change in the river's soil moisture storage. Inter-annually, though, maximum storage may occur in January when ET is relatively low. In May, both rainfall and runoff decrease more than storage does. In October when rainfall diminishes to less than half its $1xCO_2$ amount, ST exceeds it, and RO is at one of its minor peaks.

Figures 94 - 96 compares the three models' results for probable changes in the water balance components of RO (Figure 94), ET (Figure 95) and ST (Figure 96). In the figures, the karst model is blue, the no_karst model is red, and the GCM is green. The RO comparison shows that the GCM predicts the greatest positive change (an almost 3-fold increase) while the karst model predicts the greatest negative change (a 96% decrease). All three models exhibit the same tendencies in inter-annual variability. They all expect an increased peak flow in July, a minor peak flow in October and low flows in May, August and December.

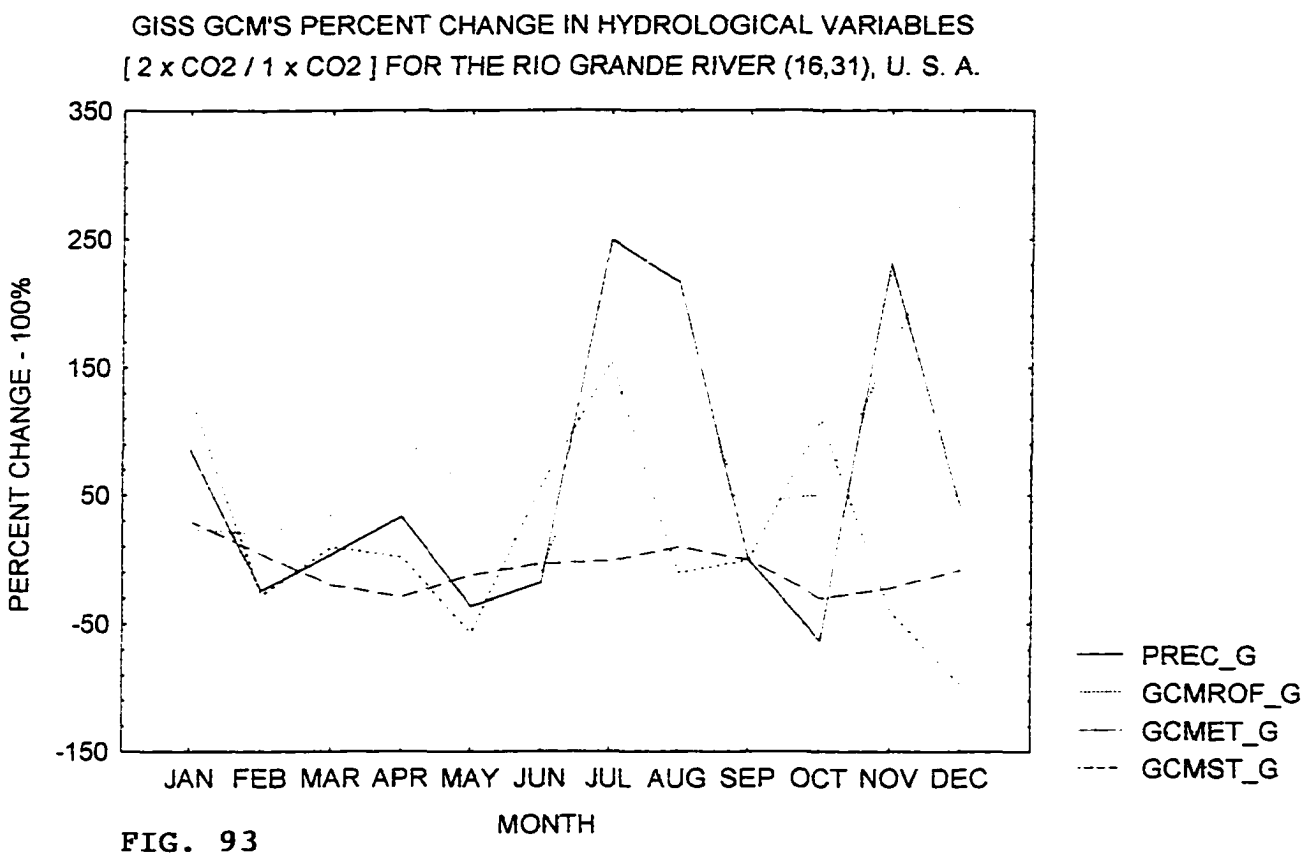

FIG. 93

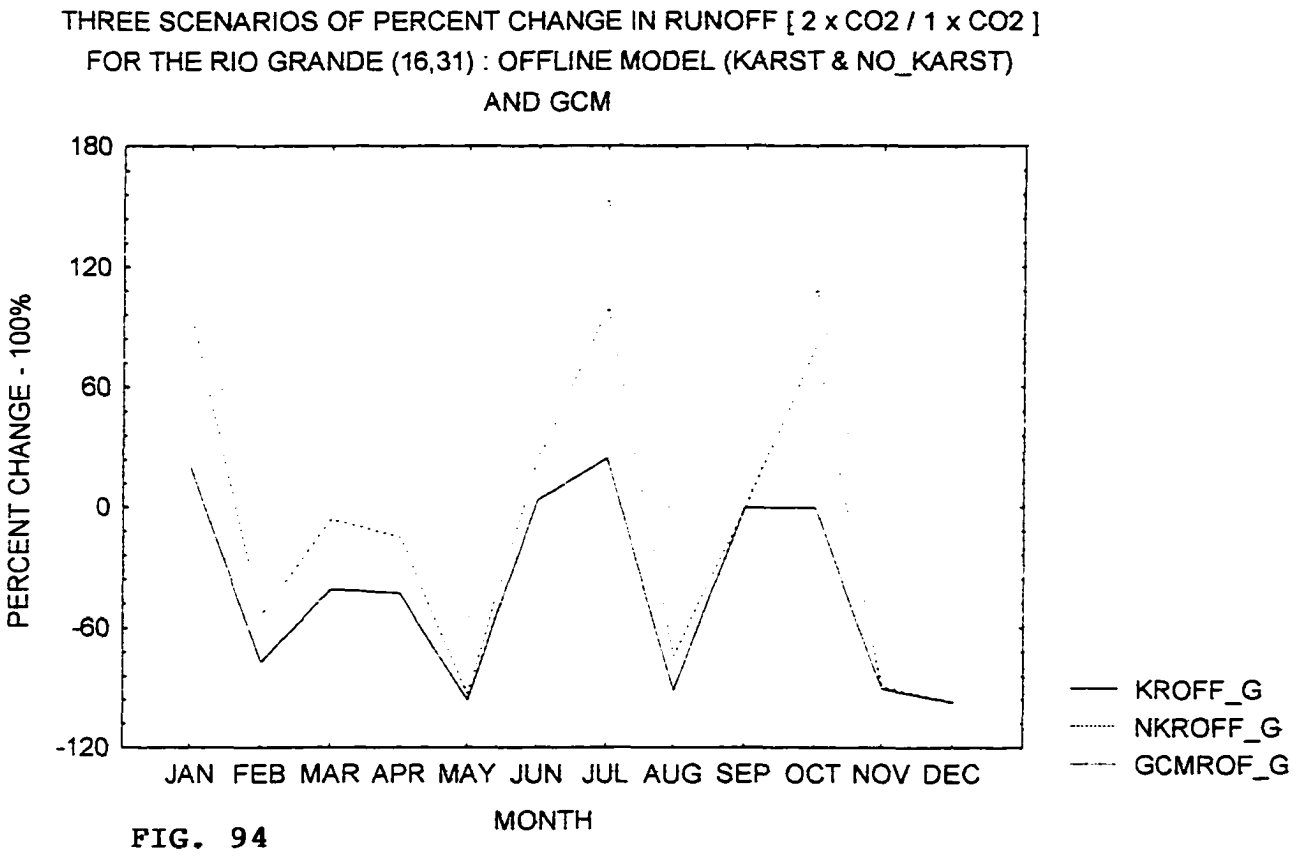

FIG. 94

In general, all three models, with the exception of the karst model in May and June, have ET increasing throughout the year in a warmer climate. For the first half of the year, the no-karst model expects the greatest increases in ET. For the latter half of the year both the GCM and the no_karst model expects similar increases in ET. Throughout most of the spring, the karst model's ET also exceeds the GCM ET. Overall, the karst model expects the least increase in ET, and it even predicts a late spring decrease in ET. The models are inconsistent in their ET predictions.

All models expect substantial depletion of soil moisture. The GCM expects the least depletion while the karst model expects the most depletion. Except for relatively minor storage increases during late winter and mid-summer, the GCM predicts a mean annual storage depletion of about 20%. Both the no_karst and the karst models expects severe storage depletion all year long. Minimum storage depletion of about 68% is predicted by the no_karst model for October while the karst model's minimum storage depletion is about 88% for the same month. The three models, though they disagree on the magnitude of the ST changes, are consistent in their inter-annual direction of change. Overall, therefore, the ST for the Rio Grande is predicted to become severely stresed in a $2xCO_2$ climate.

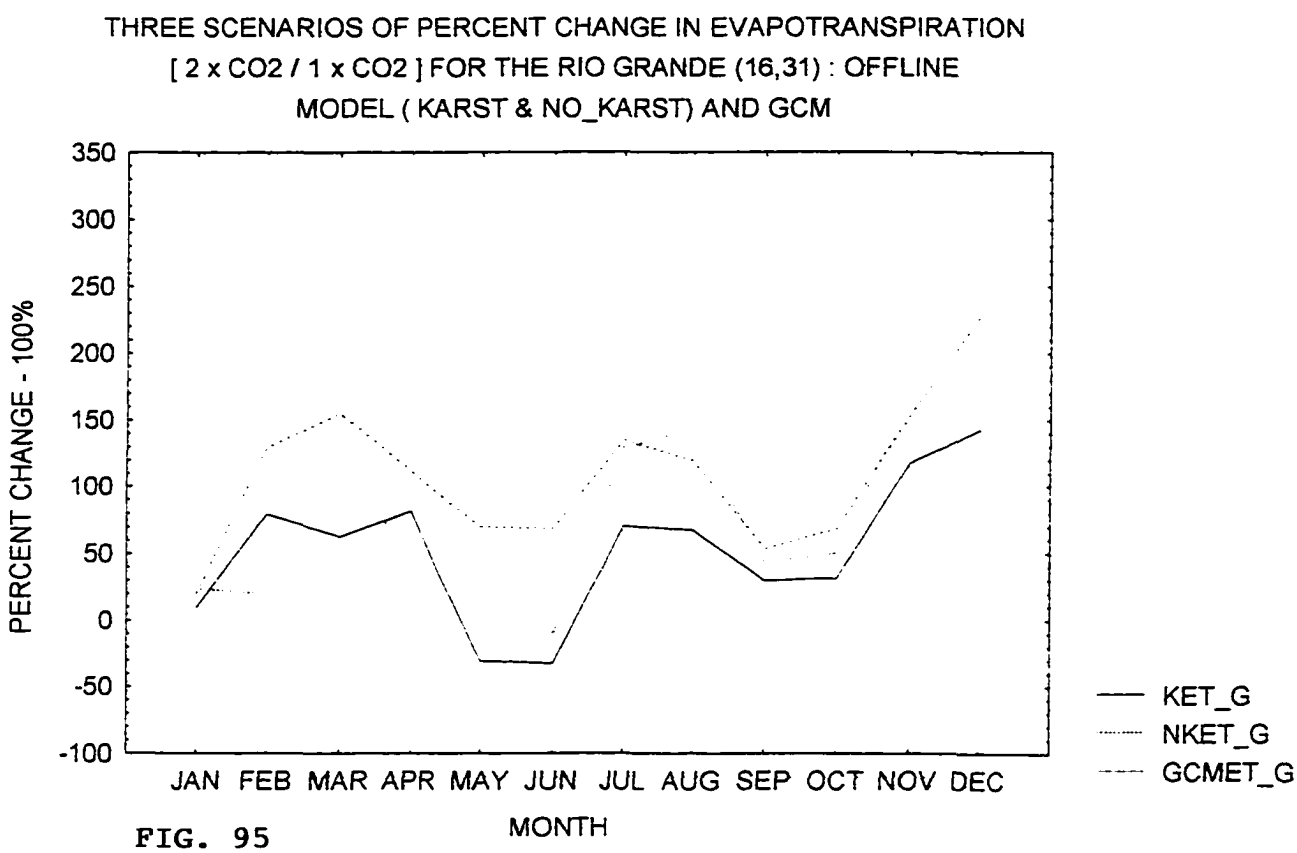

FIG. 95

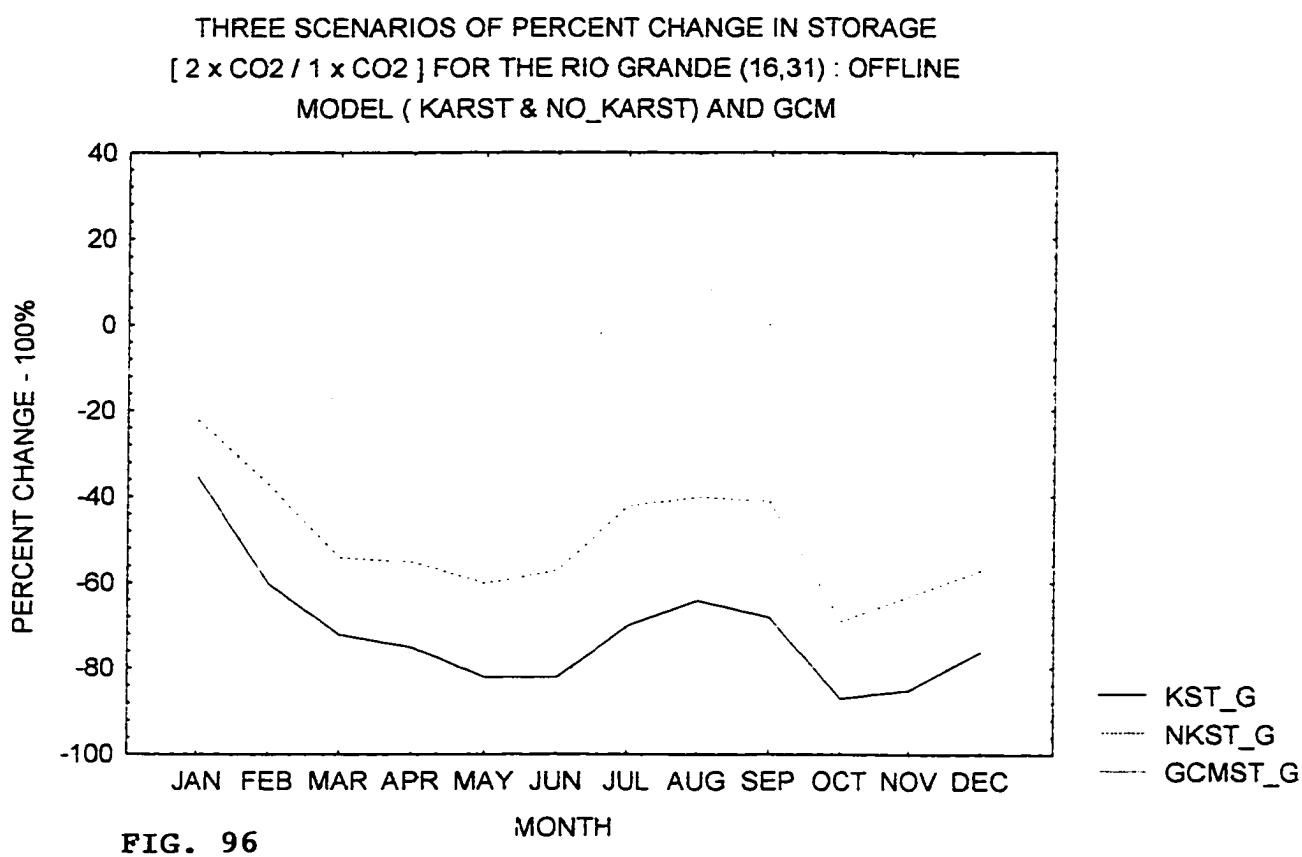

FIG. 96

9. Discussion

In its current form, the off-line version of the GISS land-surface model over-predicts runoff in karstic watersheds. Adding a karst column with pipe flow features to the model improved its simulation of observed autogenic runoff and thus gave more credence to apply the model in climate change experiments for these watersheds. Three karstic watersheds were studied. They are: Rio Cobre (Jamaica), Yangtze (China) and Rio Grande (U.S.A.). The case study was done on the Rio Cobre and then the model with its karst component was extended to the other two watersheds. Climate change analyses indicate that both the Rio Cobre and the Rio Grande may become stressed in a doubled carbon dioxide climate while the Yangtze river, though not losing total volumetric flow, may experience peak flows months later than it currently does. If data from the Yangtze and the Rio Grande were available for sensitivity analyses, both the karst and the no_karst model would do better in simulating the observed streamflow.

From the climate change results presented, the hydrologic variables respond well to precipitation. It may then be, at least in these three regions, that precipitation changes moreso than temperature changes have a greater influence on the future changes in the water balance components.

An all important concern raised by this study centers around the validity of running impact models interactively. If the off-line, no_karst model gave similar results to the GISS GCM, one would then have some confidence to expect that if karst were added to the GCM, then the impact karst has on the no_karst model, namely a reduction of autogenic streamflow, would be the same impact on the GCM. Therefore, one could also reasonably speculate as to the exacerbation or the alleviation of the overall grim streamflow predictions for the Jamaican grid-box offered at the beginning of this study by the other three GCMs [GFDL, CCCM and UKHC] if they too included karst. However, the results are convoluted, and they do not show consistent agreement between the off-line, no_karst model and the GISS GCM. Although, the off-line model is the same land-surface model as in the GISS GCM, neither replicates the other's results consistently. Impact models when run interactively, therefore, seem to give different results. The difference in results may be attributed to the dominance of feedback mechanisms inherent to the interactive model. This point can also be appreciated by noting how much more similar than the GCM predictions are the climate change predictions made by the non-interactive Sacramento Watershed model to those made via the karst and no_karst off-line models. Caution must, therefore, be exercised when results from off-line models

are used to imply climate change impacts.

10. Conclusion/Future Work

Although the model has been improved in its prediction of autogenic runoff, there is room for further improvement. The following recommendations are being made for future work: (a) Use pipe flow features as was done, but do not allow the pipes to break all the soil cover. That is, allow a shallow soil depth to cover some of the pipes. This approach is realistic because not all karst areas are outcrops. A more intricate pipe configuration system consisting of a combination of surface pipes and below surface pipes may indeed improve the model. (b) Develop a better way of applying the karst column to low streamflow. The improved model reduces the streamflow for both high and low rainfall rates. This leads to an under-prediction of low flow. (c) Since the karst landscape is dotted with holes of various irregular shapes, using circular pipes to simulate surface karst flow may not be realistic. Dr. Daniel Hillel (personal communication) suggested that fissured flow may be a more practical approach to the problem. Maloszewski and Zuber (1990), Moreno et al., (1985), Moench (1984) and Tselentis (1985) may provide some guidance along this path. (d) The amount of runoff from a karst landscape depends on the stage of development

of the karst. This developmental stage hinges on the chemical dissolution and geographical location of the karst. One may concievably modify the model's autogenic runoff via a chemical/geographical approach. (e) Similar studies should be done on other karst catchments in Jamaica and throughout the world. The pipe density of 8 pipes/m^2 was used for the three sites in this study. It needs, however, to be tested in other karst regions before generalizations can be made. (f) More than one GCM need to be utilized so as to achieve less biased results and a better range of possible climate scenarios. In addition to these recommendations, other relationships should be used to scale GCM gridbox climate variables down to catchment climate variables.

Finally, as water resources managers grapple with the possible impacts that climate change may have on their precious resource, they ought to keep the following ten mitigation and adaptation stratigies in mind:

1) Support policies that reduce greenhouse gas emissions.

2) Advice farmers to diversify crops and stay away from mono-cropping.

3) Invest in dam and reservoir development.

4) Apply techniques and structures to reduce erosion hazard (dune building, sand bypassing and breakwaters) and thus secure coastlines.

5) Monitor sea-levels.

6) Implement strict land-use guidelines.

7) Commit to measures limiting water waste and pollution.

8) Document and account for known uncertainties in water supply and demand.

9) Adhere to high professional standards in proposing solutions to existing water resource problems.

10) Insist on clear disclosure of factual information, assumptions, and conjectures behind modeling results being considered.

11. Appendix A : Historical Overview of Climate Modeling

Numerical weather prediction is the cradle from which climate modeling emerged. The ultimate goal of theoretical meteorology is to compute as accurately as possible the future state of the atmosphere based on the basic theoretical equations of mass, energy and momentum conservation which govern that state. Great hydrodynamicists and meteorologists like von Helmhotz, V. Bjerknes and L. F. Richardson were among the pioneers who laid the foundation on which the structure of numerical weather prediction was built, (Holton, 1992). Indeed, it was as early as 1910 that Richardson began to contemplate the possibility of using a complete set of hydrodynamic equations for a nonviscous, adiabatic atmosphere to create a numerical weather model. His contemplations led to the publication in 1922 of the classic treatise in the field of numerical weather prediction, *Weather Prediction by Numerical Process*. In this ground-breaking book, Richardson showed that the differential equations governing atmospheric motions can be replaced or approximated by a set of algebraic difference equations for field variables at a finite number of grid points. He further showed that by numerically calculating these algebraic difference equations of the field variables at grid points, one could extrapolate ahead in small increments of time and obtain an estimate of the future field variables.

Unfortunately, as ingenious as Richardson's approach was, his experiments failed.

Three reasons have been suggested for his failure:

1) Poor initial value specifications, especially for upper air observations.

2) Compensation (inadequate accuracy) among terms in the equation of motion.

3) Computational instability due to inappropriate choice of grid and time intervals.

After Richardson's unsuccessful attempt to obtain a reasonable forecast, numerical weather forecasting was not again attempted until after the second World War. With vastly expanded meteorological observation networks came improved initial value specifications, and the advent of digital computers capable of making the enormous arithmetic computations necessary for numerical forecasting gave new life to weather prediction. In 1948, J. G. Charney showed that the problem of compensation that Richardson encountered could be solved by systematically introducing geostrophic and hydrostatic assumptions to the dynamical equations. In so doing, sound and gravity oscillations were filtered out. Two years later, Charney et al., (1950) produced a model which made the first numerical forecast. Although this quasi-geostrophic model only forecasted the geostrophic wind at 500 mb, it paved the way for the more elaborate,

multilevel models with vertical motion fields. Six years later, Phillips (1956) developed a two-layer atmospheric model with global heating and cooling distributed latitudinally. This first true general circulation model was able to simulate the characteristic distribution of the zonal flow with mid-latitude eddies generated by baroclinic instability. Subsequent developments in modeling techniques and computer power propelled GCM advancement. Along with these developments came better understanding and parameterization of the physical processes involved. Smagorinsky (1963) contributed more realistic energy sources and sinks, Mintz (1965) incorporated orographic forcings, Smagorinsky et al., (1965) made advancements in enhancing vertical resolution, planetary boundary layer and stratospheric representations, and Manabe et al., (1965) and Manabe (1969) provided the necessary parameterizations for moist processes.

A general circulation model that treats the sea surface temperature as a specified external influence is not considered to be a full climate model. Only when the atmospheric model is coupled to an interactive ocean model that a full climate model can be produced. Many full climate models have evolved over the last thirty years. They are now sophisticated enough to do, among other things, medium and extended range weather forecasts (e.g., the GCM of ECMWF described in Holton, 1992), to advance research analyzing interactions between

distant meteorological events and the response of regional climate to sea-surface anomalies (e.g., quasi biennial oscillation, El Nino, La Nina) , and to be used as tools to assess the impact of anthropogenic activities on the future climate. Climate models, today, simulate many features of the present and past climate very well as illustrated in GARP (1979) and IPCC (1990).

The increasing numbers of GCMs differ from each other by the way in which they represent subgrid-scale processes, their choice of numerical discretization method (finite differences versus spectral methods), their vertical coordinate system and their spatial resolution. However, despite differences in design, GCMs used for climate change forecasts are consistent in their predictions of a globally warmer climate under various scenarios, IPCC (1990). They all indicate a direct proportionality between an increase in atmospheric greenhouse gas concentrations and an increase in mean global temperature. The main discrepancies between GCMs show up in their regional scale analyses. This highlights the need for higher resolution and for more detailed, consistent parameterizations of the sub-grid scale physical processes.

Research towards obtaining better GCM coupling of the ocean-atmosphere system continues, Han (1988). Work is also in progress to include both the biosphere, Sellers et al., (1988) and the cryosphere, Hibler (1988) in

GCMs as climate dependent systems. Advances in parallel processing has already begun to supply additional computational power and more complete planetary boundary layer representations can only serve to enhance GCM simulations.

12. Appendix B : Physics of the GISS Land-Surface Model

12.1 The GISS Land-surface Model

The GISS land-surface model is a physically based ground hydrology model. It is a one-dimensional model (Figure 97) that conceptualizes the land-surface as having two independent fractions - a vegetated fraction and a bare soil fraction. Within the column, the model realistically parameterizes, among other things, the hydrological processes of sub-grid scale runoff, evapotranspiration, soil moisture movement, infiltration, evaporation from intercepted precipitation and dew, evaporation from bare soil and throughfall. Figure 98 illustrates the processes included in the land-surface model. The model divides the ground beneath both bare and vegetated fractions into six soil layers. The depth of the first ground layer is 10 cm, and the depth to the impermeable, no flux boundary, last layer can be varied. Heat and mass (water) fluxes are governed by linear diffusion along the thermal gradient and Darcian flow, respectively. The surface slope of each gridbox is defined, and it is used to parameterize the sink for subsurface water, as water may leave the gridbox as "pseudo-horizontal" underground runoff. While externally driven by 30-minute meteorological data (short-wave radiation, long-wave radiation, precipitation, temperature, wind, atmospheric pressure and specific humidity), the model's internal time-step is

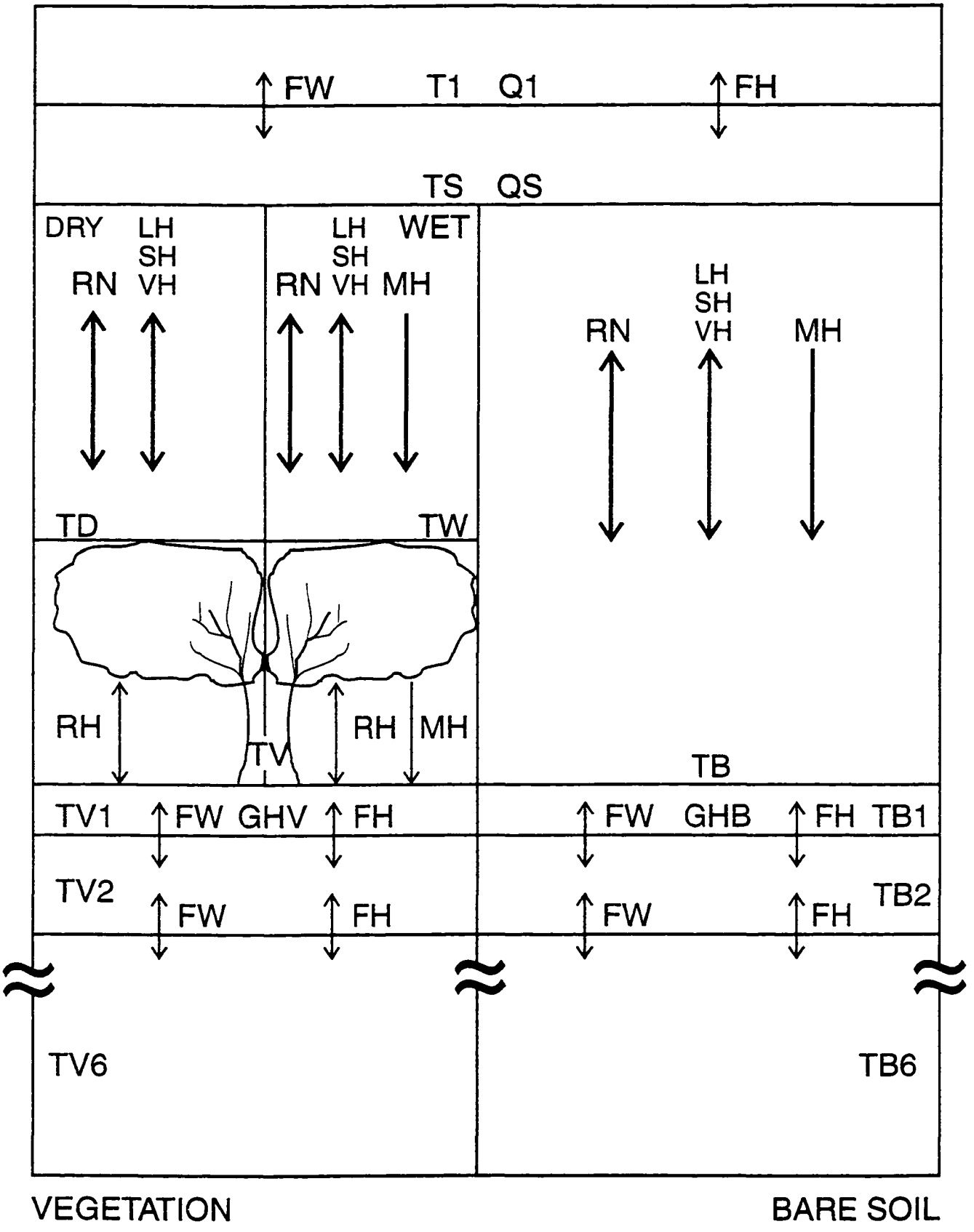

FIG. 97 Fluxes in GISS land-surface model

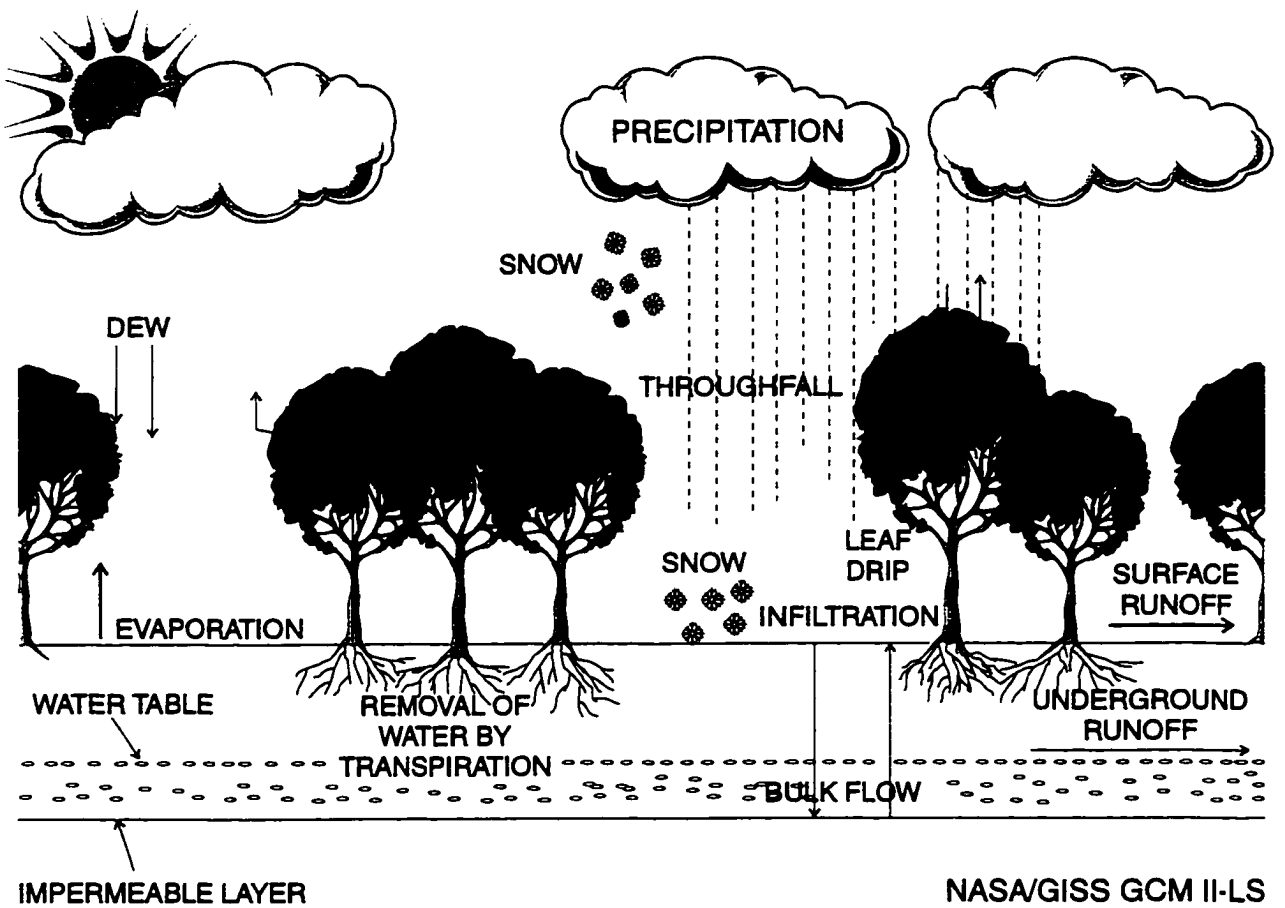

FIG. 98 Modeled processes in GISS land-surface model

determined from the various stability criteria. The model treats the vegetated canopy as a separate layer, and the ground surface is coupled to the lower atmosphere via heat and moisture fluxes.

12.2 Precipitation and Throughfall

Grid box averaged and subgrid-scale precipitation, runoff and throughfall are defined. Precipitation occurs either convectively or due to supersaturation. Within the gridbox, convective precipitation is limited to a fraction, f_p, of the grid box. According to Eltahir and Bras (1993), this fraction varies with geographic location, time of year, and from year-to-year. In the model, f_p is currently set to 10% of the grid box. Supersaturated precipitation is uniformly distributed throughout the grid box. The mean supersaturated precipitation ($\mathcal{P}$) and the mean convective precipitation $\langle P \rangle$ are related as shown below

$$\mathcal{P} = f_p \langle P \rangle \qquad \text{(B1)}$$

Entekhabi and Eagleson (1989) showed that the convective precipitation within f_p can be treated as if it were distributed according to the following exponential probability density function

$$p(P) = \frac{\exp(-P / \langle P \rangle)}{\langle P \rangle} \qquad \text{(B2)}$$

Throughfall, P_v , is precipitation that passes through the vegetative canopy. It is modeled as

$$P_v = \max (0, P - P_c) \tag{B3}$$

Where P_c is a threshold precipitation rate that must be exceeded before throughfall can occur. The model currently uses a threshold precipitation rate of (1×10^{-6} m/s) times the fraction of dry canopy. Similar to the mean runoff within f_p, the mean throughfall within f_p , $\langle P_V \rangle$, is

$$\langle P_V \rangle = \int (P - P_c)\, p(P)\, dP \tag{B4}$$

and the mean gridbox throughfall is related to $\langle P_V \rangle$ by

$$Þ = f_p \langle P_V \rangle \tag{B5}$$

The mean throughfall for the gridbox is, therefore, given by

$$Þ = \mathcal{P} \exp(- f_p P_c / \mathcal{P}) \tag{B6}$$

12.3 Soil and Vegetation

The archived 1° x 1° global soil data files of Zobler (1986) and Webb et al., (1991, 1993) provide the soil units, surface slopes, soil horizon thicknesses and soil textures which are composited to gridbox resolution for the land surface model. Soil textures are given as percentages of sand, loam, clay and peat for each soil horizon and these percentages are assumed to be invariant with depth. Bedrock, if present, is treated as though it were a soil texture. The model divides the soil within a gridbox into six layers. The thickness of the first layer is assumed to be 10 cm and the depth of the last layer is currently set to 3.5 m. Between these layers, the thicknesses of the other layers increase geometrically. Each soil layer is assigned a percent distribution of soil textures.

Matric potential and hydraulic conductivity are calculated for each layer. The general equation for matric potential is

$$H_M(\theta) = \exp(a_{-1} \theta^{-1} + a_0 + a_1 \theta + a_2 \theta^2) \qquad \text{(B7)}$$

while the general equation for hydraulic conductivity is

$$K_W(\theta) = \exp(b_{-1} \theta^{-1} + b_0 + b_1 \theta + b_2 \theta^2) \qquad \text{(B8)}$$

In the above functions, θ is the moisture content, and each texture (sand, loam, clay, peat, bedrock) has its own coefficients (a_i , b_i ; i = -1, 0, 1, 2) . The approach is to first assume a uniform matric potential across all textures within a layer. Since Eqn. (B7) is a monotonic function, it is invertible; so the equation can be rewritten from $H_M(\theta)$ to $\theta(H_M)$. This is done for each texture and then weighted according to the percentage of each texture to give the moisture content of the layer for the assumed uniform matric potential. This moisture content is then compared to the actual moisture content of the layer, since θ is a prognostic variable. The bisection method is used to select a set of H_M from tabular values of matric potential. These H_M values are used in the function $\theta(H_M)$ and the process repeated until $\theta(H_M)$ gives a value equal to the actual moisture content of the layer. Since $K_w(\theta)$ and $\theta(H_M)$, then $K_w(H_M)$. The uniform matric potential is, therefore, then used to calculate the hydraulic conductivity. A similar approach is used to find the diffusivity of the soil layer.

In the land surface model vegetation is represented by leaf area index, minimal stomatal resistance, maximum vegetation height, root density and root depth. Hansen et al. (1983) and Matthews (1983; 1984) provide the parameters for the eight vegetation types used in the model. Table B1 summarizes the vegetation types and their properties. Seven vegetation types are shown in the

table. The bare soil within a gridbox is considered to be the eighth vegetation type.

Table B1. Vegetation types and characteristics[a] specified in GISS land-surface model

	Tundra	Grassland	Shrub	Woodland	Deciduous	Evergreen	Rainforest
Min. LAI[a]	1.0	1.0	1.0	1.0	1.0	8.0	6.0
Max. LAI[b]	1.5	2.0	2.5	4.0	6.0	10.0	8.0
Min. stomatal resist.[c] ($s\ m^{-1}$)	100	100	200	200	200	300	250
Root depth (m)	0.1	1.1	1.5	2.0	2.0	2.0	0.8
Root coefficient a[d]	12.5	0.9	0.8	0.25	0.25	0.25	1.1
Root coefficient b[d]	1.0	0.9	0.4	2.0	2.0	2.0	0.4

[a] Albedo, masking depth, and roughness length are specified as in Hansen et al. (1983). Land-cover fraction is calculated as in Matthews (1984) with the percentage of desert assumed to be equivalent to the percentage of bare soil.
[b] Seasonal leaf area index (LAI) is specified as a sine function between minimum and maximum LAI, with peak LAI occurring on day of year 196.
[c] Functional coefficients relate stomatal resistance to solar radiation and temperature.
[d] For use in the cumulative root distribution function $F(z) = az^b$.

Since vegetation changes with the seasons, a sinusoidal, time varying function is used to simulate the seasonal changes in leaf area index. The sine function is defined by an amplitude, a mean value and a phase. Each vegetation type has its own sine function representation. Tropical vegetation has little dependence on seasonality, except perhaps for a wet and a dry season, and northern hemisphere vegetation has the opposite phase of southern hemisphere

vegetation.

12.4 Soil Water and Soil Heat Fluxes

The land-atmosphere system is intricately coupled. Since soil water distribution and heat fluxes affect evaporation, transpiration, runoff, soil heat transport and heat exchange between land and atmosphere, it is prudent that they be included in any modeling of the land-atmosphere system. Soil water fluxes are governed by Darcy's law

$$F_w(z) = - K_w(z) \frac{dH(z)}{dz} \qquad \text{(B9)}$$

where F_w is the soil water flux (+ve upward); K_w is the hydraulic conductivity; H is the matric potential and gravitation potential; and z is the vertical coordinate with z = 0 at the surface and increasing with depth. In the model, Darcy's equation is represented in its finite difference form with centered differences being used for the hydraulic gradient:

$$F_L = K_L (H_L - H_{L-1}) / (z_L - z_{L-1}) \qquad \text{(B10)}$$

where F_L is the soil water flux across the boundary between layer L and the layer above it, layer L - 1. K_L is the hydraulic conductivity at the boundary between layers L and L - 1. H_L is the total potential (matric plus gravitational) of layer L while z_L is the depth of layer L. In the absence of sink terms, the amount of water in layer L, w_L , depends on the flux into and out of the layer. Noting that the flux is positive in the upward direction, the rate of change of water in layer L is given by

$$\frac{dw_L}{dt} = F_{L+1} - F_L \qquad \text{(B11)}$$

where F_{L+1} is the flux into layer L.

However, since there are sinks, the complete soil water flux equation becomes

$$\frac{dw_L}{dt} = (F_{L+1} - F_L) - \Theta_L - ET_L \qquad \text{(B12)}$$

where Θ_L and ET_L are the sink terms which represent the underground runoff from layer L (a slope and interstream distance dependent term) and the evapotranspiration from layer L respectively. To prevent oversaturation of any

layer, excess water is added to the layer above. To inhibit oversaturation of the first layer, excess water becomes surface runoff.

The boundary condition at the top of the column is a flux into the first layer. This flux is the minimum of the precipitation rate and the infiltration capacity.

$$F_1 = - \min(P_r , I_{max}) \qquad \text{(B13)}$$

where P_r is the precipitation rate and I_{max} is the infiltration capacity.
The bottom boundary is impermeable. Therefore, its boundary condition is

$$F_{L+1} = 0 \qquad \text{(B14)}$$

The transport of heat within the soil includes conduction by linear diffusion along the thermal gradient and convective transport by water infiltrating the surface and water percolating through the soil. These two components of soil heat transfer are represented in the following heat flux equation:

$$F_H(z) = - K_H(z) \frac{dT(z)}{dz} + F_w(z)\, T(z)\, C_w \qquad \text{(B15)}$$

where F_H is the soil heat flux; K_H is the soil thermal conductivity; T is the soil temperature, and C_w is the specific heat capacity of water. The equation is solved in finite difference form similar to the soil water flux equation. There is no heat flux at the bottom boundary, and the land-surface model uses a forward time step.

12.5 Soil Temperature, Ice and Snow

The temperature of a soil layer is derived from the heat in the layer and from the layer's heat capacity. The heat capacity of a soil layer is the volumetric average of the soil, water and air heat capacities. The latent heat of fusion, h_f, is utilized if ice is present in the layer, and the zero reference for heat is liquid water at 0°C. The set of conditions that dictate the temperature of a soil layer is:

$$T_L = \begin{cases} H_L \,/\, (C_L + C_w W_L), & H_L > 0 \\ 0, & -h_f W_L \le H_L \le 0 \\ (H_L + h_f W_L) / (C_L + C_I W_L), & H_L < -h_f W_L \end{cases} \qquad \text{(B16)}$$

where T_L is temperature of layer L; H_L is the heat content of layer L; C_L is the heat capacity of layer L; W_L is the water content of layer L; and C_I is the specific heat capacity of ice.

The fraction of ice in a layer is expressed by the following conditions:

$$I_L / W_L = \begin{cases} -H_L / h_f W_L, & T_L = 0 \\ 1, & T_L < 0 \\ 0, & T_L > 0 \end{cases} \quad \text{(B17)}$$

where I_L is the quantity of ice in layer L. Among other things, the fraction of ice in a layer is used to proportionately reduce the hydraulic conductivity.

When the surface air temperature drops below the freezing mark, precipitation falls as snow upon either or both the canopy and the ground. Incident snow on vegetation masks a fraction of the canopy and prohibits transpiration from that snow-covered fraction. The fraction of canopy masked by snowfall, F_M, is

$$F_M = 1 - \exp(-S \div V_h G_s) \quad \text{(B18)}$$

where S is the water equivalent snow depth; V_h is the vegetation height; and G_s

is the specific gravity of snow.

Therefore, the vegetation height is inversely related to the fraction of canopy masked by snowfall.

In the model, snow is treated only in the first ground layer. The water equivalent snow depth and the heat of snow in the first layer are used to augment the total water content and total heat of that layer. To capture the effect of delayed snow melt at spring time, if layer one has more snow than ice, then the water equivalent difference of these two quantities is added to the effective precipitation for surface runoff calculations and the snow amount is adjusted to be equal to the amount of ice in the layer. This is one method of delaying the snowmelt by melting the ground ice before melting the snow.

Snow in the first layer reduces the heat conductivity of that layer. It insulates the first layer and thus diminish the heat flux between the first and the second layers. An improved snow model component is presently being tested for use in the land-surface model.

12.6 Moisture and Heat Fluxes from the Ground

Moisture and heat fluxes link the lower atmosphere and the canopy to the ground. This coupling is vital to land-surface modeling schemes. The underlying

concept of evaporation or evapotranspiration - depending on the absence or presence of vegetation - is that the actual evaporation or evapotranspiration is some fraction of the atmospheric demand - the potential evaporation or the potential evapotranspiration - for moisture. This concept is formulated as

$$E = \beta E_p \tag{B19}$$

where E is the actual evaporation or evapotranspiration; E_p is the potential evaporation or evapotranspiration; and β is an efficiency factor. In the land-surface model, E_p is parameterized using the aerodynamic approach. Therefore, evaporation from bare soil is represented as

$$F_{qB} = \rho \beta_B C_a (q_B - q_S) \tag{B20}$$

where F_{qB} is the moisture flux (evaporation) from the bare soil portion of the gridbox; q_B is the mixing ratio of saturated air; q_S is the actual mixing ratio of the surface air layer; ρ is the density of the air; C_a is the atmospheric conductance; and β_B is the evaporative efficiency of the bare ground. When β_B is equal to one, equation (B20) represents the aerodynamic potential evaporation. The model

calculates actual evaporation as the minimum of the aerodynamic potential evaporation and the maximum amount of water that can exfiltrate from layer 1 based on the Gardner-Hillel diffusivity limit (Gardner and Hillel, 1962; Hillel, 1975) plus precipitation.

$$F_{qB} = \min [\, \rho\, C_a (q_B - q_S),\ F_{GH} + \bar{P}\,] \qquad \text{(B21)}$$

The Gardner-Hillel diffusivity limit, F_{GH}, is

$$F_{GH} = D_1 \theta_1\, \pi^2 \ / \ 4\, Z_1 \qquad \text{(B22)}$$

where D_1 is the hydraulic diffusivity of layer 1, θ_1 is the relative saturation of layer 1 and Z_1 is the depth to the bottom of layer 1.

Evapotranspiration is modeled as

$$F_{qV} = \rho\, \beta_V C_a (q_C - q_S) \qquad \text{(B23)}$$

where F_{qV} is the moisture flux (evapotranspiration) from the vegetated portion of the gridbox; q_C is the mixing ratio of saturated air at the canopy; and β_V is the

evapotranspirative efficiency of the canopy. When β_V is equal to one, the canopy is wet and equation (B23) represents the aerodynamic potential evaporation. Dry portions of the canopy transpire in accordance to the canopy conductance, C_C , and the atmospheric conductance C_a .

The model's actual evapotranspiration is the minimum of the potential rate of canopy evaporation and a transpirational modifier to that potential rate. This is expressed in the following equation

$$F_{qV} = \min[\ \rho C_a(q_C - q_S),\ (\ f_W + \{f_D \div 1 + C_a / C_C\}\ )\ \rho C_a(q_C - q_S)\ ] \qquad \text{(B24)}$$

where the canopy conductance is given by

$$C_C = (\ \beta_D L_{eff} \div r_s)(\ I \div \{I + C_1\}\ )(\ \{\ T_C - C_2\ \} \div C_3\ ) \qquad \text{(B25)}$$

When the canopy is wet, plant stomata close and canopy conductance ceases. The model, therefore, uses a canopy reservoir, equation (B28), which can be filled to varying degrees and which evaporates at the potential rate.

L_{eff} is the effective leaf area index. It is the projected area of actively evaporating leaves per unit area of ground, and it is parameterized as a function of both the leaf area index, LAI, and the maximum value of L_{eff} , L_C. Jarvis et.al,

(1986) argues that this parameterization (scaling) is highly approximate. Effective leaf area indices generally range from 1 to 5 in vegetated regions. The effective leaf area index is given as

$$L_{eff}=L_C(1-e^{L/L_C}) \tag{B26}$$

The minimal stomatal resistance r_s, is a function of solar radiation, temperature, soil moisture and humidity. I is the incident solar radiation, T_C is the canopy temperature, and C_1, C_2, C_3 are parameters specified as 90 W/ m^2, 23 °C and 15 °C, respectively. β_D is the soil water availability factor. It depends on the matric potential in the soil, H(z), the wilting point, H_w, and the root density $F_r(z)$. It is specified as

$$\beta_D = [\int F_r(z) \max (\{H_w - H(z)\} / H_w, 0) \, dz] / \int F_r(z) \, dz \tag{B27}$$

As previously mentioned, Deardorff (1978) showed that the fraction of the canopy which is wet, f_W, can be represented as

$$f_W = (W_C / W_{CS})^{2/3} \tag{B28}$$

where W_C is water in the canopy (dew plus intercepted precipitation) and W_{CS} is the saturated water in the canopy, or the canopy water-holding capacity, which is assumed to be 10^{-4} m x LAI. The fractions of wet and dry canopy (f_W and f_D) sum to unity.

In the moisture flux equations, both the potential evaporation and the potential evapotranspiration are controlled by a gradient in mixing ratio. In both equations (B20) and (B23), the atmospheric conductance, C_a, is the product of the wind velocity at the surface (a reference height of about 30m) and a term representing the turbulent mixing coefficient for moisture. C_a is thus a function of the surface roughness length; it increases with increasing vegetation height. Therefore, taller ecosystems have greater atmospheric conductances than shorter ones for the same wind speed. However, for the same wind, the overall conductive efficiency, $C_c / (C_c + C_a)$, is greater for shorter ecosystems than for taller ones.

Temperature is implicitly represented in these equations ((B20) and (B23)) since

$$q_B = q_{sat}(T_B) \tag{B29}$$

$$q_C = q_{sat}(T_C) \tag{B30}$$

Temperature also plays a role in turbulent mixing. Turbulent mixing depends on atmospheric stability. Whenever T_B or T_C is greater than the temperature of the surface, T_S, the air is unstable, and warm air rises, enhancing mixing. In a stable air mass, T_B and $T_C < T_S$. This prohibits rising air and mixing. Therefore, both moisture flux equations are strongly dependent on the temperature gradient.

The sensible heat flux from both bare and vegetated soil is formulated via the aerodynamic approach. The sensible heat flux from bare soil is given as

$$F_{hB} = C_P \rho C_a (T_B - T_S) \qquad \text{(B31)}$$

while the sensible heat flux from the vegetated soil is

$$F_{hV} = C_P \rho C_a (T_c - T_S) \qquad \text{(B32)}$$

In these equations, C_P is the specific heat capacity of air at constant pressure.

12.7 Moisture and Heat Fluxes from the Surface

Both the moisture and heat fluxes from the surface layer into the first layer

of the atmosphere are calculated as in Hansen et al. (1983). The moisture flux is calculated as

$$F_{ql} = \rho K (q_S - q_1) / (Z_1 - Z_S) \quad \text{(B33)}$$

while the heat flux is calculated as

$$F_{hl} = C_P \rho K (T_S - T_1) / (Z_1 - Z_S) \quad \text{(B34)}$$

where K is the eddy diffusion coefficient and q_1 , T_1 and Z_1 are the mixing ratio, the temperature and the height of the first atmospheric layer, respectively, and Z_S is the height of the surface layer.

12.8 Moisture Flux Balance at the Surface

The surface layer of the model, which is currently set to 30m, has zero thickness and thus zero storage capacity. No mass accumulates at this layer. Whatever mass enters must be equal to the mass that leaves. Therefore, the moisture flux from the ground to the surface layer must be the same moisture flux that leaves the surface layer to the first atmospheric layer. The moisture flux

from the ground to the surface is the area weighted sum of the moisture fluxes from the bare and vegetated soil. The moisture flux from the ground is, therefore

$$F_{ql} = f_B F_{qB} + f_V F_{qV} \qquad \text{(B35)}$$

where f_B and f_V are the bare and vegetated fractions of the grid box and

$$f_B + f_V = 1. \qquad \text{(B36)}$$

The bare soil and vegetated fractions of the gridbox are f_B and f_V respectively. Combining equations (B20), (B23) and (B33) gives the following equation which represents the moisture flux balance at the surface

$$f_B \beta_B C_a (q_B - q_S) + f_V \beta_V C_a (q_C - q_S) = K (q_S - q_1) / (Z_1 - Z_S) \qquad \text{(B37)}$$

This equation can be rewritten as

$$q_S = \frac{f_B \beta_B C_a q_B + f_V \beta_V C_a q_C + K q_1 \div (Z_1 - Z_S)}{f_B \beta_B C_a + f_V \beta_V C_a + K \div (Z_1 - Z_S)} . \quad \text{(B38)}$$

Note that since β_B and β_V are functions of q_S, equation (B38) must be solved iteratively.

12.9 Heat Flux Balance at the Surface

As with moisture flux balance at the surface, the heat flux from the ground to the surface layer must be the same heat flux that leaves the surface layer to the first atmospheric layer. The heat flux from the ground to the surface is the area weighted sum of the heat fluxes from the bare and vegetated soil. The heat flux from the ground is, therefore,

$$F_{hl} = f_B F_{hB} + f_V F_{hV} \quad \text{(B39)}$$

Combining equations (B31), (B32) and (B34) yields the following equation for the heat flux balance at the surface

$$C_a (f_B T_B + f_V T_C - T_S) = K (T_S - T_1) / (Z_1 - Z_S) \quad \text{(B40)}$$

Since the ground temperature (T_G) is the area-weighted sum of the bare soil and the canopy temperatures, it can be written as

$$T_G = f_B T_B + f_V T_C \qquad \text{(B41)}$$

Equation (B40) thus becomes

$$C_a (T_G - T_S) = K (T_S - T_1) / (Z_1 - Z_S) \qquad \text{(B42)}$$

Unlike equation (B38) which has two different efficiency factors, this equation is simpler since it has only a single heat transfer coefficient for the entire gridbox.

12.10 Radiation

The net radiation over bare soil (R_{nB}) has three components: the ground's emitted longwave radiation, the absorbed, incoming, shortwave radiation and the downward longwave radiation. Equation (B43) shows the relationship between the net radiation and its components,

$$R_{nB} = - \delta T_B^4 + (1 - a_B) I + R_D \qquad \text{(B43)}$$

where δ is the Stefan-Boltzmann constant; a_B is the bare soil albedo; I is the incoming solar radiation and R_D is the downward longwave radiation.

Radiation exchange occurs between the ground beneath the canopy and the canopy itself. The net radiation from this exchange (R_{nV}) can be expressed as

$$R_{nV} = -\delta T_V^4 + \delta T_C^4 \qquad \text{(B44)}$$

The net radiation of the canopy is

$$R_{nC} = \delta T_V^4 - 2\delta T_C^4 + (1 - a_C) I + R_D \qquad \text{(B45)}$$

where T_V is the temperature of soil beneath the canopy; R_{nC} is the net radiation of the canopy and a_C is the albedo of the canopy.

12.11 Canopy Energy Balance

In the model, the canopy is treated as a layer unto itself. It has heat fluxes and a temperature. Canopy heat (H_C) changes with time as the sum of all the heat fluxes into the canopy

$$\frac{dH_C}{dt} = R_{nc} - F_{hV} - \lambda F_{qV} + F_{hP} - F_{hD} \qquad \text{(B46)}$$

where λ is the latent heat of vaporization; F_{hP} is the heat flux carried by precipitation and F_{hD} is the heat flux carried off by throughfall.

The canopy's temperature is given as

$$T_C = \begin{cases} H_C \,/\, (C_D + C_w W_C), & H_C > 0 \\ 0, & -h_f W_C \le H_C \le 0 \\ (H_C + h_f W_C)\,/\,(C_D + C_I W_C), & H_C < -h_f W_C \end{cases} \qquad \text{(B47)}$$

where W_C is the water on the canopy; C_D is the heat capacity of the dry canopy and

$$C_D = C_W (b_0 + b_1 \bar{L} + b_2 \bar{L}^2) \qquad \text{(B48)}$$

where $\bar{L}$ is the time average of the leaf area index, b_0, b_1 and b_2 are constants with dimensions of length.

12.12 Method of Solution

Since canopy heat is a prognostic variable, equations (B47) and (B41) are

used to obtain T_G at the beginning of the time step. This value of T_G is then used with the atmospheric layer 1 quantities of equation (B42) to solve for T_S. The mixing ratio at the surface, q_S , can then be obtained from equations (B38), (B21) and (B24). Finally all the fluxes are determined from the equations given in the above sections.

13. Appendix C : Karst Geomorphology

13.1 Karst Rocks

An abundance of karst rocks exist globally. Karst rocks/landforms with thicknesses of several kilometers and volumes of thousands of cubic kilometers are common. They continue to form in temperate and tropical seas on deep oceanic slopes and floors, and they are known to exist from strata as old as 3.3 billion years (Blatt et al., 1980). About one-fourth of the earth's domestic water supply is obtained from these rocks, and half the known petroleum and natural gas reserves are in karst areas (Ford and Williams, 1989). Karst rocks have additional economic value, for they supply bauxite, silver, lead, zinc, agricultural lime, cement, fine building stones and aggregate.

In order for a rock to be considered karstic by the stricter definition, at least 50% of it (by weight) must be comprised of calcium carbonate ($CaCO_3$). The greater the calcium carbonate composition of the rock, the purer a karst rock it is. The following are the most common karst rocks: limestone (the most significant karst rock), reef facies, dolomite and evaporites.

13.2 Karst Dissolution Process and Rate of Denudation

White (1988) capsulates the degradation of karst rocks/landforms in the following words: " Karstification is a process of destruction, and it runs on a one way track from the time the limestone is first exposed to weathering until the last of it disappears down the river." When karst dissolves, its constituent minerals disintegrate into individual ions or molecules which then diffuse into solution. Calcium carbonate dissolves as

$$CaCO_{3\ (solid)} \rightleftharpoons Ca^{2+} + CO_3^{2-} \qquad (C1)$$

but is only modestly soluble in pure water. Smith and Mead (1962), Gross (1964), Roques (1969) and Pitty (1966) have shown that the observed, greatly enhanced solubility of calcium carbonate is caused by carbonic acid - the source of which is atmospheric CO_2 . Carbon dioxide is one of the most soluble atmospheric gases. It, for example, is 64 times more soluble than N_2. According to Henry's Law, the solubility of CO_2 is directly proportional to its partial pressure and inversely proportional to temperature as shown in Figure 99.

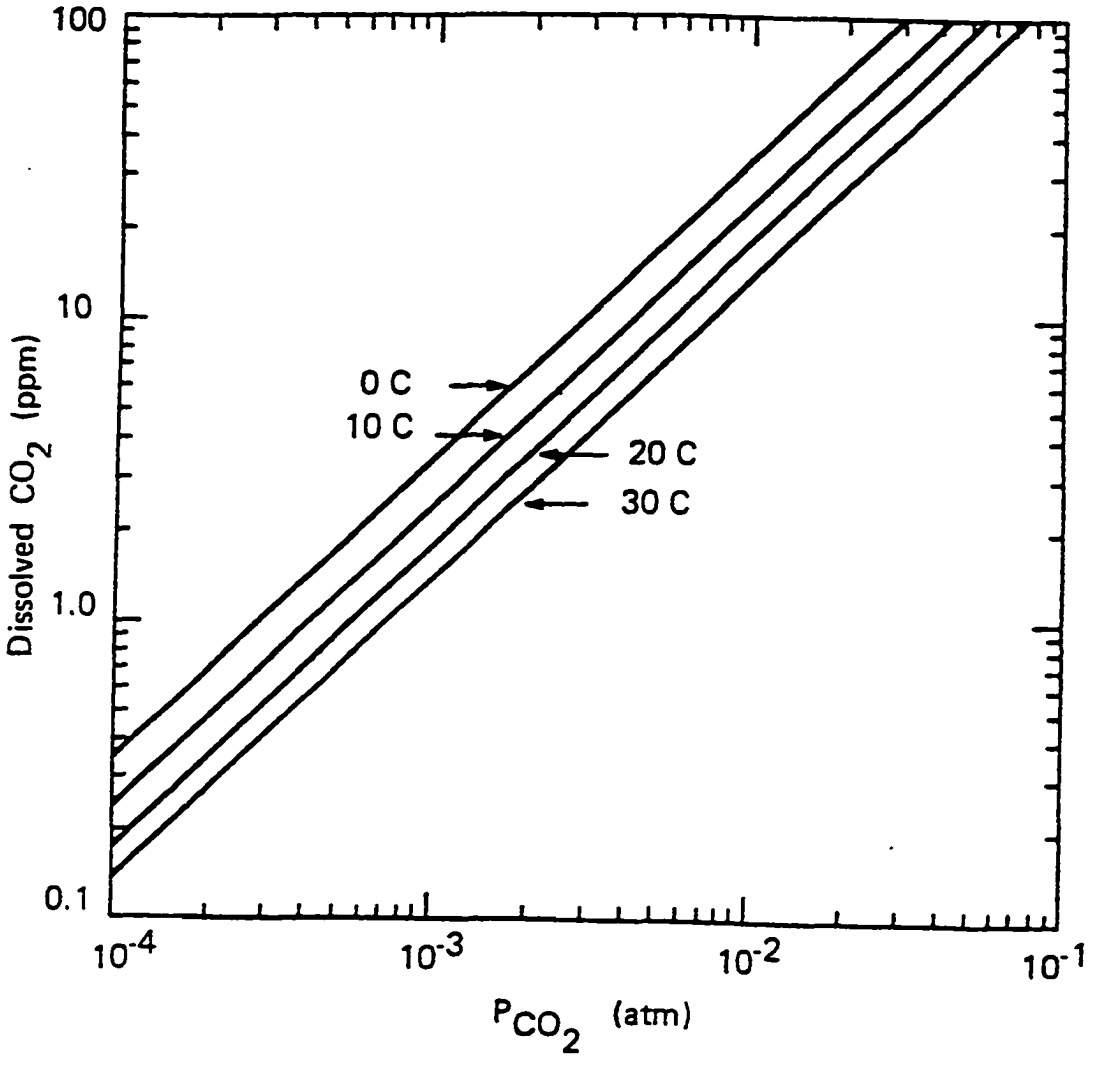

FIG. 99 Solubility of carbon dioxide as a function of the CO_2 partial pressure in the coexisting gas phase.

The partial pressure of a gas is its contribution to the total pressure exerted by a mixture of gases. Henry's Law for the dissolution of CO_2 in water can be written as

$$CO_{2\ (aqueous)} = C_{ab} \times P_{CO2} \times 1.963 \qquad (C2)$$

where CO_2 is in grams/liter, $_{ab}C$ is a temperature-dependent absorption coefficient, P_{CO2} is the partial pressure of CO_2 and 1.963 is the weight in grams of one liter of CO_2 at a pressure of one atmosphere at 20°C.

Thus,

$$CO_{2\ (gas)} \rightleftharpoons CO_{2\ (aqueous)} \qquad (C3)$$

$$CO_{2\ (aqueous)} + H_2O \rightleftharpoons \underset{\text{(carbonic acid)}}{H_2CO_3} \qquad (C4)$$

The complete process of karst dissolution may, therefore, be represented as

$$CaCO_3 + CO_2 + H_2O \rightleftharpoons Ca^{2+} + 2HCO_3^- \qquad (C5)$$

Figure (100) illustrates the dependence of karst dissolution on both the partial pressure of CO_2 and temperature. If saturated water at 250 mg/l $CaCO_3$ and 50 mg/l CO_2 is cooled (direction **C**), it can dissolve more karst; if it is warmed (direction **W**), it precipitates $CaCO_3$; if it comes in contact with air with less CO_2 (direction **L**), the CO_2 gradient robs the solution of CO_2 and forces the precipitation of $CaCO_3$; if it encounters air with more CO_2 (direction **H**), the CO_2 gradient adds CO_2 to the solution and more $CaCO_3$ is dissolved.

Karst denudation is as much a mechanical erosional process as it is a chemical one. In practice, however, karst geomorphologists have found it much easier to estimate chemical than mechanical erosion. Thus, mechanical erosion is generally ignored. This crucial omission, according to Ford and Williams (1989), may be the Achilles' heel in karst process research. Chemical erosion or solutional denudation, of karst is measured in millimeters per thousand years ($mm\ ka^{-1}$). Deductions about karst denudation via this rate can only, therefore, be strictly tenable if environmental conditions remain constant over the period. Corbel (1959a) was the first karst researcher to parameterize solutional denudation rates for karst. His well-known equation is

$$KD = 0.04(E \times T) \qquad (C6)$$

where KD (mm ka^{-1}) is the karst denudation, E is precipitation in decimeters and T (mg/l) is the mean $CaCO_3$ content. Since Corbel's equation assumes a constant limestone density of 2.5 g cm^{-3}, and since it does not consider runoff from non-karst rocks, Pulina (1972) suggested the revised equation (C7) as a more appropriate parameterization for karst denudation

$$KD = 12.6 (T - T_a) Q A^{-1} \qquad (C7)$$

where T (mg/l) is the carbonate hardness, T_a (mg/l) is the hardness carried into the basin from nonkarstic rocks, Q is the mean discharge, and A is the basin area. White (1984) went further and developed a theoretical expression for karst denudation that linked karst chemistry to environmental factors

$$KD = 100 \rho^{-1} (4 K_2)^{-1/3} (K_c K_1 K_{CO2} P_{CO2})^{1/3} (P - E) \qquad (C8)$$

where ρ is the density of the karst rock ; K_2, K_c, K_1 and K_{CO2} are, respectively, solubility constants for bicarbonate, calcite, carbonic acid and carbon dioxide; P is precipitation and E is evapotranspiration (both in mm/yr).

Based on equation (C8), White (1984) was able to deduce the following

general characteristics of karst denudation. First, karst denudation varies linearly with precipitation. Second, karst denudation is directly proportional to the cube root of the partial pressure of CO_2. This implies that since vegetated soils are richer than bare soils in CO_2 content, the more vegetated tropical and temperate climatic zones have higher karst denudation rates than the arctic/alpine climatic zone. Denudation rates in the arctic/alpine climatic zone may also be inhibited by low precipitation. There is not much distinction between temperate and tropical denudation rates. Third, although the solubility of CO_2 increases as temperature decreases, the implicit temperature dependence of the four solubility constants is such that the other three climatic variables (precipitation, evapotranspiration and the partial pressure of carbon dioxide) dominate the karst denudation process more than temperature. These deductions from equation (C8) are embodied in Figure 101.

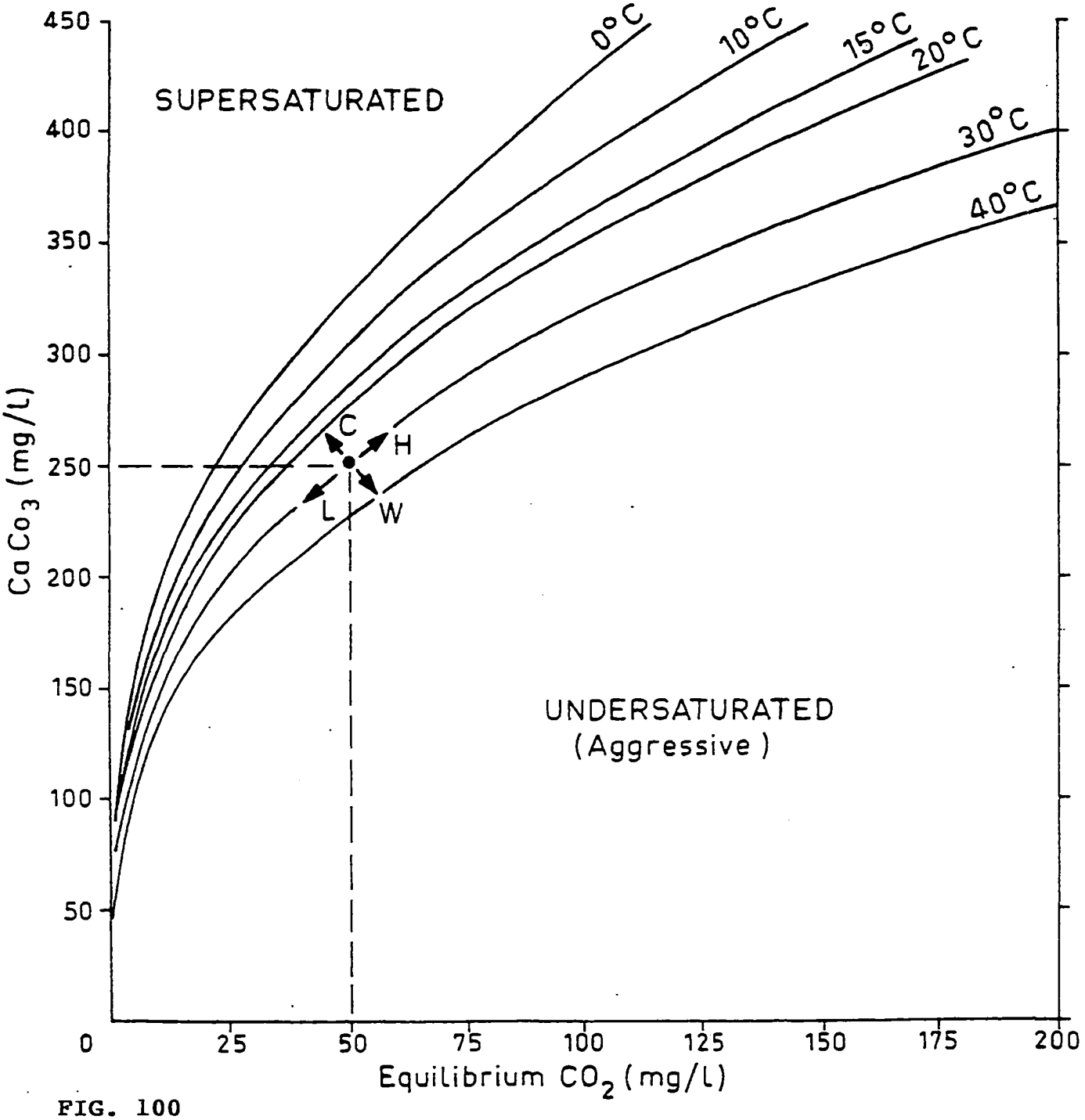

FIG. 100

Saturation equilibrium curves for solution of calcium carbonate at different temperatures as a function of equilibrium carbon dioxide in solution. After Trombe 1952.

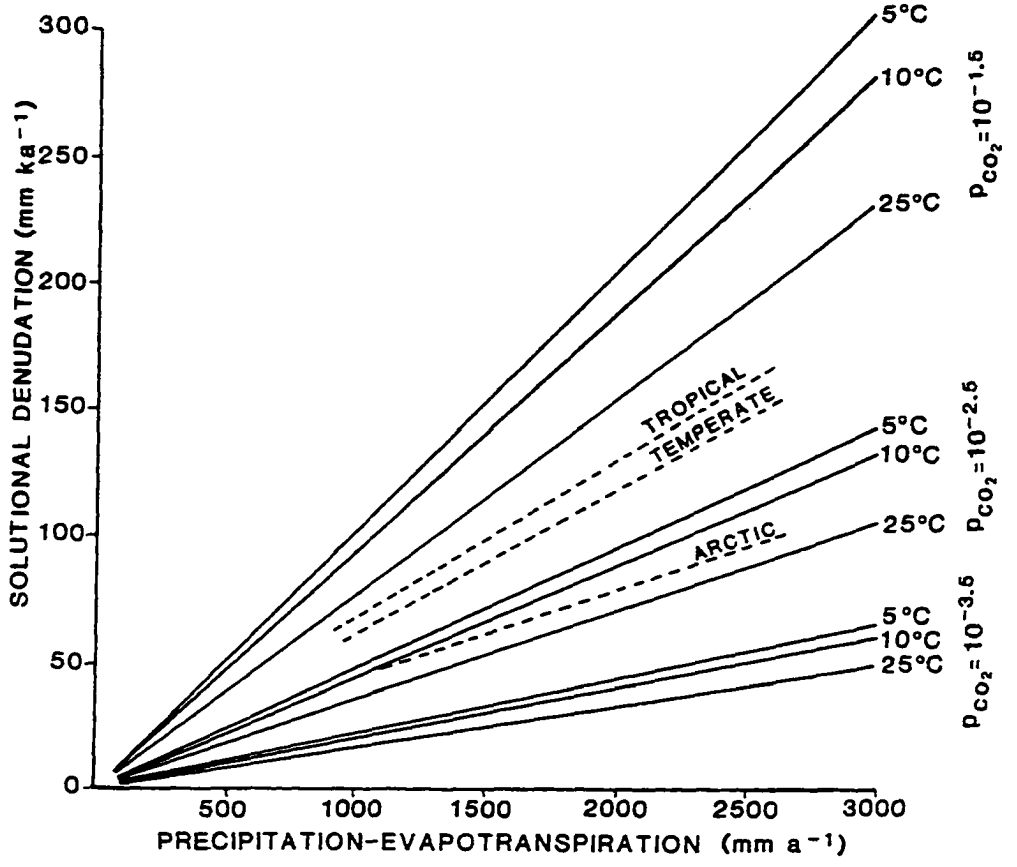

FIG. 101 Theoretical relationships of solutional denudation of limestone to water surplus and CO_2 availability under coincident conditions from White (1984) with empirical relationships derived by Smith & Atkinson (1976) superimposed as dashed lines.

14. References

Abramopoulos, F., C. Rosenzweig, B. Choudhury, 1988: Improved ground hydrology calculations for global climate models (GCMs): Soil water movement and evapotranspiration. *J. Climate*, **1**, 921-941.

Barnes, G. W., 1973: Water Quality Simulation Utilizing a Generalized Streamflow Simulation Model. Master of Science project, California State University, Sacramento.

Blatt, H. G., V. Middleton, R. Murray, 1980: *Origin of sedimentary rocks* 2nd edn. New Jersey: Prentice-Hall Inc.

Burnash, R. J. C., R. L. Ferral, R. A. McGuire, 1973: A Generalized Streamflow Simulation System - Conceptual Modeling for Digital Computers. U. S. Department of Commerce, National Weather Service and State of California, Department of Water Resources.

Carson, D. J., 1986: An introduction to the parametrization of land-surface processes. *Dynamical Climatology Tech.* Note, No. 45, Meteorological Office, METO20, Bracknell, U. K.,.

Cess, R. D., 1990: Intercomparison and interpretation of climate feedback processes in 19 general circulation models. *J. Geophys. Res.*, **95**: 16601-16615.

Charney, J. G., R. Fjortoft, J. VonNeumann, 1950: Integration of the Barotropic Vorticity Equation. *Tellus*, 2(4): 237-254.

Clapp, R. B., G. M. Hornberger, 1978: Empirical equations for some soil hydraulic properties. *Water Resour. Res.*, **14**, 601-604.

Cogley, J. G., A. J. Pitman, A. Henderson-Sellers, 1990: A land-surface for large scale climate models. Trent University Technical Note 90-1, Department of Geography, Trent University, Peterborough, Ontario, Canada, 120pp.

Corbel, J., 1959a: Erosion in karst terrain. *Ann. Geograph.* **68**, 97-120.

Cowan, I. R., 1965: Transport of water in the soil-plant-atmosphere system. *J. Appl. Ecol.*, **2**, 221-239.

Deardorff, J. W., 1977: A parameterization of ground-surface moisture content for use in atmospheric prediction models *J. Appl. Meteor.*, **16**, 1182-1185.

Deardorff, J.W., 1978: Efficient prediction of ground-surface temperature and moisture, with inclusion of a layer of vegetation, *J. Geophys. Res.*, **83**, 1889-1903.

Del Genio, A. D., 1993: Convective and large-scale cloud processes in GCMs. In: E. Raschtke and D. Jacob (Editors), Energy and Water Cycles in the Climate System. NATO ASI Series 1, Vol. 5, Springer, Berlin, pp. 95-121.

Dickinson, R. E., A. Henderson-Sellers, P. J. Kennedy, M. F. Wilson, 1986: Biosphere-Atmosphere Transfer Scheme (BATS) for the NCAR Community Climate Model, National Center for Atmospheric Research, Boulder, BO, Tech Note/TN-275+STR.

Dickinson, R. E., 1988: The force-restore model for surface temperatures and its generalizations. *J. Climate*, **1**, 1086-1097.

Dickinson, R. E., 1992: Land Surface Climate System Modeling, K. E. Trenberth, Ed., Cambridge University Press, Cambridge.

Eagleson, P. S., 1970: *Dynamic Hydrology*. McGraw-Hill Book Company, New York, 462 pp.

Eagleson, P. S., 1978: Climate, soil and vegetation, Parts 1-7. *Water Resour. Res.*, **14**, 705-776.

Eagleson, P. S., 1986: The emergence of global-scale hydrology. *Water Resour. Res.*, **22**, 6s-14s.

Eltahir, E. A. B., R. L. Bras, 1993: Estimation of the fractional coverage of rainfall in climate models. *J. Climate* 6 : 639-644.

Eyre, L. A., 1988: Water Resource Conflict. *Jamaica Journal*, 3-11.

Fincham, A., K. Ashton, 1967: Survey Expedition of Jamaica. *Trans. Cave Res. Group of GT. Britain.*

Food and Agriculture Organization (FAO), 1971: Groundwater Surveys in Two Areas of the Interior, Jamaica. Technical Reports : (1) Appraisal Report of the Pedro Plains, St. Elizabeth. (2) Appraisal Report of the Martha Brae Valley, Trelawny. (3) Water Resources Survey of the Montego River Basin.

Food and Agriculture Organization (FAO), 1972: Groundwater Surveys in Two Areas of the Interior, Jamaica. Technical Report No. 4, Summary of Hydrologic Reconnaissance on Moneague Area.

Food and Agriculture Organization (FAO), 1974: Development and Management of Water Resources, Jamaica. Technical Reports: (1) Rio Minho - Milk River Basin (2) Rio Cobre Basin (3) Dry Harbour Mountains - North Coast Basin (4) Negril Basin.

FAO/UNESCO, 1974: *Soil Map of the World*, 1:5 000 000. FAO, Paris.

Ford, D., P. Williams, 1989: *Karst Geomorphology and Hydrology*. UNWIN HYMAN press, London.

Freeze, R. A., J. A. Cherry, 1979: Groundwater, Prentice-Hall, Englewood Cliffs, New Jersey.

Gash, J. H. C., 1979: An analytical model of rainfall interception by forests. *Quart. J. Roy. Meteor. Soc.*, **105**, 43-55.

Gardner, W. R., D. Hillel, 1962: The relation of external evaporative conditions to the drying of soils. *J. Geophys. Res.*, **67**, 4319-4325.

Gleick, P. H., 1987: The Development and Testing of a water blance model for climate impact assessment: Modeling the Sacramento Basin, *Water Resources Research*, 23(6): 1049 - 1061.

Global Atmospheric Research Programme (*GARP*), 1979: World Meteorological Organization, GARP Publications.

Gregory, D., R. N. B. Smith, 1990: Canopy, Surface and Soil Hydrology. Unified Model Documentation Paper 25, Version 1. 19 pp.

Gross, M. G., 1964: Variations in the O^{18}/O^{16} and C^{13}/C^{12} ratios of diagenetically altered limestones in the Bermuda Islands. *J. Geol.*, **72** : 170-194.

Gvozdetskiy, N. A., 1965: Types of karst in the U. S. S. R. *Probl. Speleol. Res.*, 1 : 47-54.

Haaland, S. E., 1983: Simple and Explicit Formulas for the Friction Factor in Turbulent Pipe Flow, *Journal of Fluids Engineering*, vol. 105, pp 89-90.

Han, Y. J., 1988: Modelling and Simulation of the General Circulation of the Ocean. In: Physically-Based Modelling and Simulation of Climate and Climate Change, volume1, edited by M. E. Schlesinger, pages 465-508. Kluwer Academic Publishers.

Hanks, R. J., A. Klute, E. Bresler, 1969 : A Numerical Method for Estimating Infiltration, Redistribution, Drainage and Evaporation of Water from Soil. Water Resources Research, Vol. 5, No. 5, 1064 - 1069.

Hansen, J., G. L. Russell, D. Rind, P. Stone, A. Lacis, S. Lebedeff, R. A. Ruedy, L. Travis, 1983: Efficient three-dimensional global models for climate studies: Models 1 and 2. *Mon. Wea. Rev.* 111: 609-683.

Hilber, W. D., 1988: Modelling Sea Ice Thermodynamics and Dynamics in Climate Studies. In: Physically-Based Modelling and Simulation of Climate and Climate Change, volume1, edited by M. E. Schlesinger, pages 465-508. Kluwer Academic Publishers.

Hillel, D., 1975: Evaporation from bare soil under constant and diurnally fluctuating evaporativity. Soil Science 120 : 230-237.

Holton, J. R., 1992: *An Introduction to Dynamic Meteorology*, volume 48 of *International Geophysics Series*. Academic Press, Inc.

Hunt, B. G., 1985: A model study of some aspects of soil hydrology relevant to climatic modelling. *Quart. J. Roy. Meteor. Soc.*, **111**, 1071-1085.

Intergovernmental Panel on Climate Change (*IPCC*), 1990: World Meteorlogical Organization/United Nations Environmental Programme, Cambridge University Press.

Jarvis, P. G., 1976: The interpretation of the variations in leaf water potential and stomatal conductance found in canopies in the field. *Phil. Trans. Roy. Soc. London*, **273B**, 593-610.

Jarvis, P. G., K. G. McNaughton, 1986: Stomatal control of transpiration: scaling up from leaf to region. *Adv. Ecol. Res.*, **15**, 1-49.

Jianyun, Z., Z. Yiling, 1990: The Study and Application of a Rainfall-Runoff Model for Karst Regions. *Proc. Tropical Hydrology and Caribbean Water Resources*, 111-120.

Kaczmarek, Z., 1993: Water Balance Model for Climate Impact Analysis, ACTA Geophysica Polonica v.41 no. 4, 1 - 16.

Kuchler, A. W., 1983: *World map of natural vegetation*. Goode's World Atlas (16th ed.), 16-17, Rand McNally.

Leith, C. E., 1975: The design of a Statistical-Dynamical Climate Model and Statistical Constraint on the Predictability of Climate. In *The Physical Basis of Climate and Climate Modelling*. Global Atmospheric Research Programme (GARP), World Meteorological Organization, GARP Publications Series No. 16.

Leith, C. E., 1978: Predictability of Climate. *Nature*, 276:352-355.

Lettenmaier, D. P. T. Y. Gan, 1990: Hydrologic sensitivities of the Sacramento-San Joaquin River Basin, California, to global warming. *Water Resources Research* 26(1): 69 - 86.

Maloszewski, P., A. Zuber, 1990: Mathematical Modeling of Tracer Behavior in Short-Term Experiments in Fissured Rocks. *Water Resources Research,* vol 26, No. 7 : 1517-1528.

Manabe, S., J. Smagorinsky, R. F. Strickler, 1965:. Simulated climatology of a general circulation model with a hydrologic cycle. *Mon. Wea. Rev.*, **93**, 769-798.

Manabe, S., 1969: Climate and the ocean circulation: 1. The atmospheric circulation and the hydrology of the earth's surface. *Mon. Wea. Rev.*, **97**, 739-774.

Martel, E., 1910: Theory of Groundwater in Subtereanean karst. *Geography*, **21** : 126-130.

Matthews, E., 1983: Global vegetation and land use: new high-resolution data bases for climate studies. *J. Clim. Appl. Meteor.*, **22**, 474-487.

Matthews, E., 1984: Vegetation, land-use and seasonal albedo data sets: Documentation of archived data tape. NASA Technical Memorandum 86107, 12 pp.

Matthews, E., 1985: Atlas of archived vegetation, land-use and seasonal albedo data sets. NASA Technical Memorandum 86199, February 1985.

McCabe, G. J. Jr, D. M. Wolock, 1992: Effects of climate change and climatic variability on the Thornthwaite moisture index in the Delaware River Basin, *Climatic Change*, 143 - 159.

Mimikou, M. A., Y. S. Kouvopoulos, 1991: Regional climate change impacts: Impacts on water resources, Hydrologic Science Journal, 36(3): 247 - 258.

Mintz, Y., 1965: Very long-term global integration of the primitive equations of atmospheric motion. *WMO Tech. Note No. 66*, Geneva, pp. 141-155.

Moench, A., 1984: Double-Porosity Models for a Fissured Groundwater Reservoir with Fracture Skin. *Water Resources Research,* vol. 20, No 7: 831-846.

Monin, A. S., 1986: *An Introduction to the Theory of Climate.* Atmospheric Sciences Library. D. Reidel Publishing Company.

Moreno, L., I. Neretnieks, T. Eriksen, 1985: Analysis of Some Laboratory Tracer Runs in Natural Fissures. *Water Resources Research,* vol. 21, No 7: 951-958..

Morton, F. I., 1984: What are the limits on forest evaporation. *J. Hydrol.*, **74**, 373-398.

Nash, L. L., P. H. Gleick, 1993: The Colorado River and Climate Change: *The sensitivity of streamflow and water supply to variations in temperature and precipitation*, U. S. EPA 230-R-93-009.

Nemec, J, J. Schaake, 1992: Sensitivity of Water Resource Systems to Climate Variation, *Journal of Scientific Hydrology* 27(3): 327 - 343.

Nkemdirim, L. C., E. B. Jones, 1978: Flood regions in Jamaica. *Journal of Hydrological Sciences,* **23**, 63-83.

Noilhan, J., S. Planton, 1989: A simple parameterization of land surface processes for meteorological models, *Mon. Wea. Rev.*, **117**, 536-549.

Peixoto, J. P., A. H. Oort, *1995: Physics of Climate.* American Institute of Physics, New York, 4. edition.

Phillips, N. A., 1956: The general circulation of the atmosphere: A numerical experiment. *Q. J. Roy. Meteor. Soc.*, 82:123-164.

Pitman, A. J., 1988: The development and implementation of a new land surface

scheme for use in general circulation models, Ph.D. Thesis, Univ. Of Liverpool, U. K., 481 pp.

Pitman, A. J., 1991: A simple parameterization of sub-gridscale open water for climate models. *Clim. Dynamics*, **6**, 99-112.

Pitty, A. F., 1966: An Approach to the Study of Karst Water: Illustrated by Results from Poole's Cavern, Buxton. *Univ. Hull Occ. Paper Geogr.*, **5**.

Pulina, M., 1972: A comment on present-day chemical denudation in Poland. *Geogr. Polonica.* **23**, 45-62.

Richardson, L. F., 1922: *Weather Prediction by Numerical Process*, Cambridge University Press, London.

Riebsame, et al., (1994): *Rivers in :* As Climate Changes: International Impacts and Implications, Editors: Strzepek, K. and J. Smith. Cambridge University Press, Cambridge, U.K.Climatic Change, 13(1): 69 - 97.

Roberson, J. A., C. T. Crowe, 1990: *Engineering Fluid Mechanics*, Houghton Miffin Company, Boston.

Roques, H., 1969: A review of present-day problems in the physical chemistry of carbonates in solution. *Trans. Cave Res. Grp Gt Br.*, **11** : 139-164.

Rosenzweig, C., D. Hillel, 1993: Agriculture in a Greenhouse World. *National Geographic Research and Exploration.*

Rutter, A. J., 1975: The hydrological cycle in vegetation. Vegetation and the Atmosphere. Part 1, J. L. Monteith, Ed., Academic Press, London, 278 pp, 111-154.

Sellers, P. J., Y. Mintz, Y. C. Sud, A. Dalcher, 1986: A simple biosphere model (SiB) for use within general circulation models, *J. Atmos. Sci.*, **43**, 505-531.

Sellers, P. J., J. L. Dorman, 1987: Testing the SiB using point micrometeorological and biophysical data. *J. Clim. Appl. Meteor.*, **26**, 622-651.

Sellers, P. J., Y. Mintz, Y. C. Sud, A. Dalcher, 1988: A Brief Description of the Simple Biosphere Model (SiB). In: Physically-Based Modelling and Simulation of Climate and Climate Change, volume1, edited by M. E. Schlesinger, pages 307-330. Kluwer Academic Publishers.

Sellers, P. J., W. J. Shuttleworth, J. L. Dorman, A. Dalcher, J. M. Roberts, 1989: Calibrating the Simple Biosphere model for Amazonian tropical forest using field and remote sensing data. Part 1. : average calibration with field data, *J. App. Meteor.*, **28**, 727-759.

Sellers, P. J., 1992: *Biophysical Models of Land Surface processes.* Climate System Modeling, K. E. Trenberth, Ed. Kluwer Academic Publishers .

Shuttleworth, W. J., 1988b: Evaporation from Amazionian rain forest, *Proc. Roy. Soc. Lond.* **B 233**, 321-346.

Skelly, W. C., A. Henderson-Sellers, A. J. Pitman, 1991: Land surface data: Global climate modeling requirements. *Geophysical Information Systems and environmental Modeling*, M. F. Goodchild, B. O. Parks, L. T. Steyaert, Eds. Oxford University Press..

Skiles and Hanson, 1994: Responses of arid and semi-arid watersheds to increasing carbon dioxide and climate change as shown by simulation studies, *Climatic Change 26:* pg 377 - 397.

Smagorinsky, J., 1963: General circulation experiments with the primitive equations, 1. The basic experiment. *Mon. Wea. Rev.*, **93**, 99-164.

Smagorinsky, J., S. Manabe, J. L. Holloway, 1965: Numerical Results from a Nine Level General Circulation Model of the Atmosphere. *Mon. Wea. Rev.*, **93**, 727-768.

Smith, D. I., D. G. Mead, 1962: The solution of limestone. *Proc. Speleol. Soc. Univ. Bristol*, **9**: 188-211.

Sweeting, M. M., 1955: Hydrological Observations in Parts of the White Limestone Area in Jamaica. *Jour. Geol. Survey* Bulletin 2.

Sweeting, M. M., 1958: The Karstlands of Jamaica. *Jour. Geol. Survey*, **124**, 184-199.

Sweeting, M. M., 1972: *Karst landforms*, Macmillan, London.

Taylor, H. M., B. Klepper, 1978: The Role of Rooting Characteristics in the Supply of Water to Plants. *Adv. In Agron.* **30**, 99 - 128.

Tratman, E. K., 1969: *The Caves of Northwest Clare, Ireland.* Oxford University Press.

Trewartha, G. T., L. Horn, 1980: *An Introduction to Climate*. McGraw-Hill Book Co., New York, 5. edition.

Tselentis, G., 1985: An Investigation of the Relation Between Fissure Flow and Degree of Contact Area by an Electric Analogue Model. *Journal of Hydrology*, **78** : 325-330.

Verseghy, D. L., 1991: CLASS - A Canadian land surface scheme for GCMs, 1. Soil Model, *Int. J. Climatol.*, **11**, 111-133.

Versey, H. R., 1962: Older Tertiary limestones. In: V. A. Zans (Editor), *Synopsis of the Geology of Jamaica*. Geol. Surv. Dept., Kingston.

Warrilow, D. A., A.B.Sangster, A. Slingo, 1986: Modeling of land surface processes and their influence on European climate, *Dynamic Climatology Tech.* Note, No. 38, Meteorological Office, METO20, Bracknell, U. K., 94 pp.

Webb, R. S., C. E. Rosenzweig, E. R. Levine, 1991: A Global Data Set of Soil Particle Size Properties. NASA Technical Memorandum 4286.

Webb, R. S., C. E. Rosenzweig, 1993: Specifying land-surface characteristics in general circulation models: Soil profile data set and derived water-

holding capacities. Global Biogeochemical Cycles 7(1) : 97-108.

White, W. B., 1984: Rate processes: Chemical kinetics and karst landform development. In: *Groundwater as a Geomorphic Agent*, R. G. LaFleur, Ed. (Allen and Unwin, Boston), 227-248.

White, W. B., 1988: *Geomorphology and Hydrologyof Karst Terrains*. Oxford University Press.

White, M. N., M. O. Walters, S. Brooks, 1983: Water Resources Appraisal of the Upper Rio Cobre Basin. *Tech. Rep. Vol. 1.* Water Resources Division, Ministry of Local Government, Jamaica.

White, M. N., 1985: Groundwater Movement and Storage in Karstic Limestone Aquifers of Jamaica. *Jour. Geol. Soc. Jamaica*, **28**, 1-16.

Wilson, M. F., A. Henderson Sellers, 1985: A global archive of land cover and soil data for use in general circulation climate models. *J. Climatol.*, **5**, 119-143.

Wilson, M. F., A. Henderson Sellers, R. E. Dickinson, P. J. Kennedy, 1987a: Sensitivity of the Biosphere-Atmosphere Transfer Scheme (BATS) to the inclusion of variable soil characteristics, *J. Clim. Appl. Met.*, **26**, 341-362.

Xue, Y., P. J. Sellers, J. L. Kinter, J. Shukla, 1991: A simplified biosphere model for global climate studies, *J. Climate*, **4**, 345-364.

Yates, D. N., K. M. Strzepek, 1994: The impact of potential evapotranspiration methodology on the determination of river runoff. *IIASA working paper,* WP-94-96, Laxenburg, Austria.

Yates, D. N., K. M. Strzepek, 1994: Comparison of models for climate change assessment of river basin runoff. *IIASA working paper,* WP-94-45, Laxenburg, Austria.

Zans, V. A., 1958: On karst hydrology in Jamaica. *Soc. Intern. Hydrol. Sci.*, 2: 267-279.

Zobler, L., 1986: A world soil file for global climate modeling. NASA Tech. Memo. 87802.

IMAGE EVALUATION
TEST TARGET (QA-3)

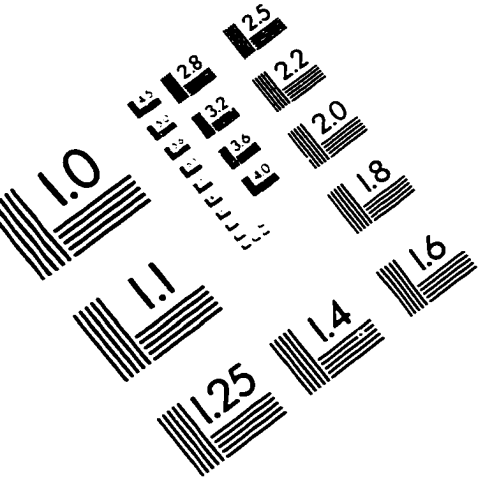

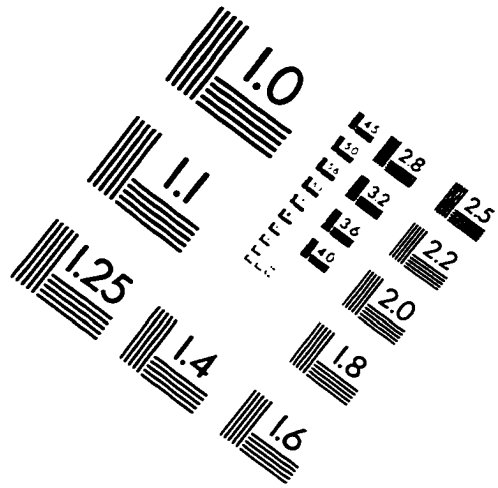

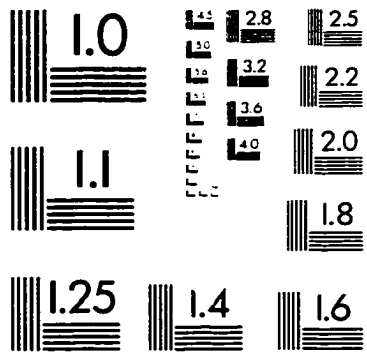

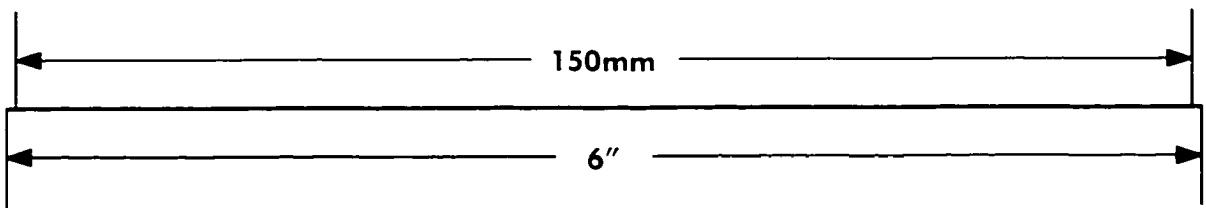

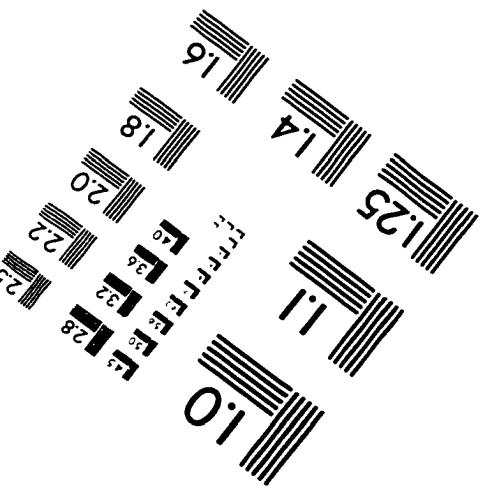

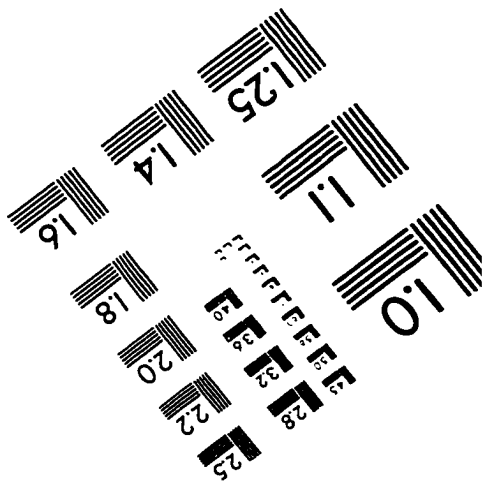

APPLIED IMAGE, Inc
1653 East Main Street
Rochester, NY 14609 USA
Phone: 716/482-0300
Fax: 716/288-5989